UNIVERSITY OF CALIFORNIA

Santa Barbara

Electrocatalysis for Energy Storage: Screening, Understanding and Improving Hydrogen Electrocatalysts in H_2-Br_2 Flow Batteries

A dissertation submitted in partial satisfaction of the

requirements for the degree Doctor of Philosophy

in Chemical Engineering

by

Nirala Singh

Committee in charge:

Professor Eric W. McFarland, Co-Chair

Professor Horia Metiu, Co-Chair

Professor Michael J. Gordon

Professor Michael F. Doherty

December 2015

The dissertation of Nirala Singh is approved.

_____

Eric W. McFarland, Committee Co-Chair

_____

Horia Metiu, Committee Co-Chair

_____

Michael F. Doherty

_____

Michael J. Gordon

May 2015

Electrocatalysis for Energy Storage: Screening, Understanding and Improving Hydrogen Electrocatalysts in H_2-Br_2 Flow Batteries

by

Nirala Singh

ACKNOWLEDGEMENTS

I would like to thank my parents, Jasprit and Teresa Singh, and brother for their support. I would also like to thank my two advisors, Professors Eric McFarland and Horia Metiu, who have been phenomenal mentors and excellent both at pushing me to work hard and giving me the freedom to try the many different projects that I was interested in. I would like to thank my other committee members, Professor Mike Gordon and Michael Doherty, for their support, and Professor Martin Moskovits for all his advice and expertise, and Professor Moskovits, Professor Galen Stucky and Professor Steve Buratto for allowing me use of their labs. I have been very fortunate to work directly with many excellent researchers, including Dr. Anna Ivanovskaya for helping to start me on the project that would end up being my thesis. I also had the pleasure of working extensively with Professor Syed Mubeen, who has been instrumental in many of the wonderful projects I have had the pleasure of working on, Dr. Sylvia Lee, Professor Jonas Baltrusaitis, Ches Upham, Dr. Ru-Fen Liu, Wei Cheng, Dr. Jonathan Burk, and Nick Economou. I would like to thank Dr. Alan Derk for being a wonderful fellow engineer and office-mate, and both Dr. Lauren Misch and Dr. Derk for being so welcoming when I joined the McFarland/Metiu lab. I greatly appreciate the phenomenal collaboration that we have had for the past four years with Kansas University, in particular Professor Trung Van Nguyen, Dr. Haley Kreutzer and Venkata Yarlagadda, and the rest of our NSF-EFRI RESTOR collaboration group. I would like to thank the visiting students and undergraduates who I have worked with, including Mark Seal, John Hiller, Amy Calgaro, Andreas Blumenstein, Andreas Poulsen, Sam Shaner, Robert Norton and Jarrod Lefton. I would like to thank all the members that have contributed to the amazing

UCSB User Facilities and Cleanroom, including Stephan Kraemer, Joe Doyle, Mark Cornish, Tom Mates, Youli Li, Miguel Zepeda, Brian Lingg, and others. I would also like to thank the many people in the Chemical Engineering offices for their invaluable help in all my day-to-day activities in the building, including Laura Crownover, the wonderful Pat White, Erica, Carina, and the rest of the staff. I would like to thank Air Products and Chemicals for the fellowship, and Dr. Fabrice Amy for his mentorship, as well as the University of Queensland and Celestien Warnaar for all the organizational help, as well as Conor Young, Matt Shaner and Tom McConnaughy.

VITA OF NIRALA SINGH
May 2015

EDUCATION

Bachelor of Science in Chemical Engineering, University of Michigan, Ann Arbor, December 2009 (summa cum laude)
Doctor of Philosophy in Chemical Engineering, University of California, Santa Barbara, June 2015 (expected)

PROFESSIONAL EMPLOYMENT

September 2010-Present	Ph.D Candidate: University of California-Santa Barbara Advisors: Eric W. McFarland and Horia Metiu • Synthesizing, characterizing, and testing electrocatalysts for a H_2-Br_2 flow battery • Artificial photosynthesis • Development of metal sulfide semiconductors • Electro-oxidation of organic wastewater
July 3 2014-August 29 2014	Staff: Dow Centre for Sustainable Engineering Innovation Supervisor: Eric McFarland • Technoeconomics of electrical energy storage • Technoeconomics of H_2-Br_2 flow battery
June 17 2013-August 23 2013	Intern: Air Products and Chemicals Energy Technology R&D Supervisor: Fabrice Amy • Technoeconomics of CO_2 capture for enhanced oil recovery
January 2010-August 2010	Intern: Transphorm, Inc. • Designing testing interface for GaN electrical power switches (possibly for smart grid incorporation)
June 2009-August 2009	Intern: Transphorm, Inc. • LabVIEW programming for device stressing system for GaN buffers, and characterization of device failures
January 2009-April 2009	Undergraduate Research: University of Michigan Advisor: Johannes Schwank • Biomass characterization for conversion to useful chemicals
July 2008-August 2008	Intern: Transphorm, Inc. • H_2 production from electrolysis and photoelectrolysis
June 2007-August 2007	Employee: University of Michigan • Development of a 'Solar Cart' for ENG 100; to charge and discharge batteries using solar cells

PUBLICATIONS

1. D.M. Fabian, S. Hu, **N. Singh**, F.A. Houle, T. Hisatomi, K. Domen, F. Osterloh, S. Ardo, Particle Suspension Reactors and Materials for Solar-Driven Water Splitting, submitted to Energ Environ. Sci., (2015)

2. **N. Singh**, E.W. McFarland, Levelized cost of energy and sensitivity analysis for the hydrogen-bromine flow battery, J. Power Sources, (2015), *288*, pp 187-198
3. M. Seal, **N. Singh**, E.W. McFarland, J. Baltrusaitis, Electrochemically Deposited Sb and In Doped Tin Sulfide (SnS) Photoelectrodes, J. Phys. Chem. C, (2015), *119*, pp 6471-6480
4. T. Nguyen, J. Masud, **N. Singh**, E. McFarland, M. Ikenberry, K. Hohn, C. Pan, and B. Hwang, A RhxSy/C Catalyst for the Hydrogen Oxidation and Hydrogen Evolution Reactions in HBr, J. Electrochem. Soc., (2015), *162*, pp F455-F462
5. **N. Singh**, J. Hiller, H. Metiu, E. W. McFarland, Investigation of the Electrocatalytic Activity of Rhodium Sulfide for Hydrogen Evolution and Hydrogen Oxidation, Electrochim. Acta, (2014), *145*, pp 224-230
6. S. Mubeen, J. Lee, W. Lee, **N. Singh**, G. D. Stucky, M. Moskovits, On the Plasmonic Photovoltaic, ACS Nano, (2014), *8*, pp 6066-6073
7. J. Masud, J. Walter, T. V. Nguyen, G. Liu, **N. Singh**, E. McFarland, H. Metiu, M. Ikenberry, K. Hohn, C. Pan, B. Hwang, Synthesis and Characterization of RhxSy/C Catalysts for HOR/HER in HBr, ECS Trans., (2014), *58*, pp 37-43
8. **N. Singh**, D. C. Upham, R. Liu, J. Burk, N. Economou, S. Buratto, H. Metiu, E. W. McFarland, Investigation of the Active Sites of Rhodium Sulfide for Hydrogen Evolution/Oxidation Using Carbon Monoxide as a Probe, Langmuir, (2014) *30*, pp 5662-5668
9. **N. Singh**, S. Mubeen, J. Lee, H. Metiu, M. Moskovits, E. McFarland, Stable electrocatalysts for autonomous photoelectrolysis of hydrobromic acid using single-junction solar cells, Energ Environ. Sci., (2014), *7*, pp 978-981
10. **N. Singh**, C. Upham, H. Metiu, E. W. McFarland, Gas-Phase Chemistry to Understand Electrochemical Hydrogen Evolution and Oxidation on Doped Transition Metal Sulfides, J. Electrochem. Soc., (2013), *160* (10), pp A1902-A1906
11. T. V. Nguyen, H. Kreutzer, V. Yarlagadda, E. McFarland and **N. Singh**, HER/HOR Catalysts for the H2-Br2 Fuel Cell System, ECS Trans., (2013), *53* (7), pp 75-81
12. S. Mubeen, J. Lee, **N. Singh**, S. Kramer, G. D. Stucky, M. Moskovits, An autonomous photosynthetic device in which all charge carriers derive from surface plasmons, Nature Nano., (2013), *8*, pp 247-251
13. S. Mubeen, J. Lee, **N. Singh**, M. Moskovits, E. W. McFarland, Stabilizing inorganic photoelectrodes for efficient solar-to-chemical energy conversion, Energ Environ. Sci., (2013), *6* (5), pp 1633-1639
14. S. Mubeen, **N. Singh**, J. Lee, G. D. Stucky, M. Moskovits, E. W. McFarland, Synthesis of Chemicals Using Solar Energy with Stable Photoelectrochemically Active Heterostructures, Nano Lett., (2013), *13* (5), pp 2110-2115
15. A. Ivanovskaya, **N. Singh**, R. Liu, H. Kreutzer, J. Baltrusaitis, T.V. Nguyen, H. Metiu, E. McFarland, Transition Metal Sulfide Hydrogen Evolution Catalysts for Hydrobromic Acid Electrolysis, Langmuir, (2013), *29* (1), pp 480-492
16. W. Cheng, **N. Singh**, J.A. Macià-Agulló, G.D. Stucky, E.W. McFarland, J. Baltrusaitis, Optimal experimental conditions for hydrogen production using low voltage electrooxidation of organic wastewater feedstock, Int. J. Hydrogen Energy, (2012), *37* (18), pp 13304-13313

AWARDS

UM James B. Angell Scholar, March 2009

Heslin Fellowship, University of California, Santa Barbara, 2010

ConvEne IGERT Fellowship, University of California, Santa Barbara, 2011

Air Products and Chemicals Fellowship, University of California, Santa Barbara, 2013

FIELDS OF STUDY

Major Field: Electrochemical energy storage

ABSTRACT

Electrocatalysis for Energy Storage: Screening, Understanding and Improving Hydrogen Electrocatalysts in H_2-Br_2 Flow Batteries

by

Nirala Singh

In a transition from a society powered by greenhouse gas-emitting fossil fuels to one powered by renewable energy, energy storage can play a key role. Of the many technology options, one of the most promising is flow batteries, especially the hydrogen-bromine flow battery, which is the focus of this dissertation. To investigate the economic feasibility of a hydrogen-bromine battery as an energy storage device, the levelized cost of energy was calculated, and a sensitivity analysis indicated that the largest improvements to the cost of energy storage will come from improving the system lifetime and efficiency. The key scientific challenges to doing so require creating stable and efficient electrocatalysts. By electrochemically and chemically screening hundreds of metal sulfide materials selected based on our best chemical knowledge, ruthenium and rhodium based metal sulfides were determined to have sufficient stability to operate as hydrogen-bromine electrocatalysts, and exhibit promising activity for hydrogen evolution and oxidation. Incorporating cobalt and nickel into ruthenium sulfide greatly increased the electrocatalyst activity, which we came to understand through combined efforts of theory and gas-phase measurements. The increased

activity is most likely due to increased rates of charge-transfer in the hydrogen evolution and oxidation reaction. However, even with incorporation of dopant atoms, the ruthenium sulfide compounds had relatively low hydrogen oxidation activity, possibly due to its semiconducting properties. Rhodium sulfide showed higher activity than even the best ruthenium sulfide materials, but still lower than platinum, although with much improved stability over platinum. Through selective synthesis of different rhodium sulfide phases, as well as poisoning experiments coupled with spectroscopy and density functional theory calculations, the activity of rhodium sulfide was determined to come from the metallic phases $Rh_{17}S_{15}$ and Rh_3S_4, in particular the metal sites on these compounds (rather than on sulfur atoms). By selectively forming these phases, the rhodium sulfide showed the highest activity, with the Rh_2S_3 and RhS_2 phases showing low activity. Efforts to improve the rhodium sulfide by incorporation of dopant atoms were not as effective as for the ruthenium sulfide compounds, as transition metals such as Fe, Co, Ni and Cu caused the formation of an inactive rhodium thiospinel phase, and platinum group metal dopants showed no improvement in the rhodium sulfide on a metal sulfide-area basis. The greatest improvements in the activity of the electrocatalyst come from smaller particle sizes of $Rh_{17}S_{15}$ and Rh_3S_4 (increased dispersion), and minimization of inactive rhodium sulfide phases.

TABLE OF CONTENTS

Preface

This dissertation describes our investigation of electrocatalysts for electrochemical energy storage in hydrogen-bromine based flow batteries. The first chapter discusses the current state of electrical energy storage and the potential for use of hydrogen-bromine flow batteries. A brief review of the theoretical framework used for electrocatalysts and the challenges that are addressed in this work is provided. An economic sensitivity analysis of the hydrogen-bromine flow battery system is developed in Chapter 2 and highlights the rationale for the work in this thesis to improve the hydrogen bromine flow battery. The methods and results of screening metal sulfide electrocatalysts for activity and stability is then presented (Chapters 3, 4 and 5). The methodologies and results of experiments used to understand the structure-composition activity relationships of the catalysts are described in Chapters 6-8, followed by work done to improve the catalysts through our understanding of their activity for the desired reactions (Chapter 9).

Chapter 1 discusses electrical energy storage, flow batteries and gives a brief background on electrochemistry and electrocatalysis as an introduction to the work in this thesis. It also includes the methodology for testing flow cells and electrocatalysts, which will be used heavily throughout the thesis.

Chapter 2 discusses the economics of electrical energy storage and the motivation behind developing robust electrochemical systems for electrical energy storage. A sensitivity analysis and detailed discussion of the hydrogen-bromine flow battery specifically considered here is included, as well as a discussion of the importance of electrocatalysts on electrochemical energy storage.

Chapter 3 discusses the synthesis and screening of mixed metal sulfides for hydrogen evolution in hydrobromic acid. Rhodium sulfide and ruthenium sulfide are identified as active

materials, with cobalt doping shown to improve the hydrogen evolution activity of ruthenium sulfide considerably.

Chapter 4 discusses the use of rhodium sulfide and cobalt ruthenium sulfide in a hydrogen-bromine flow cell. The stability of the rhodium sulfide is shown compared to platinum by testing in a bromine/bromide environment.

Chapter 5 provides further characterization of the rhodium sulfide electrocatalyst, as well as its demonstration when coupled to a semiconductor system for solar-driven photoelectrochemical electrolysis of hydrobromic acid. This work serves to show that even without a membrane system rhodium sulfide has greatly enhanced stability in hydrobromic acid, especially compared to platinum.

Chapter 6 focuses on using hydrogen-deuterium exchange experiments as a descriptor for hydrogen evolution and oxidation, both for metals and metal sulfides. This work investigates the effect of cobalt-doping on ruthenium sulfide, and indicates that charge transfer may play a larger role in the improvement of activity than surface chemistry, for this particular metal sulfide.

Chapter 7 presents a technique to identify the active site of hydrogen evolution and oxidation on rhodium sulfide. By using a selective poison of carbon monoxide, the active site of rhodium sulfide is identified to be a metal cluster in the Rh_3S_4 phase, or metal atoms in $Rh_{17}S_{15}$.

Chapter 8 demonstrates selective synthesis of the rhodium sulfide phases to further evaluate that the $Rh_{17}S_{15}$ and Rh_3S_4 phases are active, as compared to the less active Rh_2S_3 phase of rhodium sulfide. This holds for both the unsupported and carbon-supported samples. Rotating disk electrode measurements are also presented to indicate that the most active rhodium sulfide catalyst is mass-transport and not charge-transport limited for hydrogen oxidation.

Chapter 9 presents results of incorporating non-Rh metals with Rh during synthesis of metal sulfides. For certain metals a rhodium thiospinel with low activity (despite metal-sulfur stoichiometry similar to Rh_3S_4) are formed, while for platinum group metals the activity is not significantly changed, leaving the major improvements to be made by increasing electrocatalyst dispersion.

I. Electrical Energy Storage

A. Importance of energy storage

Energy transformation provides for the essentials of life (food, shelter, clean water). The availability of low-cost energy supplies enables the many wonderful technologies that allow human life today to be easier and more enjoyable that at any other time in history. For the past century, energy demand has been satisfactorily provided by abundant fossil fuels which originate from sunlight in past millennia. The ease with which these finite resources can be pulled out of the earth is being drastically reduced as they are depleted and their potentially harmful combustion products are motivating a shift to other, low-cost sustainable energy sources in order to maintain the high quality of life that we currently enjoy. Because of the intermittent nature of several of these potential replacement resources for electricity generation (wind, and solar especially), there must be reliable, inexpensive electrical energy storage systems available to make the best use of these new energy sources.

1. Current energy storage methods

Today, the largest capacity for electrical energy storage is pumped hydroelectric [1], because its cost is comparable to that of producing electricity from fossil fuels. If the cost of producing and storing renewable energy is higher than that of producing on-demand electricity, there is no economic advantage to switch to intermittent renewable energy sources (barring subsidies, carbon taxes, etc.). Unfortunately, many of the best pumped water locations for energy storage have already been tapped, so if further energy storage is required, it must make use of other technologies, which need to be capable of providing large-scale electrical energy storage. Energy storage systems that have been considered

include; flywheels, capacitors, compressed air, and electrochemical energy storage (batteries). Batteries are one of the most well-known forms of electrical energy storage and are deployed on small scales in laptop and car batteries.

Electrical energy storage systems useful for enabling renewable energy sources will need to store electrical energy on a large scale and at low cost. For grid scale systems, the drivers are slightly different than have been considered for transportation (fuel cells), and system size and weight is a smaller factor in determining the optimum systems [2]. The main drivers for energy storage systems will be scalability, durability (high number of charge/discharge cycles), and low capital and operating costs. Capacitors and flywheels have several applications for energy storage but are somewhat limited due to materials, and compressed air suffers from the same terrain limitations as pumped hydroelectric [3]. Electrochemical energy storage has the potential to meet the power and energy demands of large scale storage, if systems can be developed to match the efficiency and capital cost requirements needed to make the overall cost of energy competitive with current electricity production.

2. Electrochemical energy storage

There are many different electrochemical energy storage systems, but the common theme is that electricity is used to drive an oxidation reaction (at the anode) and reduction reaction (at the cathode) to ‘charge’ solid electrodes (solid electrode batteries) or electrolytes (flow battery), so that at a later point the battery can be discharged (by running the reactions in reverse) to recover the stored electrochemical potential as electricity [3]. Hybrid flow/solid electrode batteries also exist, where one of the reactions is that of a flow battery,

and the other is that of a solid electrode battery. The focus of this thesis will be on flow batteries, which are also sometimes referred to as flow cells or fuel cells.

B. Flow batteries

Flow batteries have an advantage over static batteries in decoupled power and energy, as the fuel (in the form of a charged set of redox couples) is stored externally, not internally as in a traditional solid electrode battery. This means that the quantity of stored electrochemical potential energy can be easily increased in magnitude to accommodate larger energy demands, without needing to increase the power of the system. The redox couples are electrochemically cycled between a charged and discharged state as the electrolyte flows past a set of electrodes where the electrochemical reactions take place (Figure 1).

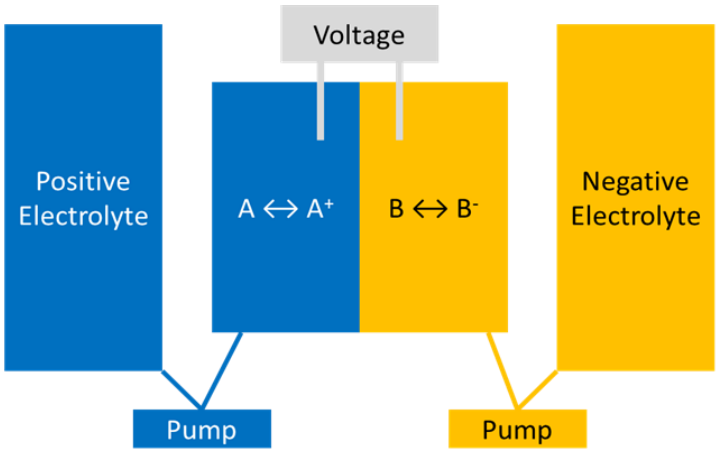

Figure 1. Diagram of a flow cell system, during charge, the positive electrolyte is oxidized at the positive electrode (A to A^+) and the negative electrolyte is reduced at the negative electrode (B to B^-). During discharge, the electrolytes are run in the reverse direction.

1. History of flow batteries

Solid electrode batteries have a long history, including many well-known batteries such as lead-acid car batteries and lithium-ion laptop batteries, but flow battery research

began in earnest in the early 1970s (and extensive work has been done on fuel cells, which are flow cells that are run in only the discharge direction). Some of the first flow cells that have been investigated are iron-chromium, investigated by NASA, where iron and chromium ions were circulated and oxidized/reduced to store electricity [3]. At a similar time, hybrid flow batteries such as zinc-bromine, zinc-chlorine were developed, where the Zn shifts between metallic Zn (solid) and zinc ions, and the halide cycles between halide ions (Br^- or Cl^-) and halogen (Br_2 or Cl_2) [2]. Vanadium has been a commonly used electrolyte, either in all vanadium or vanadium-bromine batteries. Another system includes bromine-polysulfide, which has been scaled up to 15 MW/120 MWh (one of the largest systems) [3]. Other possible full flow battery systems include hydrogen-oxygen, hydrogen-bromine or hydrogen-chlorine and hybrid flow batteries such as zinc-nickel and zinc-cerium.

2. Flow battery challenges

The major issue with the deployment of flow batteries or any large energy storage system is the cost of the electrical energy stored and delivered, which must compete with generation costs. The considerations are up-front capital costs, operation and maintenance costs, and longevity. The costs can be increased if efficiency is lowered by ohmic (losses due to resistive heating), mass transport or kinetic (discussed later) losses (Figure 2). All of these efficiency losses reduce the cost-effectiveness of the system.

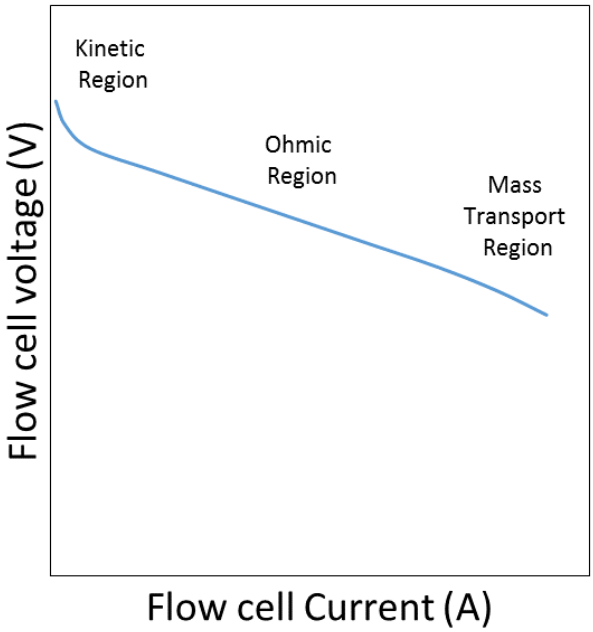

Figure 2. Flow cell during discharge and the regions of ohmic, mass transport and kinetic losses

The total cost of operating a battery, including capitals costs and operating costs must economically compete with fossil fuels such as natural gas and coal. The levelized cost of electricity is the metric by which these different systems can be compared and is considered in greater detail in Chapter 2.

3. Hydrogen-bromine flow battery

For a large-scale system, of the possible electrochemical configurations, a flow battery using H_2 and Br_2 is one of the most efficient and cost-effective methods for energy storage [4]. Advantages include lower electrode reaction losses than many other flow battery systems (leading to higher efficiencies as discussed in the following section), high power density, high energy density and reliability [5–7]. H_2-Br_2 batteries also have an advantage over H_2-Cl_2 batteries in that the Br_2 vapor pressure is lower than Cl_2 [8].

The H_2-Br_2 cell consists of a hydrogen half reaction:

$$H_2 \leftrightarrow 2H^+ + 2\,e^- \qquad 0.0V \text{ vs. NHE}$$

that occurs at a hydrogen electrode (anode during discharge) which is separated from the bromine electrode (cathode during discharge) by a proton-exchange membrane, which allows the transport of the protons. The reaction occurring at the counter electrode is the bromine half reaction:

$$Br_2 + 2e^- \leftrightarrow 2Br^- \qquad 1.09V \text{ vs. NHE}$$

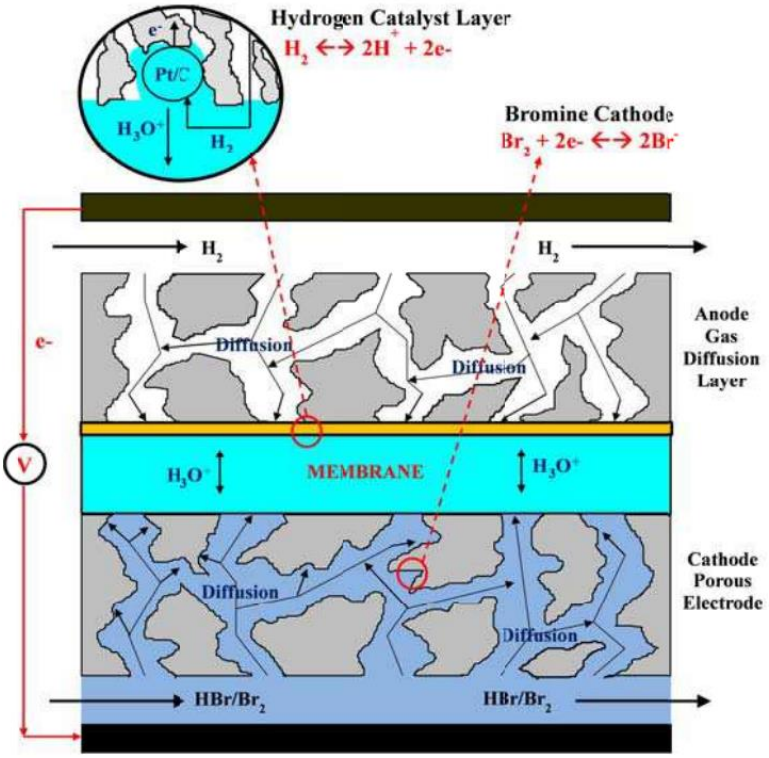

Figure 3. Schematic of a hydrogen-bromine flow battery. Reproduced with permission from ECS Trans., **53**, 75 (2013). Copyright 2013, The Electrochemical Society.

The bromine reaction proceeds rapidly even on carbon without any precious metals used as the bromine electrode [7,9]. The fast kinetics and high faradaic efficiency of the bromine reaction means very high electrical conversion efficiencies, so long as an active, stable electrocatalyst (catalyst for an electrochemical reaction) is used for hydrogen evolution (during charge) and hydrogen oxidation (during discharge).

C. The role of electrocatalysts in hydrogen-bromine flow batteries

Unlike the bromine reaction, the hydrogen reaction requires an electrocatalyst to reduce the activation barrier so that the reaction can proceed efficiently at appreciable rates. To understand electrocatalysts it is useful to review the Nernst potential, overvoltages, and materials stability.

1. Nernst potential

The electrochemical potential at which electrochemical reactions occur is governed by the Nernst potential.

$$E_{cell} = E^0_{cell} - \frac{RT}{zF} \ln Q$$

E_{cell} = Cell potential E^0_{cell} = Cell potential at standard conditions

F = Faraday constant z = number of electrons in electrode reaction

R = gas constant T = temperature

Q = ratio of activity of products and reactants

The reactions of interest for the H_2-Br_2 flow cell, and their potentials at standard conditions are:

$2H^+ + 2\ e^- \leftrightarrow H_2$ 0.0V vs. NHE

$2Br^- \leftrightarrow Br_2 + 2e^-$ 1.09V vs. NHE

Thus the overall reaction is:

$2\ H^+ + 2\ Br^- \leftrightarrow H_2 + Br_2$ $E_{cell} = 1.09V$

Thus by storing electricity in H_2 and Br_2, 1.09 eV is stored per charge transfer. The efficiency at which this can be recovered is dependent on the overvoltages of the individual

surface reactions. In practice the open circuit voltage will change beyond what the Nernst potential predicts [8].

2. Overvoltages

The overvoltages (η) are essentially the potential that is lost due to driving an electrochemical reaction (see Figure 4).

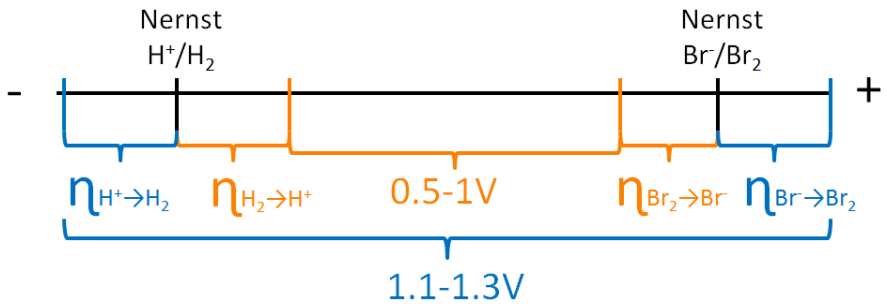

Figure 4. Overvoltages of H_2-Br_2 flow battery

During hydrogen evolution there is a current-dependent overvoltage at the hydrogen electrode that means the potential applied must be below 0.0V vs. NHE, while the corresponding bromine electrode (doing bromide oxidation when H_2 is evolved on the counter electrode) must be positive of 1.09V vs. NHE. Thus, to produce H_2 and Br_2 from HBr, the voltage required is, in reality, greater than the 1.09V that is required by the Nernst equation. During this process, known as electrolysis, the hydrogen electrode is the cathode and the bromine electrode is the anode. During discharge, for H_2 and Br_2 forming HBr, the voltage will be less than 1.09V, due to the overvoltages of $H_2 \rightarrow H^+$ and $Br_2 \rightarrow Br^-$. During discharge, the hydrogen electrode becomes the anode and the bromine electrode becomes the cathode.

The goal of the electrocatalysts in a H_2-Br_2 flow cell is to minimize these overvoltages so that the voltage recovered is as close to the voltage supplied as possible. The

efficiency is essentially the voltage recovered over the voltage provided, so long as the current supplied is the same in both cases.

The activity of an electrocatalyst and its influence on the overvoltage ideally will follow the Butler-Volmer equation.

$$j = j_0 \left\{ \exp\left[\frac{\alpha_a n F \eta}{RT}\right] - \exp\left[\frac{\alpha_c n F \eta}{RT}\right] \right\}$$

α_a = transfer coefficient for anode α_c = transfer coefficient for cathode

F = Faraday constant n = number of electrons in electrode reaction

R = gas constant T = temperature

η = overvoltage ($E - E_{eq}$) voltage beyond Nernst potential

The exchange current density (j_0) dictates the activity of the catalyst in many cases. Based on this equation, a catalyst with a high exchange current density for hydrogen evolution/oxidation would be ideal for the hydrogen electrode. In practice, the Butler-Volmer equation will not fit many catalysts, due to changes in the catalyst during oxidation, and other non-idealities, meaning it is necessary to verify that the catalyst can both do hydrogen evolution and hydrogen oxidation.

The Tafel equation is a simplistic form of the Butler Volmer equation. This is very commonly used to describe flow cell activity.

$$\Delta V = A \ln\left(\frac{i}{i_0}\right)$$

ΔV = overpotential i = current density

A = Tafel slope i0 = exchange

3. Electrocatalyst stability

In addition to being kinetically active for both directions of the half-cell reaction, these electrocatalysts must be stable in the HBr/Br_2 electrolyte. Mechanisms of corrosion may include formation of soluble compounds that dissolve into the electrolyte, as well as poisoning by bromide ions that block the active sites. It is important for the efficiency and longevity of the system that the electrocatalyst be stable. Although the hydrogen electrocatalyst is protected from bromide and bromine by the proton-exchange membrane in theory, in reality the bromide and bromine can crossover and affect the activity of the hydrogen electrocatalyst.

D. Methodology for evaluating electrocatalysts

Although the final test of electrocatalyst performance will be the performance of the flow cell, the electrocatalysts can be evaluated independently of the flow cell through many different methods. For hydrogen evolution, the exchange current density is commonly referenced as a way of understanding the activity of a catalyst. In the field of catalysis there are many methods for synthesis and characterization of catalysts outside of cells that will be discussed here as well as theoretical methods for interpreting experimental results.

1. Electrocatalytic testing methods

Cyclic voltammetry is used to understand electrochemical reactions where certain redox couples are oxidized and reduced. This can be used also to understand charge-transfer. To determine capacitance, the dependence of the anodic and cathodic currents on scan rate can be determined using cyclic voltammetry.

Rotating disk electrodes are used to measure the kinetics of electrochemical reactions. The electrode being investigated is fixed at the end of a rotating rod whose angular velocity can be controlled. As the disk is rotated, the solution is dragged by the disk and away from the center of the electrode so that new electrolyte flows in a laminar fashion to the electrode (Figure 5).

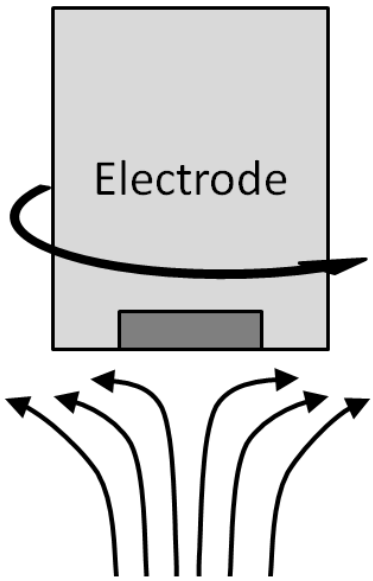

Figure 5. Rotating disk electrode

By controlling the mass transfer for the system, rotating disk electrodes are commonly used to evaluate electrocatalysts for activity by measuring the current as a function of overvoltage.

2. Catalyst synthesis

There are many standard preparations for synthesizing solid catalysts. In our work we relied most commonly on solid state synthesis using precursor salts dissolved in water then dried onto carbon (or unsupported). These salts are then exposed to a sulfur source (either volatilized sulfur or hydrogen sulfide gas) at high temperatures, which converts the chloride

or nitrate salts to a metal sulfide. This method of synthesis, when done on carbon, allows nanometer sized crystals to be formed, which maximizes the surface area of the catalyst.

3. Catalyst characterization

There are several different types of characterization methods to understand the catalyst that will be investigated. Crystalline phases that are present can be determined by measuring how X-rays diffract (XRD) in the lattice structure, giving information on long range order, but with less information to be gained from the amorphous structure of the catalyst. X-ray photoelectron spectroscopy (XPS) uses excitation of the surface (approximately top 10-20 nm) with X-rays and measurement of the kinetic energy of the excited electrons to determine binding energies, which can then be used to determine elemental composition as well as oxidation state (as oxidation state influences the binding energy). XPS is in particular relevant to catalysis as the catalyst surface is usually the most important for the reactivity. However, the ultra-high vacuum (UHV) required for XPS means that the surface may be quite different, especially from electrochemical systems where water and ions can bind to the surface and change the properties of the catalyst. Raman is a technique of exciting the catalyst using a laser to excite a sample and measuring the loss in energy after the excited bonds relaxes, reemitting a photon. This technique can give valuable information about the samples structure and bonds, and has the advantage of not being a UHV technique. Infrared Spectroscopy is a complementary technique to Raman, where the absorption of light is measured rather than the reemitted light from a laser pulse, as used in Raman. Another technique which is sometimes referred to as spectroscopy, although it does not strictly involve interaction between the sample and light is known as temperature

programmed desorption, where the temperature at which an adsorbed species desorbs is used to understand the binding strength of that species to the catalyst surface.

4. Theoretical methods

In addition to experimental techniques used to understand the catalyst, calculations have been useful in understanding the activity of catalysts, and in particular the activity of hydrogen evolution on metals [10]. The binding energy of atoms onto catalyst surfaces (which can be calculated using Density Functional Theory) can help to understand activity through the use of Brønsted-Evans-Polanyi relations and the Sabatier principle. Brønsted-Evans-Polanyi relations indicate that the activation energy between two 'similar' reactions is proportional to the difference of their reaction energy. The Sabatier principle uses this concept to estimate that the optimum intermediate binding energy for a catalyst is as close to the average energy of the product and reactant as possible, thus neither binding too strongly or too weakly. For example, for the hydrogen evolution, if the reactant (a proton and an electron) and the product (a hydrogen molecule) are both used as the reference energy of 0, the ideal hydrogen binding energy to a catalyst for this reaction is close to 0. Metals such as Pt have hydrogen binding energies close to zero, so are active for hydrogen evolution and oxidation. Thus, metals that have calculated hydrogen binding energies close to zero are likely to have high hydrogen evolution and oxidation activity.

Calculations can also be used to understand the effect of poisoning on catalysts surfaces. For example, if a poison molecule, such as carbon monoxide, has a stronger binding energy than a reactant (such as hydrogen), it is likely that the carbon monoxide could bind to the site and block a reaction from occurring.

E. State-of-the-art in electrocatalysts

For a flow battery system, a major challenge is the hydrogen electrode, where a electrocatalyst must be capable of *both* hydrogen oxidation as well as hydrogen evolution, while maintaining stability in HBr and Br_2. The main electrochemical systems that operate in corrosive halide media are the previously attempted H_2-Br_2 or H_2-Cl_2 energy storage systems, chloralkali process that has been used industrially for decades, where the anode reaction is the production of chlorine in an acidic environment, and hydrochloric acid electrolysis.

1. Hydrogen-bromine flow cell electrocatalysts

For the previously used H_2-Br_2 flow cells, platinum group metals are the most common hydrogen electrocatalyst and have been used for most systems described in the literature [6,7,11,12]. Platinum is corroded in bromine/bromide environments, but thick metal films can be used such that the corrosion rate can allow for longer lifetimes [13]. However, nanoparticulate, highly active catalysts such as those used for H_2-O_2 fuel cells would be ideal. Nanoparticulate metals such as platinum supported on carbon, though very active for hydrogen evolution [11,14], generally suffer from issues such as bromide poisoning which reduces their activity [11,15,16].

2. Chloralkali electrocatalysts

Years of work have been put into developing structurally stable anode electrodes for chloralkali plants, which is one of the main triumphs of electrocatalysis [17]. However the issues in these systems are somewhat different than the H_2-Br_2 system, as the cathode (hydrogen evolution) is in a basic media, meaning metals that are unstable in acid (such as

nickel) can be used. The main electrocatalyst breakthrough for the chloralkali system is the $RuO_2/IrO_2/TiO_2$ 'dimensionally stable anode' which greatly improved the performance of the systems beyond the previously used carbon anodes, which had high overvoltages and would rapidly deteriorate in the presence of co-evolved O_2 and require costly shutdowns [17]. We hope to emulate the success of these systems by developing a similarly stable hydrogen electrode that will not be the limiting factor of a H_2-Br_2 system. Although the actual $RuO_2/IrO_2/TiO_2$ electrodes may not be the solution to the H_2-Br_2 electrocatalyst issue, it certainly serves as guidance to ways to approach solving such an issue.

3. Hydrochloric acid electrocatalysts

Commercial hydrochloric acid electrolysis consists of an oxygen reduction cathode using metal chalcogenide electrocatalysts which may serve as a starting point for potential materials [18,19]. The oxygen reduction electrocatalyst that is currently used for HCl electrolysis is Rh_xS_y/C. Tungsten carbides have been found to be instable in the electrolyte [19]. What remains to be seen is if the metal sulfides are active for hydrogen evolution and hydrogen oxidation. Some metal sulfides (MoS_2, RuS_2) [20,21], as well as some metal oxides such as ruthenium oxide [22,23], appear to be inactive for hydrogen oxidation, although active for hydrogen evolution. For RuO_2, this is believed to be because the reduced sites that are necessary for the electrocatalysts to occur are only formed under a cathodic potential, and cannot be kinetically formed by H_2 gas. Doping of metal sulfides has been seen to increase the hydrogen evolution activity [24,25], and motivates investigation into the effect of doping for electrocatalysts. The effect of doping on molybdenum disulfide, is believed to be the introduction of new active sites for hydrogen evolution, or improvement in the activity of the preexisting electrocatalytic sites [25,26], and we wish to understand

whether similar effects are seen in different metal sulfides that may also be of interest in our systems. Compositional modifications and doping may serve to produce electrocatalysts that behave as bidirectional electrocatalysts, successful for both the charging and discharging phase of the flow cell reaction.

F. Motivation and objectives of this thesis work

Currently, there is no stable and efficient electrocatalyst for the HBr flow cell system. The overarching goal of this project is to develop and understand electrocatalysts that will be stable and active for use in the interconversion of HBr to H_2-Br_2 for the purpose of energy storage. This will include building on the existing literature and expanding the field with new catalysts that are optimized for the conditions of the H_2-Br_2 flow battery.

In this dissertation several questions will be addressed including:

1) How important is the electrocatalyst in determining the levelized cost of electricity of stored energy in a H_2-Br_2 flow battery?
2) Can we identify electrocatalysts that are active for HER and HOR while maintaining stability in the presence of bromide and bromine?
3) What are the relationships between electrocatalyst structure/composition and activity for HER/HOR and what are the active sites?
4) How can we improve existing, stable electrocatalysts for HER/HOR using the understanding of the structure/composition/activity relationships?

We hypothesize that stable and active metals, metal oxides and metal sulfides exist and that be selectively screening candidates we can identify interesting electrocatalysts and eliminate unstable and inactive electrocatalysts. We use both traditional methods as well as high-throughput screening methods such as parallel investigation of the electrochemical

reactions, and rapid synthesis to map a space of interesting materials. Screening of stability can easily be done by eliminating those catalysts that are corroded in the electrolyte, as well as looking at the wealth of corrosion literature available for HBr/Br_2.

For the interesting catalysts that show promise for activity and stability, we use characterization methods such as those described previously to understand what contributes to the activity. The history of catalysis activity indicates that the active site is not always the site that is most abundant in the catalyst, and we will need to use techniques to understand how the reactants interact with the catalyst surface, and which of these interactions actually go on to form the final product and which merely serve as bystander reactions. It is also important for us to understand how the catalyst behaves while the reaction is undergoing, which may be different than under ex situ conditions.

We further hypothesize that the activity for both HER and HOR can be improved, by doping and selective synthesis of the active sites, while maintaining the stability in the corrosive environment. Doping has shown great promise in improving the catalytic activity of many materials, by modifying the electronic structures of the catalyst. Once we understand what is required to have an active catalyst, we can select ideal dopants to tune the catalysts to the conditions we desire. By varying synthesis conditions such as temperature and time, optimization of the number of active sites that are present can maximize our activity as well as the use of the catalyst material.

References

[1] B. Dunn, H. Kamath, J.-M. Tarascon, Electrical energy storage for the grid: a battery of choices., Science (80-.). 334 (2011) 928–35. doi:10.1126/science.1212741.

[2] A.Z. Weber, M.M. Mench, J.P. Meyers, P.N. Ross, J.T. Gostick, Q. Liu, Redox flow batteries: a review, J. Appl. Electrochem. 41 (2011) 1137–1164. doi:10.1007/s10800-011-0348-2.

[3] P. Leung, X. Li, C. Ponce de León, L. Berlouis, C.T.J. Low, F.C. Walsh, Progress in redox flow batteries, remaining challenges and their applications in energy storage, RSC Adv. 2 (2012) 10125. doi:10.1039/c2ra21342g.

[4] G.H. Schuetz, Hydrogen Producing Cycles Using Electricity and Heat-Hydrogen Halide Cycles: Electrolysis of HBr, Int. J. Hydrogen Energy. 1 (1977) 379–388.

[5] W. Glass, G.H. Boyle, Performance of Hydrogen-Bromine Fuel Cells, in: Fuel Cell Syst., 1969: pp. 203–220.

[6] G.G. Barno, S.N. Frank, T.H. Teherani, L.D. Weedon, Lifetime Studies in H2/Br2 Fuel Cells, J. Electrochem. Soc. 131 (1984) 1973–1980.

[7] K.T. Cho, P. Ridgway, A.Z. Weber, S. Haussener, V. Battaglia, V. Srinivasan, High Performance Hydrogen/Bromine Redox Flow Battery for Grid-Scale Energy Storage, J. Electrochem. Soc. 159 (2012) A1806–A1815. doi:10.1149/2.018211jes.

[8] K.T. Cho, P. Albertus, V. Battaglia, A. Kojic, V. Srinivasan, A.Z. Weber, Optimization and Analysis of High-Power Hydrogen/Bromine-Flow Batteries for Grid-Scale Energy Storage, Energy Technol. 1 (2013) 596–608. doi:10.1002/ente.201300108.

[9] T. Van Nguyen, H. Kreutzer, V. Yarlagadda, E. McFarland, N. Singh, HER/HOR Catalysts for the H2-Br2 Fuel Cell System, ECS Trans. 53 (2013) 75–81.

[10] J.K. Nørskov, T. Bligaard, A. Logadottir, J.R. Kitchin, J.G. Chen, S. Pandelov, et al., Trends in the Exchange Current for Hydrogen Evolution, J. Electrochem. Soc. 152 (2005) J23. doi:10.1149/1.1856988.

[11] V. Livshits, A. Ulus, E. Peled, High-power H2/Br2 fuel cell, Electrochem. Commun. 8 (2006) 1358–1362. doi:10.1016/j.elecom.2006.06.021.

[12] R.J. Charleston J., Hydrogen-Bromine Fuel Cell Advance Component Development, 1988.

[13] J. Luttmer, D. Konrad, I. Trachtenberg, Electrode materials for hydrobromic acid electrolysis in Texas Instruments' solar chemical converter, J. Electrochem. Soc. 132 (1985) 1054–1058. http://link.aip.org/link/?JESOAN/132/1054/1 (accessed June 2, 2011).

[14] H. Kreutzer, V. Yarlagadda, T. Van Nguyen, Performance Evaluation of a Regenerative Hydrogen-Bromine Fuel Cell, J. Electrochem. Soc. 159 (2012) F331–F337. doi:10.1149/2.086207jes.

[15] G.G. Barna, S.N. Frank, T.H. Teherani, Oxidation of H2 at Gas Diffusion Electrodes in H2SO4 and HBr, J. Electrochem. Soc. 129 (1982) 2464–2468.

[16] M. Goor-Dar, N. Travitsky, E. Peled, Study of hydrogen redox reactions on platinum nanoparticles in concentrated HBr solutions, J. Power Sources. 197 (2012) 111–115. doi:10.1016/j.jpowsour.2011.09.044.

[17] S. Trasatti, Electrocatalysis: understanding the success of DSA®, Electrochim. Acta. 45 (2000) 2377–2385. doi:10.1016/S0013-4686(00)00338-8.

[18] J.M. Ziegelbauer, A.F. Gullá, C. O'Laoire, C. Urgeghe, R.J. Allen, S. Mukerjee, Chalcogenide electrocatalysts for oxygen-depolarized aqueous hydrochloric acid electrolysis, Electrochim. Acta. 52 (2007) 6282–6294. doi:10.1016/j.electacta.2007.04.048.

[19] A.F. Gullá, L. Gancs, R.J. Allen, S. Mukerjee, Carbon-supported low-loading rhodium sulfide electrocatalysts for oxygen depolarized cathode applications, Appl. Catal. A Gen. 326 (2007) 227–235. doi:10.1016/j.apcata.2007.04.013.

[20] J.L. Bonde, New Materials for Hydrogen Evolution, 2008.

[21] H. Zhang, Y. Verde-Gómez, A.J. Jacobson, A. Ramirez, R.R. Chianelli, Preparation and Characterization of Metal Sulfide Electro-catalysts for PEM Fuel Cells, in: Mater. Res. Soc. Symp. Proc., 2003: pp. 3–8.

[22] L.D. Burke, N.S. Naser, Metastability and electrocatalytic activity of ruthenium dioxide cathodes used in water electrolysis cells, J. Appl. Electrochem. 35 (2005) 931–938. doi:10.1007/s10800-005-5290-8.

[23] J. Ahn, R. Holze, Bifunctional electrodes for an integrated water-electrolysis and hydrogen-oxygen fuel cell with a solid polymer electrolyte, J. Appl. Electrochem. 22 (1992) 1167–1174. doi:10.1007/BF01297419.

[24] A. Sobczynski, A.J. Bard, A. Campion, M.A. Fox, T.E. Mallouk, S.E. Webber, et al., Catalytic Hydrogen Evolution Properties of Nickel-Doped Tungsten Disulfide, J. Phys. Chem. 93 (1989) 401–403.

[25] J. Bonde, P.G. Moses, T.F. Jaramillo, J.K. Nørskov, I. Chorkendorff, Hydrogen evolution on nano-particulate transition metal sulfides, Faraday Discuss. 140 (2008) 219–231. doi:10.1039/b814058h.

[26] A.B. Laursen, S. Kegnæs, S. Dahl, I. Chorkendorff, Molybdenum sulfides—efficient and viable materials for electro - and photoelectrocatalytic hydrogen evolution, Energy Environ. Sci. 5 (2012) 5577. doi:10.1039/c2ee02618j.

II. Levelized cost of electricity and sensitivity analysis for the hydrogen-bromine flow battery

 Supporting information available online.

Abstract

The technoeconomics of the hydrogen-bromine flow battery are investigated. Using existing performance data the operating conditions were optimized to minimize the levelized cost of electricity using individual component costs for the flow battery stack and other system units. Several different configurations were evaluated including use of a bromine complexing agent to reduce membrane requirements. Sensitivity analysis of cost is used to identify the system elements most strongly influencing the economics. The stack lifetime and round-trip efficiency of the cell are identified as major factors on the levelized cost of electricity, along with capital components related to hydrogen storage, the bipolar plate, and the membrane. Assuming that an electrocatalyst and membrane with a lifetime of 2000 cycles can be identified, the lowest cost market entry system capital is 220 \$ kWh^{-1} for a 4 hour discharge system and for a charging energy cost of 0.04 \$ kWh^{-1} the levelized cost of the electricity delivered is 0.40 \$ kWh^{-1}. With systems manufactured at large scales these costs are expected to be lower.

A. Introduction

Global prosperity requires a reliable and low-cost sustainable supply of energy. Forty percent of the United States' energy consumption is electricity and its production results in 30% of all US greenhouse gas emissions [1].

Forty percent of electricity use is from baseload facilities operating under efficient, steady-state conditions [2]. Time-varying usage and the peak demands of consumers is provided by a combination of load following plants, with capacity factors of 30-40% [2], short start-up times, and lower efficiencies than baseload facilities, and peaker plants, which have capacity factors of 10-15%. The price of electricity produced by a peaker is more expensive than off-peak energy, due to low capacity factors [3] and efficiencies. Incorporation of renewable power generation from wind and photovoltaic power stations to combat emissions will only cause more fluctuations in supply, resulting in the need for more peaker plants.

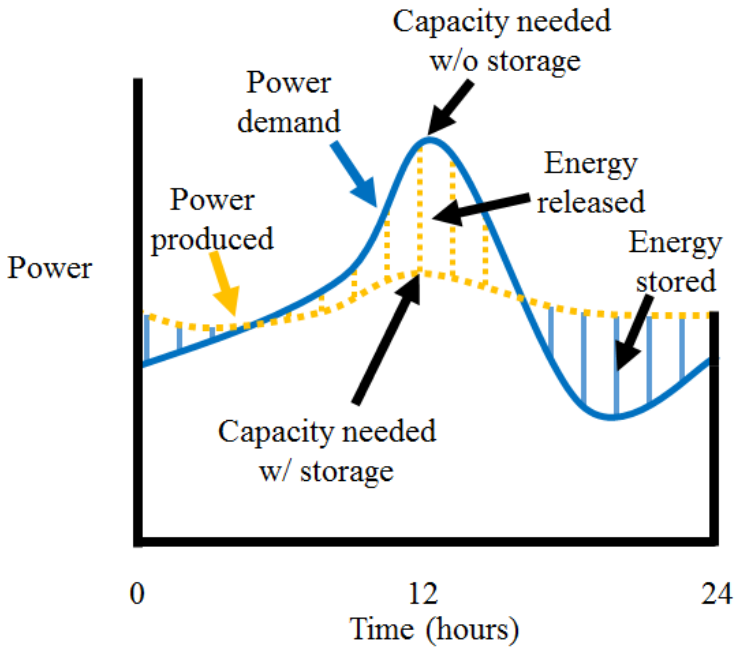

Figure 1. Power demand (blue curve) and power produced if storage is used (orange curve) as a function of time. Without electricity storage, the power produced must equal power demand, therefore the maximum power production capacity must match the maximum power demand. With energy storage, energy can be stored (blue shaded areas) when power generation exceeds power demand, then released (orange shaded area) when power demand exceeds supply. The maximum power capacity without storage is much higher than with storage.

Electrical energy storage of lower cost and higher efficiency fossil fuel and nuclear baseload power, and intermittent renewables to match supply and demand through load-leveling might be an alternative to fossil fuel-based load following and peaker plants, Figure 1. Currently, stored electrical energy provides only 2% of the electricity used in the US [4]. The relatively small fraction reflects the relatively high cost of widely available electrical energy storage compared to peak and load following power generation. If electrical energy storage can deliver electricity for a lower price than producing it on demand, or if there are other reasons a power generation system cannot be deployed (noise pollution, etc.), energy storage will be used rather than peaker or load following plants.

The US DOE has set cost targets for economic grid-scale energy storage systems of 150 \$ kWh^{-1} installed with 1 hour discharge [5], and ARPA-E has a target of 100 \$ kWh^{-1} [6]. The lifetime of the energy storage system plays a large role in the economic feasibility of the system [7], thus, metrics incorporating the system cycle lifetime are also used, such as the capital cost per charge-discharge cycle (\$ kWh^{-1} $cycle^{-1}$) or the levelized cost of electricity. The levelized cost of electricity is calculated by amortizing the capital cost over the lifetime of the system, and including the cost of the electricity needed to charge the system. The levelized cost of electricity allows for direct comparison of different energy systems, including primary generation systems such as natural gas peakers. A discussion of the levelized cost and the method used here to calculate it are included in the Supplementary Information. The DOE target for energy storage systems is a levelized cost of 0.10 \$ kWh^{-1} $cycle^{-1}$ [5].

Grid-level energy storage is an enormous potential market now only addressable cost-effectively by pumped hydroelectric energy storage (PHES) and to a lesser extent compressed air energy storage (CAES), Figure 2 [8,9]. PHES provides 99% of U.S. bulk

energy storage capacity with enormous peak power potential, 128,000 MW [4]. PHES round-trip energy efficiencies are typically 70-80% [10], due to losses during pumping of water to an elevated reservoir (charge) and in recovery of the gravitational energy by a turbine (discharge). CAES is nearly as cost-effective as PHES in certain locations [11], and has a round-trip efficiency of approximately 70% [12], with inevitable losses due to compression and expansion. Geographical limitations and environmental concerns limit the capacity of both PHES and CAES. Markets for higher-cost, smaller-scale energy storage exist and are discussed in several publications [4,9]. Because of the higher levelized cost of electricity of electrochemical systems, currently they are relegated to these higher value markets (see Table S1 for examples), rather than grid-scale storage.

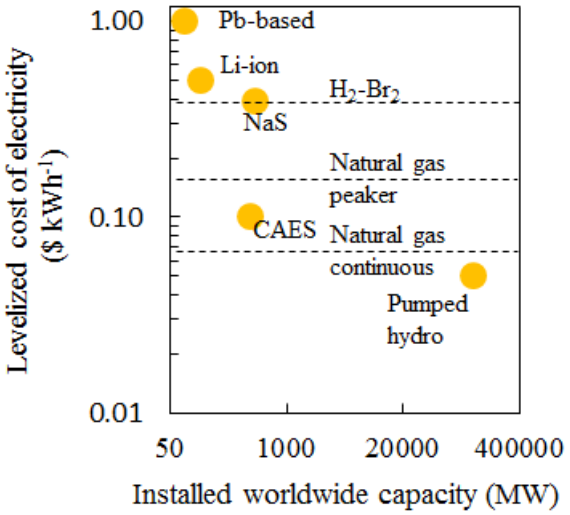

Figure 2. Installed capacity for electrical energy storage systems (2012) [4] vs. levelized cost of electricity estimates [11,55,56] for Pb-based (lead acid-based batteries), Li-ion (lithium ion batteries), NaS (sodium sulfur batteries), CAES (compressed air energy storage) and pumped hydro (pumped hydroelectric energy storage). Levelized costs of electricity [11] are for 20 years lifetime unless otherwise indicated, (H_2-Br_2 system lifetime assumed to be ~5 years). NaS battery cost based on recent data [57]. Levelized costs of electricity calculated in this work for H_2-Br_2 flow battery and natural gas peaker (4 hour operation per day) and continuously operated plants (23.5 hour operation per day) are included as dotted lines. Detailed calculations included in the Supplementary Information.

The most widely used rechargeable electrochemical energy storage systems are solid electrode batteries such as lithium ion, nickel cadmium, lead acid, and sodium sulfur which store energy as electrochemical potential energy in solid electrodes. Automotive and portable electronics applications use lead acid and lithium ion batteries while most stationary applications use lead acid and molten salt (sodium sulfur) battery systems. The limitations of solid electrode batteries include energy storage density of their electrodes and the mass transfer limited rates of reaction at the electrodes.

In electrochemical flow batteries the energy is stored in the electrochemical potential of redox active species in the electrolyte itself rather than the solid electrodes. The electrochemical reaction rates can be higher than solid electrode batteries facilitated by convective mass transport in the flowing reactant streams allowing higher power density and energy density and decreasing the costs ($ kW^{-1}, $ kWh^{-1}) [13]. Flow battery systems can undergo full charge and discharge cycles at a lower cost per kWh per cycle than non-flow batteries [7] and have long cycle lifetimes because they do not rely on the stability of a repetitively stressed solid electrode structure.

Importantly, in flow batteries the power and energy functionalities are decoupled; the electrochemical potential in the electrolyte can be stored in arbitrarily large vessels separate from the power generating electrodes. For typical applications, 4 hours of storage is required for a ratio of power to energy of 1 kW to 4 kWh. Hybrid flow batteries have one electrode where energy is stored in a solid electrode and thus do not decouple power and energy. Examples of flow and hybrid flow batteries include all-vanadium, zinc-bromide and hydrogen-bromine systems, typically operated at 60-80% round trip energy efficiency. Tables S2-4 summarize advantages and disadvantages of some solid electrode, hybrid, and flow batteries.

The hydrogen-bromine flow battery has been investigated as a potentially low-cost electrical storage option [14,15], however calculation of the levelized cost of electricity is necessary to compare to other technologies. By calculating the cost drivers of the system, and identifying potential improvement, the cost-effectiveness of the hydrogen-bromine system may be increased. The analysis used in this work assumes a relatively a low production volume to understand entry-level system costs. It is assumed that initial commercial applications will allow for increasing production rates with the potential for still lower costs and larger market opportunities. The levelized cost of electricity for the hydrogen-bromine flow battery system evaluated in this work is indicated in Figure 2 (discharging 4 hours per day). Also shown for comparison are typical costs for energy delivered from a natural gas peaker plant operating 4 hours per day and for 23.5 hours per day, calculated using the same criteria as the hydrogen-bromine flow battery. If the price of hydrogen-bromine flow batteries energy storage systems can be lowered to compete with the market price of wholesale electricity, these energy storage systems could be used for grid load-leveling.

In this article we describe the results of our investigations of the following questions:

1. What system components affect the capital cost of a hydrogen-bromine battery most?
2. How do complexing agents influence the cost of the hydrogen-bromine battery?
3. What is the levelized cost of electricity for a hydrogen-bromine battery system under conditions similar to load-leveling for grid applications?
4. What is the future market for a hydrogen-bromine flow battery and what technical and engineering challenges remain for its implementation?

B. Methods

A bottom up, component level, system cost model of the hydrogen-bromine flow battery was constructed. Individual components and additional costs were obtained from vendor quotes and/or discussions with battery manufacturers, and from prior studies on H_2/O_2 fuel cells [16] and H_2/Br_2 flow systems [6]. The cost model was coupled with a performance model for the H_2/Br_2 flow battery system [6] to estimate the costs per unit of delivered energy.

The cost estimates were based on modular systems consisting of uniform stack sizes and electrolyte tank sizes. The cost will scale with a component proportional to power (stack, pumps, and valves) and a component proportional to energy (electrolyte tanks). For items that are priced per unit area, the cost will be related to power through the operating power density of the system.

1. Prior economic analyses of hydrogen-halogen batteries

Several cost analyses of the hydrogen-bromine [6] and the similar hydrogen-chlorine flow batteries [17] exist in the literature. The majority of cost estimates for the system stacks are based on work done by Directed Technologies, Inc. in pricing H_2/O_2 proton exchange membrane fuel cells [16], with modifications as needed. Other existing estimates include proposals such as TVNs' ARPA-E project proposal claiming 125 \$ kWh^{-1} [18].

Differences in prices between the hydrogen-bromine study of 2013 (737 \$ kWh^{-1}) [6] and hydrogen-chlorine study in 1981 (240 \$ kWh^{-1} in 2013 dollars [17]) are due to changes in the understanding of the system and differences in total discharge time (1 hour for H_2/Br_2 and 10 hours for H_2/Cl_2). The cost at 10 hours discharge for the optimized hydrogen-bromine system was closer to 200 \$ kWh^{-1} [6]. The work reported here builds on earlier

studies, and examines the sensitivity of levelized cost of electricity on costs of different operating factors and components to determine the most important elements of the battery and battery system. As production rate will influence the total cost (larger manufacturing volume lowering overall cost), a one-to-one comparison between systems must account for production scale.

2. Economic assumptions

Major assumptions in this analysis include:

- Prices are reported in 2013 US dollars accounting for inflation [19]
- Bipolar plates costs are approximately 50% materials cost and 50% fabrication costs (when considering the effect of hydrogen pressure required on bipolar plate cost) [20]
- Production rates are based on costs for fuel cell units at a production rate of 1,000 to 30,000 units per year [6,16] (low-scale manufacturing, where higher production scale will greatly decrease the costs
- Estimate for stack size (number of cells, etc.) from previous works [6]
- Costs from bottom up evaluation are based on Design for Manufacture and Assembly (DFMA ®) [21]
- Shunt currents are ignored
- Pumping energy use is accounted for as an additional 2% efficiency loss
- Performance model based on prior published experiments [6]
- Faradaic efficiency of 100% assumed [6]
- Battery lifetime based on a membrane lifetime of 16,000 hours (for PEM systems) [22]

- Discount rate of 13% assumed for capital, with no taxes assumed
- Cost of electricity (for off-peak charging) assumed to be 0.04 \$ kWh^{-1} for base case
- One complete discharge-charge cycle per day assumed
- 4 hour discharge assumed for calculating levelized cost of electricity, as a typical time needed for supplying electricity for peak demand, unless otherwise noted

3. Hydrogen-bromine battery chemistry and operation

Several published reports of performance of hydrogen-bromine flow batteries exist [6,14,15,23–27]. EnStorage has tested their hydrogen-bromine flow battery at the kW scale and holds several patents on the construction and operation of the battery [28–32]. Both Lawrence Berkley National Laboratory and TVN Systems, Inc. developed systems with government funding. All share the same basic operational conditions and chemistry, described below. The extensive work has served to greatly improve the current densities and power densities of the hydrogen-bromine cells and further improvements are expected.

Electrochemical reactions involved

The H_2-Br_2 cell (depicted schematically in Figure 3) consists of a hydrogen half reaction:

1) $H_2 \leftrightarrow 2H^+ + 2\ e^-$ 0.0V vs. NHE

that occurs at a hydrogen electrode (anode during discharge, labeled as Figure 3a) which is separated from the bromine electrode (cathode during discharge, labeled as Figure 3c) by a proton-transporting membrane (labeled as Figure 3b). The reaction occurring at the counter electrode is the bromine half reaction:

2) $Br_2 + 2e^- \leftrightarrow 2Br^-$ 1.09V vs. NHE

Hydrogen is fed as a gas (Figure 3d) and bromine (complexed Br_3^-) is fed in hydrobromic acid as a liquid (Figure 3e).

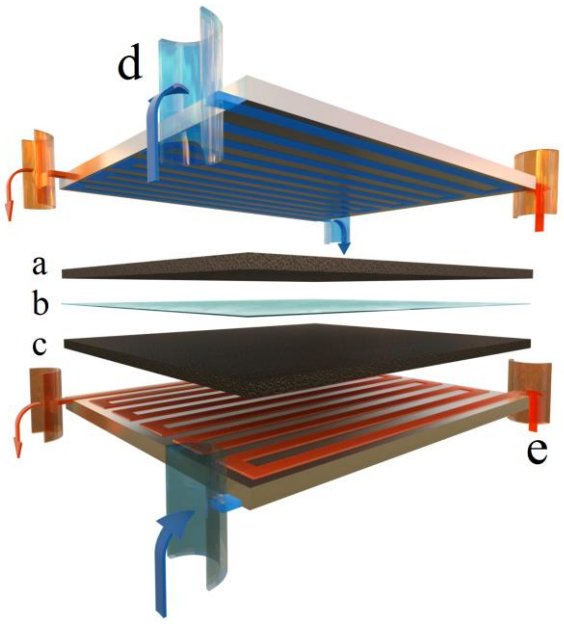

Figure 3. Schematic of one cell of the hydrogen-bromine flow battery system a) hydrogen diffusion layer electrode, b) membrane, c) bromine electrode, d) hydrogen feed, e) hydrobromic acid/bromine feed

Carbon is sufficient to catalyze the bromide reactions, but a platinum group metal electrocatalyst (typically platinum or its alloys, although rhodium sulfide can be used [33–36]) is required to catalyze the hydrogen reactions. The hydrogen electrocatalyst is typically supported on carbon to maintain high dispersion. The concept of a membrane-less system [37] is not considered in this study as it is uncertain whether long-term laminar flow can be maintained.

Process overview

A simplified diagram showing the full hydrogen-bromine system is shown in Figure 4. The schematic shows the major components required for the conversion of hydrobromic acid to hydrogen and bromine during charge, and recombination to reform HBr during

discharge. Hydrogen is stored in a pressurized tank (~30 bar at full charge down to 2 bar at full discharge) which during discharge is fed through a manifold to one section of the stack with a recycle loop passing through a set of Venturi ejectors.

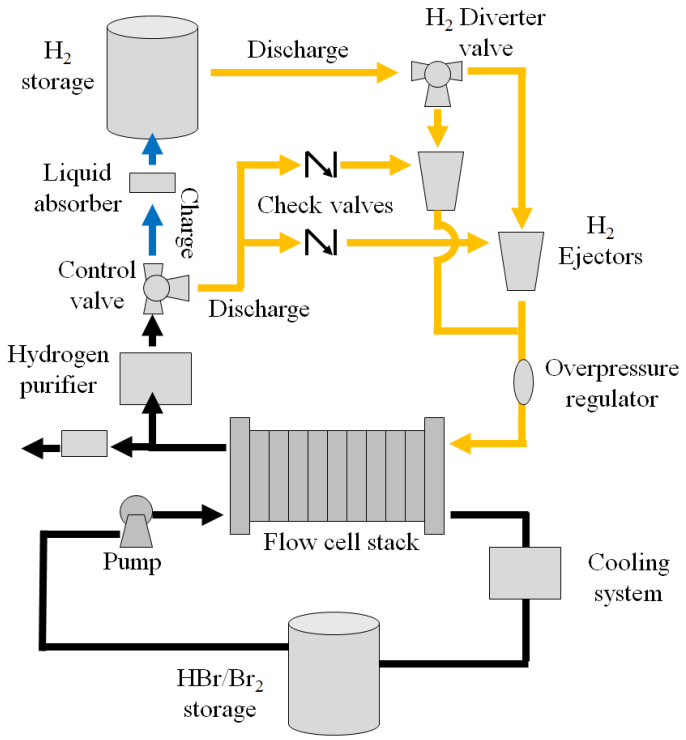

Figure 4. Simplified hydrogen-bromine flow diagram

During charge a control valve is switched so that the hydrogen produced repressurizes the hydrogen tank after depletion during discharge. Liquid molecular bromine (or Br_2 in a molecular complex) and hydrobromic acid are stored in separate or shared tanks and delivered to the stack with a pump as needed. Cell inefficiencies result in excess heat, which must be removed from the electrolyte (typically by air-cooling using fans). The system temperature must be maintained between room temperature and 58 °C (the bromine boiling point [6]. As the system is charging, bromine (Br_2) builds up in the tank, and is discharged and converted back to bromide ions when electricity is required.

The design of the hydrogen side of the flow battery stack is based on the hydrogen side of H_2/O_2 fuel cell stacks and proton exchange membrane electrolyzers. The design of the bromine side of the flow battery stack is based on bromine electrodes from bromine-based hybrid flow batteries such as a zinc bromine flow battery. Figure 5 shows a schematic of the stack, consisting of a complete cell, current collectors and an end plate for pressing the components together (Figure 5a). The current collector (Figure 5b) serves to transfer the current generated or supplied during operation to external circuitry. The cell consists of gaskets (not pictured), a bipolar plate flow field (Figure 5c), a negative hydrogen gas diffusion layer with electrocatalyst layer (Figure 5d), a membrane (Figure 5e), a positive electrode for bromine reactions (Figure 5f), and another bipolar plate (Figure 5g) that provides the positive electrode flow for the electrode depicted in Figure 5f.

Several cells are in each stack (note that the schematics are not representative of the actual number of cells in the stack). A complete cell consists of both sides of a bipolar plate, a negative hydrogen gas diffusion layer with electrocatalyst, a membrane, a positive electrode for bromine reactions, and any required gaskets.

The bipolar plate consists of a flow field (facing upward) for the bromine electrolyte, and an interdigitated or serpentine flow field (facing downward) for hydrogen. The top of the topmost bipolar plate directly contacts the current collector and does not contact electrolyte. The negative (bottom part) of the flow field directly contacts an electrically conductive gas-diffusion layer that allows hydrogen flow. This gas-diffusion layer contacts the membrane, and an electrocatalyst layer is embedded in between the membrane and the negative GDL to catalyze the hydrogen reactions. Below the membrane is a positive electrically-conducting bromine electrode layer (not a gas diffusion layer as the bromine electrolyte is liquid). This

layer serves to catalyze the bromine oxidation and reduction reactions. The top of the next bipolar plate is a flow field that serves to provide electrolyte to the positive bromine layer.

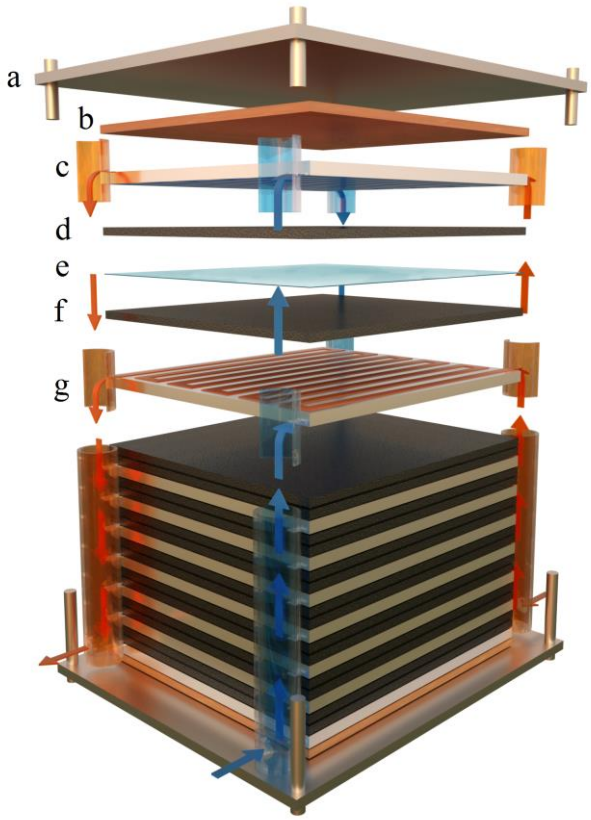

Figure 5. Hydrogen-bromine stack. a) end plate, b) current collector, c) bipolar plate, d) negative electrode (hydrogen electrode), e) membrane, f) positive electrode (bromine electrode), g) second bipolar plate. Feeding the electrolyte are manifolds, with hydrogen feed colored blue and hydrobromic acid/bromine colored orange. At the bottom of the stack is a second current collector and end plate.

Hydrogen is supplied through a manifold (indicated by the blue cylinder, hydrogen is indicated by blue arrows in Figure 5) to the flow field to pass through the gas-diffusion layer and react partially before leaving the cell. Bromine electrolyte is introduced through a separate manifold (orange in Figure 5) to flow through the bromine flow field and pass through the positive electrode.

Flow battery operation and lifetime

The current and power density of the system dictate the stack area required to supply a given power and energy. The operating current density (power density) will influence the system's efficiency (operating at higher current densities require lower efficiencies). The efficiency model used here is based on the current density vs. voltage curves for a 'Gen 4' hydrogen-bromine system [6]. The calculations of the efficiency are included in the Supplementary Information.

Cycle lifetime has been tested for lab-scale H_2/Br_2 cells [6], and commercial batteries reported H_2/Br_2 lifetimes of 10,000 cycles [38], although it is unclear whether this is full capacity cycling. For our study, we assumed the lifetime to be dependent on the lowest lifetime material, potentially the membrane (Nafion or PVDF/Silica). For Nafion, the lifetime is approximately 16,000 hours [22] (lifetime assumed in this study), which at a 4 hour discharge (8 hours per cycle), would be 2,000 cycles.

4. Stack components

Schematics of the stack components discussed in this section are shown in Figure 4 and 5. Further discussion of the stack components is included in the Supplementary Information, along with methods for calculating the overall cost of the components per kWh.

Membrane

The purpose of the membrane is to minimize bromine and hydrogen crossover, electrically separate the electrodes to avoid short circuits, and transport ions (protons). The membrane must survive in acid and bromine and withstand cell compression and pressure gradients between the hydrogen and bromine section. The type and thickness of membrane material, and the use of complexing agents (discussed later) to minimize crossover of

bromide/bromine will depend on how resistant the hydrogen electrocatalyst is to bromide and bromine. The membrane thickness and electrolyte concentration [6] will determine membrane resistance (approximately 25-30% of the total cell resistance [39]).

The two membrane options considered are Nafion and a microporous PVDF/silica membrane (30% PVDF, 10% silica, 60% pore volume [26]). Nafion can also be blended with other materials to avoid bromide/bromine crossover [40], but in this work these materials are not considered. The microporous membranes have higher ohmic resistance than Nafion, and are not as effective at preventing crossover, but are less expensive. The cost of Nafion used here is 350 \$ m^{-2} for a 15-25 μm thick, reinforced membrane [6], with price dependent on the thickness of the Nafion, reinforcement and the production scale of the Nafion. Microporous membranes are roughly 10% the cost of Nafion, 35 \$ m^{-2}. Nafion has a lifetime in a chloralkali cell of 2-5 years [41], and is typically the limiting factor in flow battery lifetime.

Bipolar plates and electrodes

The bipolar plate used to control the cell flow fields must be conductive and corrosion-resistant. The thickness (and material cost) of the bipolar plate will increase linearly with hydrogen pressure, but if the pressure in the stack is too low, external compression or larger storage tanks are required.

Bipolar plates are made from either stamped stainless steel 316L with corrosion-resistant vias through nonconductive coating, or conductive plastic molded into flow fields for the hydrogen and bromine. The bipolar plate cost estimates from previous work is 300 \$ m^{-2} [6]. Low production volumes and high pressure requirements were assumed as well as corrosion resistance. The bipolar plate cost used here assumes the material cost (50% of cost [20]) is linearly related to maximum hydrogen pressure (with 300 \$ m^{-2} assumed at 30 bar)

giving a pressure-dependent bipolar plate cost of 300 \$ m^{-2} *[1 +0.5* ($P_{max\ H2}$-30 bar)/30 bar].

One side of the bipolar flow field supplies hydrogen to the negative gas diffusion layer. The gas-diffusion electrode allows hydrogen to pass to the electrocatalyst at the membrane, while drawing current to the bipolar plate. The negative electrode generally is carbon and made hydrophobic by Teflon coating (to avoid mass transport limits of hydrogen to the electrocatalyst). The cost assumption of the carbon cloth gas diffusion layer is 90 \$ m^{-2} [6].

The other side of the bipolar flow field supplies bromine electrolyte to the positive electrode. The positive electrode allows electrolyte to pass into contact with the Nafion. The cost used here is 70 \$ m^{-2} for high surface area hydrophilic carbon electrodes [6].

Negative electrocatalyst and ink

The purpose of the negative electrocatalyst is to catalyze the hydrogen evolution and oxidation reaction while maintaining stability. The ink consists of electrocatalyst and binding agents (typically Nafion) to maintain contact between the negative gas-diffusion layer, the electrocatalyst layer, and the membrane. Potential electrocatalysts are platinum and its alloys [29] or rhodium sulfide [33,34] which is stable even in the presence of bromide and bromine. Hydrogen presence and cathodic potential can inhibit corrosion of platinum [25].

For this study, an electrocatalyst that is stable and resistant to poisoning in bromide/bromine such as rhodium sulfide [33–36] is assumed. The cost of electrocatalyst and binder assumed in this study is 50 \$ m^{-2} assuming an electrocatalyst loading of 0.05 mg cm^{-2}.

Other stack components

Current collectors electrically connect the stack to the load or electricity supply, and one is required at both the top and bottom of the full stack. Because they do not contact the electrolyte corrosion is not a concern. The cost we used here is copper at 10 $ m^{-2}.

Gaskets are required that are made of inexpensive polymers that can be injection molded. Tie rods made of steel are used to help compress the stack. The cost of gaskets/tubings and tie rods is assumed to be 28 $ m^{-2} [6].

The membrane electrode assembly (MEA) is encased in a frame to give it structure. High density polymers are assumed for this study costing 50 $ m^{-2} of electrode area.

End plates compress the entire stack of MEAs and are typically made of stainless steel. Only one set of endplates is required for a full stack, not per cell, therefore, the endplate cost will be dependent on the number of cells chosen per stack. On a cost per unit stack area, we assumed a price of 10 $ m^{-2}.

5. Balance of plant

The balance of plant consists of components that support the stack operation by supplying electrolyte and controlling temperature.

Hydrogen tank and compression

One of the biggest challenges for the hydrogen-bromine flow battery compared to other flow battery systems is pressurized hydrogen storage. Typical storage pressure is 30 bar [6] for proton exchange membrane electrolyzers. Lower hydrogen pressures decrease the cost of the bipolar plates required and the reinforcement of the membranes. However, we assumed a minimum pressure of 2 bar is required, as the pressure does not appear to have

significant effect on performance beyond that pressure [42–44]. The ideal hydrogen pressure is calculated by minimizing the levelized cost of electricity of the system.

The cost of hydrogen storage from Proton Inc, on site has been quoted at 2.5 \$ L^{-1} [6] at 30 bar and 1000 \$ kg^{-1} [45] from DTI, and similar costs per kg are reported [46], with carbon fiber storage costs predicted to be as low as 600 \$ kg^{-1} [47]. For this study we used a price of 1000 \$ kg_{H2}^{-1}. The amount of storage required is discussed in the Supplementary Information.

The hydrogen must be pressurized during charge (the pressure will be reduced during discharge). The two possible methods are electrochemical compression or an external compressor. The cost of an external compressor is very high, 0.06 \$ kg^{-1} for compressor hardware related costs and 0.08 \$ kg^{-1} for electricity [45]. The system can be electrochemically pressurized at 400 psi more than the halogen side and to a total of 600 psi [17]. For this study electrochemical compression is assumed.

Hydrogen valve system

The hydrogen valve system provides hydrogen to the flow battery during discharge, as well as pressurized hydrogen to the storage tank during charge. Hydrogen is provided by the hydrogen storage tank to a Venturi ejector which is co-fed from the effluent of the fuel cell. Two ejectors, a high and low flow are used in parallel to achieve a wide operating range [21]. Hydrogen is always available to the electrode, making platinum dissolution by bromine less of an issue, as hydrogen is always present to react with bromine.

The cost of the hydrogen valve system is based on the flow rate of hydrogen required, and does not scale with the hydrogen storage amount (unlike the other parts of the balance of plant). The cost of the system, consisting of several components [21] is 1000 \$

kg_{H2}^{-1} hr, based on the hydrogen tank and valve system being approximately the same cost at 1 hour discharge.

Electrolyte

The electrolyte required for the system is hydrobromic acid (converted to hydrogen and bromine during operation). The electrolyte concentration affects conductivity, transport properties (such as viscosity [6]), total kWh required, and the state of charge concentration of bromine. Earlier reports have shown that the optimum concentration to minimize the system cost depends on the discharge time [6]. For a 4 hour system the system cost is minimized at 4.8 M HBr, and for a 1 hour system the cost is minimized at 3.1 M HBr. At full charge this will go to 1 M Br_2 and approximately 1 M HBr for 1 hour discharge. The price we used for 48% HBr is 1.5 \$ kg^{-1}, and the amount of electrolyte required is calculated in the Supplementary Information assuming 4M HBr at 0% state of charge.

Complexing agents

Bromine complexing agents can prevent crossover and significantly reduce the vapor pressure of bromine, reduce corrosivity, reduce free bromine and increase safety. Complexing agents have been used successfully in zinc bromide systems [48], but inhibition of bromine kinetics has not been quantitatively studied in great detail [49]. However, for a hydrogen-bromine cell, polyethylene glycol as a complexing agent was seen to reduce the discharge currents considerably (at the same voltage the current was approximately 1.4 times higher for the PEG free system than with 0.1 M PEG-1000) [50]. Free Br_2 increases the discharge performance [6] but the free Br_2 harms the efficiency of the charging cycle, and so a 1 to 1 concentration of HBr to Br_2 was viewed as the ideal concentrations [6].

Common complexing agents are polyethylene glycol [50] or quaternary ammonium salts such as Methyl Ethyl Pyrrolidinium Bromide (MEP). The cost of MEP is approximately 40 \$ kg^{-1} and is the price used in this work.

Cooling systems

Cooling systems maintain the temperature of the flow battery and avoid membrane overheating which can lead to dehydration or degradation. Although less cooling is required in hydrogen-bromine flow batteries than hydrogen fuel cells, as the efficiency of the hydrogen-bromine system is much higher, the adiabatic temperature rise of the system still requires cooling to maintain reasonable temperatures (see Supplementary Information). Unlike hydrogen-oxygen fuel cells, the bromine liquid electrolyte can remove most of the heat and thus air cooling can be used, similar to zinc bromine batteries. The cost of air cooling used in this analysis is 50 \$ kW^{-1}.

Power electronics

Inverters are required to convert DC electricity supplied from the battery to AC. These costs are independent of the chemistry of the battery that is used. Some detectors are required to measure the state of charge of the battery, and monitor power. A price of 1000 \$ kW^{-1} is used for the power electronics, complete site preparation and installation [6].

Pumps and flow control

The pump supplies electrolyte to the positive (bromine) electrode and must be stable in the bromide/bromine and acid. The hydrobromic acid/bromine electrolyte is typically maintained at ambient pressures, to avoid the high-cost of pumping a high pressure electrolyte. H_2/O_2 proton exchange membrane electrolyzers typically have pressurized hydrogen, but water is pumped in and oxygen is produced at atmospheric pressures to avoid high-pressure oxygen safety problems and reduce system costs [51,52]. For a hydrogen-

bromine system, a pressure gradient helps eliminate water droplets from the hydrogen side of the flow cell, improve mass transport for the hydrogen side, and avoid electrolyte crossover [32]. Brushless DC magnetic drive pumps are appropriate for the system, at a cost of 15 \$ L^{-1} min [6], with a required flow rate per kWh of 2.5 L min^{-1}, based on discussions with flow battery manufacturers. Flow meters are also required, with an additional cost (1 \$ L^{-1} min) [53]).

HBr/Br_2 tank

The HBr/Br_2 tank must be stable for the electrolyte and sized to store the needed electrolyte. A corrosion resistant polyethylene tank is proposed, ranging in price from 1.5 \$ L^{-1} [6] to 0.25 \$ L^{-1} [53], with a price of 0.5 \$ L^{-1} used here. Two tanks can be used, so that the most concentrated solution is used during discharge, and the least concentrated solution is used during charge. This could increase efficiency of charge and discharge, but because the single pass conversion is low, if two separate tanks were used, more electrolyte is needed. At a liquid electrolyte flow rate of 2.5 L min^{-1} (per kWh) and 4 hour discharge time, and electrolyte energy density of 8 L kWh^{-1}, approximately 75 times the electrolyte would be required for two separate tanks than if the electrolyte was circulated. The 75 times increase in electrolyte cost is too high to merit using two tanks that are kept separate, unless the pump rate can be drastically reduced. Therefore we assume only one tank is used with recirculated electrolyte.

Pipe material

The piping of the electrolyte must be inert to the electrolyte. Polyvinyl chloride is selected for the analysis.

6. Assembly

The manufacturing cost of the stack assembly is 180 \$ m^{-2} and 150 \$ kW^{-1} [6]. This is an estimate for low-volume manufacturing from the mentioned reference.

7. Cost model

The hydrogen-bromine battery capital costs were calculated based on component costs summarized in Table 2, with operating conditions in Table 1 and discussed above. The efficiency was chosen by minimizing the overall levelized cost of electricity by varying the current density and calculating the efficiency from a linear fit to the performance of the 'Gen 4' system [6]. Lower efficiencies required higher current and power densities, meaning higher utilization of the stack, but less of the electricity could be recovered. The efficiencies of the system were calculated using equations 3 and 4:

$$3)\quad \eta(\text{discharge}) = \frac{1.1\ \text{V} - \frac{i \times 0.65V}{3\text{mA/cm}^2}}{1.1\ \text{V}} - 2\%(\text{pumps})$$

$$4)\quad \eta(\text{charge}) = \frac{1.1\ \text{V}}{1.1\ \text{V} + \frac{i \times 0.65V}{3\text{mA/cm}^2}} - 2\%(\text{pumps})$$

Table 1. Operating conditions for hydrogen-bromine system

Operating condition	Base case	Units
Lifetime (4 hour charge)	2000	cycles
Lifetime (1 hour charge)	8000	cycles
$C_{HBr\ discharged}$	4	M
$C_{HBr\ charged}$	1	M
$C_{Br2\ charged}$	1.5	M
$C_{Br2\ discharged}$	0	M

During cost minimization, the hydrogen pressure was also varied to minimize the cost. The cost estimate will also depend on the discharge time (4 hours or 1 hour used here). Other factors influencing the cost are the choice of membrane (Nafion or PVDF/silica), use of complexing agents (MEP), and the effect of the complexing agent on the kinetics.

Table 2. Component costs for hydrogen-bromine system

Component	Cost	Units
Electricity cost	0.04	$ kWh^{-1}
Membrane (Nafion)	350	$ m^{-2}
Membrane (silica/PVDF)	35	$ m^{-2}
Bipolar plate	300 [1+½(P_{H2}-30 bar)/30 bar]	$ m^{-2}
Negative GDL	90	$ m^{-2}
Positive electrode	70	$ m^{-2}
Collectors	5	$ m^{-2}
Electrocatalyst & Ink	50	$ m^{-2}
Gaskets/tubing/tie rods	28	$ m^{-2}
MEA Frame	50	$ m^{-2}
End plates	10	$ m^{-2}
Hydrogen tank	1000	$ kg_{H2}^{-1}
Venturi ejector	500	$ kg_{H2}^{-1} hr
Valves	500	$ kg_{H2}^{-1} hr
Electrolyte	1.5	$ $kg_{48\%HBr}^{-1}$
Complexing agent (MEP)	48.5	$ kg_{Br2}^{-1}
Cooling	50	$ kW^{-1}
Power electronics	1000	$ kW^{-1}
Pumps	15	$ L^{-1} min
Flow meters/sensors	72	$ m^{-2}
HBr/Br_2 tank	0.5	$ L^{-1}
Labor per Power	150	$ kW^{-1}
Labor	180	$ m^{-2}

C. Results and Discussion

1. Influence of complexing agents on capital costs

To investigate the impact of the complexing agent, three test cases were used for analysis, assuming that if a Nafion membrane is used, complexing agents are not required,

- Case 1 with no complexing agents used, a Nafion membrane, similar to previous work [6]

- Case 2 with 1 M MEP used as a complexing agents and a silica/PVDF membrane used. In this case the effect of polyethylene glycol as a complexing agent on the bromine kinetics and therefore current density [50] is included, (the effect of PEG was used due to a lack of data on the effect of MEP on the bromine kinetics). The increased resistance of the silica/PVDF membrane compared to a Nafion membrane was not incorporated into the model
- Case 3 with 1 M MEP, silica/PVDF membrane and assuming no effect of complexing agent on current density

A summary of the capital cost per kWh and per kW for each of the three cases is shown in Figure 6, for both 4 hour discharge and 1 hour discharge. The costs will be different than earlier work for 1 hour discharge from a hydrogen-bromine system [6] because the efficiency used here is chosen to minimize the levelized cost of electricity. The capital cost per kWh for 4 hour discharge is lower than for 1 hour as only the balance of plant scales with increased energy capacity (assembly also scales with power and area) [6]. The balance of plant costs dominate the capital costs of the system for the 4 hour discharge time, and are an appreciable portion even for the 1 hour discharge, as found in previous work [6]. The optimized conditions used to minimize the levelized cost of electricity and generate the costs shown in Figure 6 are shown in Table 3 (for 4 hour discharge) and Table 4 (for 1 hour discharge).

Table 3. Optimized conditions for 4 hour discharge

	Case 1	Case 2	Case 3
Current density	0.64 A cm^{-2}	0.38 A cm^{-2}	0.61 A cm^{-2}
Power density	6.12 kW m^{-2}	3.89 kW m^{-2}	5.89 kW m^{-2}
Round trip efficiency	74.3%	76.1%	76.1%
Hydrogen pressure	30.8 bar	25.0 bar	30.3 bar
Levelized cost of electricity	0.396 \$ kWh^{-1}	0.489 \$ kWh^{-1}	0.478 \$ kWh^{-1}

Table 4. Optimized conditions for 1 hour discharge

	Case 1	Case 2	Case 3
Current density	0.85 A cm^{-2}	0.52 A cm^{-2}	0.85 A cm^{-2}
Power density	7.76 kW m^{-2}	5.09 kW m^{-2}	7.77 kW m^{-2}
Round trip efficiency	68.1%	70.2%	70.0%
Hydrogen pressure	22.5 bar	18.6 bar	22.6 bar
Levelized cost of electricity	0.646 \$ kWh^{-1}	0.689 \$ kWh^{-1}	0.672 \$ kWh^{-1}

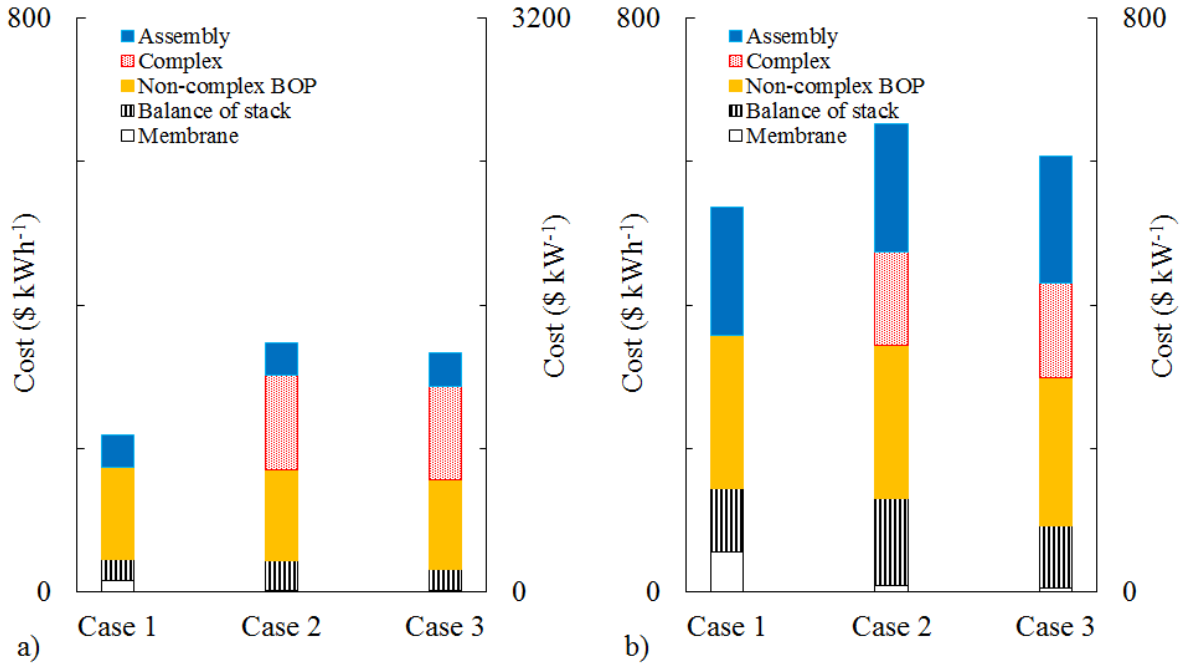

Figure 6. Capital cost per kWh and per kW for different schemes. Case 1 is for no complexing agent, case 2 with complexing agent using the effect of complexing agent from polyethylene glycol data on the current density [50], and case 3 with MEP complexing agent but assuming no inhibition of complexing agent on current density a) for a 4 discharge, b) for a 1 hour discharge. Power electronics costs are not included in this analysis.

The optimized efficiencies for a smaller discharge time are lower for the 1 hour systems because the stack plays a larger role in the cost for shorter discharge times, and therefore it is ideal to operate at higher current densities to minimize stack area. In addition, the hydrogen pressure optimized for 1 hour discharge was lower than for 4 hours (20 bar compared to 30 bar). This is because lower hydrogen pressure decreases bipolar plate costs, and the stack plays a larger role in the cost for 1 hour discharge than for 4 hour discharge.

The same electrolyte concentration was used for the 1 hour and 4 hour discharge, although it was determined previously that the optimal electrolyte concentration depends on discharge lifetime [6].

The complexing agent cases (2 and 3) are much higher cost, despite avoiding use of a Nafion membrane. For a shorter discharge time, the capital costs are closer for the complexing agent cases, but in order for the complexing agent systems to be less expensive than using Nafion (case 1), the system has to be designed for only 15 minute discharge (Figure S2).

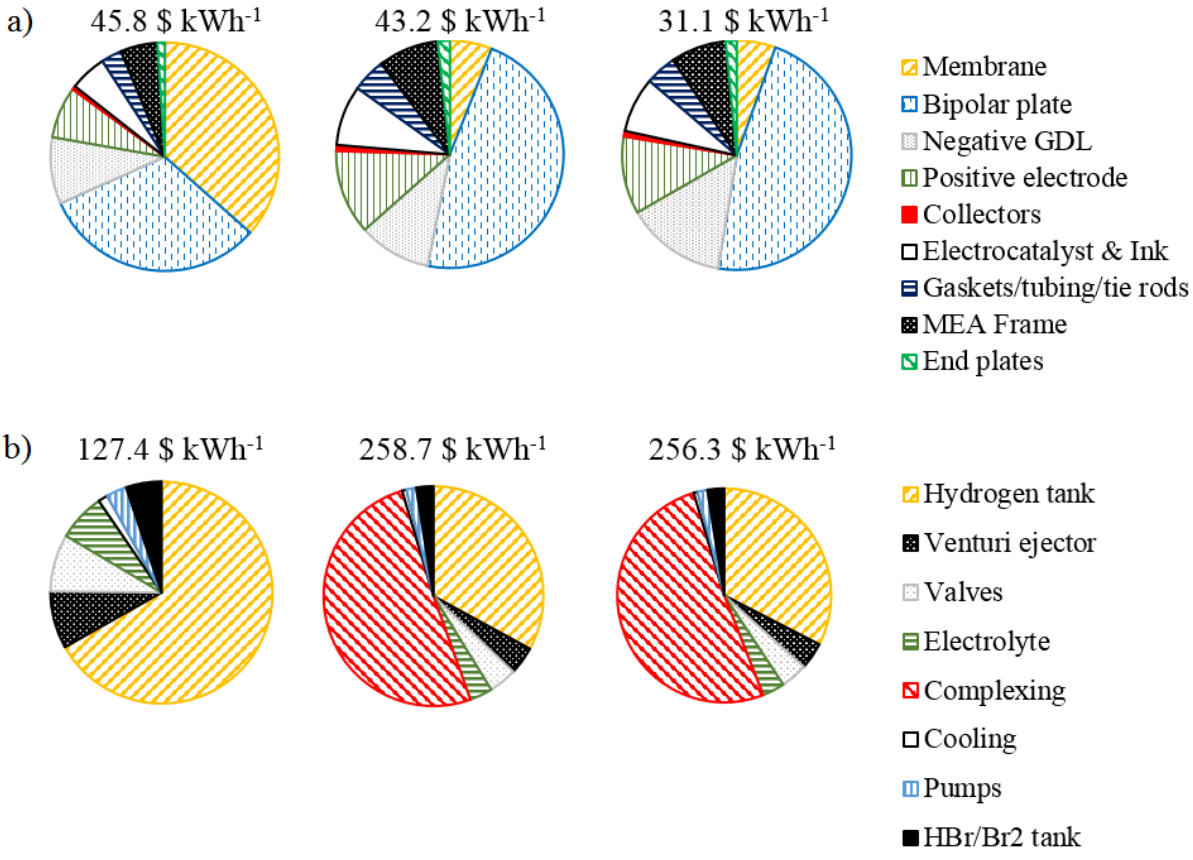

Figure 7. a) Flow cell stack break down of cases 1, 2 and 3. Stack cost per kWh also included. b) Balance of plant break down of cases 1, 2 and 3. Discharge of 4 hours used.

The breakdown of case 1, 2 and 3 stack costs for 4 hour discharge is in Figure 7a. The major stack costs for case 1 are bipolar plates and membranes, as also shown in

previous work [6]. The major cost for cases 2 and 3 is the bipolar plates, because in these cases the membrane was a less expensive PVDF and silica membrane and so plays less role in the total cost. For a change in discharge time, the stack cost distribution will change based on changes in hydrogen pressure which affect bipolar plate costs.

The balance of plant costs for a 4 hour discharge system, shown in Figure 7b, are dominated by costs related to hydrogen or complexing agents, with liquid electrolyte costs predicted to be lower than in previous work [6]. For a change in discharge time, the balance of plant distribution will change slightly, as with increasing discharge time, the hydrogen valve system, cooling and pumping system will play a smaller role (as they do not scale with increasing energy, unlike the rest of the balance of plant). Cooling costs may decrease even further, as the heat will be dissipated over a larger electrolyte volume and will require less cooling for the same power. Differences in case 2 and 3 distribution are due to the differences in the optimized hydrogen storage pressure.

2. Levelized cost of electricity for hydrogen-bromine system

Although the capital cost is an important, and frequently reported, method of evaluating battery cost, the most important metric is the levelized cost of electricity (and the value that should be minimized, rather than minimizing capital cost). The levelized cost is calculated as described in the Supplementary Information. For this analysis, a discharge time of 4 hours and charge time of 4 hours is assumed with one cycle per day. A discount rate of 13% and a charging electricity price of 0.04 \$ kWh^{-1} is assumed. For this investigation we assumed the same current density for both charging and discharging. In a real world scenario, the time of charging and discharging would be based on the system application and the current density of charging and discharging could be different (for example, a system

may be charged for 12 hours during the night, and then supply power for only 4 hours during peak demand, or alternatively may be required to charge at high current densities during the day if connected to a solar panel, and then discharge slowly over the night). Thus, the levelized costs minimized here are not general to the hydrogen-bromine battery, but are specific to the assumptions used.

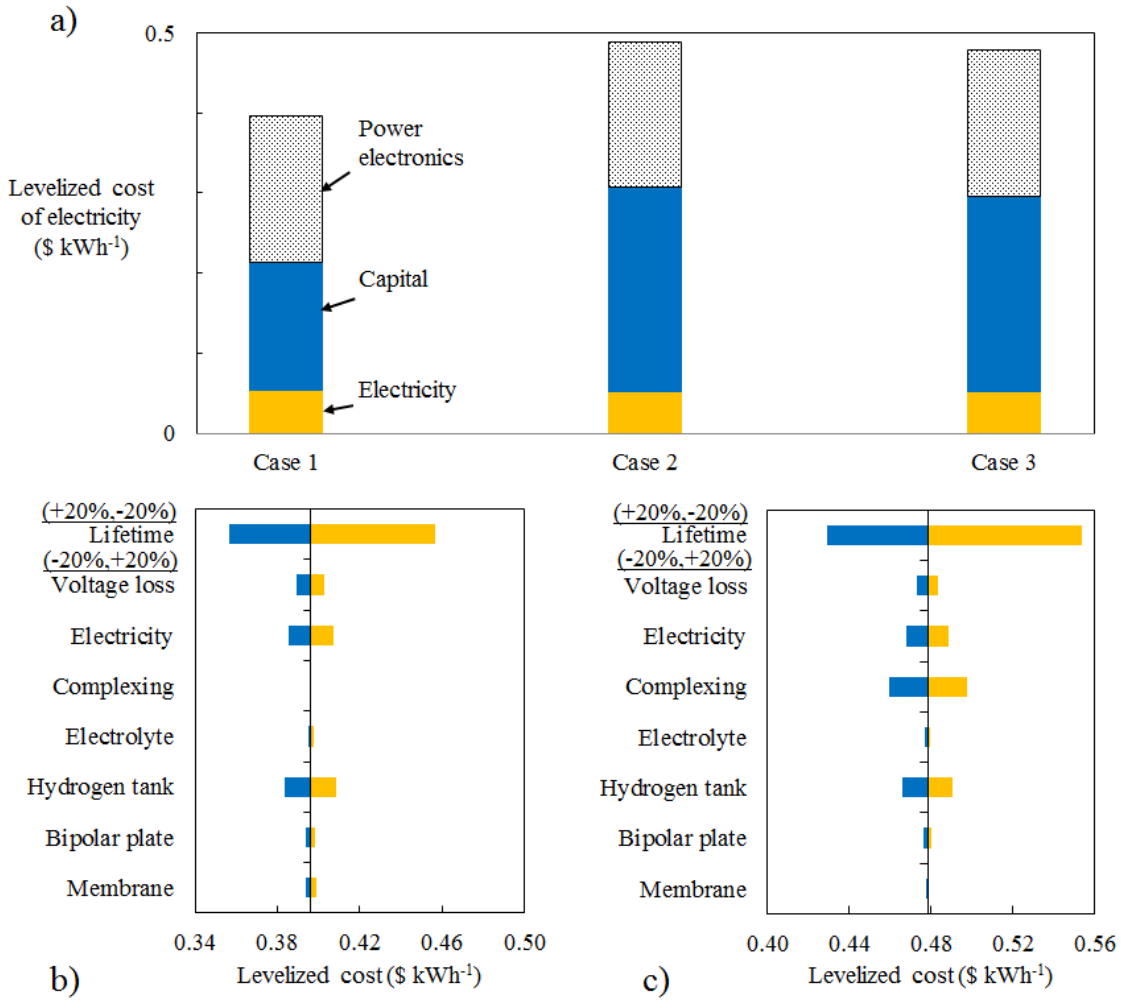

Figure 8. a) Levelized cost of electricity of a hydrogen-bromine battery for 4 hour discharge (8 hour total cycle, 1 per day) and sensitivity analysis of levelized cost of electricity for b) case 1 (Nafion membrane with no complexing agents) for 4 hour discharge and c) case 3 (complexing agent used with PVDF/silica membrane, assuming no adverse effects on kinetics) for 4 hour discharge

The minimized levelized costs of electricity for cases 1, 2 and 3 are shown in Figure 8a. The costs are minimized by varying the hydrogen pressure and current density used as

described above. The lifetime assumed for the hydrogen-bromine system is that of the membrane, making the levelized cost estimates an over-approximation. In a real system, the membrane could be replaced without having to replace the entire system, which could decrease the levelized cost of electricity.

From Figure 8a it is evident that power electronics play a large role in the total levelized cost. This cost is independent of the type of battery used, but is important when comparing levelized costs of electricity from a battery system to peaker systems such as natural gas or diesel. The contribution from the flow battery is competitive with other electrochemical systems when calculated for similar conditions. The levelized cost of electricity for this system is between that of lithium ion (on the higher end) and compressed air energy storage/solid sulfur batteries (see Figure 2). Based on the market scale of these other energy storage systems, and assuming a proportional relationship between the market scale and the levelized cost of energy, the hydrogen-bromine batteries (at a production scale discussed here), would have a market on the order of 100 MW (see Figure 2). If the levelized cost of electricity could be reduced, the hydrogen-bromine system would become more competitive with other energy storage systems, or even with peaker production systems powered by natural gas or diesel. Currently, natural gas peaker plants evaluated with a lifetime of 20 years, and a capital cost of 1 \$ W_{peak}^{-1}, at a natural gas cost of 4 \$ $MMBtu^{-1}$ operating for 4 hours per day would have a levelized cost of electricity of 0.14 \$ kWh^{-1}, not including any electronic infrastructure.

3. Sensitivity analysis of the levelized cost of electricity

Sensitivity analysis was performed to identify which components might be modified or improved to affect cost. The sensitivity results for case 1 are shown in Figure 8b, for a

discharge time of 4 hours. We examined sensitivity of electrolyte cost and hydrogen storage cost (representing balance of plant costs), bipolar plate and membrane costs (representing flow cell stack costs), voltage losses of the stack (representing flow cell performance) electricity costs and lifetime. The base case values for these variables are shown in Table 3. As power electronics costs are not a major focus of this analysis, we left them out of the sensitivity analysis, but from the contribution shown in Figure 8a these play a large role in the end cost.

To decrease the membrane and bipolar cost, lower cost materials can be used for the bipolar plate, and the membrane thickness could potentially be reduced. If the bipolar plates are extremely sensitive to corrosion the costs can increase dramatically (if for example they must be machined from tantalum or niobium). The membrane cost could increase if the thickness of the membrane required is larger than expected (due to issues with leaks, crossover, or maintaining pressure differential). Hydrogen tank costs can be influenced by of new methods of storage, such as potentially lower cost carbon fiber containers.

The lifetime has a large effect on the levelized cost, indicating the need for materials that can last for thousands of cycles. Membranes lifetimes typically control fuel cell stack lifetimes, and so improving the membrane lifetime can contribute strongly to the levelized cost. However, for H_2/Br_2 batteries, electrocatalysts can limit lifetimes unless new materials are developed [34].

The electrolyte concentration is important to maintain high activity as its cost is not a large portion (so long as it is circulated). As is evident from Figure 8b, requiring two tanks (and the subsequent order of magnitude increase in total electrolyte required) would greatly increase the levelized cost of electricity and confirmed our decision to use only one tank with recirculation. The cost of the electricity for charging is one of the larger influence on

the levelized cost. The hydrogen tank cost is especially significant, and presents a large opportunity for reduction in cost.

The performance of the battery (power density at a given efficiency) also affects the levelized cost significantly, indicating that further improvements in the efficiency of the battery can have large influences on the cost of electricity. However, the large effect of a decrease in lifetime on the levelized cost of electricity indicates that durability of the system may be more important than minor improvements in performance (voltage loss).

The sensitivity analysis for case 3 is shown in Figure 8c. In addition to the other parameters investigated for case 1, the complexing agent cost is included. The complexing cost could be reduced if MEP can be replaced by less expensive polyethylene glycol, so long as the bromine kinetics are not too dramatically affected. However, a 20% reduction in complexing agent cost (dropping the case 3 LCOE from 0.478 \$ kWh^{-1} to 0.459 \$ kWh^{-1}) would not be sufficient to reach the LCOE of the non-complexing agent case (0.396 \$ kWh^{-1}), and the complexing agent cost would need to be reduced by nearly 90% for the case 3 LCOE to be below the base case LCOE for case 1. The membrane has low effect on the LCOE for case 3 due to the lower cost contribution of the silica/PVDF membrane compared to the Nafion membranes.

4. Availability of hydrogen-bromine system materials

The scale at which the hydrogen-bromine system can be deployed (independent of economics) depends on the availability of the materials used in construction of the battery. The main components necessary will be the electrolyte (hydrogen bromide/bromine), as well as the platinum group metal-based electrocatalysts. Although bromine production (600,000 tons $year^{-1}$) is not as large-scale as zinc (12 million tons $year^{-1}$), copper (17 million tons $year^{-}$

^{1}), or lead (8 million tons year^{-1}), it still is much larger than electrolytes for the vanadium flow cell (56,000 tons vanadium year^{-1}). If 1 GW of energy is desired (4 GWh capacity assuming 4 hour discharge), only 4% of one year's worth of bromine production would be required (see Supplementary Information).

The low loading of Rh or Pt that would be used (0.05 mg cm^{-2}) means nearly a GW per year of power capacity could be built using 0.25% of yearly production of rhodium as seen in Table S5. This would only be limiting for grid-scale systems, and even then scale may be feasible if precious metals were recovered for reuse.

5. Economic challenges

The fundamental economic challenge for electrical energy storage is that today and for the foreseeable future the cost of producing large quantities of electricity on demand from fossil fuels is lower than the cost of storing electricity using electrochemical energy storage [7]. There are smaller markets such as small off-grid power systems, locations of abnormally high low-cost supply or high-price demand, and locations restricting air or noise pollution, where electrochemical energy storage systems are competitive. As the price of energy storage is lowered, more of the market will become available for electrochemical storage systems where they might have impact on reducing the necessity of inefficient fossil fueled peaker plants, and allow for greater integration of renewables.

At 0.40 $ kWh^{-1} the hydrogen-bromine flow battery system is too high for grid-level or any price-sensitive application. The costs of the hydrogen-bromine system can be significantly lowered if the costs of the battery stack and power electronics can be reduced. Currently, the costs are competitive with other flow or stationary battery cell system, and thus can compete in the same markets.

6. Technical challenges

The hydrogen-bromine system cost is most sensitive to lifetime, current density, the hydrogen pressure, bipolar plate materials and construction methods, and the use of complexing agents to reduce the membrane cost.

The system lifetime has a large impact on the levelized cost of electricity. Developing electrocatalysts with long-term activity in both bromide and bromine is important to reducing cost. Metal sulfides have more stability in bromide/bromine than platinum metal or platinum metal alloys, although with slightly poorer performance [33–36]. The sensitivity analysis performed here indicates that improving the performance of the electrocatalysts can also significantly decrease the levelized cost of electricity. Only at unrealistically large production volumes will catalyst material shortages be limiting and the cost of the electrocatalysts is insignificant; it is lifetime that matters. Electrocatalyst development is focused on stability and builds on the work in stable metal sulfides [33,34]. Work is ongoing in screening for new materials, selective synthesis to maximize the active phases, and the use of substitutional doping to improve existing materials [33,54].

Significant increases in the current density of the hydrogen-bromine battery have contributed to making the system more cost-effective [25,26,39]. Continuing improvements in current density will further minimize the stack cost. Apart from developing more active electrocatalysts and higher conductivity membranes, optimizing ion concentrations [6] and improving mass transport can increase the practical current density and lower the levelized cost of electricity.

The high cost of hydrogen storage is a major limitation of the hydrogen-bromine system compared to other flow battery systems, especially as it scales with energy storage capacity, unlike the stack which scales with power. Lower hydrogen pressure during storage

leads to lower bipolar plate costs, however, a larger amount of hydrogen needs to be stored (to maintain a minimum pressure of 2 bar when the system is discharged). For a system with a 4 hour discharge time and a hydrogen storage costs of 1000 \$ kg^{-1}, and bipolar plate costs of 300 \$ m^{-2} at 30 bar, our model indicated that the ideal storage hydrogen pressure was dependent on whether a complexing agent was used. The range was 28-31 bar for a 4 hour discharge to 18-22 bar for a 1 hour discharge. These findings are in agreement with previous work indicating 30 bar as the typical hydrogen operating pressure (based on the pressure used for proton exchange membrane electrolyzers) [6]. The costs of hydrogen storage can be reduced if lower cost storage materials are commercially available [47].

Lowering the bipolar plate cost is important to reducing the stack cost. Corrosion is a major issue, which can be overcome by several techniques, either using a system similar to that used in fuel cells, corrosion-resistant vias through nonconductive coating, or by use of less expensive materials such as conductive carbon polymer composites that are molded and/or machined to contain flow field geometries.

The membrane cost is an important factor in the overall system cost. As in many other electrochemical applications, low-cost membranes, with high ionic conductivity, and resistant to crossover are needed and their availability has progressed rather slowly. Membrane requirements might be relaxed when and if low-cost bromine complexing agents are available to effectively reduce the concentration of free bromine driving crossover. The system safety would also be increased by reduction of the bromine concentration (and thus vapor pressure). A bromine complexing agent will reduce the free bromine concentration, however, the bromine reaction rates on the electrodes would also be expected to decrease. The concentration of free bromine affects bromine kinetics [6]; however, the effect of complexing agents will depend upon the rate of uptake and release and has not been studied

quantitatively in detail. The high cost of the best available complexing agents suggests the more cost-effective solution to minimize bromine crossover is to use a highly selective membrane rather than complexing agents, for discharge times more than fifteen minutes. The ideal complexing agent has not been identified, however, in zinc bromine batteries, MEP is generally selected. If the cost of the complexing agent can be reduced, they may be an economical alternative to high-cost Nafion membranes. For example, if the complexing agent cost was the same as polyethylene glycol (a low-performance bromine complexing agent, nearly a tenth the cost of MEP) the levelized cost of electricity for a case with complexing agents could be 0.39 \$ kWh^{-1}, compared to 0.40 \$ kWh^{-1} for the membrane-only case described here.

D. Conclusions

The demonstrated efficiency and high current density of the hydrogen-bromine flow battery system allows for a relatively small power specific stack surface area (m^2 W^{-1}) and thus a reduced stack size and cost. The hydrogen-bromine technology is expected to be cost-competitive with the lowest cost flow battery systems which have applicability for small to medium-scale applications with an approximately 1 GW market in the U.S. The lifetime of the stack and hydrogen storage cost are the major factors responsible for the present high levelized cost of electricity delivered by a HBr flow battery system. Assuming that electrocatalysts and membrane components with 2000 cycle lifetimes are available, the system can produce a levelized cost of electricity of 0.40 \$ kWh^{-1} for a 4 hour discharge, cycling once per day at a charging electricity price of 0.04 \$ kWh^{-1}. The major unit costs for a conventional hydrogen-bromine flow battery stack are the bipolar plate and the membrane. The overall system cost is highly dependent on the hydrogen storage tank, valve system, and

power electronics cost. The choices for the cell membrane are limited to relatively costly products and bromine complexing agents, which would allow less costly alternatives, are expensive at present. For any realistic deployment scenario, the supply of stack materials is unlikely to be a limiting factor for hydrogen-bromide flow batteries.

Acknowledgements

Support for this work was provided by the University of Queensland, Dow Centre for Sustainable Engineering Innovation and the NSF (EFRI-1038234). The authors would like to acknowledge the contributions of Joe Lane, Daniel Klein-Maruschamer, Professor Horia Metiu, Professor Michael Doherty and Alex Winter for helpful discussions and their assistance in preparing the manuscript.

References

[1] Sources of Greenhouse Gas Emissions. Available from: http://www.epa.gov/climatechange/ghgemissions/sources.html [accessed 08.25.14]

[2] M. Cordaro, Understanding Base Load Power. What it is and Why it Matters, 2008.

[3] S. van der Linden, Energy. 31 (2006) 3446.

[4] B. Decourt, R. Debarre, Electricity Storage. SBC Energy Institute, 2013.

[5] DOE, Grid Energy Storage, 2013.

[6] K.T. Cho, P. Albertus, V. Battaglia, A. Kojic, V. Srinivasan, A.Z. Weber, Energy Technol. 1 (2013) 596.

[7] Z. Yang, J. Zhang, M.C.W. Kintner-Meyer, X. Lu, D. Choi, J.P. Lemmon, J. Liu, Chem. Rev. 111 (2011) 3577.

[8] K. Bradbury, L. Pratson, D. Patiño-Echeverri, Appl. Energy. 114 (2014) 512.

[9] P. Denholm, J. Jorgenson, M. Hummon, T. Jenkin, D. Palchak, B. Kirby, O. Ma, M. O'Malley, The Value of Energy Storage for Grid Applications, 2013.

[10] C.-J. Yang, Pumped Hydroelectric Storage, 2012.

[11] P. Komor, J. Glassmire, Electricity Storage and Renewables for Island Power, 2012.

[12] F. Meyer, Compressed air energy storage power plants, 2007.

[13] J. Rugolo, M.J. Aziz, Energy Environ. Sci. 5 (2012) 7151.

[14] R.S. Yeo, D.-T. Chin, J. Electrochem. Soc. 127 (1980) 549.

[15] G.G. Barno, S.N. Frank, T.H. Teherani, L.D. Weedon, J. Electrochem. Soc. 131 (1984) 1973.

[16] B. James, J. Kalinoski, K. Baum, Mass-Production Cost Estimation for Automotive Fuel Cell Systems, 2010.

[17] K.L. Hsueh, D. Chin, J. Mcbreen, S. Srinivasan, J. Appl. Electrochem. 11 (1981) 503.

[18] Hydrogen Bromine Battery. Available from: http://arpa-e.energy.gov/?q=slick-sheet-project/hydrogen-bromine-battery [accessed 08.20.14]

[19] Inflation Calculator. Available from: http://www.usinflationcalculator.com/ [accessed 10.06.14]

[20] C. Wanh, Development of Low Cost PEMFC Metal Bipolar Plate, 2011.

[21] J. Marcinkoski, B.D. James, J.A. Kalinoski, W. Podolski, T. Benjamin, J. Kopasz, J. Power Sources. 196 (2011) 5282.

[22] About PEM fuel cells. Available from: http://www.nedstack.com/faq/about-pem-fuel-cells [accessed 08.25.14]

[23] R.J. Charleston J., Hydrogen-Bromine Fuel Cell Advance Component Development, 1988.

[24] H. Kreutzer, V. Yarlagadda, T. Van Nguyen, J. Electrochem. Soc. 159 (2012) F331.

[25] K.T. Cho, M.C. Tucker, M. Ding, P. Ridgway, V.S. Battaglia, V. Srinivasan, A.Z. Weber, ChemPlusChem. 80 (2014) 402.

[26] V. Livshits, A. Ulus, E. Peled, High-power H2/Br2 fuel cell, Electrochem. Commun. 8 (2006) 1358–1362. doi:10.1016/j.elecom.2006.06.021.

[27] W. Glass, G.H. Boyle, Performance of Hydrogen-Bromine Fuel Cells, in: Fuel Cell Syst., 1969: pp. 203–220.

[28] E. Peled, A. Blum, A. Aharon, Method of manufacturing proton-conducting membranes US 2012/0312696 A1, 2012.

[29] E. Peled, A. Blum, A. Aharon, N. Travitsky, Y. Konra, K. Saadi, V. Zel, M. Goor, M. Alon, R. Gorenshtein, Catalysts and electrodes for fuel cells US 2012/0308907 A1, 2012.

[30] E. Peled, A. Blum, A. Aharon, Y. Konra, V. Zel, K. Saadi, Bipolar plates and regenerative fuel cell stacks including same US 2012/0308911 A1, 2012.

[31] E. Peled, A. Blum, Electrochemical systems and methods of operating same US 2012/0295172 A1, 2012.

[32] E. Peled, A. Blum, A. Aharon, N. Travitsky, Y. Konra, I. Tsamir, V. Zel, K. Saadi, M. Alon, R. Gorenshtein, Energy storage and generation systems US 2012/0299384 A1, 2012.

[33] A. Ivanovskaya, N. Singh, R.-F. Liu, H. Kreutzer, J. Baltrusaitis, T. Van Nguyen, H. Metiu, E. McFarland, Langmuir. 29 (2013) 480.

[34] T. Van Nguyen, H. Kreutzer, V. Yarlagadda, E. McFarland, N. Singh, ECS Trans. 53 (2013) 75.

[35] J. Masud, J. Walter, T. Van Nguyen, G. Lin, N. Singh, E. McFarland, H. Metiu, M. Ikenberry, K. Hohn, C.-J. Pan, B.-J. Hwang, ECS Trans. 58 (2014) 37.

[36] N. Singh, S. Mubeen, J. Lee, H. Metiu, M. Moskovits, E.W. McFarland, Energy Environ. Sci. (2014) 1.

[37] W.A. Braff, M.Z. Bazant, C.R. Buie, Nat. Commun. 4 (2013) 2346.

[38] EnStorage Inc. Israel. Available from: http://www.enstorageinc.com/?cmd=news.0&act=read&id=30 [accessed 08.02.14]

[39] K.T. Cho, P. Ridgway, A.Z. Weber, S. Haussener, V. Battaglia, V. Srinivasan, J. Electrochem. Soc. 159 (2012) A1806.

[40] J.W. Park, R. Wycisk, P.N. Pintauro, ECS Trans. 50 (2012) 1217.

[41] Applied processes and techniques. Available from http//www.ineris.fr/ippc/sites/default/interactive/brefca/bref_gb_ptmo.htm [accessed 08.10.14]

[42] M.A.R.S. Al-baghdadi, H.A.K.S. Al-janabi, Turkish J. Eng. Environ. Sci. 29 (2005) 235.

[43] J.-Y. Lee, J. Joo, J.K. Lee, S. Uhm, E.S. Lee, J.H. Jang, N.-K. Kim, Y.-C. Lee, J. Lee, Korean J. Chem. Eng. 27 (2010) 843.

[44] M.C. Tucker, K.T. Cho, A.Z. Weber, G. Lin, T. Van Nguyen, J. Appl. Electrochem. 45 (2014) 11.

[45] W.A. Amos, Costs of Storing and Transporting Hydrogen, 1998.

[46] S.M. Ali, J. Andrews, Low-cost storage options for solar hydrogen systems for remote area power supply, in: World Hydrog. Energy Conf. Lyon Fr. June 2006, 2006.

[47] B.D. James, Hydrogen Storage Cost Analysis, Preliminary Results, 2012.

[48] P. Leung, X. Li, C. Ponce de León, L. Berlouis, C.T.J. Low, F.C. Walsh, RSC Adv. 2 (2012) 10125.

[49] A.Z. Weber, M.M. Mench, J.P. Meyers, P.N. Ross, J.T. Gostick, Q. Liu, J. Appl. Electrochem. 41 (2011) 1137.

[50] L.A. Kosek J., Investigation of bromine complexed hydrogen/bromine regenerative fuel cells for portable electric power, 1984.

[51] K. Ayers, PEM Electrolysis R & D Webinar, 2011.

[52] M. Hamdan, PEM Electrolysis Webinar Giner, 2011.

[53] McMaster-Carr. Available from: http://www.mcmaster.com/ [accessed 10.06.14]

[54] N. Singh, J. Hiller, H. Metiu, E. McFarland, Electrochim. Acta. 145 (2014) 224.

[55] A.A. Akhil, G. Huff, A.B. Currier, B.C. Kaun, D.M. Rastler, S.B. Chen, A.L. Cotter, D.T. Bradshaw, W.D. Gauntlett, DOE / EPRI 2013 Electricity Storage Handbook in Collaboration with NRECA, 2013.

[56] M. Barry, Power Generation Technology Data for Integrated Resource Plan of South Africa, 2012.

[57] V. Viswanathan, M. Kintner-Meyer, P. Balducci, C. Jin, National Assessment of Energy Storage for Grid Balancing and Arbitrage, 2013.

[58] G.N. Doty, D.L. McCree, F.D. Doty, Proc. ES2010. (2010) 6.

[59] B.D. Rastler, New demand for energy storage, Electric Perspectives, September/October (2008) 30.

[60] U.S. Energy Information Administration (EIA). Available from: http://www.eia.gov/forecasts/capitalcost/ [accessed 10.06.14]

[61] Clean & Efficient - America's Natural Gas Alliance. Available from: http://anga.us/issues-and-policy/power-generation/clean-and-efficient#.VEwhuPnF9Yw [accessed 10.06.14]

[62] S. Eckroad, Vanadium Redox Flow Batteries, 2007

III. Transition metal sulfide hydrogen evolution catalysts for hydrobromic acid electrolysis

Abstract

Mixed metal sulfides containing combinations of W, Fe, Mo, Ni, and Ru were synthesized and screened for activity and stability for the hydrogen evolution reaction (HER) in aqueous hydrobromic acid (HBr). Co- and Ni-substituted RuS_2 were identified as potentially active HER electrocatalysts by high-throughput screening (HTS), and the specific compositions $Co_{0.4}Ru_{0.6}S_2$ and $Ni_{0.6}Ru_{0.4}S_2$ identified by optimization. Hydrogen evolution activity of $Co_{0.4}Ru_{0.6}S_2$ in HBr is greater than RuS_2 or CoS_2 and comparable to Pt and commercial Rh_xS_y. Structural and morphological characterizations of the Co-substituted RuS_2 suggest that the nanoparticulate solids are a homogeneous solid solution with a pyrite crystal structure. No phase separation is detected for Co substitutions below 30% by X-ray diffraction. In 0.5 M HBr electrolyte the Co-Ru electrode material synthesized with 30% Co rapidly lost approximately 34% of the initial loading of Co; thereafter, it was observed to exhibit stable activity for HER with no further loss of Co. Density Functional Theory calculations indicate that the S_2^{2-} sites are the most important for HER and the presence of Co influences the S_2^{2-} sites such that the hydrogen binding energy at sufficiently high hydrogen coverage is decreased compared to ruthenium sulfide. Although showing high HER activity in a flow cell, the reverse reaction of hydrogen oxidation is slow on the RuS_2 catalysts tested when compared to platinum and rhodium sulfide, leaving rhodium sulfide as

the only suitable tested material for a regenerative HBr cell due its stability compared to platinum.

A. Introduction

The electrolysis of hydrohalic acids, in particular HBr and HCl, has several potential applications for the production of hydrogen,[1-3] production or recovery of halogens,[3-7] and in reversible flow cells for energy storage.[8-13] In energy-storage applications HBr electrolysis is particularly attractive because the relatively low decomposition voltage[14, 15] of HBr is below the oxygen evolution potential and the reactions at both the hydrogen and bromine electrodes are relatively fast.[13, 16] Further, bromine is earth-abundant and a liquid at room temperature, and readily separated from hydrogen.[15, 16]

An aqueous solution of HBr and Br_2 ("red acid") is an extremely corrosive electrolyte and the identification of electrode materials that are electrochemically active and stable in it is challenging. In previously developed electrolytic cells[14, 16] the kinetics of the hydrogen evolution reaction (HER) have been shown to be limiting, and improved hydrogen electrode materials are required. The rates can be increased using high-surface-area metallic nanoparticulate catalysts but unfortunately bromine is known to bind strongly to metals and the catalysts are unstable with respect to corrosion in HBr.[14] There has been considerable interest in finding materials for electrocatalysts that are sufficiently stable to allow the utilization of nanodispersed particles to maintain high reaction rates.[17, 18]

There are indications that transition metal sulfides (TMS) might provide active and stable electrocatalytic materials. Commercially, rhodium sulfide is known to be a stable and active cathode catalyst for oxygen-reduction-assisted electrolysis of hydrochloric acid.[19, 20]

Density functional theory (DFT) calculations have been helpful in assessing the HER thermodynamics on various electrodes. The free energy of hydrogen bound to a surface atom can be calculated by DFT and is commonly used as a predictor for HER activity.[21] If the adsorption free energy of hydrogen to the surface is small, the activity is high, because hydrogen (H) can adsorb well and can be removed from the surface as molecular hydrogen (H_2) without a high activation energy.[21] TMS show activities and hydrogen adsorption free energies similar to the more active metal catalysts.[22, 23] The hydrogen adsorption energy to MoS_2 is 0.1 eV,[24] compared to –0.1 eV for Pt at the same hydrogen coverage,[21] predicting that MoS_2 and Pt would have comparable activities for hydrogen evolution. The hydrogen evolution rates on MoS_2 nanoparticles are slightly below those of the most-active noble metal catalysts, indicating that the theoretical predictions can be reliable and the calculated hydrogen binding energy is a good indicator of HER activity for metal sulfides.[22]

It is possible to optimize the catalytic activity of the industrial hydrodesulfurization sulfide catalysts by substituting them with Co or Ni[25-27] to modify the properties of the surface. It is hoped that substitution may decrease the activation barrier for hydrogen activation and change the activity for hydrogen evolution.

There are two specific families of metal sulfides that are worth focusing on for hydrogen electrocatalysts in aqueous HBr electrolyte due to activity, stability and the ability to synergistically interact with substituted metals. The transition metals (Ru and *3d* transition metals from Mn to Zn) form disulfides with pyrite structure. Mixed metal pyrites can be synthesized in bulk as solid solutions for a large range of compositional variations.[28, 29] Pyrites are conductive semi-metals or narrow gap semiconductors,[29] which is necessary for electrocatalysis. Mo and W disulfides are also interesting. MoS_2 is an active catalyst for

HER, and Co and Ni promote HER activity of nanoparticulate carbon (or SiO_2) supported Mo and W disulfides.[30, 31]

This background prompted us to investigate the stability and activity of substituted transition metal sulfides as hydrogen evolution electrocatalysts for hydrobromic acid electrolysis. We attempt here to answer the following questions:

1. Can the hydrogen evolution activity of known transition metal sulfides be increased by substitution with a second metal species, and can we use high-throughput experimentation methods to rapidly identify candidate mixed metal sulfides?

2. What are the quantified activities of the most-active transition metal sulfides identified by high-throughput screening and how do they compare to industrially used hydrogen electrode materials?

3. What are the stabilities of the metal sulfides in the corrosive conditions of HBr that would be typical of an electrolyzer during both operation and shutdown and what is the mechanism of corrosion?

4. How does the hydrogen electrode based on TMS perform in a H_2-H_2 flow cell?

5. Can the density functional theory (DFT) be helpful in understanding the experimental observations?

B. Methods

1. Preparation of catalysts, inks and electrodes

Vulcan X72 high-surface-area carbon was impregnated with an aqueous solution of metal salts (4.3 mL of 1 M solution per one gram of carbon for all solutions, or equivalent volume of Mo and W precursors to load 4.3 mmol metal per gram carbon). Wet powders were dried in the furnace at 100 °C for 1 hour. The dried powders were exposed to 50% H_2S

(in N_2) in a tube furnace reactor using a temperature profile of 10 °C/min ramp followed by a 3-hour dwell at 300 °C prior to cooling to room temperature. Samples were synthesized in small ceramic crucibles; 7 mg of carbon was used for one sample preparation. Up to 48 samples were prepared in the furnace simultaneously.

The metal precursors used for the synthesis of transition metal sulfide catalysts (either as pure monometallic sulfides or as metal sulfides with substitutions) are listed in Table 1 along with the ratios of sulfur to metal determined by Energy Dispersive X-ray Spectroscopy (EDS) and the structure determined by X-ray Diffraction (XRD).

Table 1.[(a)] Precursors, atomic ratios of sulfur to metal ([S]/[M]) in synthesized TMS as determined by EDS, and structure as determined by XRD for metal sulfides prepared

Metal	Precursor	[S]/[M]	Structure	Metal	Precursor	[S]/[M]	Structure
Cr	$Cr(NO_3)_3 \cdot 9H_2O$	—	—	Cu	$CuCl_2$	—	—
Mn	$MnCl_2$	—	—	Mo	$H_3PMo_{12}O_{40}$	2.0	H
Fe	$FeCl_3 \cdot 6H_2O$	1.9	P	Ru	$RuCl_3$	1.9	P
Co	$CoCl_2 \cdot 6H_2O$	1.7	P	Rh	$RhCl_3(H_2O)_x$	—	—
Ni	$NiCl_2 \cdot 6H_2O$	2.5	P	W	$H_3PW_{12}O_{40}$	2.3	H

(a) Standard deviation of atomic ratios determined by EDS varied from 5 to 20% of the average values. In the structure type column pyrite and hexagonal type structures are denoted by "P" and "H" respectively.

Inks were made from a suspension of 3 mg catalyst, 5 mL of 1:1 vol.% mixture of 2-propanol (HPLC grade, Fisher Scientific) and deionized water, and 17.5 µL of 5 wt.% Nafion™ solution (Aldrich). The inks were sonicated in an ultrasonic bath at room temperature for 2 hours and distributed on 0.05-cm^2 glassy carbon supports. For high-throughput screening, 3 µL of the inks were distributed over the electrode substrates on glassy carbon (see details on substrate preparation in the Supporting Information); catalyst loading was 36 µg/cm^2.

Inks were applied to a 0.178-cm^2 area glassy carbon disk (Pine Instrument Co.) from two 8 μL aliquots, and dried in ambient air after each application for the RDE experiments. The nominal loadings for all RDE experiments were 54 $\mu g/cm^2$ (geometric).

Electrodes on Toray™ carbon paper (Fuel Cell Store Inc.) were prepared by dispersing catalyst inks on rectangular strips 1 cm x 3 cm. Concentrated inks were prepared by dispensing 6 mg catalyst in 1 mL of 1:1 vol.% mixture of 2-propanol and deionized water, and 35 μL of 5 wt.% Nafion™ solution. An area of 2 cm^2 was covered with 0.164 mL of ink for a catalyst loading of 0.5 mg/cm^2. The electrodes for the O_2/Ar/air samples were prepared in the same manner as that for the 48-hour corrosion test.

2. High-throughput screening for hydrogen evolution activity

Prior to taking images, the array of electrocatalysts ("library") was tested in 0.5M HBr solution, purged with argon for 10 minutes, and conditioned by performing five cycles of potential sweeps from 0 to –0.4 and back to 0 V *vs.* Standard Hydrogen Electrode (SHE). Images of the library were taken using a color CCD camera "SPOT Insight Color digital camera" (Diagnostic Instruments, Inc.) controlled by LabVIEW™ software developed by the authors. An overhead projector was used as a light source to enhance the digital images of the library. The potential of the working electrode was controlled relative to Ag/AgCl reference electrode during the measurements (later recalculated to the potential relative to SHE) and varied linearly from 0 to -0.325 V at a rate of 5 mV/s, confirmed by a calibration performed immediately prior to the test. A diagram of the experimental system along with a more detailed explanation of the setup is shown in Figure S1.

3. Electrochemical test methods

A Pine Instrument MSRX Rotating Disk Electrode was used to measure the activity of the metal sulfides in a two-compartment electrochemical cell with cathode and anode compartments separated by a silica frit diaphragm and a Nafion™ membrane. The counter electrode was a platinum mesh and the reference electrode was Ag/AgCl. Cyclic voltammetry was performed using EG&G 270A potentiostat in argon-saturated 0.5M HBr solution.

4. H_2-H_2 regenerative cell test

A 2.25-cm^2 flow battery consisting of Al endplates, stainless steel current collectors, graphite flow distributors and a six-layer (cathode-GDL/CL/Membrane/CL/MPL/GDL-anode) membrane electrode assembly (MEA) made by TVN Systems, Inc., was used with a Nafion 112 membrane. The cathode contained 0.75-mg Pt catalyst/cm^2 loading (30% Pt on Vulcan 72X), and the anode contained 0.75-mg catalyst/cm^2 loading of RuS_2, $CoRuS_2$, Rh_xS_y or Pt. Interdigitated flow fields were used to improve mass transport to the electrodes.[32] The cell was tested at room temperature (22 °C). Hydrogen at 3 psig was continuously circulated through the cell both at the anode and cathode at 2206 mL/min, so that the oxidation reaction was hydrogen oxidation, and the reduction reaction was hydrogen evolution. Changing the polarity of the electrodes reversed which electrode was acting as the cathode and which was acting as anode. A potentiostat/galvanostat (Arbin Instruments) was used to control the cell potential. The data reported represent average values collected over 2 minutes.

5. Analysis of corrosion products

Measurement of dissolution products

Dissolution product concentrations were measured by Inductively Coupled Plasma-Atomic Emission Spectroscopy (ICP-AES) calibrated using standards obtained from High-Purity Standards (Cat. # 100013-2 for Co and # 100046-2 for Ru).

Measurement of gaseous products

A Stanford Research Systems Residual Gas Analyzer (SRS RGA) model 200 Mass Spectrometer was used to measure the concentrations of gas due to corrosion by injecting 0.25 -1 mL by volume of gas into the spectrometer, and measuring the response of M/Z 34.

Qualitative chemical test for hydrogen sulfide and sulfate ions

To test whether corrosion produced hydrogen sulfide, 350 μL of the 6M HBr solution was neutralized with 350 μL of 6M NaOH, then 23 mg of lead nitrate (corresponding to 0.1M lead nitrate in solution) was added.

A standard analytic test[33] for detection of sulfate ions in the test solutions was used. Eight mg of $Ba(NO_3)_2$ powder was added to 500 μL of the test solution and the presence of sulfate ions (as HSO_4^-) would be confirmed by the formation of white precipitate ($BaSO_4$). A control solution with sulfate ions verified the test, and a control solution of H_2S did not form a white precipitate, indicating selectivity of the test for sulfate. $Ba(NO_3)_2$ may also react with sulfite (SO_3^{2-}) to form a white precipitate, but SO_3^{2-} is unstable in acidic media, and forms SO_2.

6. Structure, composition, and morphology characterization

X-ray diffraction data were collected on an X'Pert Powder diffractometer (PANalytical, Inc.) with a Cu Kα source (corresponding to a photon wavelength of 1.54 Å).

For the measurement of lattice parameters, the position of the (200) diffraction peak of RuS_2 was precisely determined against a known Si (111) peak position from Si mixed with the sample.

Scanning and transmission electron microscopy (SEM and TEM) of the powder electrocatalysts was performed with a FEI XL40 Sirion FEG Digital Scanning Microscope with Energy Dispersive X-ray Spectroscopy System and a FEI T20 electron microscope operating at 200 keV. TEM samples were prepared by suspending the sample in ethanol then using a micropipette to deposit the sample on a polycarbon grid.

High-resolution and survey XPS scans were collected using Kratos Axis Ultra spectrometer (Kratos Analytical, Manchester, UK) equipped with a monochromated 1486.6 eV aluminum Kα source having a 500-mm Rowland circle silicon single-crystal monochromator. All binding energies (BE) were referenced to carbon black (conductive carbon) C 1s at 284.4 eV. Data processing and quantification was done using commercially available CasaXPS.[34] Further details on the XPS measurements are included in the Supporting Information.

7. Computation methods

For the DFT[35] calculations we used spin-polarized, generalized gradient approximation with the Perdew-Burke-Ernzerhof (PBE) functional.[36] The core electrons were described by the projector augment-wave (PAW) method[37] implemented by Kresse and Joubert[38] in the VASP 4.6 program. The energy cut off for plane-wave expansion was set to 350 eV. No symmetry was imposed during structure relaxation. A correction to the total energy to remove artificial dipole effects was included.[39] The slabs used in the calculations consist of three stoichiometric layers. The atomic positions in the bottom layer were fixed at

the bulk positions that were calculated by using a 5×5×5 k-grid for the cubic pyrite bulk structure. In all calculations the positions of the adsorbates and of the atoms in the top two stoichiometric layers were obtained by minimizing the total energy without symmetry constraints. In all cases we examined several spin states and report here the ones that have the lowest energy. The geometry optimization was considered satisfactory when the largest force on an individual atom was less than 20 meV/Å.

C. Results

1. Synthesis of mixed metal sulfides based on W, Fe, Mo, Ni, and Ru

Synthesis of pyrite type TMS

The sulfides synthesized from Ru, Fe, and Ni precursors have a pyrite structure (Figures S2, S3 and S4). EDS analysis shown in Table 1 indicates that the sulfur-to-metal molar ratios in Ru and Fe sulfides are close to the stoichiometric value of two for disulfides. Ni sulfide is sulfur-rich.

The synthesis reaction starting from Ru (or Fe) chloride is:

$$2\ RuCl_3 + 4\ H_2S \leftrightarrow 2\ RuS_2 + 6\ HCl + H_2$$

Experimental observation suggested that ruthenium sulfide synthesis is very sensitive to the synthesis temperature: increasing the temperature from 300 to 350 °C resulted in two-phase crystalline compounds (verified by XRD): RuS_2 and Ru metal. Analysis of reactive gas mixture by differential mass-spectrometry showed the presence of about 6% H_2 in H_2S/N_2 gas source cylinder at room temperature. Ruthenium chloride may react with hydrogen according to the following equation:

$$2\ RuCl_3 + 3\ H_2 \leftrightarrow 2\ Ru + 6\ HCl$$

Gas product analysis by differential mass spectroscopy did not show chlorine gas in the mixture.

The synthesis reaction starting from Ni chloride is:

$$NiCl_2 + 2\ H_2S \leftrightarrow NiS_2 + 2\ HCl + H_2$$

Morphological and structural change with substitution concentration in pyrites

Substitution with Fe and Ni resulted in formation of pyrite structures with no other crystalline phases present in XRD. All pyrite peak positions were shifted to the higher (Fe) or lower (Ni) 2θ angles with an increase in substitution concentration, in agreement with the lattice parameter variation in mixed pyrite solid solution (labeled "$Fe_xRu_{1-x}S_2$ theoretical" and "$Ni_xRu_{1-x}S_2$ theoretical", respectively, in Figure S5). Similar to Vegard's law for alloys, pyrites can form a continuous range of solid solutions where the lattice parameter changes linearly with the substitution concentration.[29] Solid solutions were formed for $Fe_xRu_{1-x}S_2$ and $Ni_xRu_{1-x}S_2$ materials for $0 < x < 0.6$ with no phase separation.

The lattice parameter of $Co_xRu_{1-x}S_2$ was found to decrease with the molar ratio x for $x < 0.3$ to 0.4. The linear dependence is consistent with the theoretical lattice contraction of mixed Co-Ru pyrite solid solution (labeled "$Co_xRu_{1-x}S_2$ theoretical" in Figure S5). At higher concentrations ($x > 0.3$ - 0.4) the lattice parameter becomes independent of concentration. At high concentrations of cobalt, specifically $x = 0.5$ and 0.6, an additional phase was observed by XRD and identified as the pentlandite structure Co_9S_8. Finally, material synthesized from a pure cobalt precursor ($x = 1$) was found to crystallize in the pyrite structure of CoS_2.

At low Mn and Cu concentrations, the data suggest that there was substitution into the crystal lattice of RuS_2 as observed by the pyrite lattice expansion at $x < 0.2$ and $x < 0.3$, respectively. Mn-substituted RuS_2 was found to experience phase separation with growth of

a second phase of Mn_2S (alabandite structure) at $x \geq 0.4$. Cu-substituted RuS_2 did not show any other crystalline phases except pyrite due to either low degree of crystallinity or high degree of significant dispersion of a second phase.

The morphology of Co-substituted ruthenium sulfide materials with different concentration of Co substitution was examined by TEM and SEM. The average size of RuS_2, NiS_2, and FeS_2 crystalline domains, denoted τ, were estimated using fits to the Scherrer equation of the X-ray diffraction peaks.[40] A summary of these crystalline domains is shown in Table 2 calculated using a shape factor k = 0.8 with an instrumental broadening of 0.1 degree.

Table 2. Crystallite size of synthesized metal sulfides on carbon measured by X-ray diffraction (Figures S1 – S3) and calculated by Scherrer equation.

Metal sulfide	RuS_2	NiS_2	FeS_2
Crystallite size (from Scherrer equation), nm	13-16	40	23

TEM studies confirmed the nanoparticulate morphology of the RuS_2 sample with particle sizes of ~10 nm (Figure S6a). The RuS_2 nanoparticle size was not affected by the introduction of small amounts of Co or Ni (20%), as can be seen from the TEM image (Figure S6b). The morphology of RuS_2 with 60% cobalt content (x = 0.6) was examined by SEM. Large crystallites (~0.5 μm) of Co_9S_8 were observed by SEM (Figure S6c). The morphology of the 100% Co sample by SEM showed that the material has a low degree of dispersion and consists of submicron particles supported on carbon (Figure S6d).

Examination of NiS_2 and FeS_2 samples by SEM did not reveal particulates that were distinguishable from the 50 nm carbon particles suggesting that the sulfide particles were either too small to visualize or, more likely, of an indistinguishable size compared to the carbon (sulfide sizes were estimated from the Scherrer equation, see Table 2).

The characterization of Mo and W sulfides is explained in detail in the Supporting Information section (Figures S9-S12).

2. Screening by bubble evolution or gas detection

Reactivity screening of a collection of the synthesized TMS materials for hydrogen evolution was performed by observing hydrogen-bubble growth at the surface of the catalysts during cyclic voltammetry scans. A library of 228 different catalyst samples based on mixed W, Fe, Mo, Ru, and Ni disulfides with the substituted metal molar concentrations ranging from 5% to 60% (for RuS_2) and 10 to 50% (for WS_2, FeS_2, MoS_2 and NiS_2) was prepared and screened. The layout of the library together with HER activity screening image under applied potential of -0.33 V vs. NHE are shown in Figure 1.

In the image, hydrogen bubbles are visualized by the high-intensity reflections. Based on the relative density of bubbles forming on the various samples, the substituted RuS_2 samples were the most active catalysts in the library (Figure 1). Apart from substituted ruthenium sulfides, the WS_2 substituted with Ru and Rh, FeS_2 substituted with Rh, and MoS_2 substituted with Ru and Rh also showed significant gas evolution activity. Although TMS substituted with Rh (WS_2, FeS_2) showed significant activity, we excluded them from our choice of the catalysts due to the high cost of Rh. The Co-substituted RuS_2 library showed sufficient activity to be considered as promising cost-effective catalyst candidates for the hydrogen evolution reaction. Among substituted NiS_2 catalysts (Figure 1b), the Ru-substituted samples showed the highest relative activity for HER under these conditions.

A. Substituted RuS_2

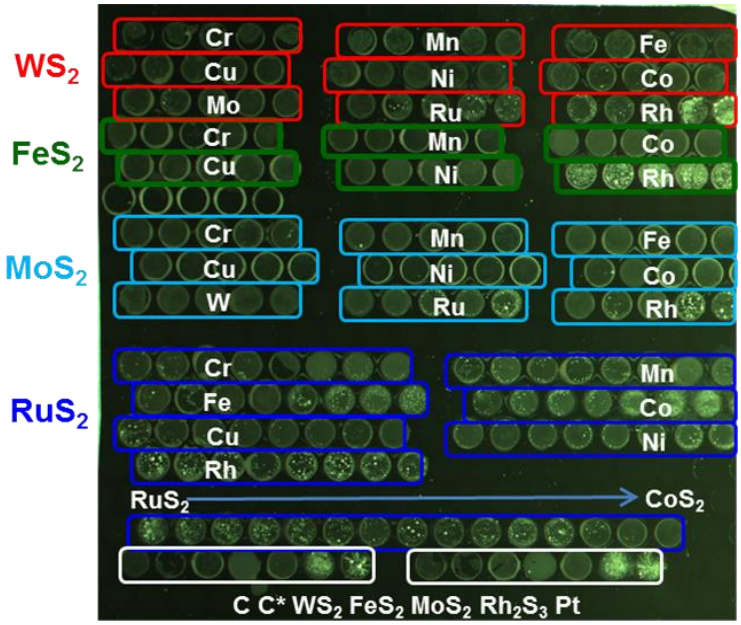

B. Substituted NiS_2

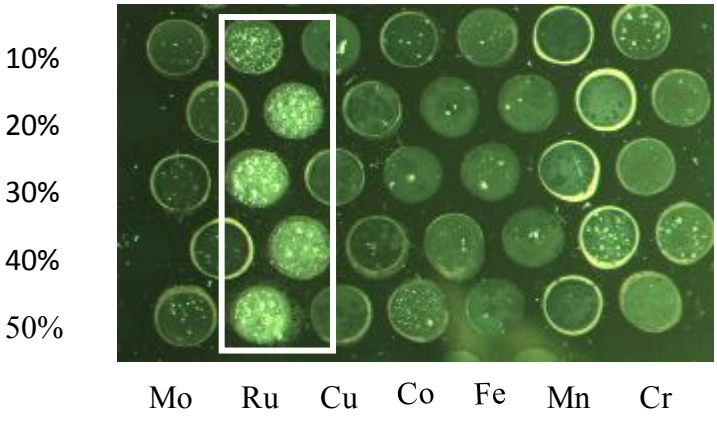

Figure 1. TMS catalyst libraries during the test using the system depicted in Figure S1. On the layout map: A) substituted RuS_2 catalysts with the substituted metal molar concentrations ranging from 5% to 60% (left to right) and substituted WS_2, FeS_2, MoS_2 catalysts with substituted metal molar concentrations ranging from 10% to 50% (left to right). On the image: hydrogen evolution in 0.5M HBr under potential of –0.33 V vs. NHE. The amount of bubble evolution is used to identify high-activity materials. B. Nickel sulfide catalyst library evolving hydrogen in 0.5M HBr under a potential of -0.33 V vs. NHE. The density of the bubbles is used to identify high-activity materials. The dopant concentration ranges from 10-50%.

3. Activity of Transition metal sulfides for HER

Optimization as a function of substitution metal concentration

Materials identified as active catalysts by high-throughput screening were further tested for hydrogen-evolution activity by cyclic voltammetry. Co-substituted RuS_2 samples with different substituted metal concentrations show that the logarithm of the current varies linearly with the potential in the potential window between –0.13 and –0.05 V (Figure S13). This linear region was attributed to a regime of kinetically controlled current and was used for the determination of the Tafel slopes. It has been shown[41] that under the assumption of fast proton adsorption (Volmer step), a Tafel slope varying between 40 mV/decade (mV/dec) and 118 mV/dec (values are dependent on the surface coverage) indicates that HER is likely accomplished through the reaction of a hydrogen atom with a proton, i.e. the Volmer-Heyrovsky mechanism. The Tafel slopes determined for the Co-substituted RuS_2 samples, with substitution concentrations varying from 5 to 60% are about 65-75 mV/dec. The Tafel slope for the pure RuS_2 sample is approximately 107 mV/dec, and is distinct from that of the Co-substituted samples. These results indicate the reaction on Co-substituted RuS_2 proceeds through a Volmer-Heyrovsky mechanism and that substitution with Co enhances the activity of HER.

The geometric current densities at an overpotential of –0.33V measured for hydrogen evolution during HBr electrolysis for samples with different cobalt concentration are shown in Figure 2. The optimal catalyst compositions were approximately 30-40% Co-substituted RuS_2 and ~60% Ni-substituted RuS_2. Interestingly, the highest activity of Co-substituted RuS_2 corresponds to a Co concentration at which the material is observed to begin to form separate phases. Therefore, poorly dispersed Co_9S_8 phase is not an active catalyst for HER. Studies of morphology indicate that the size of solid pyrite solution mixed-phase

nanoparticles does not change noticeably as a function of a substitution for small concentrations (up to 20%), which may indicate little change in the surface area with increasing concentrations of Co.

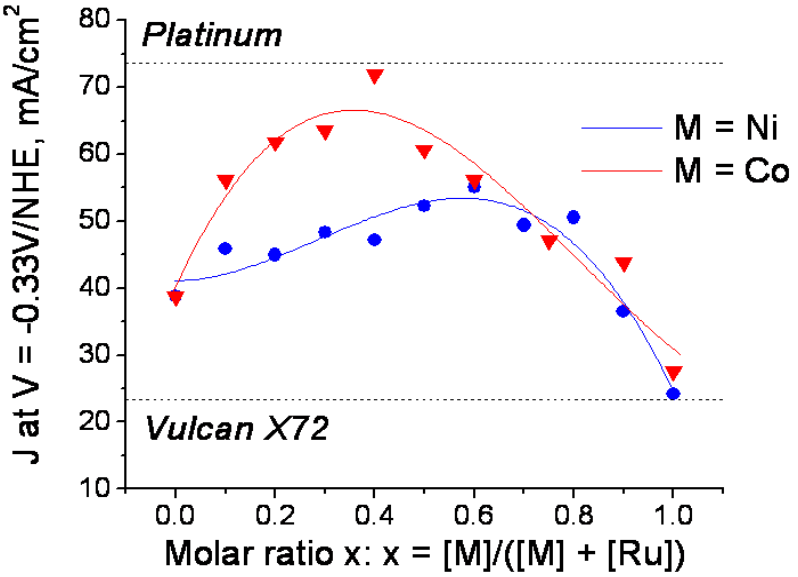

Figure 2. Current density at V = –0.33 mV versus NHE extracted from cyclic voltammetry HER scan run at 5 mV/s in 0.5M HBr as a function of molar ratio x (x = [M]/([M]+[Ru])) of substitutions M (M= Ni or Co). Here x = 0 corresponds to pure RuS_2 and x = 1 to pure NiS_2 or CoS_2.

Figure 3 shows the data from cyclic voltammetry of the most active catalysts (30 and 40% Co-substituted RuS_2 and 60% Ni-substituted RuS_2) along with RuS_2, Pt on carbon (of same loading on metal basis), and Vulcan X72 carbon support with no catalyst.

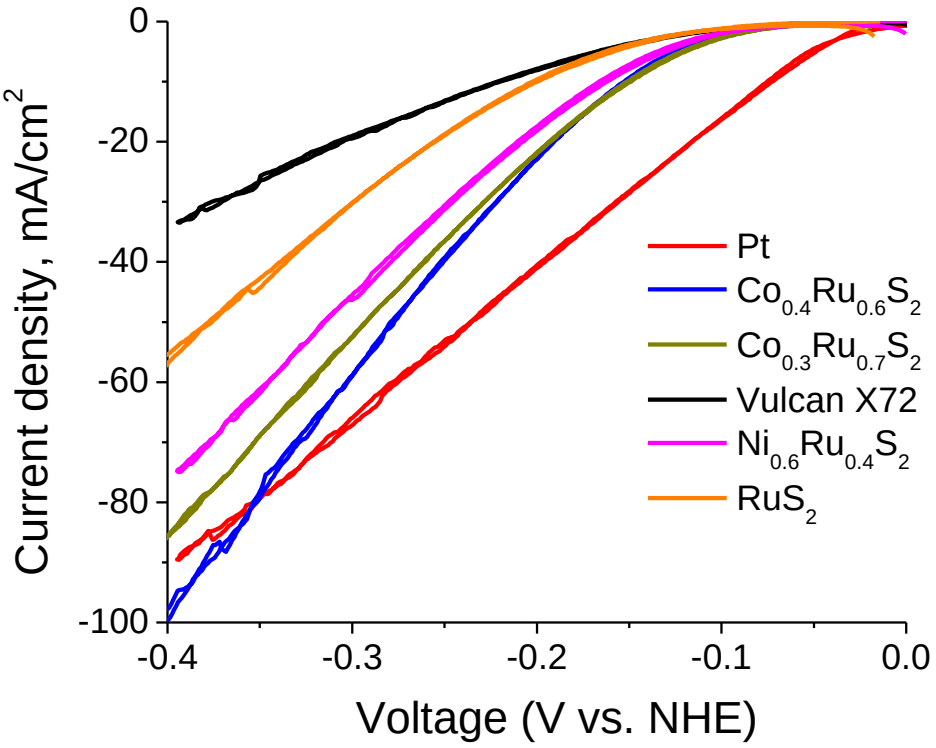

Figure 3. Cyclic voltammetry of hydrogen evolution reaction in 0.5M HBr (purged with argon) on Vulcan X72 carbon, platinum 30% catalyst on carbon, RuS_2 30% on metal basis on carbon, $Co_{0.3}Ru_{0.7}S_2$ 30% on metal basis on carbon, $Ni_{0.6}Ru_{0.4}S_2$ 30% on metal basis on carbon, $Co_{0.4}Ru_{0.6}S_2$ 30 % on metal basis on carbon. Ink loading was 0.54 μg/cm^2. The voltage was cycled at a rate of 20 mV/s. The current density is normalized to the geometric surface area. The Pt performance is most likely governed by ohmic resistance appearing as a result of corrosion.

The results shown in Figures 2 and 3 indicate that the activity of RuS_2 is greatly improved by substitution with nickel or cobalt. The current densities of the most active Co-substituted RuS_2 samples are approximately two times higher than that of pure RuS_2 (Figure 2). At overpotentials higher than 0.35 V, 40% Co-substituted RuS_2 shows higher hydrogen evolution rates than platinum under the same metal weight loading basis (Figure 3).

H_2-H_2 cell performance

In order to evaluate the performance of TMS catalysts as the hydrogen electrode in a regenerative $H_2/Br_2/HBr$ flow cell, electrodes made of RuS_2, $Co_{0.3}Ru_{0.7}S_2$, commercial Rh sulfide, and Pt were tested for both HER and hydrogen oxidation reaction activity in the H_2/H_2 cell described in the experimental section. The positive voltage portion of the current-voltage plot corresponds to HER occurring on the electrode specified on the plot legend (Figure 4). Results show that the HER activity of the $Co_{0.3}Ru_{0.7}S_2$ is greatly enhanced compared to RuS_2 in a system similar to $H_2/Br_2/HBr$ regenerative flow cell: at an overpotential of 0.15 V, $Co_{0.3}Ru_{0.7}S_2$ develops current about 17 times higher than that of RuS_2. In order to drive the cell at current density 0.1 A/cm^2, $Co_{0.3}Ru_{0.7}S_2$ requires an overpotential only 110 mV higher than that of Pt.

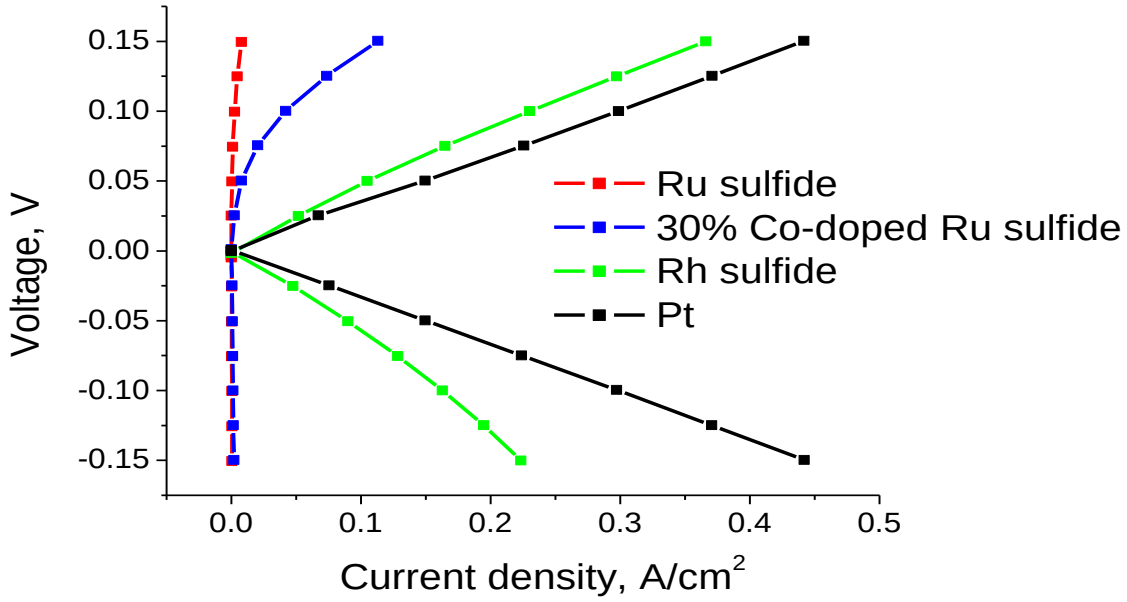

Figure 4. Current-voltage curves with specified catalyst in H_2-H_2 cell. Catalyst loading 0.75 mg/cm^2 of listed catalyst. Hydrogen pressure: 3 psig, flow rate: 2206 mL/min. Counter electrode catalyst was Pt loaded on carbon. The specified electrode is operating as a hydrogen evolution catalyst at positive voltages, and a hydrogen oxidation catalyst at negative voltages. Co substitution increases the hydrogen evolution activity for the RuS_2, however both the ruthenium sulfide and Co-doped ruthenium sulfide show low hydrogen oxidation activity.

Although the Rh-sulfide catalyst maintained high activity for both the HER and hydrogen oxidation reactions, neither pure nor Co-substituted RuS_2 was active as a hydrogen oxidation catalyst. Investigation of hydrogen oxidation activity is beyond the scope of the paper. Nonetheless, these in-cell tests demonstrate the high activity of Co-substituted RuS_2 for HER, and that, unlike Rh-sulfide or Pt, the Co-substituted RuS_2 electrocatalyst is not a suitable bipolar catalyst for regenerative H_2/Br_2/HBr flow cell application.

4. Stability under hydrogen evolution and during shutdowns

Chronopotentiograms of the synthesized catalysts together with the catalysts used as a reference (rhodium sulfide BASF catalyst, platinum 30% catalyst on carbon, and carbon used as a support material for the synthesis) in 0.5M HBr are shown in Figure 5. All the electrocatalysts except MoS_2 were observed to be stable in 0.5M HBr with a stable voltage at constant current over the experimental period. The stability was further verified by conducting cyclic voltammograms before and after the chronopotentiometry study (not shown). Only MoS_2 showed variations between the cyclic voltammograms before and after constant current testing. Although there is improvement seen during the chronopotentiometry of the MoS_2, the lack of stability (gas-phase hydrogen was detected when the catalyst was exposed to HBr) eliminates this material as a potential electrocatalyst. The current may also be coming from a corrosion reaction, and not from H_2 production. It is also possible that corrosion of the MoS_2 particles is exposing more of the edge sites that have been shown to be the active sites for H_2 evolution.[22] Any large change in the voltage apart from the initial change is due to changes in the electrocatalyst. The initial increase in the magnitude of voltage is expected from the development of a concentration gradient in the cell due to local consumption of H^+ ions (the reference electrode was situated 2-3 cm apart

from the working electrode in the same compartment). The higher increase in voltage required for Pt relative to the TMS may be due to the effect of bromide-ion poisoning of the catalyst surface. In addition to apparent stability, the voltage shows relative hydrogen evolution efficiencies. Rh_xS_y and Pt are the best-performing catalysts followed closely by the $Co_{0.3}Ru_{0.7}S_2$ electrocatalyst. To verify that the measured current was from hydrogen production, we measured the evolution of hydrogen with the $Co_{0.3}Ru_{0.7}S_2$ and Pt catalysts, using Mass Spectrometry (MS). The rate of hydrogen evolution was 1 mol of H_2 per 2 moles electrons for both catalysts, indicating near 100% Faradaic efficiency. There was no H_2S evolved into the gas phase measurable above the noise level (± 0.037%) by differentially pumped MS.

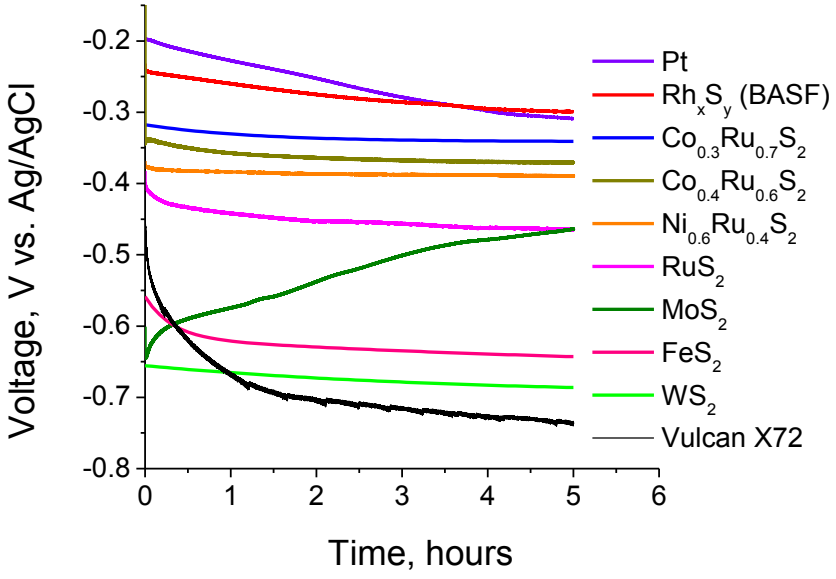

Figure 5. Chronopotentiometry (11 mA/cm^2) using a two-compartment rotating disk electrode cell, with an electrolyte of 0.5M HBr purged with argon. The catalyst loading was 0.54mg/cm^2 on an electrode rotating at 2500 rpm. The larger the voltage, the less efficient the electrocatalyst is for the hydrogen evolution. Platinum performance degrades over time. There is a possibility of MoS_2 becoming more active under HER conditions, possibly due to corrosion that increases the active surface area. However, the final MoS_2 activity and instability in HBr/Br_2 is too low for use as an active electrocatalyst.

The stability of the 30% Co-substituted RuS_2 catalyst under conditions close to HBr electrolyzer operation was investigated in extended duration testing (48 hour) in more-concentrated HBr (3M). The potential of the working electrode was measured periodically with respect to an Ag/AgCl reference. The potential of the electrode and hydrogen evolution were observed to be stable over the experimental period (Figure S14), and superior to platinum, which is unstable under such conditions (Figure S15). The variation of voltage during the 48-hour test was attributed to the sensitivity of the measurement to the position of the reference electrode in the cell due to the formation of a diffusion layer in the vicinity of the cathode.

Samples of the electrolyte were extracted during the HER test and elemental compositions of Co, Ru, and S were analyzed as a function of test duration. It was found that about 25±7% of cobalt present in the catalyst sample dissolved during the initial 5 hours of HER (Figure 6). The result was compared to measurements of the catalyst stability with no applied electrode bias, which represents a "shutdown" of the electrolytic cell. Under the no-bias condition, 34±8% of initial cobalt in the electrocatalyst dissolves into solution during the first 5 hours of the exposure. Slower dissolution rates and smaller dissolved Co concentrations in HBr for the electrode under applied cathodic bias as compared to no bias can be attributed to the protective role of the negative potential. The electric field favors re-deposition of positively charged metal cations that may leave the unbiased catalyst surface.

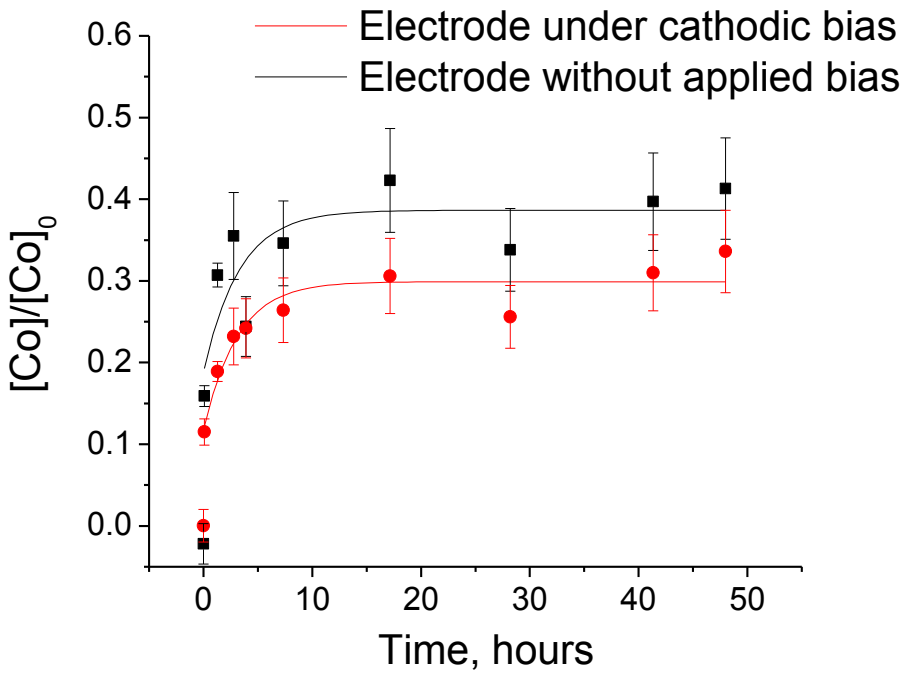

Figure 6. The fraction of the initial cobalt loading dissolved over time in 3M HBr with and without an applied bias for hydrogen evolution. The applied bias was adjusted for a charge density of 100 mA/cm^2. The electrodes were made by loading electrocatalyst onto Toray^{TM} carbon paper.

5. Corrosion reactions

The catalyst stability was further tested by prolonged exposure to heavily concentrated HBr (6M), under argon atmosphere. In order to perform this test, 3 mg of catalysts were exposed to 1mL of 6M HBr for 2 weeks under continuous stirring at room temperature. The corrosion products were evaluated by testing the composition of corrosion gas, dissolved ions and surface modification.

Composition of gas phase corrosion products

Gas-phase chemical corrosion tests did not detect any H_2S formed (detection limit 0.037%) after exposing $Co_{0.3}Ru_{0.7}S_2$ and RuS_2 to HBr. Similar tests did not detect any hydrogen or sulfur dioxide as gaseous corrosion products.

Composition of liquid phase corrosion products

The results of the ICP-AES tests showed dissolution of (relative to the starting amounts) 2.3% ruthenium for RuS_2, and 30% cobalt and 0.7% ruthenium for $Co_{0.3}Ru_{0.7}S_2$. Background sulfur content in the electrolyte and from the air made exact sulfur composition determination unfeasible. The fraction of total cobalt dissolved in 6M HBr was approximately the same as the fraction of cobalt dissolved in 3M HBr in either chemical or electrochemical exposure. The standard deviation in this measurement did not exceed 10%. The absence of a black precipitate by the lead nitrate test verified that no H_2S formed by corrosion. The presence of a white precipitate by $Ba(NO_3)_2$ addition indicates the sulfur is going into acidic solution from the catalyst as HSO_4^-. The corrosion rate and amount was found to be independent of O_2 availability (Figure S16). We believe that the Co that is dissolving is from an inactive portion of the catalyst, along with sulfate species from the catalyst surface. Once the inactive phase containing Co is dissolved, the remaining pyrite-phase electrocatalyst is stable without further corrosion, even after exposure to a fresh HBr solution, with no Co in solution. For use as an electrocatalyst, Co-substituted RuS_2 could be pretreated to remove the inactive Co, followed by recovery of the remaining stable electrocatalyst. Longer-term studies of corrosion on the time scale of months will be more helpful in determining the extended stability of this catalyst.

Characterization of catalyst surface after corrosion

X-ray diffraction analysis of the 30% Co-substituted RuS_2 material after 5 hours of exposure to 3M HBr showed no observed shift in the lattice parameter of the pyrite structure or new reflections indicating new crystalline phases.

The XPS evaluation of the surface elemental composition (Figure S17) reveals that the surface of the synthesized 30% Co-substituted RuS_2 material is sulfur-rich (as compared

to the expected bulk composition) with a Ru:S ratio of approximately 4.2 (48.3 at.% of the total) for the freshly prepared sample and 3.9 (53.7 at.% of the total) for the sample after HBr exposure (Table S1). Oxygen present on the surface (38.1 and 31.0 at. % of total for freshly prepared sample and the sample after HBr exposure, respectively) may originate from oxygen chemically adsorbed on carbon, water molecules physisorbed on the high-surface-area material, or oxygen coordinated to sulfur. According to the high-resolution O 1s spectra (Figure S18), no oxygen coordinated to metal was observed on either of the samples (529.2 eV for O 1s in RuO_2 or 529.6 eV for O 1s in CoO). High-resolution S 2p spectra (Figures S19 and S20) reveal two distinct types of sulfur bonding on the surface: one with binding energies typical for S 2p in RuS_2 (labeled S_2^{2-}) and the other with energies close to that in compounds where oxygen is bound to sulfur (labeled S-O). This observation is consistent with spectroscopic analysis of a single-crystal RuS_2 (100) surface[42] that also showed no indication of Ru-O bonds and explained the presence of S-O bonds on the surface by the formation of S-S-O neutral species. The quantitative analysis of high-resolution sulfur 2p XPS spectra (last 2 columns in Table S1) indicates that the ratio of sulfur bound to metal to the sulfur bound to oxygen increases from 76.7 to 90% as a result of the exposure to HBr. The ratio of Ru to Co changes from 5.8 to 9.9 as a result of material treatment with HBr.

The amount of oxygen and sulfur in S-O bonding state on the surface was reduced after exposure to HBr, corresponding to the S-O group detected dissolving into solution. There was no significant change in the amount of surface cobalt, after the initial loss of 34% of the original cobalt observed in the ICP-AES solution experiment. This discrepancy is likely due to the error in quantification of the surface cobalt concentrations at low amounts

of cobalt. Detection of cobalt may be inaccurate and diminished because of the energy loss associated with its high binding energy.[34]

The activity of the catalyst is unchanged when the cobalt dissolves into solution; therefore, we conclude that the soluble cobalt is inactive for HER. There was no detection of Ru-O bonds by high-resolution XPS, meaning that the remaining ruthenium was still ruthenium sulfide.

An additional issue is the possibility of poisoning of the RuS_2 electrode by bromine crossing over from the HBr electrode. Our experiments show that this is not the case. DFT calculations indicate that Br does not adsorb on the (111) surface (the free energy change is 0.2 eV) but it does bind to the (100) surface (the free energy change is -0.63 eV). This means that there are faces in the polycrystalline electrode that will have sites that are not blocked by Br. It is not clear how Br adsorption on the (100) surface will affect electrochemistry.

D. Computational

1. The models of the RuS_2 surface

The models used in the DFT calculations for the RuS_2 surface are shown in Figure 7. Figure 7a shows the 2×2 supercell (a = 11.32 Å) used for calculations for the (100) surface. When this face is cut it exposes S_2 pairs and Ru atoms that are coordinated with 5 sulfur atoms each belonging to a S_2 pair. All sulfur atoms in the surface are paired and each sulfur pair is coordinated with 5 Ru atoms, 4 in the surface plane and one in the layer below. In bulk RuS_2 the anions are S_2^{2-}, similar to peroxides not to oxides, and the two sulfur atoms in each S_2 pair are equivalent. However on the (100) surface they are not: the one labeled SP_{4c} (Figure 7a) is coordinated to 3 Ru atoms (two in the surface layer and one in the layer below)

and one sulfur atom. The S atom labeled SP_{3c} is coordinated to two Ru atoms in the top layer (there is no Ru atom in the layer below) and a sulfur atom. The bond length of the sulfur pairs at the surface is the same as in the bulk (the calculated S-S bond length in bulk is 2.21Å): this is surprising considering that to form the surface we had to cut S-Ru bonds.

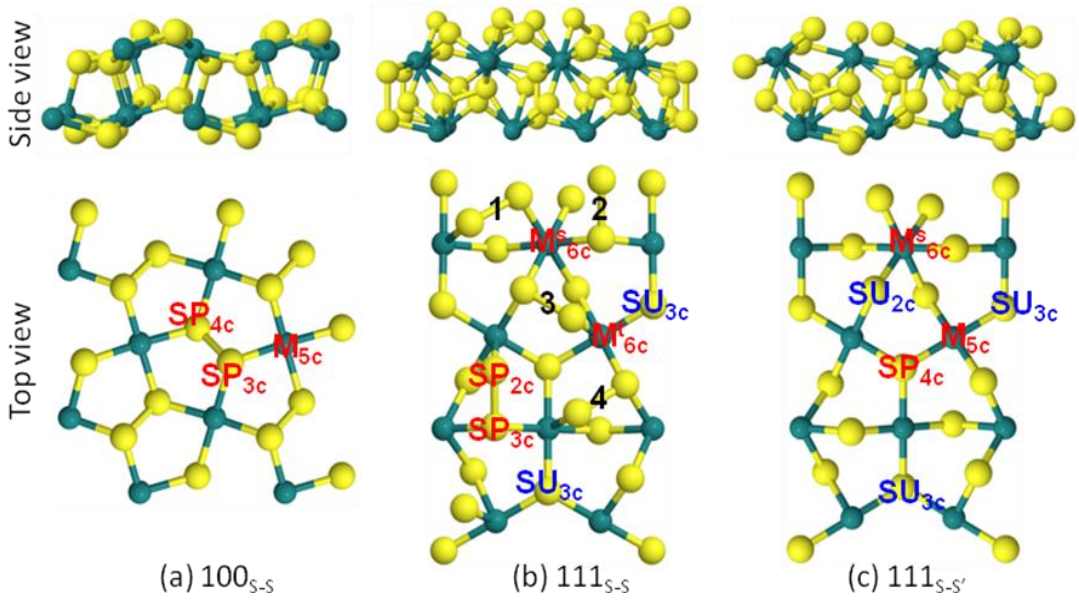

Figure 7. The supercell used in the DFT calculations. We show here two atomic layers in the side view; three atomic layers were used in the calculations.

The (111) face can be cut in two ways, shown in Figure 7b,c and denoted by $(111)_{S\text{-}S}$ and $(111)_{S\text{-}S'}$, respectively. The metal atoms on the $(111)_{S\text{-}S}$ surface (Figure 7b) are 6-coordinated, as in the bulk. This face has three kinds of sulfur atoms: the one labeled SP_{2c} is coordinated with one Ru atom and one S atom; the one labeled SP_{3c} is connected to two Ru atoms and one S atom; the one labeled SU_{3c} needs a separate explanation. Frechard and Sautet[43-47] have shown that the surface formed by removing two sulfur atoms from supercell of the (111) face results in a surface with lower energy. We have followed this work and removed two sulfur atoms from the supercell, which now no longer has the RuS_2 stoichiometry. The two sulfur atoms that were bonded to the sulfur atoms that have been

removed are labeled SU_{3c}. In spite of having cut the S-S bond, when S atoms are removed, the SU_{3c} atoms do not bind hydrogen as strongly as the SP_{2c} binds hydrogen. The bond length in the sulfur pair on $(111)_{S\text{-}S}$ surface (Figure 7b) is shorter by 0.14 Å than the same bond in the bulk (2.21 Å). This correlates with the fact that the Bader charge on the pair in the surface layer is smaller by half than that of a pair in the bulk. To form the $(111)_{S\text{-}S'}$ surface we cut all S-S bonds and this face has no S_2 pairs on it.

Each supercell contains three atomic layers and the vacuum space above the slab is 16.5 Å. For the (100) surface (Figure 7a) a 1×1×1 k-grid gives the same results as 2×2×1; for the (111) surface (Figure 7b,c) calculations with 2×4×1 k-grid points give the same results as do calculations with a 3×6×1 set.

2. Hydrogen adsorption free energies on different faces of RuS_2

To calculate the free-energy changes in the electrode reaction we use a method devised in Nørskov's group.[21, 48] The essential point is the use of the reaction taking place at the standard hydrogen electrode (SHE) as a reference for the equilibrium calculations. The details of the derivations are given in the Supporting Information.[49-51]

The hydrogen evolution reaction in general follows two mechanisms: The Volmer-Heyrovsky pathway, which consists of the charge transfer step (Volmer reaction):

$$\left(H^+ + e^-\right) + * \rightarrow H*, \tag{1}$$

and the reaction of a proton with the adsorbed hydrogen to form gaseous H_2 (Heyrovsky reaction):

$$H* + \left(H^+ + e^-\right) \rightarrow H_{2(g)}. \tag{2}$$

For the Volmer-Tafel pathway, the second step is accomplished by chemical recombination of two adsorbed hydrogen atoms on the surface into H_2:

$$2H^* \rightarrow H_{2(g)}. \quad (3)$$

We have calculated the activation barrier for the reaction in Equation 3 using the nudged elastic-band method[52,53] and found it to be equal to 1.72 eV on RuS_2 $(111)_{S\text{-}S}$ surface and 0.94 on the $(100)_{S\text{-}S}$ surface. The barrier for the associative desorption is 1.08 eV on RuS_2 $(111)_{S\text{-}S}$ surface and 1.14 eV on the (100) surface. This means that the Tafel mechanism is not operative in this system. This is also intuitively clear because the binding sites of the H atoms are far apart and dissociative adsorption would require stretching the H_2 molecule (which has a short bond length) by a large amount before the energy can be lowered by the formation of bonds between the H atoms and the surface. This means that the dissociative adsorption will have a high activation energy, as the calculations show. This qualitative rule suggests that the barrier to dissociative adsorption of H_2 will be high for all sulfides on which the binding sites for H are far apart.

The energies of reaction (1), calculated from DFT, (ΔE_{H^*}, see Equation S11) are given in Table 3 along with the change in free energy at zero voltage. The binding energy of H to the SP_{2c} site on the $(111)_{S\text{-}S}$ surface is lower than that the binding energy to the SU_{3c} site by 0.14 eV, while the binding energy to SP_{3c} is higher than on the other two sites. Furthermore, since the supercell has six SP_{2c} sites and two SU_{3c} sites and the binding energies to them are close, we treat these sites as being equivalent. Otherwise we would have to consider that the adsorbed H forms a binary lattice gas, with two kinds of sites and two different coverages. While this is possible it does not seem worthwhile given the errors

inherent in the DFT calculations and the fact that our main goal is to compare the free energy of adsorption on different faces.

Table 3. ΔE_{H^*} (eV) is the binding energy of a H atom to various surface sites. ZPE_{H^*} is the zero point energy of the adsorbed hydrogen atom. ΔG_{H^*} is the free energy of the reaction $H^+ + e + * \rightarrow H^*$ (Equation 4) in a 0.5M HBr solution, at zero voltage ($\Delta U_{SHE} = 0$), at 298 K and a H_2 pressure of 1 bar. The upper part of the table shows the results for various binding sites on three faces of RuS_2. The empty cells in the table indicate that H does not bind on the corresponding site (for example, H does not bind on the SP_{4c} site of the $(100)_{S\text{-}S}$ face. The lower part of the table shows the same results for the Co substituted surface. The ZPE_{H^*} is not shown because it is the same as on the unsubstituted surface. The two columns having the heading M_{5c} (for the $(100)_{S\text{-}S}$ face) give the values of ΔE_{H^*} and ΔG_{H^*}(eV) when H binds to the Co substitution that replaced a Ru on the M_{5c} site (these values are –0.16 and 0.09, respectively). The column with heading Ru (below the heading M_{5c}) gives the lowest binding energy (and free energy) when H binds to one of the surface Ru atoms in the Co-substituted RuS_2. On the $(111)_{S\text{-}S}$ and $(111)_{S\text{-}S'}$ surfaces, the results for the substituted surface are for Co replacing the Ru atom on the M_{6c}^t site (Figure 7b). The H coverage in all calculations is 1 H per 8 sulfur sites.

RuS_2									
adsorption site	$(100)_{S\text{-}S}$			$(111)_{S\text{-}S}$			$(111)_{S\text{-}S'}$		
	SP_{3c}	SP_{4c}	M_{5c}	SP_{2c}	SP_{3c}	SU_{3c}	SU_{2c}	SU_{3c}	M_{5c}
ΔE_{H^*} (eV)	**0.78**	-	**0.37**	**-0.49**	**-0.1**	**-0.35**	**-0.81**	**-0.65**	**0.08**
ZPE_{H^*} (eV)	0.22	-	0.2	0.23	0.23	0.24	0.23	0.23	0.19
ΔG_{H^*}(eV)	**1.02**	-	**0.59**	**-0.24**	**0.16**	**-0.09**	**-0.56**	**-0.40**	**0.29**
RuS_2 substituted with Co									
adsorption site	$(100)_{S\text{-}S}$			$(111)_{S\text{-}S}$			$(111)_{S\text{-}S'}$		
	SP_{3c}	SP_{4c}	M_{5c}	SP_{2c}		SP_{3c}	SU_{3c}	SU_{2c}	SU_{3c}	M_{5c}
			Co	Ru	**Next to Co**	Next to Ru				
ΔE_{H^*} (eV)	**0.54**	-	**-0.16**	**0.09**	**-0.44**	**-0.54**	**-0.09**	**-0.45**	**-0.87**	**-0.57**	-
ΔG_{H^*}(eV)	**0.79**	-	**0.07**	**0.32**	**-0.19**	**-0.29**	**0.17**	**-0.15**	**-0.63**	**-0.31**	-

The trends in the free energy $\Delta G_{H^*}^{Ads}$ for the Volmer step (Equation 1) are the same as those in the energy ΔE_{H^*} of the reaction $1/2\,H_{2(g)} \rightarrow H^*$. For example, the free energy change $\Delta G_{H^*}^{Ads}$, for the proton neutralization and binding to the SP_{3c} site of the $(100)_{S\text{-}S}$ surface, is 1.02 eV which is much higher than that for the same reaction on the SP_{2c} site on the $(111)_{S\text{-}S}$ surface, which is –0.24 eV. Similarly ΔE_{H^*} changes from 0.78 eV to –0.49 eV. Negative values of ΔG indicate that a reaction is thermodynamically spontaneous: the more

negative ΔG, the greater the driving force for the reaction. Positive values usually indicate that the reaction will not take place. The results are discussed further in Section 4.3.2.

3. Effect of cobalt substitution on hydrogen adsorption energy on sulfur sites

Changes in geometry

In this section we calculate how the free energy of proton neutralization is affected by the substitution of a surface Ru atom with a Co atom. The Ru-S bond length in bulk RuS_2 is 2.37 Å, while the Co-S distance in bulk CoS_2 is 2.31 Å. Because of this near equality in the bond lengths, we do not expect that substituting a Ru atom with a Co atom would cause a large geometry disruption. The computations show this to be true. The $(111)_{S\text{-}S}$ face has two non-equivalent Ru sites, labeled M_{6c}^{t} and M_{6c}^{s} in Figure 7b. The 6-coordinated M_{6c}^{s} ruthenium atom is bonded to three S atoms in the second layer (with a Ru-S bond length equal to 2.34Å) and to three sulfur atoms in the surface layer (with a Ru-S bond length equal to 2.39Å). All S atoms connected to the M_{6c}^{s} Ru belong to S-S pairs. The Ru atom on the M_{6c}^{t} site is also coordinated to six S atoms but only five of them belong to a S_2 pair. The remaining S atom is not paired because one of the S atoms in the pair has been removed when we formed the non-stoichiometric surface.[43-47] Only two of the six sulfur atoms are in the top sulfur layer (Figure 7b).

Substituting a Ru atom in the surface layer of RuS_2 $(111)_{S\text{-}S}$ with a Co atom causes slight, but noticeable, geometry changes. The Co placed in the M_{6c}^{t} site is shifted towards the bulk by 0.14 Å (as compared to the position where the replaced Ru was located). No metal sulfur bonds are broken when Co replaces Ru. The largest Co-S distance is 2.39 Å while the largest Ru-S distance (in the surface of the unsubstituted RuS_2) is 2.47 Å. The

shortest Co-S bond is 2.24 Å while the shortest Ru-S bond in the unsubstituted RuS_2 is 2.29 Å. For the M_{6c}^{s} site, the largest Co-S distance (in Co-substituted RuS_2) is 2.33 Å while the largest Ru-S distance (in surface of the unsubstituted RuS_2) is 2.39 Å. The smallest Co-S distance (in Co-substituted RuS_2) is 2.29 Å while the smallest Ru-S distance (in the surface of the unsubstituted RuS_2) for Ru is 2.34 Å. The Co atom is shifted towards the bulk by only 0.05 Å (as compared to the position of the replaced Ru atom).

On the $(100)_{S\text{-}S}$ face (Figure 7a), the 5-coordinated Ru atom labeled as M_{5c} has non-equivalent Ru-S bond lengths. The length of the Ru bond with the S atom from subsurface is 2.23Å and it is the shortest. Among the four Ru-S bonds in the plane of the surface, two have the same length as in bulk but the other two are changed slightly (one is shorter by 0.06Å, the other is longer by 0.03Å, than bulk bond lengths). The number of Co-S bonds is the same as the number of Ru-S bonds. The length of the bond with the sulfur atom in the subsurface layer is the same as that of the Ru-S bond. The other four Co-S bonds are slightly shorter than the Ru-S bonds.

When substituting RuS_2 with Co, we replace a divalent cation with another divalent atom. Work on substituted (doped) oxides, for which extensive calculations have been performed, indicates that such a substitution does not cause a very substantial change in the chemical properties of the neighboring atoms.[54] By analogy, we expect that Co will not change substantially the chemical activity of the S atoms. Nor do we expect that the chemical activity of the Co ion will be very different from that of the Ru ion.

Changes in the free energy of the reaction $H^+ + e + * \rightarrow H*$

We evaluated the effect of surface cobalt concentration by computing the DFT adsorption energies ΔE_{H*} for two different (111) surface models (see Section 3 in

Supporting Information). Decreasing Co and H concentration does not affect H binding energy to S. The adsorption energies for the H atom bound to the sites near to cobalt dopant are found to become stronger by 0.1 eV than to the site without the presence of Co on the surface (see Figure S21). This is a small change but it does affect the free energy at room temperature.

The changes in free energies $\Delta G_{H^*}^{Ads}$ (computed from Equation S10) for the reaction (1) when θ=0.125 and $\Delta U_{\mathrm{SHE}} = 0$, are given in Table 3. The substitution increases slightly the thermodynamic driving force for the reaction. The effect is particularly large for the $(100)_{\mathrm{S\text{-}S}}$ face where the presence of Co changes $\Delta G_{H^*}^{Ads}$ from 0.59 to 0.08 eV. When examining free energies one should keep in mind that $\Delta G_{H^*}^{Ads}$ for this reaction is affected by the voltage. Therefore an impossible reaction ($\Delta G_{H^*}^{Ads} > 0$) can be performed if the voltage is changed to make $\Delta G_{H^*}^{Ads}$ negative.

In Figure 8, we present the free energy diagrams for the hydrogen evolution reaction

$$2\left(H^+ + e^-(\mathrm{W})\right) \rightarrow H_{2(g)} \tag{4}$$

taking place at –0.1 Volts, in the 0.5M HBr solution, at room temperature and a hydrogen pressure of 1 bar. Since the thermodynamic properties depend only on free energy differences, we take the free energy of $G(H_2+*)$ of the gaseous H_2 and the clean surface * (i.e. no H adsorbed on it) to be zero. This is convenient because this state is not affected by changes in the electrode potential. On this scale the free energy $G(H^*+ H^+ + e^-)$ of the state in which H is adsorbed on the surface is equal to $-\Delta G_{H^*}^{Des}$ (Equation S13) and the free energy $G(2(H^+ + e^-) + *)$ of the clean surface with H^+ ions in solution and an electron e^- in the electrode is equal to $-\Delta G_{H^*}^{Ads} - \Delta G_{H^*}^{Des}$.

Figure 8a shows the free energy diagram for the $(111)_{S\text{-}S}$ surface. The right-hand side panel (shaded in blue) shows the change of the free energy of the state $2(H^+ + e^-) + *$ with the electrode potential –0.1 V. The middle panel (shaded in green) shows the free energies for the state $(H^+ + e^-) + H^*$ where the adsorption of H on different sulfur sites at hydrogen coverages $\theta = 0.125$ (blue and black) and $\theta = 0.875$ (green dashed). Here $\theta = n_H/n_L$, where n_H is the number of H atoms on the surface and n_L is the number of lattice sites. As we explained earlier, when we calculate the coverage we do not take into account that there are three different sulfur sites for H adsorption. Therefore, n_L is equal to 8 surface sulfur sites (6 SP_{2c} sites plus 2 SU_{3c} sites). Strictly speaking, for one hydrogen adsorbed on the SP_{3c} site on the $(111)_{S\text{-}S}$ face we should have used $n_L = 6$ and $\theta = 0.167$ to calculate the contribution from configuration entropy, however, the effect of such modification on the free energy is very small (~0.04 eV).

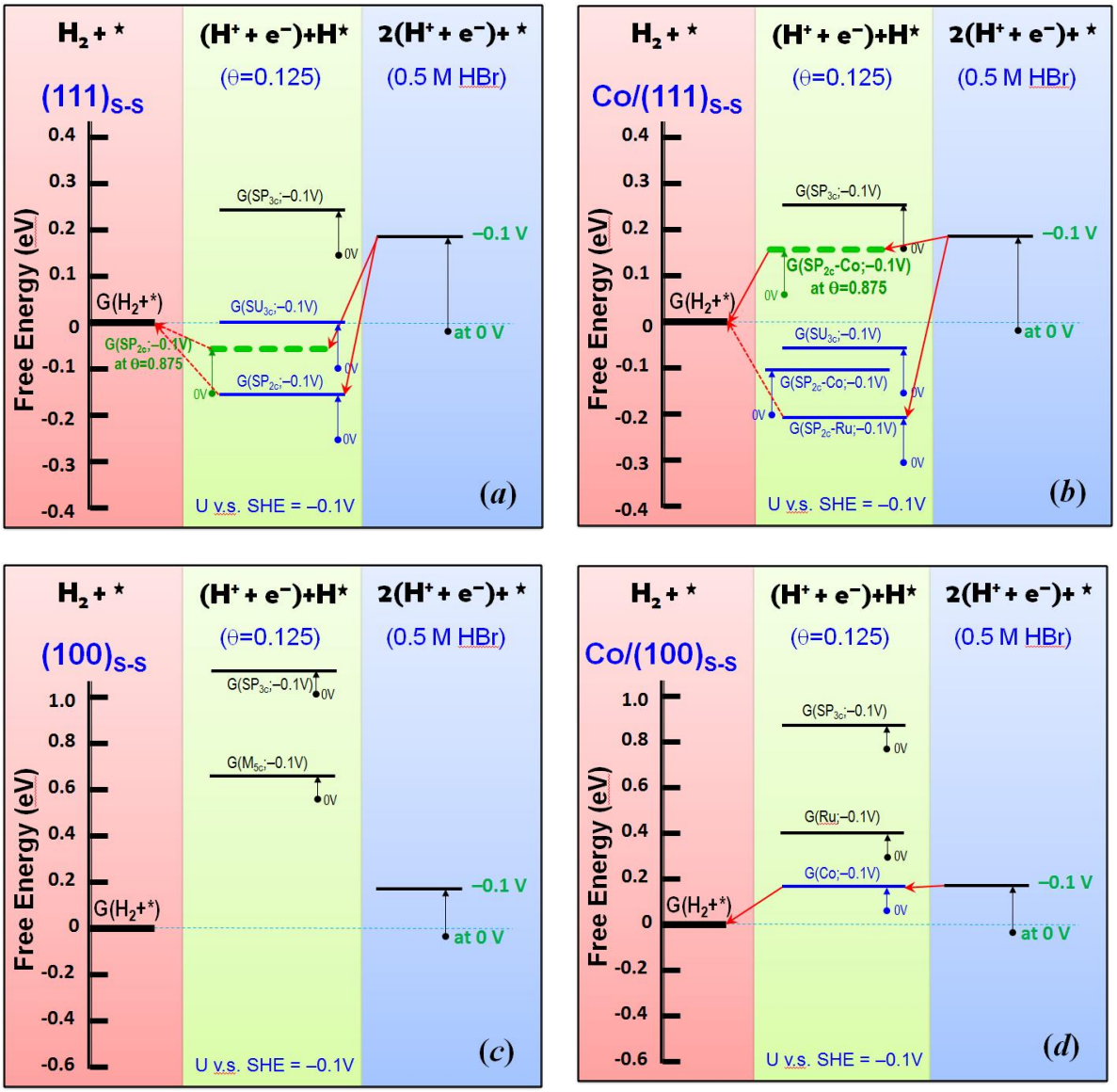

Figure 8. Free energy diagram for the reaction ($2(H^+ + e^-) \rightarrow H_{2(g)}$) in 0.5M HBr, at 298K, 1 bar of hydrogen pressure and at –0.1 Volts. In each diagram, the left panel (shaded in red) shows the free energy of the gas phase molecular hydrogen and the metal sulfide surface, which is taken here to be zero. The middle panel (shaded in green) shows the free energy of a proton with the adsorbed hydrogen, and the right panel (shaded in blue) shows the free energy of the hydrated proton in the solution and the electron in sulfide electrode. The dots indicate the free energies at zero voltage. The horizontal lines show the free energies at the voltage indicated in the figure. The notation G(X;V), where X=SP_{2c}, SP_{3c}, SU_{3c}, M_{5c}, indicates the hydrogen adsorption site; the notation X=SP_{2c}-Co denotes H-adsorption sulfur site nearest to the cobalt dopant. The site labels are defined in Figure 7. (a) Gives the free energy diagram for undoped RuS_2 $(111)_{S\text{-}S}$ surface; (b) The same diagram for Co-doped RuS_2 $(111)_{S\text{-}S}$ surface; (c) the diagram for undoped RuS_2 $(100)_{S\text{-}S}$ surface; (d) the diagram for the Co-doped RuS_2 $(100)_{S\text{-}S}$ surface.

The free energy change for hydrogen adsorption on a surface depends on the coverage. We examined the hydrogen adsorption free energy at different coverages on the $(111)_{S\text{-}S}$ and the Co-substituted $(111)_{S\text{-}S}$ surfaces, according to the reaction:

$$\tfrac{1}{2}\, H_{2(g)} + n_H\, H^* \rightarrow (n_H+1)\, H^* \qquad (5)$$

Our calculations show that the free energy of the reaction (1) does not change significantly when the coverage varies from 0.125 to 0.75. Because of this we only show the free energies for $\theta = 0.125$ and $\theta = 0.875$ in Figure 8a,b.

We need to emphasize that we are calculating a "constrained" free energy that assumes that somehow the coverage can be controlled and fixed at a given value. Ordinary thermodynamic equilibrium calculations would determine the equilibrium value of the coverage by setting the ΔG for the two reactions (Equations 1 and 2) equal to zero and solving these equations for θ. These constrained calculations provide the following information: if ΔG for one of the reactions is positive, the reaction is impossible at the fixed coverage; if $\Delta G < 0$ then the reaction is thermodynamically possible, at the fixed coverage. Note that the initial state $(2(H^+ + e^-)+*)$ and the final state $(H_2 + *)$ are the same in all four diagrams. If the electrode potential is zero, the reaction $2(H^+ + e^-)+* \rightarrow H_2 + *$ is impossible because ΔG is slightly positive ($\Delta G_{\mathrm{HER}} = \Delta G_{H^*}^{Ads} + \Delta G_{H^*}^{Des} = 0.024\,\mathrm{eV}$ at 298K, the H_2 pressure of 1 bar, in a 0.5M HBr solution). However a slight change to a negative electrode potential will make the reaction possible.

We examine next each diagram to find out which intermediate state $((H^+ + e^-)+H^*)$ is thermodynamically possible. In Figure 8a, for the face $(111)_{S\text{-}S}$, at zero electrode potential, the conversion of H^+ to adsorbed hydrogen is possible for H bound to SU_{3c}, or SP_{2c} but the conversion to H adsorbed on the SP_{3c} site is not possible. Unfortunately, the

desorption of H to form gas-phase H_2 is not thermodynamically allowed from SU_{3c} or SP_{2c}. Therefore neither of the final states (H_2 in gas) can be reached at zero potential. However the reaction is possible if the voltage is more negative than –0.1 Volts, because this will lift up the free energies of the intermediate and the initial state, while the free energy of the final state will not change.

The diagram in Figure 8b, which shows calculations performed on the Co-substituted $RuS_2\,(111)_{S\text{-}S}$ surface, can be interpreted in the same way as Figure 8a. At zero voltage and a coverage of θ=0.125 there is at least one step with positive ΔG as one goes from $2H^+$ to $H_{2(g)}$. At a voltage of –0.1 Volts the conversion of $2H^+$ to $H_{2(g)}$ is possible through adsorption of H on the SP_{2c} sites near the Co dopant at a coverage of 0.875. This may explain the increase of activity observed for Co-substituted RuS_2.

Figure 8c gives the free energies for the undoped $RuS_2\,(100)_{S\text{-}S}$ surface. We find that none of the intermediate states considered here (i.e. H adsorbed on M_{5c} or on SP_{3c}) is a thermodynamically possible intermediate (at θ = 0.125) unless the negative electrode potential is close to –0.3 Volts. Substituting this surface with Co is again beneficial since the state with H adsorbed on the Co substitution can become an intermediate at a small negative electrode potential (see Figure 8d).

Figure 9a shows the free energy diagrams for the reaction $H_{2(g)} \rightarrow 2(H^+ + e^-)$ for the $RuS_2\,(111)_{S\text{-}S}$ surface and Figure 9b shows the diagram for the Co-doped $RuS_2\,(111)_{S\text{-}S}$. In both calculations the hydrogen coverage was 0.125 and the voltage is +0.1 Volts. The dissociative adsorption of $H_{2(g)}$ is thermodynamically allowed on both surfaces but the desorption of surface hydrogen atoms is not. However, at a coverage at θ=0.875 the Co-doped RuS_2(111)S-S surface the reaction $H_{2(g)} \rightarrow 2(H^+ + e^-)$ is thermodynamically allowed.

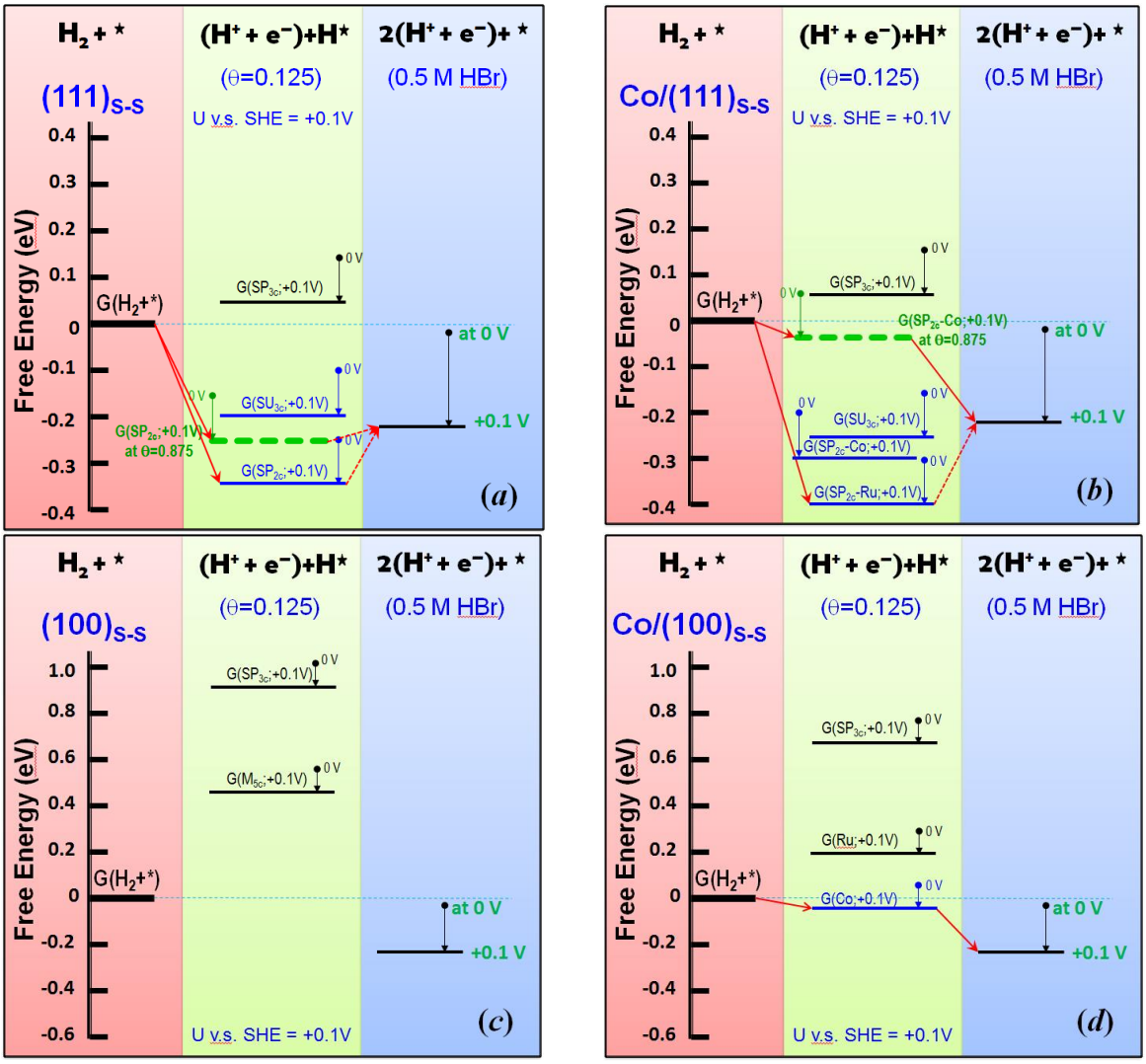

Figure 9. Free energy diagram for HOR ($H_{2(g)} \rightarrow 2(H^+ + e^-)$) in 0.5M HBr, at 298K, 1 bar of hydrogen pressure and at voltage +0.1 Volts. The details are the same in Figure 8.

The free energy diagrams for a undoped RuS_2 $(100)_{S\text{-}S}$ surface and for a Co-doped RuS_2 $(100)_{S\text{-}S}$ surface are shown in Figures 9c and 9d, respectively. For a voltage of 0.1 Volts the reaction $H_{2(g)} \rightarrow 2(H^+ + e^-)$ is thermodynamically forbidden on the undoped surface and it is allowed on the doped one. The active site is the Co dopant (i.e. that is the favored H adsorption site).

In summary, the DFT calculations show that doping RuS_2 with Co is thermodynamically favorable for both hydrogen oxidation and reduction. On the (111)

surface the Co dopant helps by weakening the S-H bond (at high H-coverage) and on the (100) the dopant helps by providing a binding site of the H atom.

Given the errors inherent in both DFT and the models used for the system, one should consider these conclusions to be qualitative. One should keep it in mind that, although the reactions are thermodynamically possible for both reaction pathways (HER and HOR) the calculations say nothing about the kinetics especially in the case of charge transfer reactions. For the reactions that do not involve charge transfer the calculation of the activation energy is possible and we provided one example that show that H_2 dissociative adsorption and H_2 desorption have high barriers and therefore may be the rate limiting steps.

E. Conclusions

We have established that Ni and Co substitutional dopants in the surface of RuS_2 increase the electrocatalytic activity for hydrogen evolution. The dopant is likely to affect the interaction of the neighboring sulfur sites with hydrogen. The doped ruthenium sulfides were more active than pure ruthenium sulfide, but their activity is lower than that of rhodium sulfide. The doped ruthenium sulfide is less expensive (~$110/oz Ru)[55] than rhodium sulfide (~$1000/oz Rh) and more stable than platinum which is passivated by bromine and is unstable in HBr. The Co-doped RuS_2 electrocatalyst seems to have two kinds of Co atoms on the surface: one dissolves rapidly in HBr and the other remains on the surface. The latter is the one that improves the activity of the doped RuS_2.

The cobalt-doped ruthenium sulfide greatly enhanced the hydrogen evolution activity in a regenerative HBr flow cell compared to the undoped ruthenium sulfide, although the activity was less than that of Rh_xS_y. For the reverse reaction, hydrogen oxidation, the cobalt-substituted ruthenium sulfide was inactive and thus not a useful bipolar electrocatalyst in a

regenerative H_2/Br_2/HBr flow cell. The Rh_xS_y catalyst was nearly as active as fresh platinum for the hydrogen evolution and hydrogen oxidation reactions.

Thermodynamic calculations using DFT and a simple model of the surface show that the role of the Co substitution is to lower the free energy of the adsorbed hydrogen atoms. The calculations also suggest that the $(111)_{S\text{-}S'}$ face is less active than the $(100)_{S\text{-}S}$ and $(111)_{S\text{-}S}$ faces.

Acknowledgements

The authors would like to thank Dr. Tom Mates, Mr. Yichi Zhang, Dr. Arnold Forman, Dr. Young-Si Jun and Mr. Alan Derk for helpful discussions and critical manuscript proofing. Financial support was by the National Science Foundation (EFRI-1038234) and the Air Force Office of Scientific Research (FA9550-12-1-0147). N.S. is supported by a Fellowship from the ConvEne IGERT Program (NSF-DGE 0801627). The MRL Central Facilities are supported by the MRSEC Program of the NSF under Award No. DMR 1121053; a member of the NSF-funded Materials Research Facilities Network (www.mrfn.org). We made use of the California NanoSystems Institute Computer Facility, funded in part by the National Science Foundation (CHE 0321368).

References

1. Sivasubramanian, P.; Ramasamy, R. P.; Freire, F. J.; Holland, C. E.; Weidner, J. W. Electrochemical hydrogen production from thermochemical cycles using a proton exchange membrane electrolyzer. *International Journal of Hydrogen Energy* **2007,** *32*, 463-468.

2. Simpson, M. F.; Herrmann, S. D.; Boyle, B. D. A hybrid thermochemical electrolytic process for hydrogen production based on the reverse Deacon reaction. *International Journal of Hydrogen Energy* **2006,** *31*, 1241-1246.

3. Gupta, A. K.; Parker, R. Z.; Hanrahan, R. J. Solar-assisted production of hydrogen and chlorine from hydrochloric-acid using hexachloroiridate (III) and (IV). *International Journal of Hydrogen Energy* **1993,** *18*, 713-718.

4. Barmashenko, V.; Jorissen, J. Recovery of chlorine from dilute hydrochloric acid by electrolysis using a chlorine resistant anion exchange membrane. *Journal of Applied Electrochemistry* **2005,** *35*, 1311-1319.

5. Kaabak, L. V.; Stepnova, N. P.; Khudenko, A. V.; Tomilov, A. P. Low-waste process for preparing ketopantolactone, with electrochemical recovery of bromine. *Russian Journal of Applied Chemistry* **2003,** *76*, 1315-1318.

6. Berndt, K.; Dolle, V.; Kreutzberger, G. Production of chlorine from escape hydrochloric acids by electrolysis. *Chemische Technik* **1969,** *21*, 607-610.

7. Nawrat, G.; Kopyto, D.; Gonet, M. Integrated diaphragm-cathode systems in the process of electrolysis production of chlorine. *Przemysl Chemiczny* **2007,** *86*, 866-871.

8. Yeo, R. S.; McBreen, J.; Tseung, A. C. C.; Srinivasan, S.; McElroy, J. An electrochemically regenerative hydrogen-chlorine energy-storage system - electrode-kinetics and cell performance. *Journal of Applied Electrochemistry* **1980,** *10*, 393-404.

9. Yeo, R. S.; McBreen, J.; Srinivasan, S. Electrochemically regenerative hydrogen-chlorine energy-storage system - electrode-kinetics and cell performance. *Journal of the Electrochemical Society* **1979,** *126*, C379-C379.

10. Gileadi, E.; Srinivasan, S.; Salzano, F. J.; Braun, C.; Beaufrere, A.; Gottesfeld, S.; Nuttall, L. J.; Laconti, A. B. Electrochemically regenerative hydrogen-chlorine energy-storage system for electric utilities. *Journal of Power Sources* **1977,** *2*, 191-200.

11. Tang, T. E.; Frank, S. N.; Barna, G.; Teherani, T. Regenerative hydrogen bromine fuel-cell energy-storage system. *Journal of the Electrochemical Society* **1984,** *131*, C323-C323.

12. Yeo, R. S.; Chin, D. T. Hydrogen-bromine cell for energy-storage applications. *Journal of the Electrochemical Society* **1980,** *127*, 549-555.

13. Yeo, R. S.; Hseuh, K. L.; Chin, D. T.; McBreen, J.; Srinivasan, S. Hydrogen-bromine fuel-cell for energy-storage applications. *Journal of the Electrochemical Society* **1979,** *126*, C135-C135.

14. Schuetz, G. H.; Fiebelmann, P. J. Electrolysis of hydrobromic acid. *International Journal of Hydrogen Energy* **1980,** *5*, 305-316.

15. McDaniel, N. D.; Bernhard, S. Solar fuels: Thermodynamics, candidates, tactics, and figures of merit. *Dalton Transactions* **2010,** *39*, 10021-10030.

16. Luttmer, J. D.; Konrad, D.; Trachtenberg, I. Electrode materials for hydrobromic acid electrolysis in Texas Instruments' solar chemical converter. *Journal of the Electrochemical Society* **1985,** *132*, 1054-1058.

17. Zhang, J.; Sasaki, K.; Sutter, E.; Adzic, R. R. Stabilization of platinum oxygen-reduction electrocatalysts using gold clusters. *Science* **2007,** *315*, 220-222.

18. Koh, S.; Leisch, J.; Toney, M. F.; Strasser, P. Structure-activity-stability relationships of Pt-Co alloy electrocatalysts in gas-diffusion electrode layers. *Journal of Physical Chemistry C* **2007,** *111*, 3744-3752.

19. Gulla, A. F.; Gancs, L.; Allen, R. J.; Mukerjee, S. Carbon-supported low-loading rhodium sulfide electrocatalysts for oxygen depolarized cathode applications. *Applied Catalysis A-General* **2007,** *326*, 227-235.

20. Ziegelbauer, J. M.; Gulla, A. F.; O'Laoire, C.; Urgeghe, C.; Allen, R. J.; Mukerjee, S. Chalcogenide electrocatalysts for oxygen-depolarized aqueous hydrochloric acid electrolysis. *Electrochimica Acta* **2007,** *52*, 6282-6294.

21. Norskov, J. K.; Bligaard, T.; Logadottir, A.; Kitchin, J. R.; Chen, J. G.; Pandelov, S. Trends in the exchange current for hydrogen evolution. *Journal of the Electrochemical Society* **2005,** *152*, J23-J26.

22. Jaramillo, T. F.; Jorgensen, K. P.; Bonde, J.; Nielsen, J. H.; Horch, S.; Chorkendorff, I. Identification of active edge sites for electrochemical H_2 evolution from MoS_2 nanocatalysts. *Science* **2007,** *317*, 100-102.

23. Li, Y. G.; Wang, H. L.; Xie, L. M.; Liang, Y. Y.; Hong, G. S.; Dai, H. J. MoS_2 nanoparticles grown on graphene: An advanced catalyst for the hydrogen evolution reaction. *Journal of the American Chemical Society* **2011,** *133*, 7296-7299.

24. Hinnemann, B.; Moses, P. G.; Bonde, J.; Jorgensen, K. P.; Nielsen, J. H.; Horch, S.; Chorkendorff, I.; Norskov, J. K. Biomimetic hydrogen evolution: MoS_2 nanoparticles as catalyst for hydrogen evolution. *Journal of the American Chemical Society* **2005,** *127*, 5308-5309.

25. Raybaud, P. Understanding and predicting improved sulfide catalysts: Insights from first principles modeling. *Applied Catalysis A-General* **2007,** *322*, 76-91.

26. Chianelli, R. R.; Berhault, G.; Raybaud, P.; Kasztelan, S.; Hafner, J.; Toulhoat, H. Periodic trends in hydrodesulfurization: In support of the Sabatier principle. *Applied Catalysis A-General* **2002,** *227*, 83-96.

27. Chianelli, R. R. Periodic trends transition metal sulfide catalysis: Intuition and theory. *Oil & Gas Science and Technology-Revue De l'Institut Francais Du Petrole* **2006,** *61*, 503-513.

28. Bither, T. A.; Bouchard, R. J.; Cloud, W. H.; Donohue, P. C.; Siemons, W. J. Transition metal pyrite dichalcogenides high-pressure synthesis and correlation of properties. *Inorganic Chemistry* **1968,** *7*, 2208-2220.

29. Weber, T.; Prins, H.; van Santen, R. A. *Transition metal sulphides : Chemistry and catalysis.* Kluwer Academic Publishers: Boston, 1998; p 364.

30. Bonde, J.; Moses, P. G.; Jaramillo, T. F.; Norskov, J. K.; Chorkendorff, I. Hydrogen evolution on nano-particulate transition metal sulfides. *Faraday Discussions* **2008,** *140*, 219-231.

31. Sobczynski, A.; Bard, A. J.; Campion, A.; Fox, M. A.; Mallouk, T. E.; Webber, S. E.; White, J. M. Catalytic hydrogen evolution properties of nickel-doped tungsten disulfide. *Journal of Physical Chemistry* **1989,** *93*, 401-403.

32. Nguyen, T. V. A gas distributor design for proton-exchange-membrane fuel cells. *Journal of the Electrochemical Society* **1996,** *143*, L103-L105.

33. Thompson, R. B. *Illustrated guide to home chemistry experiments*. O'Reilly Media/Make: 2008; p 432.

34. *CasaXPS*, 2.3.15.

35. a) Hohenberg, P.; Kohn, W. Inhomogeneous electron gas. *Physical Review* **1964,** *136*, B864-B871.; b) Kohn, W.; Sham, L. J. Self-consistent equations including exchange and correlation effects. *Physical Review* **1965,** *140*, A1133-A1138

36. Perdew, J. P.; Burke, K.; Ernzerhof, M. Generalized gradient approximation made simple. *Physical Review Letters* **1996,** *77*, 3865-3868.

37. Blochl, P. E. Projector augmented-wave method. *Physical Review B* **1994,** *50*, 17953-17979.

38. Kresse, G.; Joubert, D. From ultrasoft pseudopotentials to the projector augmented-wave method. *Physical Review B* **1999,** *59*, 1758-1775.

39. Neugebauer, J.; Scheffler, M. Adsorbate-substrate and adsorbate-adsorbate interactions of Na and K adlayers on Al(111). *Physical Review B* **1992,** *46*, 16067-16080.

40. Jenkins, R.; Snyder, R. *Introduction to X-ray powder diffractometry*. John Wiley & Sons Inc.: 1996; p 432.

41. Gileadi, E. *Physical electrochemistry : Fundamentals, techniques and applications*. Wiley-VCH: Weinheim, 2011; p 394.

42. Kelty, S. P.; Li, J.; Chen, J. G.; Chianelli, R. R.; Ren, J.; Whangbo, M. H. Characterization of the RuS_2(100) surface by scanning tunneling microscopy, atomic force microscopy, and near-edge X-ray absorption fine structure measurements and electronic band structure calculations. *Journal of Physical Chemistry B* **1999,** *103*, 4649-4655.

43. Grillo, M. E.; Sautet, P. Density functional study of the structural and electronic properties of RuS_2(111): II. Hydrogenated surfaces. *Surface Science* **2000,** *457*, 285-293.

44. Grillo, M. E.; Smelyanski, V.; Sautet, P.; Hafner, J. Density functional study of the structural and electronic properties of RuS_2(111) I. Bare surfaces. *Surface Science* **1999,** *439*, 163-172.

45. Frechard, F.; Sautet, P. Hartree-Fock ab-initio study of the geometric and electronic-structure of RuS_2 and its (100)-surface and (111)-surface. *Surface Science* **1995,** *336*, 149-165.

46. Frechard, F.; Sautet, P. Chemisorption of H_2 and H_2S on the (100) surface of RuS_2: An ab initio theoretical study. *Surface Science* **1997,** *389*, 131-146.

47. Frechard, E.; Sautet, P. RuS_2(111) surfaces: Theoretical study of various terminations and their interaction with H_2. *Journal of Catalysis* **1997,** *170*, 402-410.

48. Norskov, J. K.; Rossmeisl, J.; Logadottir, A.; Lindqvist, L.; Kitchin, J. R.; Bligaard, T.; Jónsson, H. Origin of the overpotential for oxygen reduction at a fuel-cell cathode. *Journal of Physical Chemistry B* **2004,** *108*, 17886-17892.

49. Metiu, H. *Physical chemistry: Statistical mechanics*. Taylor & Francis Group, LLC: 2006; p 292.

50. Metiu, H. *Physical chemistry: Thermodynamics*. Taylor & Francis Group, LLC: 2006; p 694.

51. Robinson, R. A.; Stokes, R. H. *Electrolyte solutions* Courier Dover Publications: 2002; p 587.

52. Henkelman, G.; Uberuaga, B. P.; Jónsson, H. A climbing image nudge elastic band method for finding saddle points and minimum energy paths. *Journal of Chemical Physics* **2000,** *113*, 9901-9904

53. Henkelman, G.; Jónsson, H. Improved tangent estimate in the nudge elastic band method for finding minimum energy paths and saddle points. *Journal of Chemical Physics* **2000,** *113*, 9978-9985.

54. Metiu, H.; Chretien, S.; Hu, Z. P.; Li, B.; Sun, X. Y. Chemistry of lewis acid-base pairs on oxide surfaces. *Journal of Physical Chemistry C* **2012,** *116*, 10439-10450.

55. http://www.infomine.com/investment/metal-prices/ruthenium/

IV. HER/HOR Catalysts for the H_2-Br_2 Fuel Cell System

Reproduced from T. V. Nguyen, H. Kreutzer, V. Yarlagadda, E. McFarland, N.Singh, ECS Transactions, **53**, 75, (2013).

Abstract

Large scale deployment of renewable power sources like wind and solar require energy storage because of their intermittent nature. The Hydrogen-Bromine (H_2-Br_2) fuel cell system is considered to be a suitable electrical energy storage system because of its high energy capacity, high round-trip conversion efficiency and low cost. While no precious metals are needed to catalyze the bromine reactions, the hydrogen (HER/HOR) reactions require a catalyst that is highly active, to keep the performance high and the cost low, and stable and durable in the highly corrosive HBr/Br_2 environment of the cell as required by the extended life of this application. Platinum, while having very high catalytic activity for the HER/HOR reactions, is not stable in the HBr/Br_2 environment. An alternative catalyst is needed. This paper discusses the performance and stability of various HER/HOR catalysts that we have evaluated for this fuel cell system.

A. Introduction

Renewable energy sources, like wind and solar, could supply a significant amount of electrical energy, but integration of these sources into the electrical grid system poses major challenges due to their intermittent nature and unpredictable availability. Consequently, renewable energy sources like wind and solar can be fully exploited only if efficient, safe and reliable electrical energy storage (EES) systems are provided. Current technologies that are based on stationary batteries permit storage in small quantities that may be sufficient for

some transportation and residential applications. Major industrial storage needs including those associated with smart grids are likely to be much larger in magnitude that may be met only by flow systems like flow batteries or regenerative fuel cells which have the scale-up capabilities that stationary batteries don't [1].

Of the various flow battery systems being considered for the large-scale electrical energy storage application, the hydrogen-bromine system has gained considerable attention because of its high round-trip conversion efficiency, made possible by the fast kinetics of the hydrogen and bromine electrode reactions, high power density capability, high energy storage capacity, low cost active materials, simplicity and reliability [2-6]. The discharge and charge reactions occurring in an acid-based H_2-Br_2 flow battery during operating are as follows. During the discharge cycle, hydrogen molecules (H_2) are oxidized to form hydronium (H^+) ions at the hydrogen electrode and bromine molecules (Br_2) are reduced to bromide ions (Br^-) at the bromine electrode. The hydronium ions migrate across a proton-conducting membrane to the bromine electrode and combine with the bromide ions to form hydrobromic acid (HBr) as shown below:

$$Br_2 + 2e^- \longleftrightarrow 2\ Br^-,\ E^0 = 1.09\ V.$$

The hydronium ions migrate to the hydrogen side of the fuel cell and are reduced to H_2,

$$H_2 \longleftrightarrow 2\ H^+,\ E^0 = 0.0\ V,$$

The overall reaction is

$$H_2 + Br_2 \longleftrightarrow 2HBr,\ E^0_{cell} = 1.09V.$$

During charge the reverse reactions occur. Figure 1 shows a schematic of a H_2-Br_2 flow battery system with the chemical and physical processes occurring within the cell.

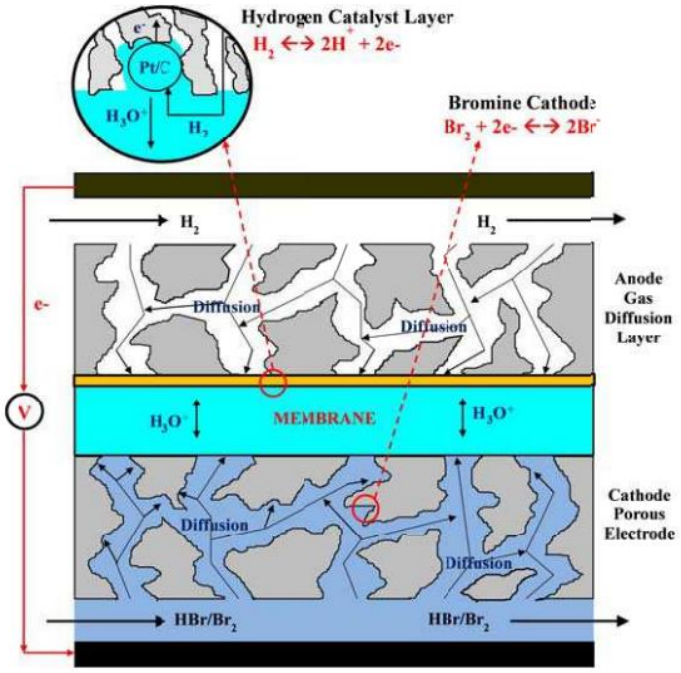

Figure 1. Schematic of a H_2-Br_2 fuel cell

While no precious metals are needed to catalyze the bromine reactions, the hydrogen oxidation and evolution (HOR/HER) reactions require a catalyst that is highly active, to keep the performance high and the cost low, stable and durable in the highly corrosive HBr/Br_2 environment of the cell as required by the extended life of this application. Note that ionic conduction at the hydrogen electrode and between the hydrogen and bromine electrodes is provided by the proton-conducting polymer phase in the hydrogen electrode and the protonconducting membrane, while ionic conduction at the bromine electrode is provided by the hydrobromic acid solution. So, theoretically, the hydrogen catalyst material should be selected for activity and stability in the proton-conducting polymeric phase only. However, during the operation of a H_2-Br_2 cell, HBr and Br_2 could cross from the bromine side to the hydrogen side potentially leading to the corrosion and poisoning of the catalyst used at the hydrogen electrode.

Platinum catalyst that is currently used in the acid-based hydrogen-oxygen fuel cells, while having very high catalytic activity for the HER/HOR reactions, is not stable in the HBr/Br_2 environment. Consequently, alternative HER/HOR catalyst materials are needed for this system. Prior works have shown that transition metal sulfides (TMS) have exhibited high stability in similarly corrosive environment. For example, rhodium sulfide has demonstrated to be a stable and active catalyst for the oxygen reduction reaction in oxygen-reduction-assisted electrolysis of hydrochloric acid [7-8]. This paper discusses our evaluation of various TMS and doped TMS for HER/HOR in HBr solutions and in a H_2-Br_2 cell.

B. Experimental

The platinum, TMS and doped TMS catalysts were screened for HER in HBr solutions and then tested in a H_2-Br_2 cell under both charge and discharge to evaluate their HER/HOR performance. Inks of platinum, TMS and doped TMS catalysts on carbon support (Vulcan XC72) were prepared by mixing the catalysts with a 1:1 vol % mixture of 2-propanol and deionized water and a 5wt % Nafion solution (Aldrich). For the RDE study, the catalyst inks were applied on a 0.178 cm^2 glassy carbon RDE and tested in a 0.5 M HBr solution under both galvanostatic and potentiostatic modes. For the H2-Br2 fuel cell study, the catalyst inks were applied (~0.5 mg/cm^2 loading) on the micro-porous surface of a bi-layer porous carbon gas diffusion layer (SGL35BC by SGL Carbon). The catalyst surface of the gas diffusion layer was then hot-pressed onto a Nafion 212 membrane to form a half membrane electrode assembly. This half membrane electrode assembly was placed in physical contact with either a plain carbon (SGL10AA) bromine electrode or hot pressed onto an electrode made of Pt/C coated bi-layer porous carbon gas diffusion layer

(SGL35BC) to form a complete membrane electrode assembly (MEA). These MEA's were tested in a 2.25 cm^2 fuel cell at room temperature (22 °C) with interdigitated flow fields [9] on both sides of the cell under either the H2-H2 mode in which hydrogen is applied to both sides of the flow cell, or the H2-Br2 mode with hydrogen fed to one side and Br_2/HBr solution to the other side. Hydrogen gas at 3 psig was continuously circulated through the hydrogen side. A photograph of the H_2-Br_2 cell is shown in Figure 2.

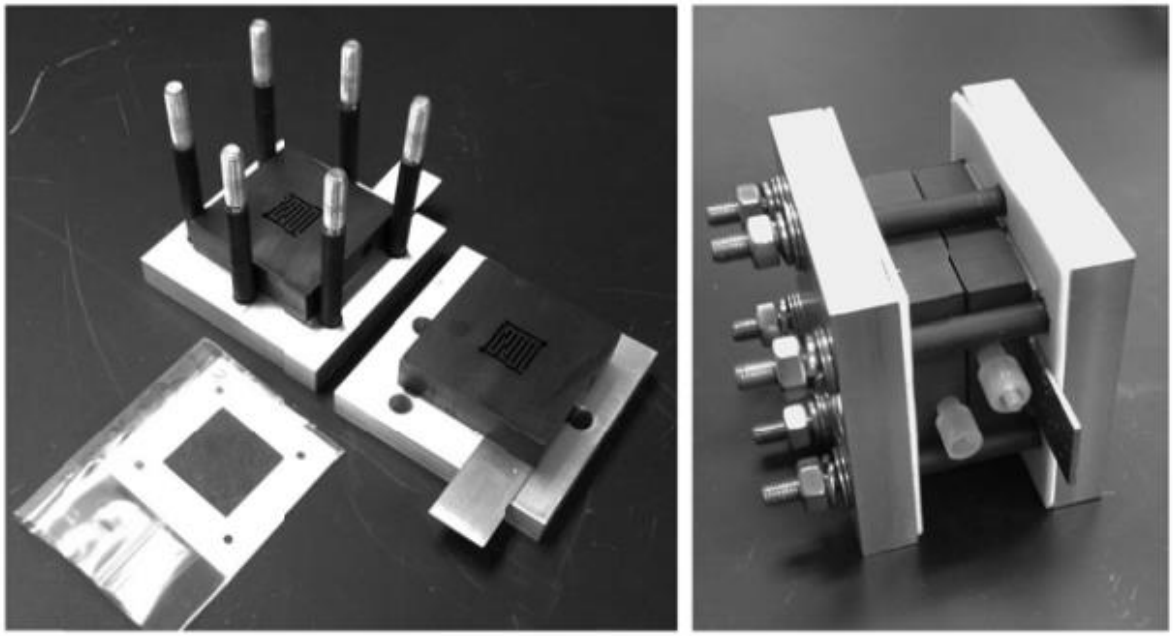

Figure 2. H_2-Br_2 fuel cell components used in the study

C. Results and Discussion

Figure 3 shows the RDE chronopotentiometric results of carbon supported platinum, TMS and doped TMS catalysts tested at 2500 rpm in 0.5 M HBr solutions. For the galvanostatic study the electrode was held at 11 mA/cm^2. The results show that while platinum is the most active HER catalyst in the group, it loses its activity quickly in the HBr solution. The TMS and cobalt-doped TMS materials show high stability even though their initial activies are lower than that of platinum. The rhodium sulfide materials are expressed

as Rh_xS_y because it consists of multiple phases where the active phase is not known for certain. However, results from prior works and our ongoing studies have shown that the active phase is most likely to be Rh_3S_4 because the Rh_2S_3 phase is a semiconductor with low electronic conductivity [7-8].

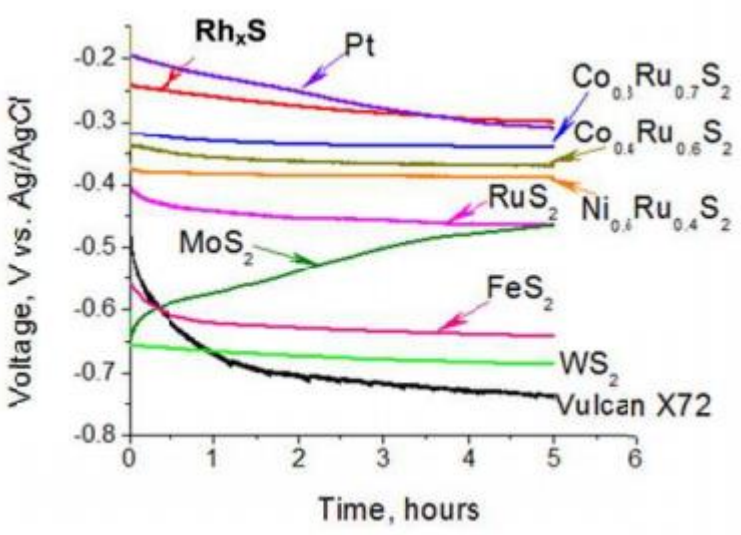

Figure 3. Chronopotentiometric results of platinum and some TMS and doped TMS catalyst materials in 0.5 M HBr solutions at an applied current of 11 mA/cm^2 [Ref. 10]

Figure 4 shows the test results in a H_2-Br_2 cell under the H_2-H_2 (hydrogen pumping) mode. In this mode, hydrogen was applied to both the electrodes (i.e., working electrode) with the catalyst material of interest and the electrode on the other side of the membrane electrode assembly, which served as a counter electrode. The counter electrode in this case consisted of a bi-layer gas diffusion electrode loaded with carbon-supported platinum catalyst. When the working electrode is in the anodic mode (cell potential above zero), hydrogen molecules at the working electrode are oxidized to hydronium ions. The hydronium ions migrate across the membrane to the electrode on the other side of the membrane where they are reduced back to hydrogen molecules. The opposite occurs when a negative potential is applied to the cell. All the catalyst loadings used for the hydrogen

electrodes were around 0.75 mg/cm^2 . The results in Figure 4 show that the rhodium sulfide catalyst has HER/HOR activities close to those of platinum and that the HER activity of the rhodium sulfide catalyst is slightly higher than its HOR activity. The results also show that the ruthenium sulfide and cobalt-doped ruthenium sulfide materials exhibit some HER activities but almost no HOR activities.

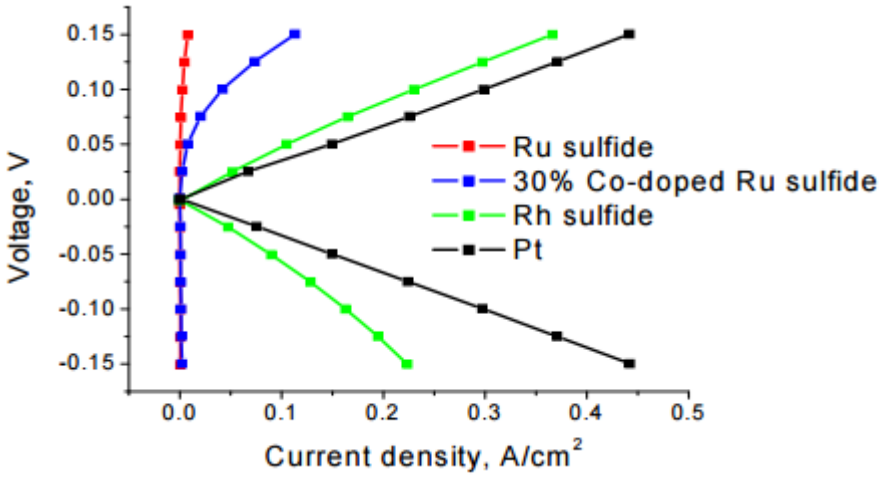

Figure 4. HER/HOR activities of platinum and ruthenium sulfide and cobalt-doped ruthenium sulfide materials in a H_2-H_2 fuel cell [Ref. 10]

Based on the results obtained from the RDE and H_2-H_2 cell studies, MEAs consisting of Nafion 212 membranes and hydrogen electrodes made of Rh_xS_y on carbon support (Toray XC72) and bromine electrodes made of plain carbon porous substrate (SGL10AA) were assembled and tested in a H_2-Br_2 fuel cell. Hydrogen at 3 psig was circulated continuously through the hydrogen electrode, and a solution of 2M/2M HBr/Br_2 solution was fed to the bromine electrode at a constant volumetric flow rate of 1.6 cc/min. The fuel cell was operated for a few hours and then left standing overnight to evaluate the stability of the catalyst in the HBr/Br2 solution. The results are shown in Figure 5. Also, included in Figure 5 for comparison are the results from a similar H_2-Br_2 cell with a Pt/C hydrogen electrode.

The catalyst loadings in the hydrogen electrode for both cells were approximately 0.5 mg/cm^2.

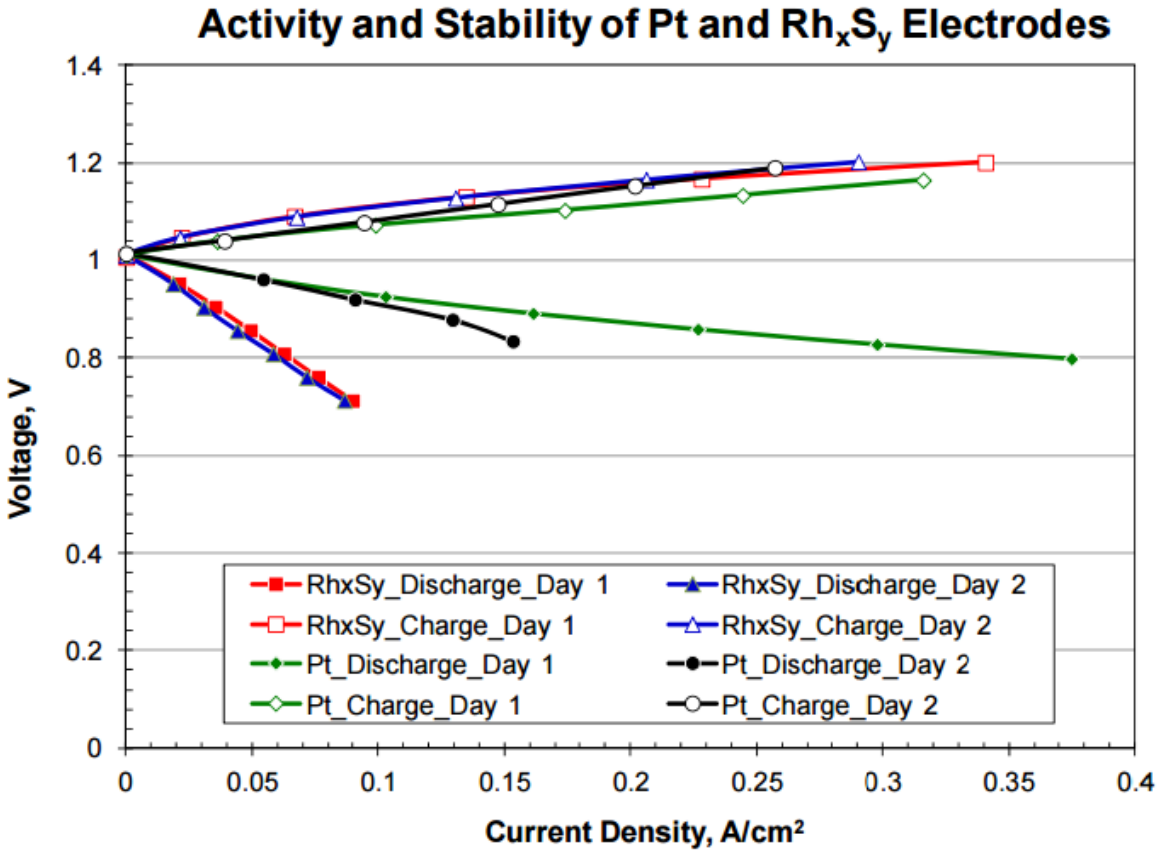

Figure 5. Performance of Rh_xS_y and Pt as hydrogen electrode catalysts in a H_2-Br_2 fuel cell

Similar to the H_2-H_2 mode results in Figure 4, the fuel cell data in Figure 5 show that the HER activity of the rhodium sulfide catalyst is comparable to that of platinum while its HOR activity is slightly lower. These results also show that, in support of the earlier chronopotentiometric results in Figure 3, while the rhodium sulfide catalyst has lower catalytic activities than those of platinum, it has higher stability.

D. Summary

The Hydrogen-Bromine (H_2-Br_2) fuel cell system is a suitable electrical energy storage system because of its high energy capacity, high round-trip conversion efficiency and

low cost. While no precious metals are needed to catalyze the bromine reactions, the hydrogen (HER/HOR) reactions require a catalyst that is highly active, to keep the performance high and the cost low, and stable and durable in the highly corrosive HBr/Br_2 environment of the cell as required by the extended life of this application. Platinum, while having very high catalytic activity for the HER/HOR reactions, is not stable in the HBr/Br_2 environment. An alternative catalyst is needed. Transition metal sulfides like rhodium sulfides are potential catalysts for the hydrogen electrode in a H_2-Br_2 fuel cell because of its high stability and activity in the HBr/Br_2 environment

Acknowledgements

The authors wish to acknowledge the financial support of this work by the Nation Science Foundation through grant no. EFRI-1038234.

References

[1]. T. Nguyen and R. Savinell, "Flow Batteries," Electrochemical Society Interface, Vol. 19, No. 3, 54-56 (2010).

[2]. Werner Glass and G.H. Boyle, "Performance of Hydrogen-Bromine Fuel Cells," Advances in chemistry series, 47, 203 (1965).

[3]. G. G. Barna, S. N. Frank and D. Weedon, "Lifetime Studies in H2/Br2 Fuel Cells," J. Electrochem. Soc., 131, 1973 (1984).

[4]. Livshits, A. Ulus, and E. Peled, "High-power H2/Br2 fuel cell," Electrochem. Comm., Vol. 8, 1358-1362 (2006).

[5]. Haley Kreutzer, Venkata Yarlagadda, and Trung Van Nguyen, "Performance Evaluation of a Regenerative Hydrogen-Bromine Fuel Cell," J. Electrochem Soc., 159(7), F331 (2012).

[6]. Kyu Taek Cho, Paul Ridgeway, Adam Z. Weber, Sophia Haussener, Vincent Battagalia, and Venkat Srinivasan, “High Performance Hydrogen/Bromine Redox Flow Battery for GridScale Energy Storage,” J. Electrochem. Soc., 159(11), A1806 (2012).

[7]. A.F. Gulla, L. Gancs, R. J. Allen, and S. Mukerjee, “Carbon-supported low-loading rhodium sulfide electrocatalysts for oxygen depolarized cathode applications,” Appl. Catal. A, 326, 227 (2007).

[8]. J.M. Ziegelbauer, A.F. Gulla, C. O’Laoire, C. Urgeghe, R.J. Allen, and S. Mukerjee, “Chalcogenide electrocatalysts for oxygen-depolarized aqueous hydrochloric acid electrolysis,” Electrochim. Acta, 52, 6282 (2007).

[9]. T. Nguyen, “A Gas Distributor Design for Proton Exchange Membrane Fuel Cells,” J. Electrochem. Soc., Vol. 143, L103-L105 (1996). 10. A. Ivanovskaya, N. Singh, R.-F. Liu, H. Kreutzer, J. Baltrusaitis, T.V. Nguyen, H. Metiu, E.W. McFarland, “Transition Metal Sulfide Hydrogen Evolution Catalysts for Hydrobromic Acid Electrolysis,” Langmuir, 29(1), 480-492 (2013).

V. Stable electrocatalysts for autonomous photoelectrolysis of hydrobromic acid using single-junction solar cells

Reproduced from N. Singh et. al., Energy and Environmental Science, 2014, 7, 978-981 with permission from The Royal Society of Chemistry. Supporting information available online.

Abstract

Metal sulfides that are stable in bromine were investigated as electrocatalysts for hydrogen evolution in a photoelectrochemical device converting HBr to H_2*(g)* and Br_2*(l)*. The photoanode was stabilized against photocorrosion using a poly(3,4-ethylenedioxythiophene) poly-(styrenesulfonate) (PEDOT:PSS) coating. Low loadings of rhodium sulfide nanoparticles were used as cathode electrocatalyst in place of platinum resulting in substantial improvement in the performance of a GaAs-based photosynthetic cell.

A. Introduction

Direct solar-to-chemical conversion, artificial photosynthesis, is an attractive and sustainable route to the production of valuable chemicals and fuels that can be used directly, or as energy storage media [1,2]. Solar photelectrolysis of hydrogen halides (e.g. HBr) to hydrogen and a halogen (e.g. Br_2) is particularly interesting since the process is electrochemically efficient and the products are valuable [3–6]. However, the instability of most efficient photoelectrodes in strong acids has impeded the exploitation of this process.

Although the semiconductor anode can be stabilized through the use of protective coatings such as PEDOT:PSS [7], there is sufficient crossover of the bromine

produced to corrode and poison most hydrogen evolution cathode materials (e.g. platinum). The development of hydrogen evolution electrocatalysts that are stable in the halogen/halide electrolyte is crucial for this solar-to-chemical system to be useful. Of course metal electrocatalyst films (such as those of platinum/iridium) can be made thick enough to allow long catalyst life [4]. This, however, is a costly solution that also reduces light collection due to reduced transparency. Clearly, a catalyst consisting of dispersed nanoparticles is desirable, but unfortunately platinum group metals are not stable as nanoparticles in halogen/halide electrolytes [8,9]. A number of metal sulfides might be good candidate materials since they have been shown to be stable as oxygen depolarized cathodes for chlorine production from hydrochloric acid [10–14] and as hydrogen evolution cathodes for the electrolysis of HBr [15].

In this communication we demonstrate the advantage of rhodium sulfides as a cathode electrocatalyst in a photoelectrochemical device consisting of a single-junction gallium arsenide (GaAs) cell that photoelectrochemically electrolyzes HBr with simulated sunlight as the only energy input. This work shows how the design of a stabilized electrocatalyst coating can facilitate the use of a high efficiency buried semiconductor junction which would otherwise corrode in most useful electrolytes.

B. Results and Discussion

To examine the stability of a cathode electrocatalyst in a Br^-/Br_3^- environment, cyclic voltammograms (CV) were measured in fuming HBr (Figure 1). For the initial cycles (≤5), both Pt/C and Rh_xS_y/C electrodes prepared on ITO using a Nafion binder (see Electronic Supporting Information for details) exhibited a strong catalytic wave with hydrogen evolution onset at -0.1 V vs. Ag/AgCl electrode. However as the number of cycles increased,

hydrogen evolution at the Pt/C surface decreased, with no detectable currents after 360 cycles (Figure 1a). We speculate that the rapid decrease from 350 to 360 cycles is because the Pt catalyst is continuously corroded but not limiting current until approximately 350 cycles when the last remnants of the Pt are still available. At approximately 350 cycles the last of the catalyst is removed and the activity drops to zero (by 360 cycles). The electrochemical stability of Pt films or Pt/C as a hydrogen evolution electrocatalyst for HBr electrolysis is likely limited by the instability of the nanoparticulate Pt in the presence of Br^- /Br_3^-. This is believed to be due Br^- binding to the Pt, blocking active sites [16,17], and the dissolution of Pt in the presence of Br_3^-, which forms through the reaction of Br^- with bromine. Although a membrane can be used to block Br_3^- transport, crossover can still occur, allowing the bromine that is formed on the counter electrode to corrode the Pt/C. In contrast, the activity of an electrode in which the Pt/C catalyst was replaced with Rh_xS_y/C remains constant after a small initial decrease, as shown in Figure 1b in which the stability of the Rh_xS_y is compared to that of Pt. A possible reason for the initial decrease in activity for Rh_xS_y/C is desorption of physically adsorbed catalyst due to insufficient Nafion binder. The procedure used was optimized for deposition of catalysts onto a glassy carbon electrode, and further optimization may be helpful in improving the adsorption of the catalyst on a PEDOT:PSS coated surface. It is also possible that Br^- reduces the Rh_xS_y activity rapidly to a lower, but stable steady-state activity. The mechanism for the decreased anodic current for the Rh_xS_y/C catalyst after several scans is unclear and merits further investigation.

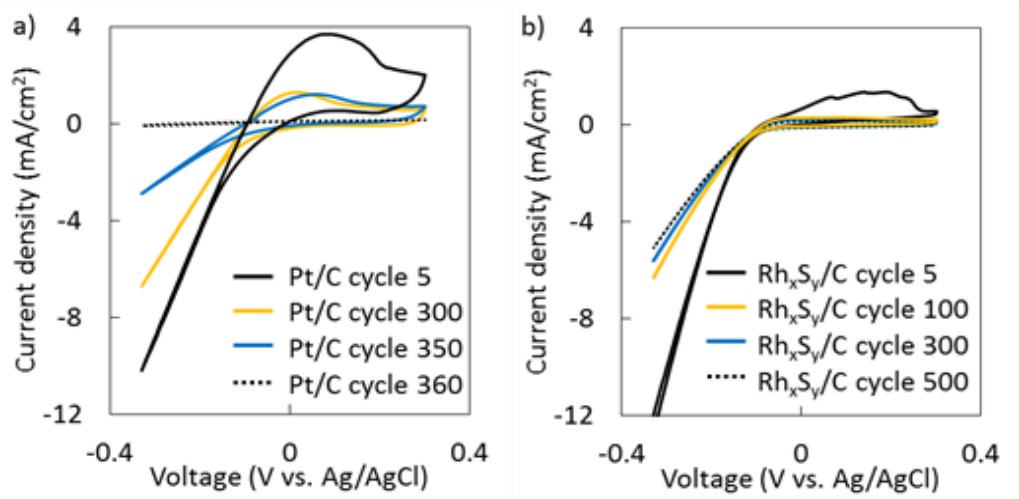

Figure 1. Cyclic voltammograms showing hydrogen evolution using a) Pt/C and b) Rh_xS_y/C both deposited on an ITO electrode from inks. The scan rate was 20 mV/s, with Ag/AgCl reference electrode and Pt counter electrode. The electrolyte was fuming HBr with no separator between counter and working electrode. The Rh_xS_y/C reaches a stable HER activity, while with time the Pt/C corrodes and the activity is severely reduced.

The stability of the sulfide catalyst is also demonstrated by the minimal dissolution of Rh_xS_y after exposure of the catalyst to 6 M HBr, 6M HCl and 6M $HClO_4$ for two weeks (Table 1). In addition, the crystallinity of Rh_xS_y/C measured by X-ray diffraction did not change after 4 hours of continuous cycling in fuming HBr. The stability of the Rh_xS_y electrocatalyst makes it an excellent (and cost effective) replacement as the hydrogen evolution electrocatalyst for photoelectrolysis of HBr. Although rhodium is expensive, the metal loading used in the photocathode is extremely low, 0.0432 mg/cm^2 (the same loading of metal would be made by a 35 nm thick film of Rh, or 20 nm of Pt). The cost is approximately \$20/m^2 for either metal, which for a 10% efficient system would equal ~\$0.20/W_{peak}. (See ESI for discussion).

Table 1. Percentage of Rh dissolved after exposure to 6M HBr, HCl, $HClO_4$ for two weeks

Acid	Rh dissolved (%)
HBr	2.1 ± 0.2
HCl	4.7 ± 0.2
$HClO_4$	2.9 ± 0.2

The solid state IV curve under illumination for a commercial p-n GaAs cell is known, allowing it to be compared in the same plot with I-V performance data from the electrocatalysts used in a photoelectrochemical device. To compare to conditions in a PEC device, the electrocatalysts are oriented facing away from one another and have the same area as the final cell to be tested, thus accounting for any mass transfer limitations within the cell. The predicted operating photocurrent and voltage of an autonomous photoelectrochemical system consisting of a p-n junction with electrocatalysts deposited on both the anode and the cathode, are given by the intersection of the solid-state semiconductor IV curve and the electrochemical current-voltage relation of the electrocatalysts deposited on the semiconductor device faces (Figure 2a) [18].

After the electrocatalysts have been applied onto the semiconductor anode and cathode, the operating current density of the device under illumination was measured by the rate of hydrogen gas evolution (using a gas chromatograph). The initial rate is consistent with the current density calculated by the solid state IV measurement of the GaAs device and the catalyst IV curve (Figure 2b).

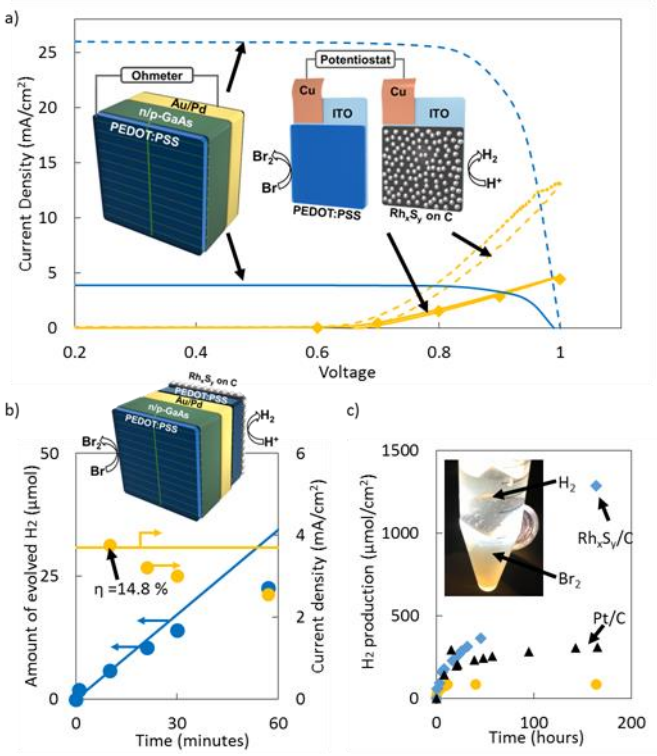

Figure 2. a) The current and voltage relationships of: two-electrode system using a Rh_xS_y/C on PEDOT cathode and PEDOT anode in 48wt% HBr as an uncompensated (solid orange line) and IR compensated (dotted orange line) cyclic voltammogram, and 10 minute averaged constant potential (orange dots) compared with the solid state IV curve for a commercial GaAs single junction cell under 100 mW/cm^2 illumination (blue dotted line) and 15 mW/cm^2 (blue line), the schematics of the two-electrode system and the solid state solar cell measurement are shown in the inset. b) gas chromatography measured hydrogen production (blue dots), corresponding current density (orange dots) for the GaAs with Rh_xS_y/C cathode electrocatalyst depicted in (a), and hydrogen production (blue line) and current density (orange line) predicted by the intersection of the solid state IV measurement of the GaAs device and the electrochemical IV curve of HBr electrolysis. The electrolyte was 8.4 M HBr and the illumination was 15 mW/cm^2. The efficiency is obtained from the starting open circuit voltage in the electrolyte (0.6 V) multiplied by the current density divided by the illumination (15 mW/cm^2). The schematic of the wireless system is shown in the inset of b). c) hydrogen production rate showing long-term stability of the overall device, due to the use of the stable Rh_xS_y catalyst instead of Pt. Samples are non-O_2 plasma etched before PEDOT:PSS deposition (orange), anode etched in O_2 plasma prior to PEDOT:PSS spincasting with Rh_xS_y/C on the cathode (blue) or Pt/C (black). These samples were illuminated by 60 mW/cm^2 and the overall efficiency after 164 hours of operation was 0.4% for the Rh_xS_y/C sample (blue). The system under operation is shown in the inset of (c), with hydrogen forming at the top (cathode) and bromine collecting after forming at the bottom (anode).

The initial efficiency of the best performing device, at 15 mW/cm^2 illumination, was 14.8%. The use of Rh_xS_y instead of Pt extends the device lifetime (Figure 2c), because the poisoning/corrosion of the electrocatalyst does not inhibit the production of hydrogen. Transmission electron microscopy images (Figure S3) did not show significant change in the structure of the catalyst and by energy dispersive x-ray spectroscopy no significant changes in Rh-S stoichiometry were observed (see ESI). Corrosion was observed on areas of the device that were not completely coated in PEDOT:PSS at the anode, which lead to decreases in the efficiency of the device due to the decreased active area of GaAs. Reloading the Rh_xS_y/C catalyst did not, however, greatly improve the H_2 production of the device suggesting that, for the GaAs/Rh_xS_y system, factors other than the cathode electrocatalyst are responsible for the decrease in efficiency with time (Figure S8). The overall efficiency of the device after 100 hours was 1.2% when illuminated at 15 mW/cm^2, (Figure S9) and 0.4% at 60 mW/cm^2 for 164 hours.

Following sustained production of bromine and hydrogen, the back reaction of bromine reduction to bromide ions resulted in a decrease in the Faradaic efficiency of the hydrogen evolution reaction, which might account for the drop in hydrogen production. A potential solution would be to place a membrane onto the cathode electrocatalyst, or to complex the bromine molecules with an agent such as polyethylene glycol [19] to reduce the quantity of bromine present at the cathode. Additionally, supporting the Rh_xS_y on a material that is unreactive in the bromine back reaction (in place of carbon) may improve the selectivity for hydrogen production. However, replenishing the solution with fresh HBr, thus reducing the amount of Br_2 present produced only a minimal increase in efficiency. Also,

PEDOT:PSS did not fully coat the GaAs anode unless an O_2 plasma etching step was used on the GaAs, resulting in much lower rates of H_2 evolution after ~12 hours of operation as shown in Figure 2c.

The effect of exposure to 3M HBr on the surface composition of Rh_xS_y/C is shown by XPS characterization (Figure 3a and b).

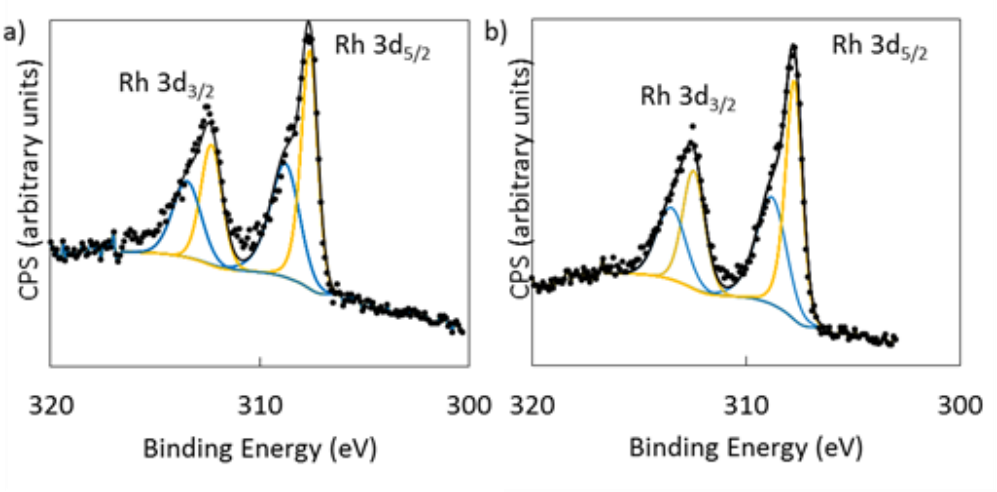

Figure 3. High resolution XPS scan for a) as prepared and b) HBr exposed Rh_xS_y/C for Rh. The raw data is in black dots. The data was fitted to a peak (black curve) using a combination or the orange (307.7 eV Rh $3d_{5/2}$ peak) and blue (308.8 eV $Rh3d_{5/2}$) peaks and the ratio of their areas was used for comparison of Rh oxidation states.

The ratio of oxidation states of Rh measured by the Rh 3d binding energy was relatively unchanged by exposure to HBr: 1) 1.19:1 of 307.6 eV:308.8 eV Rh(IV) prior to exposure of HBr, and 2) 1.25:1 of 307.7:308.8 eV Rh(IV) after exposure to HBr. The 308.8 eV peak may correspond to Rh(IV) [20], and 307.7 eV peak may correspond to a slightly oxidized Rh species. The XPS observed concentration of Rh at the surface (Figure S10), did not vary significantly, consistent with the electrochemical and chemical stability shown in Figure 1. Full XPS survey scans and high resolution scans are shown in Figure S10-13.

C. Conclusions

In conclusion, a GaAs based photoelectrochemical device was stabilized for an HBr environment by coating the anode with PEDOT:PSS and activating the cathode side for hydrogen production with a Rh_xS_y hydrogen evolution electrocatalyst dispersed on carbon using a Nafion binder. The free-standing device structure under illumination produced hydrogen and bromine without external bias or any other electrical connections for over 150 hours in fuming HBr. This performance far exceeds that of a Pt cathode electrocatalyst. The structure and processing steps may be used with most high efficiency semiconductors suggesting that efficient and stable electrocatalysts may be developed for numerous light absorbers, including such otherwise unstable semiconductors as chalcogenides and phosphides that, as a result, may be used for efficient as well as durable solar photoelectrocatalysis.

Acknowledgements

N. S. is supported by the ConvEne IGERT Program (NSF-DGE 0801627). Tom Mates assisted with XPS measurements. This work was partially supported by the MRSEC Program of the National Science Foundation under Award No. DMR 1121053. Helpful discussions with Shane Ardo are greatly appreciated.

References

[1] M.D. Archer, Electrochemical aspects of solar energy conversion, J. Appl. Electrochem. 5 (1975) 17–38. doi:10.1007/BF00625956.

[2] K. Rajeshwar, P. Singh, J. DuBow, Energy conversion in photoelectrochemical systems — a review, Electrochim. Acta. 23 (1978) 1117–1144. doi:10.1016/0013-4686(78)85064-6.

[3] J.D. Luttmer, I. Trachtenberg, Performance Predictions for Solar-Chemical Convertors by Computer Simulation, J. Electrochem. Soc. 132 (1985) 1820–1824.

[4] J. Luttmer, D. Konrad, I. Trachtenberg, Electrode materials for hydrobromic acid electrolysis in Texas Instruments' solar chemical converter, J. Electrochem. Soc. 132 (1985) 1054–1058. http://link.aip.org/link/?JESOAN/132/1054/1 (accessed June 2, 2011).

[5] W. McKee, Development of the Spherical Silicon Solar Cell, IEEE Trans. Components, Hybrids, Manuf. Technol. 5 (1982) 336–341. doi:10.1109/TCHMT.1982.1136008.

[6] J.S. Kilby, J.W. Lathrop, W.A. Porter, Solar Energy Conversion, 1977.

[7] S. Mubeen, J. Lee, N. Singh, M. Moskovits, E.W. McFarland, Stabilizing inorganic photoelectrodes for efficient solar-to-chemical energy conversion, Energy Environ. Sci. 6 (2013) 1633–1639. doi:10.1039/c3ee40258d.

[8] G.H. Schuetz, P.J. Fiebelmann, Electrolysis of Hydrobromic Acid, Int. J. Hydrogen Energy. 5 (1980) 305–316.

[9] T. Van Nguyen, H. Kreutzer, V. Yarlagadda, E. McFarland, N. Singh, HER/HOR Catalysts for the H2-Br2 Fuel Cell System, ECS Trans. 53 (2013) 75–81.

[10] J.M. Ziegelbauer, A.F. Gullá, C. O'Laoire, C. Urgeghe, R.J. Allen, S. Mukerjee, Chalcogenide electrocatalysts for oxygen-depolarized aqueous hydrochloric acid electrolysis, Electrochim. Acta. 52 (2007) 6282–6294. doi:10.1016/j.electacta.2007.04.048.

[11] J.M. Ziegelbauer, D. Gatewood, A.F. Gullá, M.J. Guinel, F. Ernst, D.E. Ramaker, et al., Fundamental Investigation of Oxygen Reduction Reaction on Rhodium Sulfide-Based Chalcogenides, J. Phys. Chem. C. 113 (2009) 6955–6968.

[12] A.F. Gullá, L. Gancs, R.J. Allen, S. Mukerjee, Carbon-supported low-loading rhodium sulfide electrocatalysts for oxygen depolarized cathode applications, Appl. Catal. A Gen. 326 (2007) 227–235. doi:10.1016/j.apcata.2007.04.013.

[13] J. Ziegelbauer, V. Murthi, C. Olaoire, A. Gullá, S. Mukerjee, Electrochemical kinetics and X-ray absorption spectroscopy investigations of select chalcogenide electrocatalysts for oxygen reduction reaction applications, Electrochim. Acta. 53 (2008) 5587–5596. doi:10.1016/j.electacta.2008.02.091.

[14] J.M. Ziegelbauer, D. Gatewood, S. Mukerjee, D.E. Ramaker, In Situ X-ray Absorption Spectroscopy Studies Of Water Activation On Novel Electrocatalysts For Oxygen Reduction Reaction In Acid Electrolyte, ECS Trans. 1 (2006) 119–128.

[15] A. Ivanovskaya, N. Singh, R.-F. Liu, H. Kreutzer, J. Baltrusaitis, T. Van Nguyen, et al., Transition metal sulfide hydrogen evolution catalysts for hydrobromic acid electrolysis., Langmuir. 29 (2013) 480–492. doi:10.1021/la3032489.

[16] V. Livshits, A. Ulus, E. Peled, High-power H2/Br2 fuel cell, Electrochem. Commun. 8 (2006) 1358–1362. doi:10.1016/j.elecom.2006.06.021.

[17] J.. Orts, R. Gómez, J.. Feliu, Bromine monolayer adsorption on Pt(110) surfaces, J. Electroanal. Chem. 467 (1999) 11–19. doi:10.1016/S0022-0728(99)00005-4.

[18] O. Khaselev, A. Bansal, J.A. Turner, High-efficiency integrated multijunction photovoltaic/ electrolysis systems for hydrogen production, Int. J. Hydrogen Energy. 26 (2001) 127–132.

[19] L.A. Kosek J., Investigation of bromine complexed hydrogen/bromine regenerative fuel cells for portable electric power, 1984.

[20] Y. Abe, Rhodium and Rhodium Oxide Thin Films Characterized by XPS, Surf. Sci. Spectra. 8 (2001) 117. doi:10.1116/11.20010801.

VI. Gas-Phase Chemistry to Understand Electrochemical Hydrogen Evolution and Oxidation on Doped Transition Metal Sulfides

Reproduced with permission from J. Electrochem. Soc., 160, A1902 (2013). Copyright 2013, The Electrochemical Society. Supporting information available online.

Abstract

RuS_2 and cobalt-doped RuS_2 are good catalysts for electrochemical hydrogen evolution in a hydrogen bromine proton exchange membrane based electrochemical flow cell, but their activity for hydrogen oxidation is low. We used temperature-programmed reaction to study the formation of HD from gaseous H_2 and D_2, catalyzed by these electrode materials. We found that they are active for HD exchange at room temperature and conclude that electrochemical hydrogen oxidation is not limited by the inability of the electrodes to adsorb or dissociate hydrogen. Therefore, we further conclude that the low activity for hydrogen electrooxidation on these semiconducting chalcogenides is due to electronic factors which limit the ability of the semiconductors to accept electrons or pass current. We recommend therefore the use of conducting compounds stable in HBr.

A. Introduction

Electrical energy storage using HBr electrolysis combined with electricity production by the reactions of H_2 and Br_2 in a fuel cell has long been considered a potentially efficient process [1,2]. One advantage of the bromine based system is that both the Br_2 reduction and oxidation have high charge transfer efficiency, whereas other electrooxidations, especially oxygen evolution, are often energetically and kinetically inefficient. In addition, there are several electrodes for bromine production stable in HBr. Unfortunately, we do not have

stable and active electrodes for hydrogen oxidation in the HBr system. Platinum, which is used as a hydrogen evolution (HER) and oxidation (HOR) catalyst in other systems, is poisoned and corroded in the HBr/Br_2 electrolyte [1]. Several metal sulfides such as RuS_2, $Co_{0.3}Ru_{0.7}S_2$ and Rh_xS_y are corrosion-resistant and perform the hydrogen reduction reasonably well [3]. However, RuS_2 and Co-doped RuS_2 are relatively inactive for hydrogen oxidation compared to the much more expensive Rh_xS_y [3]. To convert H_2 to H^+ the electrode must be able to adsorb H_2 and to accept electrons produced by the reaction. It is possible that H_2 adsorption or dissociation on the sulfide surface limits hydrogen oxidation on the electrode. To investigate whether this is the case we study the reaction of H_2 with D_2 to form HD, by gas-phase temperature-programmed reaction (TPR) and with steady-state reaction measurements. Measurements of this kind are relevant to hydrogen oxidation electrochemistry because H_2 contacts the electrode surface from gas bubbles. Since H_2 adsorption and dissociation do not involve charge transfer, H_2-D_2 exchange allows us to differentiate between gas-phase and electrochemical interaction of hydrogen with the surface.

The effect of hydrogen-surface bond-strength on the electrochemistry of hydrogen evolution/oxidation has been studied for a variety of systems [4–16]. It was concluded that for active electrochemical hydrogen oxidation and reduction an electrode must bind hydrogen, but not too strongly. In this context, measurements of H_2-D_2 exchange are of interest: slow HD exchange means poor electrode performance. Moreover, it is likely that in an inefficient electrode that performs H_2-D_2 exchange rapidly, the charge transfer process is rate limiting. Electrooxidation takes place only if the electron produced (e.g. $\frac{1}{2}\ H_2 \rightarrow H^+ + e^-$) can enter the conduction band or fill available hole states (if present) in the valence band. Moreover, for either mechanism the electrode material must have sufficient conductivity to

continuously remove the charge from the surface to the charge collector. We lump together these requirements under the name "electronic factors" as opposed to the catalytic factors associated with processes that do not involve charge transfer (such as H_2 chemisorption or dissociation). We argue below that measurements of H_2-D_2 exchange help separate catalytic effects from electronic effects for hydrogen evolution.

Here we use H_2-D_2 exchange measurements to help clarify two specific issues. 1. In previous work we have shown [3] that Co-doped RuS_2 is active for hydrogen evolution, but not for hydrogen oxidation. Is this because of an inability to dissociate hydrogen? 2. Co-doped RuS_2 is more active [3] for hydrogen evolution than RuS_2. Does this happen because Co-doped RuS_2 adsorbs H_2 and dissociates it more efficiently than RuS_2? We find that in both cases an electronic factor rather than surface catalysis must be invoked to understand these observations.

B. Experimental

1. Preparation and Characterization of Catalysts

Metallic cobalt and copper were prepared by thermal decomposition of copper(II) nitrate and cobalt nitrate to form oxides by calcination at 350 °C for 12 hours (for copper) or 200 °C for 10 hours (for cobalt). The oxides were reduced with hydrogen at 400 °C for 16 hours (for copper) or 20 hours (for cobalt) to form the metal. Ruthenium metal was purchased from Sigma-Aldrich and reduced in hydrogen at 400 °C for 1 hour prior to use. Platinum on carbon was used (from E-TEK).

We synthesized RuS_2 and Co-doped RuS_2 on XC-72 conductive carbon, which is commonly used in fuel cell catalysis; we also synthesized unsupported metal sulfide particles. The metal sulfides on carbon were synthesized as reported previously [3].

Although the active surface area is difficult to determine, the crystallite sizes were in the range of 13-16 nm [3]. We used methods that result in a pure, metal-free sulfide phase because we wanted to make sure that no metallic particles are present (which would interfere with the H_2-D_2 exchange measurements).

The carbon supported RuS_2 and $Co_{0.3}Ru_{0.7}S_2$ were formed by exposing the chloride precursors to H_2S, at 350 °C for 3 hours. The amounts were chosen to give 30 wt% loading of Ru atoms (in the sulfide) on carbon. These same catalysts were used for both the gas-phase measurements and electrochemical measurements.

The XRD measurements (X'Pert powder diffractometer; PANalytical, Inc. with a Cu Kα source, 1.54 Angstroms) on the doped ruthenium sulfides synthesized this way show a lattice parameter shift corresponding to cobalt substitution in ruthenium sulfide. XPS (Kratos Analytical, Manchester, UK) detects cobalt in the surface region of the doped sulfide [3].

We also synthesized unsupported doped sulfides to compare to the carbon supported electrocatalysts. Details of the synthesis are included in the Supplementary Information.

Preparation of Carbon-Supported Electrocatalysts

The ruthenium and cobalt doped ruthenium sulfide ($Co_{0.3}Ru_{0.7}S_2$), prepared by a method discussed previously [3], were used for both electrochemical and gas-phase measurements. For the electrochemical measurements, an ink was prepared from the catalyst with a Nafion binder and deposited onto either a Toray carbon paper electrode, at a catalyst loading of 120 μg/cm^2, or a glassy carbon support for rotating disk electrode experiments [3].

2. Gas Phase Measurement of H_2/D_2 Exchange

Hydrogen and deuterium were continuously fed to a catalyst bed, which is a 6-mm-diameter quartz tube with quartz wool on either end of the bed. The tube was placed inside a stainless steel heating-block whose temperature is controlled (Omega, CSC32). The block consists of two heating cartridges, and two channels for air and cold nitrogen gas (boil-off from liquid nitrogen cylinder). The reactor tube was connected to a differentially pumped mass spectrometer (Stanford Research Systems-Residual Gas Analyzer) which samples the gas through a leak valve. The flow rate of hydrogen and deuterium (from Praxair) were controlled by a glass float valve, and the effluent was at atmospheric pressure. The typical pressure drop across the reactor was 20-150 Torr. The temperature at which HD forms (Figures S3-S5) is used to compare the activity of the different catalysts for H_2-D_2 exchange. The onset temperature for determining when H_2-D_2 exchange occurs was defined as the temperature where the HD signal (averaged over 5 sample points) at the reactor effluent has risen beyond one standard deviation of the baseline (-50 °C). For platinum, that did appreciable H_2-D_2 exchange (relative to a blank sample) at the minimum reactor temperature, -50 °C was used as the onset temperature.

3. Electrochemical Measurement of Hydrogen Evolution and Hydrogen Oxidation

Electrochemical measurements on glassy carbon were done using a rotating disk electrode (RDE) in 0.1 M H_2SO_4 using a Ag/AgCl reference electrode and Pt mesh counter electrode using a Bio-Logic potentiostat. For the measurements on Toray paper the electrolyte was 0.1 M H_2SO_4. To perform hydrogen oxidation, the electrolyte was purged with Ar or with H_2.

C. Results and Discussion

1. Using H_2-D_2 Exchange to Understand Interaction of Hydrogen with the Catalyst Surface

In order to show how the H_2-D_2 exchange rate can be used as a descriptor for the electrochemical hydrogen evolution activity, when charge-transfer is not limiting, we have measured the onset temperature of H_2-D_2 exchange. The onset temperature at which H_2-D_2 exchange is observable (called from now on the exchange temperature and denoted T_{ex}) depends on either adsorption rate, or the rate of exchange among the adsorbed species, or the rate of desorption of HD. In Figure 1 we have plotted the exchange temperature versus the calculated Gibbs free energy ΔG_H for the reaction ½ $H_2(g)$ + S → H/S, where S is the surface and H/S is the surface with hydrogen atoms on it. The dependence of T_{ex} on $|\Delta G_H|$ appears linear.

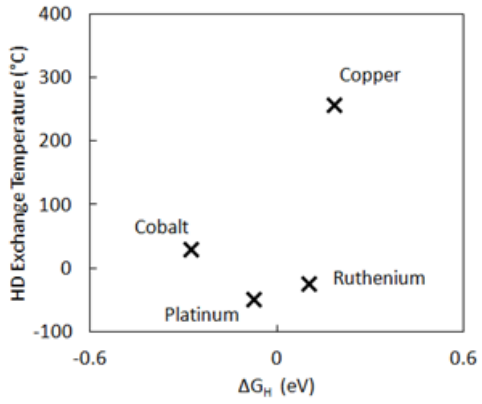

Figure 1. The minimum temperature required for H_2-D_2 exchange, plotted against the calculated Gibbs free energy of hydrogen adsorption [7]. The pressure of H_2 was 0.05 atm and D_2 was 0.13 atm. The minimum temperature measurable in the reactor was -50 °C.

If we think of T_{ex} as a proxy for the activation energy (the higher T_{ex}, the higher the activation energy of the rate limiting process in the exchange rate) then this linearity is consistent with the Brønsted-Evans-Polanyi (BEP) rule. T_{ex} for Co is high because

desorption is thermodynamically limited (ΔG_H is negative). For Cu the opposite is true: ΔG_H is positive and adsorption is unfavorable. We can also understand on this basis, why T_{ex} for Pt and Ru is low: there is hardly any thermodynamic opposition to either adsorption or desorption. We note that T_{ex} for Pt may be lower than the value reported here because our reactor cannot be cooled below -50 °C.

All results seem understandable on the basis of calculated values of ΔG_H. As the values of ΔG_H are dependent on the coverage of hydrogen, discrepancies between the H_2-D_2 exchange rate and the ΔG_H in previous works [15,16] have been attributed to the higher coverages at high pressures of hydrogen, which causes exceptionally high H_2-D_2 exchange rates for Ru beyond that expected by the ΔG_H. It would appear from Figure 1 that this is not the case for the samples tested in this work, as Ru did not show higher H_2-D_2 exchange rates than Pt, possibly due to the lower combined pressure of H_2 and D_2 (1 bar in previous works [15,16], but ~0.2 bar here with balance argon).

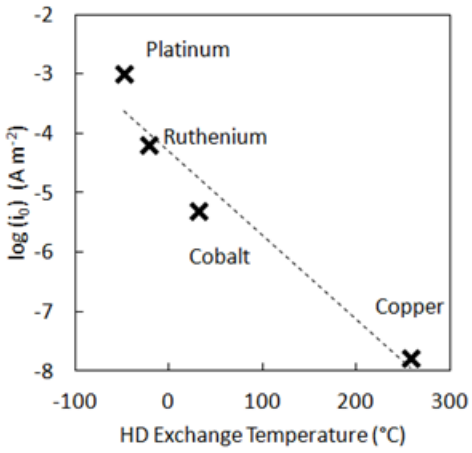

Figure 2. The temperature at which H_2-D_2 exchange starts plotted against the hydrogen evolution/oxidation exchange current density for the specified materials. The exchange current density values for Pt [17], Ru [18], Co [6,19], and Cu [6] are taken from literature. The dotted line is to guide the eye.

In Figure 2 we plot the natural logarithm of the exchange current density (taken from literature sources [6,23-25]) versus the exchange temperature. We see that the exchange current density is lower for metals with high T_{ex} and the dependence is roughly linear (Pt T_{ex} is lower than -50 °C but we cannot find the true value because our reactor temperatures is limited to T > -50 °C). For the materials shown, which, as metals, are known to not be charge transfer limited for hydrogen evolution, it is apparent that the rate of H_2-D_2 exchange (represented by Tex) is an excellent descriptor for the hydrogen evolution rate. This is easily understood because the surface chemistry reaction for HER and the H_2-D_2 exchange reaction should be rapid on similar catalyst surfaces.

2. Reason for Low HOR Activity on Ruthenium Sulfide

One of the questions we address here is why RuS_2/C and Co-doped RuS_2/C do not perform electrochemical hydrogen oxidation in electrochemical flow cells [3] or in rotating disk experiments (Figure 3). If a catalyst performs H_2-D_2 exchange efficiently, and HOR very poorly, it is likely that the rate determining step is related to charge transfer, rather than the ability to dissociate hydrogen. This is the case for $Co_{0.3}Ru_{0.7}S_2$/C, which performs hydrogen exchange at room temperature (Table 1, also in Figure 5) but not HOR. The electron produced by hydrogen oxidation must be accepted by the conduction band, or by holes in the valence band. It is possible that this process is shut down because the energy of the conduction band is too high or the hole-concentration is too low (the absence of p-dopants).

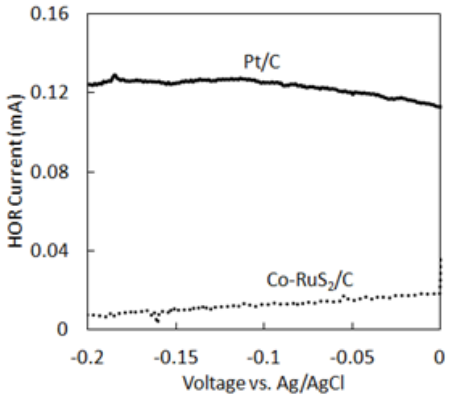

Figure 3. Hydrogen oxidation current at the Pt/C and Co-RuS_2/C electrodes. The hydrogen oxidation current presented here is the difference between the current measured while purging with H_2 (with H_2 in solution) and that measured while purging with Ar (without H_2 in solution). The measurements with H_2 purging and Ar purging (rather than the difference) are shown in Figure S6. The hydrogen oxidation current is much larger for Pt/C than Co-RuS_2/C, to a larger degree than the difference in the HER differences for these two catalysts. The electrolyte was 0.5 M HBr on a glassy carbon RDE under 2500 rpm rotation.

Table 1. H_2-D_2 Exchange Rates at Room Temperature (22 °C)

Catalyst	Flow Rate	pH_2, pD_2	H_2-D_2 Exchange Rate (mol HD/mol metal*hr)
$Co_{0.3}Ru_{0.7}S_2$/C	49 ccm	4.13 kPa H_2, 18.6 kPa D_2	0.45

The rate could be also slowed by low electrode conductivity. Support for semiconducting behavior as the reason behind low oxidation currents is seen in experiments that show unsupported n-type RuS_2 requires illumination to provide charge carriers for oxidation reactions [20,21].

To further understand the activity of HOR, the hydrogen oxidation current (Figure 3) was measured by comparing cyclic voltammograms in either H_2 or Ar purging, for both Pt/C and $Co_{0.3}Ru_{0.7}S_2$/C in an RDE (Figure S6). For charge-transfer limited reaction the oxidation current should be nearly independent of the rotation rate, as seen for RuS_2 in Fe^{2+} oxidation

without illumination [21]. If the rate-limiting step is not charge transfer, the current should increase with the rotation rate using an RDE. The independence of the HOR current on the RDE rotation rate (500 to 2000 rpm), for $Co_{0.3}Ru_{0.7}S_2$/C, (see Figs. S7 and 4) along with the ability to perform H_2-D_2 exchange at room temperature, indicates again that charge transfer is most likely limiting the hydrogen oxidation.

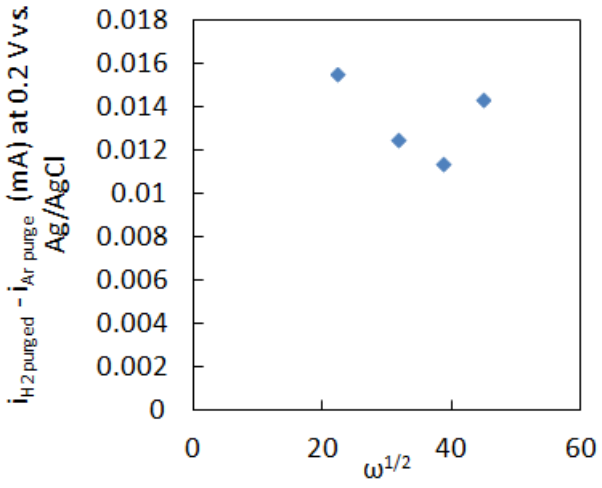

Figure 4. Hydrogen oxidation current taken from Figure S7 at 0.2 V as a function of square root of the rotation rate. The hydrogen oxidation current was measured as the difference in the currents with Ar purging (w/o H_2 in solution) and H_2 purging (w/ H_2 in solution).

Another possibility is that the active catalyst is a reduced surface that becomes 'available' at potentials below 0 V vs. RHE (thus the electrocatalyst would be active for HER, but inactive for HOR).

3. Understanding Doped Ruthenium Sulfides using H_2-D_2 Exchange

Here we compare the ability of a material to catalyze the HER/HOR to the gas-phase H_2-D_2 exchange temperature with its electrochemical activity. The effect of Co promotion in MoS_2 is seen in increased electrochemical hydrogen evolution [22] as well as increased H_2-D_2 exchange rate [23]. For cobalt ruthenium sulfide[3] ($Co_{0.3}Ru_{0.7}S_2$/C), we have previously shown that there is substitutional doping of the Co into the RuS_2 structure, with no

detectable secondary Co containing phase [3]. Contrary to what has been seen for Co doped MoS_2 we find that $Co_{0.3}Ru_{0.7}S_2/C$ is more active [3] than RuS_2/C (see the cyclic voltammograms in Figure 5a), but the exchange temperature is higher for the doped sulfide (Figure 5b). Similar gas-phase H_2-D_2 exchange results were obtained for the unsupported catalyst.

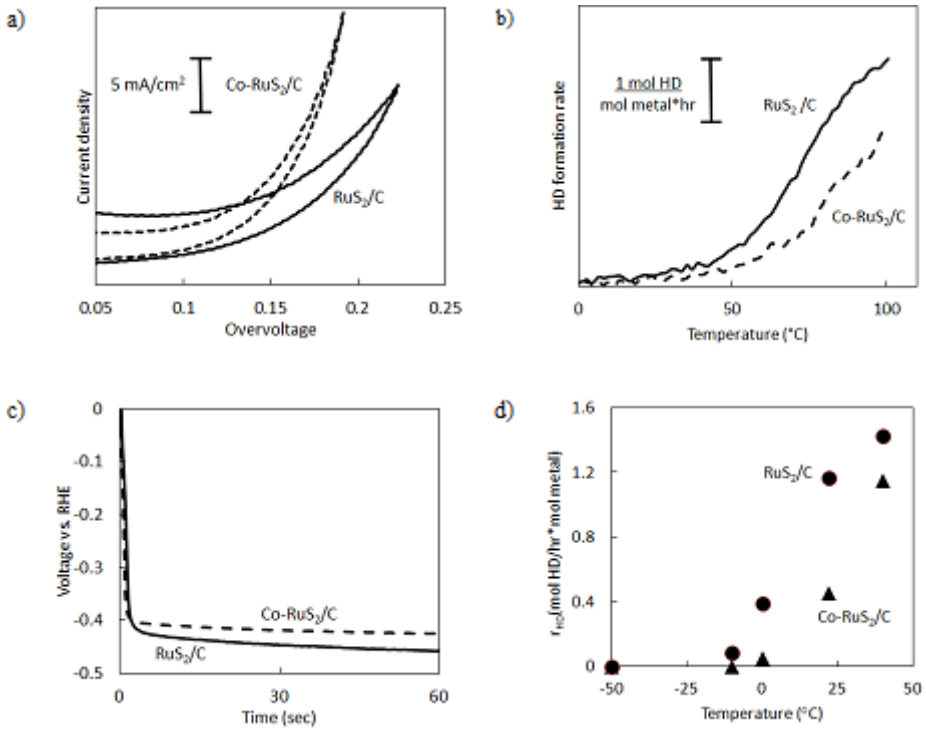

Figure 5. (a) Hydrogen evolution current as a function of overvoltage for $Co_{0.3}Ru_{0.7}S_2/C$ and RuS_2/C catalysts supported on Toray paper (40 µL high loading on 2 cm^2), in 0.1 M H_2SO_4, at a scan rate of 100 mV/s, at room temperature. (b) Temperature programmed reaction of H_2 with D_2. The amount of HD formed is plotted versus temperature. The temperature ramp rate was 10°C/min. (c) Chronopotentiograms at -10 mA/cm^2 under 1000 rpm stirring (stir bar) (d) Constant temperature measurements of the H_2-D_2 exchange rate for doped and undoped catalysts.

A chronopotentiogram of the $Co_{0.3}Ru_{0.7}S_2/C$ and RuS_2/C catalysts again shows the higher electrochemical activity of the doped compound (Figure 5c), but steady state measurements of the rate of H_2-D_2 exchange show that the undoped compound is more active for this gas-phase reaction (Figure 5d). The advantage of the steady state

measurements for the HD exchange rate is to minimize concerns about temperature gradients in the catalyst bed caused by temperature ramping.

These results suggest that doping with Co affects the electronic factors controlling hydrogen oxidation and not the adsorption-desorption of hydrogen. This may also explain why Co doping increases RuS_2 ORR activity in HCl, rather than reducing Cl^-/Br^- poisoning [24] (the effect of doping on HER activity was not dependent on the anion in our experiments). The effect of semiconducting structure of degenerately doped ruthenium sulfide crystals on the Tafel slope has previously been shown [25], and the Co doping may be affecting the charge transfer here by affecting the transport of charge carriers.

D. Conclusions

Both Co-doped RuS_2 and undoped RuS_2 are active for H_2-D_2 exchange to HD at room temperature and thus their relative inactivity for electrochemical hydrogen oxidation is not related to an inability to dissociate hydrogen. Instead, the lack of activity for hydrogen oxidation is most likely related to RuS_2's inability to accept electrons or transport charge efficiently, because it is a semiconductor. It is possible that the catalyst is only active under reducing conditions (potentials negative of 0 V vs. RHE), but we believe, based on the previous work [20,21] on single crystal RuS_2, that it is more likely that the semiconducting properties are controlling (at least in part) the activity of the catalyst. This tells us that the ability to dissociate H_2 at room temperature is a necessary but not sufficient criterion for a HER/HOR catalyst, and the ability to do charge transfer is especially important for materials such as sulfides or other semiconductors. We believe that the enhancement in HER activity for Co-RuS_2 is due to an increase in the ability for the charge transfer reaction to occur. This may also account for the increase in activity seen for Co-doped ruthenium sulfide for oxygen

reduction for catalyst prepared the same way [24], instead of an effect in decreased anion poisoning. It appears to us that one can avoid the above difficulties by using highly conductive electrodes for hydrogen evolution. Unfortunately, electrodes consisting of metals (e.g. Pt, Ni, etc) are poisoned or unstable in aqueous HBr. One needs to look for more conductive compounds (other than metals) such as semi-metals and highly doped semiconductors that are also stable in HBr. The high performance of Rh_3S_4, which is metallic, supports this view.

Acknowledgements

N.S. is supported by the ConvEne IGERT Program (NSF-DGE 0801627). Funding was provided by U.S. Department of Energy, Office of Science, Office of Basic Energy Sciences, under Contract No. DE-AC02-06CH11357. Management, operation and acquisition of equipment for the X-ray facility is supported by the Materials Research Laboratory: an NSF Materials Research Science and Engineering Center (MRSEC).

References

[1] G.H. Schuetz, P.J. Fiebelmann, Electrolysis of Hydrobromic Acid, Int. J. Hydrogen Energy. 5 (1980) 305–316.

[2] R.S. Yeo, D.-T. Chin, A Hydrogen-Bromine Cell for Energy Storage Applications, J. Electrochem. Soc. 127 (1980) 549–555.

[3] A. Ivanovskaya, N. Singh, R.-F. Liu, H. Kreutzer, J. Baltrusaitis, T. Van Nguyen, et al., Transition metal sulfide hydrogen evolution catalysts for hydrobromic acid electrolysis., Langmuir. 29 (2013) 480–492. doi:10.1021/la3032489.

[4] R. Parsons, The rate of electrolytic hydrogen evolution and the heat of adsorption of hydrogen, Trans. Faraday Soc. 54 (1957) 1053–1063.

[5] B.E. Conway, J.O. Bockris, Electrolytic Hydrogen Evolution Kinetics and Its Relation to the Electronic and Adsorptive Properties of the Metal, J. Chem. Phys. 26 (1957) 532–541.

[6] S. Trasatti, Work Function, Electronegativity, and Electrochemical Behaviour of Metals III. Electrolytic Hydrogen Evolution in Acid Solutions, Electroanal. Chem. Interfacial Electrochem. 39 (1972) 163–184.

[7] J.K. Nørskov, T. Bligaard, A. Logadottir, J.R. Kitchin, J.G. Chen, S. Pandelov, et al., Trends in the Exchange Current for Hydrogen Evolution, J. Electrochem. Soc. 152 (2005) J23. doi:10.1149/1.1856988.

[8] W. Schmickler, S. Trasatti, Comment on "Trends in the Exchange Current for Hydrogen Evolution" [J. Electrochem. Soc., 152, J23 (2005)], J. Electrochem. Soc. 153 (2006) L31. doi:10.1149/1.2358294.

[9] J.K. Nørskov, T. Bligaard, a. Logadottir, J.R. Kitchin, J.G. Chen, S. Pandelov, et al., Response to "Comment on 'Trends in the Exchange Current for Hydrogen Evolution' [J. Electrochem. Soc., 152, J23 (2005)]," J. Electrochem. Soc. 153 (2006) L33. doi:10.1149/1.2358292.

[10] L.A. Kibler, Hydrogen Electrocatalysis, ChemPhysChem. 7 (2006) 985–91. doi:10.1002/cphc.200500646.

[11] J. Greeley, J.K. Nørskov, L.A. Kibler, A.M. El-Aziz, D.M. Kolb, Hydrogen evolution over bimetallic systems: understanding the trends., ChemPhysChem. 7 (2006) 1032–5. doi:10.1002/cphc.200500663.

[12] B. Hinnemann, P.G. Moses, J. Bonde, K.P. Jørgensen, J.H. Nielsen, S. Horch, et al., Biomimetic hydrogen evolution: MoS2 nanoparticles as catalyst for hydrogen evolution., J. Am. Chem. Soc. 127 (2005) 5308–9. doi:10.1021/ja0504690.

[13] E. Santos, W. Schmickler, Electrocatalysis of hydrogen oxidation-theoretical foundations., Angew. Chem. Int. Ed. Engl. 46 (2007) 8262–5. doi:10.1002/anie.200702338.

[14] E. Santos, A. Lundin, K. Pötting, P. Quaino, W. Schmickler, Model for the electrocatalysis of hydrogen evolution, Phys. Rev. B. 79 (2009) 235436. doi:10.1103/PhysRevB.79.235436.

[15] M. Johansson, O. Lytken, I. Chorkendorff, The sticking probability for H2 on some transition metals at a hydrogen pressure of 1 bar., J. Chem. Phys. 128 (2008) 034706. doi:10.1063/1.2825296.

[16] E.M. Fiordaliso, S. Murphy, R.M. Nielsen, S. Dahl, I. Chorkendorff, H2 splitting on Pt, Ru and Rh nanoparticles supported on sputtered HOPG, Surf. Sci. 606 (2012) 263–272. doi:10.1016/j.susc.2011.10.004.

[17] J.O. Bockris, I.A. Ammar, A.K.M.S. Huq, The Mechanism of the Hydrogen Evolution Reaction on Platinum Silver and Tungsten Surfaces in Acid Solutions, J. Phys. Chem. 61 (1957) 879–886.

[18] A.T. Kuhn, P.M. Wright, The cathodic evolution of hydrogen on ruthenium and osmium electrodes, J. Electroanal. Chem. 27 (1970) 319–323.

[19] Z.A. Iofa, W. Pao-Ming, Effect of Adsorbed Halide Ions on the Electrochemical Reactions Occurring in the Corrosion of Cobalt in Acid Solutions, Zhurnal Fiz. Khimii. 37 (1963) 2300–2304.

[20] H.-M. Kuhne, H. Tributsch, Energetics and Dynamics of the Interface of RuS2 and Implications for Photoelectrolysis of water, J. Electroanal Chem. 201 (1986) 263–282.

[21] H. Colell, N. Alonso-Vante, H. Tributsch, Interfacial behaviour of semiconducting RuS2 electrodes : a kinetic approach, J. Electroanal. Chem. 324 (1992) 127–144.

[22] J. Bonde, P.G. Moses, T.F. Jaramillo, J.K. Nørskov, I. Chorkendorff, Hydrogen evolution on nano-particulate transition metal sulfides, Faraday Discuss. 140 (2008) 219–231. doi:10.1039/b814058h.

[23] E.J.M. Hensen, G.M.H.J. Lardinois, V.H.J. de Beer, J.A.R. van Veen, R.A. van Santen, Hydrogen – Deuterium Equilibration over Transition Metal Sulfide Catalysts : On the Synergetic Effect in CoMo Catalysts, J. Catal. 187 (1999) 95–108.

[24] J.M. Ziegelbauer, A.F. Gullá, C. O'Laoire, C. Urgeghe, R.J. Allen, S. Mukerjee, Chalcogenide electrocatalysts for oxygen-depolarized aqueous hydrochloric acid electrolysis, Electrochim. Acta. 52 (2007) 6282–6294. doi:10.1016/j.electacta.2007.04.048.

[25] H. Colell, N. Alonso-Vante, C. Fischer, P. Bogdanoff, S. Fiechter, H. Tributsch, Novel Semiconducting Ternary Compounds: IrxRu1-xS2 ($0.005 < x < 0.5$) for Oxygen Evolution Electrocatalysis, Electrochim. Acta. 39 (1994) 1607–1611.

VII. Investigation of the active sites of rhodium sulfide for hydrogen evolution/oxidation using carbon monoxide as a probe

Abstract

Carbon monoxide (CO) was observed to decrease the activity for hydrogen evolution, hydrogen oxidation and H_2-D_2 exchange on rhodium sulfide, platinum and rhodium metal. The temperature at which the CO was desorbed from the catalyst surface (detected by recovery in the H_2-D_2 exchange activity of the catalyst) was used as a descriptor for the CO binding energy to the active site. The differences in the CO desorption temperature between the different catalysts showed that the rhodium sulfide active site is not metallic rhodium. Using density functional theory the binding energy of CO to the Rh sites in rhodium sulfide is found comparable to the binding energy on Pt. Coupled with experiment this supports the proposition that rhodium rather than sulfur atoms in the rhodium sulfide are the active site for the hydrogen reaction. This would indicate the active site for hydrogen evolution/oxidation as well as oxygen reduction (determined by other groups using X-Ray Absorption Spectroscopy) may be the same.

A. Introduction

Electrical energy storage is necessary for adoption of time-varying wind or solar resources. Pumped hydroelectric and compressed air energy storage are the most widely used technologies, but both methods depend on geographical considerations and the number of available locations limit their ultimate capacity. To increase the capacity of electrical energy

storage for use in large scale deployment of intermittent renewable energy sources, other cost-effective technologies must be developed.

An H_2/Br_2 proton exchange membrane based electrochemical flow battery is a potential option for large-scale energy storage due its fast electrode kinetics (high efficiency) and the inherent advantage of flow cells over storage batteries which decouple energy and power density (due to external storage) [1,2]. In highly acidic H_2/Br_2 flow cells Rh_xS_y/C is the most active and stable hydrogen electrocatalyst [3], it is also stable in cells based on HCl/Cl_2 [4–8]. Traditional catalysts such as Rh and Pt are unstable due to crossover of the bromine or chlorine.

We wish to understand the active sites of the mixed phase Rh_xS_y/C catalyst, consisting of $Rh_{17}S_{15}$, Rh_2S_3 and Rh_3S_4, to further improve its activity and maximize the use of Rh. The active site for oxygen reduction on the mixed phase Rh_xS_y ($Rh_{17}S_{15}$, Rh_3S_4 and Rh_2S_3) has been determined to be on the Rh_3S_4 phase, specifically the cluster of Rh atoms in the Rh_3S_4 structure involving Rh-Rh clusters, determined using Synchrotron-based X-ray absorption spectroscopy [5,8]. It is possible this is the same active site for the HER/HOR (and by extension the H_2/D_2 exchange).

The active site of a catalyst can be investigated by selective poisoning while monitoring the catalyst activity. Carbon monoxide acts as a poison for HER and HOR on Pt/C. For platinum, there are two types of CO binding, linearly bonding and bridge bonding [9], which serve to block the adsorption of hydrogen that is required for HER/HOR. Similarly, CO adsorption can affect the H_2-D_2 exchange rate [10], a reaction which helps describe the surface chemistry rate for HER and HOR [11]. We expect that because sulfur is known to have an effect on how CO binds to metals such as Pt [12], Ru [13] and Rh, the CO binding to a metal sulfide will be different than the binding to a metal [14–17]. We studied

how carbon monoxide binds and changes HER and HOR activity and H_2-D_2 exchange on the rhodium sulfide catalysts compared to metals such as platinum and rhodium to help differentiate between the active sites and understand how those active sites may be formed preferentially to increase the activity of rhodium sulfide. The strength of CO binding on metal sulfides and metals can be determined through the use of temperature programmed desorption of CO [18], where the temperature of desorption is proportional to the binding strength of CO to the catalyst surface. The CO binding energy can also be calculated *ab initio* using density functional theory (DFT) on the different candidate active sites and compared to the experimental results to better understand the surface electrocatalytic activity.

The questions addressed in this work are:

1. How does the presence of carbon monoxide affect the H_2-D_2 exchange rate in the gas-phase on Rh_xS_y/C and how does this compare to electrochemical (aqueous) HER/HOR?
2. Does carbon monoxide bind to the active sites of Rh_xS_y/C for HER/HOR and decrease the activity in a similar manner to Pt/C?
3. What is the binding strength of CO to rhodium sulfide and how does it compare to platinum and rhodium metal?
4. What is the DFT-calculated binding strength of CO to selected phases of rhodium sulfide and can this be coupled with experiment to determine the active sites of the rhodium sulfide?

In brief, we see that CO poisons Rh_xS_y both in electrochemical and gas-phase measurements, and based on the binding strength to the active site, the metallic rhodium sites on the Rh_3S_4 phase are the most likely to be contributing to hydrogen evolution and oxidation.

B. Experimental

1. Electrocatalyst Preparation

Pt/C was purchased from E-Tek. A commercial Rh_xS_y/C designed for oxygen depolarized cathodes for hydrochloric acid electrolysis was purchased from BASF. The Rh_xS_y/C catalyst consists of $Rh_{17}S_{15}$, Rh_2S_3 and Rh_3S_4. Rh/C was purchased from Sigma-Aldrich. Rh_2S_3/C was synthesized by depositing 1M solution of $Rh(NO_3)_3$ on Vulcan XC-72R conductive carbon, then exposing it to H_2S at 400 °C for 1 hour in a horizontal tube furnace (ramp rate was 10 °C/min).

2. Preparation of Catalyst Inks

The carbon supported electrocatalysts (6 mg of catalyst per 1 mL solution, 35 µL 5 vol% Nafion) were ultrasonicated in a 1 mL solution of 1:1 water and isopropyl alcohol using Nafion as a binder to form an ink for the electrochemical measurements.

3. Electrodes for three-electrode electrochemical measurements

Rh_xS_y/C, Rh/C and Pt/C are loaded onto Toray carbon paper and used as electrodes (with a loading of 150 micrograms of catalyst per square centimeter). The reference electrode used was Ag/AgCl and the counter electrode was platinum mesh. The electrolyte was 0.1 M H_2SO_4. A Biologic potentiostat was used for electrochemical measurements. Carbon monoxide was bubbled into the electrolyte to test the effect of carbon monoxide on the electrochemical activity.

4. Fuel Cell Measurements

Fuel cell measurements were conducted on a fuel cell test station (Scribner Model 850C) using a 1 cm^2 active area cell. Membrane electrode assemblies (MEAs) were prepared using both Rh_xS_y/C and Pt/C as the anode catalyst, with a loading of 1 mg catalyst per cm^2. The cathode catalyst layer was 0.5 mg/cm^2 of Pt/C in both cases. Anode, cathode and cell

temperature were held at 65 °C with 15 psi of back pressure. H_2 and Air (Praxair) were supplied as fuel and oxidant at flow rates of 100 and 300 mL/minute, respectively. For the effect of CO, 1 mL of CO (Praxair) was injected into the anode H_2 stream (thus exposing it to the anode catalyst) and the effect on the current-voltage curve was monitored over several hours.

5. X-Ray Diffraction

X-Ray diffractograms were collected using an X'Pert powder diffractometer (PANalytical, Inc.) with a Cu Kα source (photon wavelength 1.54 Angstroms).

6. Gas-phase Hydrogen-Deuterium Exchange Rate

Hydrogen and deuterium (Praxair) are fed through glass float valves into a 6-mm-diameter quartz tube reactor with solid catalyst held in place by quartz wool. The tube was placed into a stainless steel heating-block whose temperature is controlled (Omega, CSC32). The block had two heating cartridges, two channels for air or cold nitrogen gas for cooling. The outlet of the reactor tube was connected to a differentially pumped mass spectrometer (Stanford Research Systems, Residual Gas Analyzer) through a leak valve. The amount of HD at the reactor outlet was measured to determine the rate of H_2-D_2 exchange.

The effect of carbon monoxide on the H_2-D_2 exchange activity was tested in three ways. First, carbon monoxide was injected as a pulse into the reactor with a syringe while inert gas was continuously flowed. The recovery of the activity as a function of time was evaluated by monitoring the time to return to 50% of the original HD exchange rate. Second, to test the effect of carbon monoxide exposure time on the time required for H_2-D_2 exchange rate recovery, CO was flowed over the catalyst for one hour instead of injected via a syringe. The time to recover activity was measured while only inert gas was flowed over the catalyst. No major changes in the recovery rate were seen for rhodium sulfide when comparing

continuous CO flow to a pulse injection. For the third method of examining the effect of CO on the catalyst surface, 1% CO in H_2 was used in the feed stream instead of pure H_2, while measuring the H_2-D_2 exchange rate as a function of temperature using the mass spectrometer.

7. Temperature Programmed Desorption of Carbon Monoxide

Carbon monoxide was adsorbed on the catalyst in a quartz tube reactor at room temperature for 12 hours (overnight). The temperature was then cooled in carbon monoxide using the outlet of a liquid nitrogen Dewar to -50 °C and then the reactor was flushed of carbon monoxide using a flow of argon. The temperature was then ramped to 150 °C. The effluent of the reactor was monitored by mass spectrometry for carbon monoxide, attributed to desorption of adsorbed carbon monoxide on the catalyst surface.

8. Infrared Measurements

Diffuse Reflectance Infrared Fourier Transform Spectroscopy (DRIFTS) measurements were done on a sample made by mixing the catalyst with potassium bromide (a ratio of 1:200 by weight was used). The powder was loaded into the Praying Mantis Diffuse Reflectance Accessory (Harrick Scientific) and the temperature was controlled with a heating element and cooled with ice water. The effect of preheating at 120 °C for 15 hours to remove water from the sample was tested and found not to improve the signal to noise ratio in the region of interest. A background spectrum was collected at a reduced (10 °C) temperature, then 10% CO in Ar was flown through the cell at room temperature using mass flow controllers, and later the sample was cooled to 10 °C and CO was flushed out by pure argon while spectra were taken. The FTIR spectrometer was a Nicolet 4700 (Thermo Electron Corporation).

9. Computational details

The theoretical calculations use density-functional theory (DFT) [19,20] with the generalized gradient approximation (GGA) functional of Perdew, Burke and Ernzerhof (PBE) [21]. The core-valence electron were taken into account via the projector-augmented-wave (PAW) method [22,23]. A plane wave basis set with a kinetic energy cutoff of 500 eV was used to construct Kohn-Sham wavefunctions. We include dipole correction to eliminate spurious interactions due to periodicity. When solving the spin-polarized Kohn-Sham equations, electronic relaxation stops when the total energy difference between iterations is less than 10^{-4} eV. The ionic relaxations were completed when the forces between atoms are less than 0.02 eV/Å. All calculations are performed using VASP simulation package.

For bulk calculations, 4x4x4 k-point grids are utilized for relaxation. The calculated lattice constants are slightly improved by using this grid and are comparable with the experimental results [24,25]: a=8.53Å, b=6.03Å and c=6.18Å for orthorhombic Rh_2S_3; a=10.45Å, b=10.86Å, c=6.29Å, and β=107.9° for monoclinic Rh_3S_4; and 9.98Å for cubic $Rh_{17}S_{15}$.

Although the surface structures and compositions of our samples are complicated, DFT simulations allow individual studies of sulfide surfaces, which could give insights to our proposed experimental studies. We have searched for surface models from different ways of cutting stoichiometric sulfide planes along different facets, and examined the surface formation energies (see Supporting Information: Table S1). In this joint study, we report the first-principles computed CO binding energies as well as the hydrogen adsorption free energies using the surface models having the lowest surface energy for each of the three Rh_xS_y compounds, i.e. Rh_2S_3, Rh_3S_4, and $Rh_{17}S_{15}$. These DFT studies aim for understanding a general trend of CO binding strength to these three compounds, based on the assumption that those facets with least surface energies are most likely to appear in the polycrystalline

material. While similar assumptions have been frequently made it is not clear that they are reliable.

It is also known that using PBE energy functional overestimates the chemisorption energy [26]. Here, the computed CO binding energies using the same PBE energy functional are utilized for understanding the trend of CO binding strengths on these considered surfaces.

C. Results and Discussion

1. Effect of Carbon Monoxide Poisoning on Electrochemical HER/HOR Activity

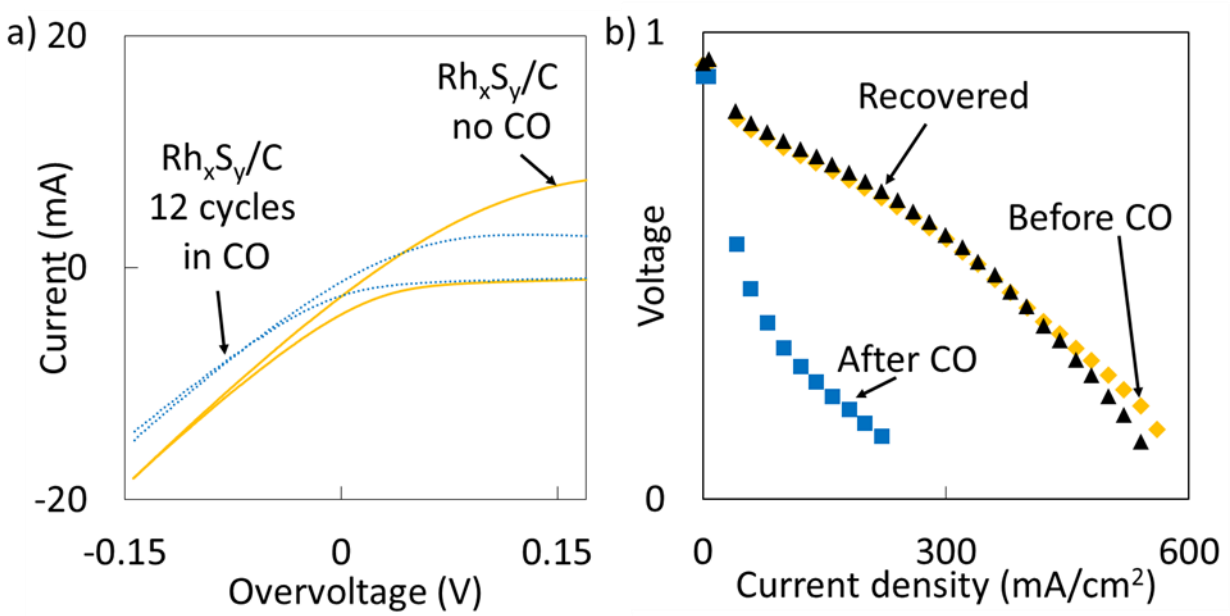

Figure 1. a) Cyclic voltammograms of Rh_xS_y/C loaded on conductive carbon Toray paper in 0.1 M H_2SO_4 with and without CO bubbled into the solution. During the measurement the activity continually dropped as the CO was bubbled through the solution. Rh/C and Pt/C shows similar behavior. b) Rh_xS_y/C used as an anode catalyst in a H_2/O_2 fuel cell, before and after exposure to CO in the H_2 feed (anode), then following recovery

The hydrogen evolution and hydrogen oxidation activity of Rh_xS_y/C is reduced by exposure to carbon monoxide in the electrolyte (Figure 1). The hydrogen oxidation activity appears more hindered than the hydrogen evolution upon addition of CO, which may be related to the surface coverage of CO changing as a function of potential, although further

investigation would be required to verify this. Thus, similar to Pt/C, it appears as if carbon monoxide binds to the active site of the Rh_xS_y catalyst, blocking sites from contributing to the HER/HOR reaction. The active site of the Rh_xS_y/C catalyst may be on any of the several available phases (see Figure S1 for XRD characterization of the Rh_xS_y/C catalyst as well as the catalyst shown to be mostly Rh_2S_3/C by XRD).

2. Effect of Carbon Monoxide Poisoning on H_2/D_2 Exchange on Rh_xS_y/C and Pt/C

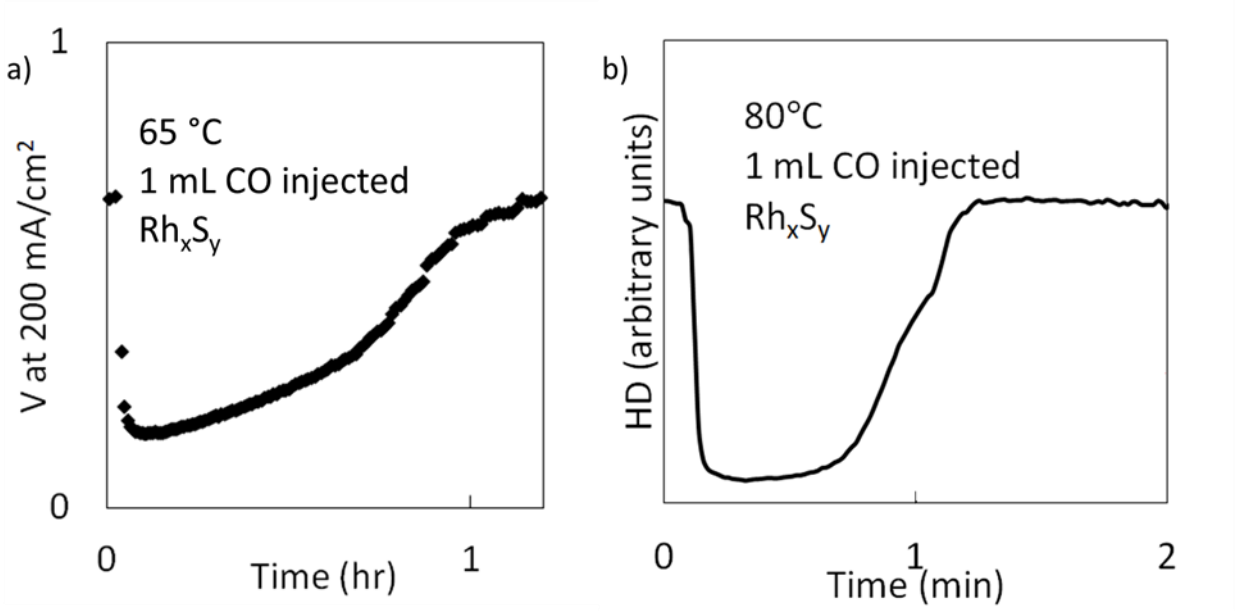

Figure 2. a) The voltage at 200 mA/cm^2 current density for the Rh_xS_y anode fuel cell, as a function of time, following a pulse of CO in the H_2 stream. Temperature was 65 °C. b) The H_2/D_2 exchange rate at 80 °C on Rh_xS_y/C, and the effect of the addition of a 1 mL pulse of CO (at time t = 0). The CO pulse affects the rate of H_2/D_2 exchange, but after the CO in the reactor gas-phase passes through, the rate of H_2/D_2 exchange begins to recover. The time required for the activity to recover to 50% of the initial activity is recorded, as a representation of the rate of recovery, likely due to desorption of CO adsorbed on the active sites during the CO pulse.

The activity of Rh_xS_y/C for hydrogen oxidation in a fuel cell as well as H_2-D_2 exchange in the gas-phase is reduced by exposure to carbon monoxide (Figure 2). This indicates that in both electrochemical and gas-phase systems carbon monoxide decreases the activity on rhodium sulfide, likely by adsorption on the active electrocatalytic sites, in a

similar manner to the effect of CO on Pt. With time, the H_2-D_2 exchange activity begins to recover, due to desorption of carbon monoxide from the active sites of rhodium sulfide. The rate of recovery of the activity can thus be related to the rate of desorption of carbon monoxide from the active sites of rhodium sulfide. To compare the effect of CO exposure time on the rate of recovery, the Rh_xS_y/C catalyst was exposed to CO for one hour (to ensure surface saturation). The rate of recovery of activity did not differ between the pulse and the one hour exposure indicating the surface is saturated with 1 mL pulse of CO.

3. Desorption Temperature of Carbon Monoxide from the Active Site of Rh_xS_y/C and Pt/C to Compare Binding Strengths

The time required for the recovery of H_2-D_2 exchange activity on Rh_xS_y/C and Pt/C (as CO desorbs from the surface) is inversely proportional to the temperature (Figure 3). From the rate of activity recovery, the relative binding strength of CO on the active sites can be determined. Since the desorption temperature of CO from Rh_xS_y/C is higher than Pt/C, it stands to reason that the binding strength of CO on the active site of Rh_xS_y/C is higher (or comparable) to that on Pt/C.

The desorption temperature of CO from rhodium sulfide, as detected by mass spectrometry in the absence of H_2-D_2, (30-50 °C, Figure S2) matches the temperature at which the activity of rhodium sulfide recovers following the pulse of carbon monoxide (Figure 3). This finding further supports desorption of carbon monoxide as the reason for the recovery of the H_2-D_2 exchange activity on the rhodium sulfide.

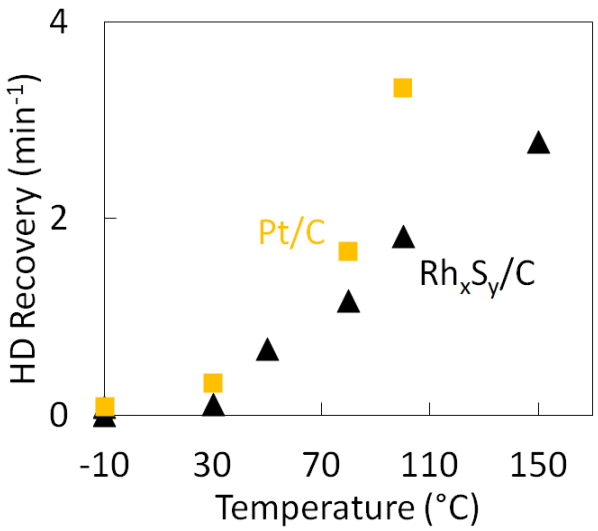

Figure 3. The rate (described simplistically as the inverse of time for Rh_xS_y/C and Pt/C catalyst to recover to 50% of the initial activity after exposure to CO) of CO desorption as a function of temperature. This gives information on the thermal energy required for desorption of carbon monoxide from the active sites of the catalyst, which is related to the binding strength of the CO to the catalyst.

The higher binding energy of CO to Rh_xS_y/C than Pt/C is corroborated by the higher temperature required for Rh_xS_y than for Pt or Rh to begin HD formation from H_2-D_2 in the presence of a continuous partial pressure of CO (Figure 4).

The increase in HD formation, Figure 4, is due to the desorption of the CO from the active sites. We know this because at very low temperatures, in the absence of CO, the HD reaches equilibrium conversion for Rh/C, Pt/C and Rh_xS_y/C. There is an initial match in the Rh/C and Rh_xS_y/C HD response below 100 °C, which may be due to small amounts of Rh metal in the Rh_xS_y/C catalyst, not detectable by XRD. The exposure at high temperatures to H_2/D_2/CO mixtures did not appear to have an effect on the activity of the Rh_xS_y catalyst (Figure S3). The Rh_2S_3/C catalyst desorbed CO at higher temperatures than the Rh_xS_y/C catalyst, indicating a difference in the Rh_xS_y/C and Rh_2S_3/C catalyst; likely due to the different surfaces binding sites.

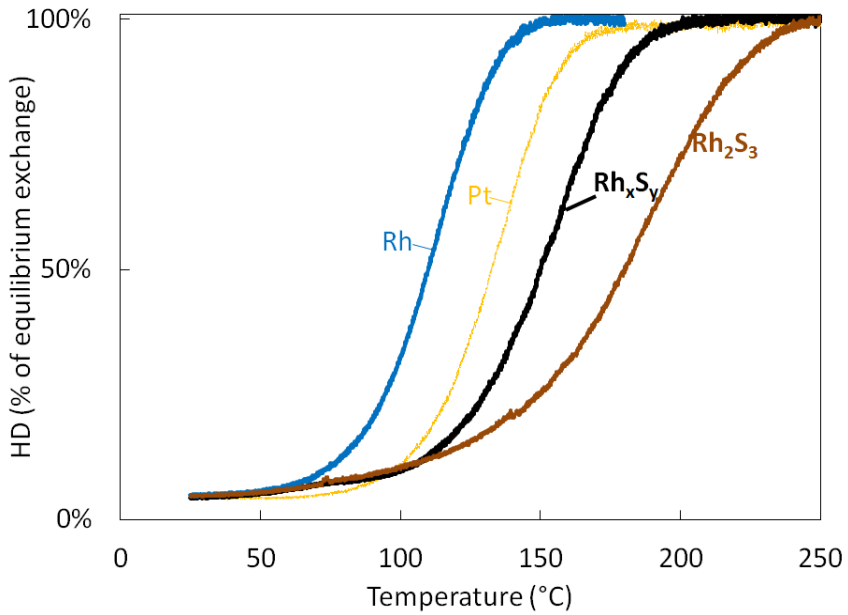

Figure 4. H_2-D_2 exchange in the presence of 1% CO as a function of temperature. The feed was 1% CO in H_2 with D_2. The HD signal measured by mass spectrometer was normalized to the equilibrium H_2-D_2 exchange. The catalysts indicated (Rh, Pt, Rh_xS_y, Rh_2S_3) are all supported on carbon.

4. Vibrational Spectra of Carbon Monoxide Adsorbed on Rh_xS_y/C and Pt/C

The rhodium sulfide sample showed less resolution of the absorption peaks than platinum; however, there were reproducible absorptions observed at ~2035 cm^{-1} and 2090 cm^{-1} after exposure to CO (Figure 5). These stretches match a gem-dicarbonyl binding seen in the literature for rhodium exposed to sulfur [15]. The Pt/C sample showed a much more defined absorption peak at 2067 cm^{-1}, possibly corresponding to linear CO. It is possible that this binding of carbon monoxide is blocking the active sites for hydrogen evolution, and that desorption of this carbon monoxide results in the observed increase in activity. The temperature at which the carbon monoxide begins desorbing, resulting in a recovery of activity (begins recovery at 30 °C for Pt, 30-50 °C for Rh_xS_y) does not match the temperature at which the vibrational spectra of adsorbed CO disappear (~100 °C for Pt and Rh_xS_y), indicating that there may be CO bound to both the catalyst active site and non-active sites.

When CO desorbs from the active site (at temperatures below ~100 °C), the H_2-D_2 exchange activity (Figure 3) recovers, however there may still be adsorbed CO on the non-active sites, which may appear in the DRIFTS measurement.

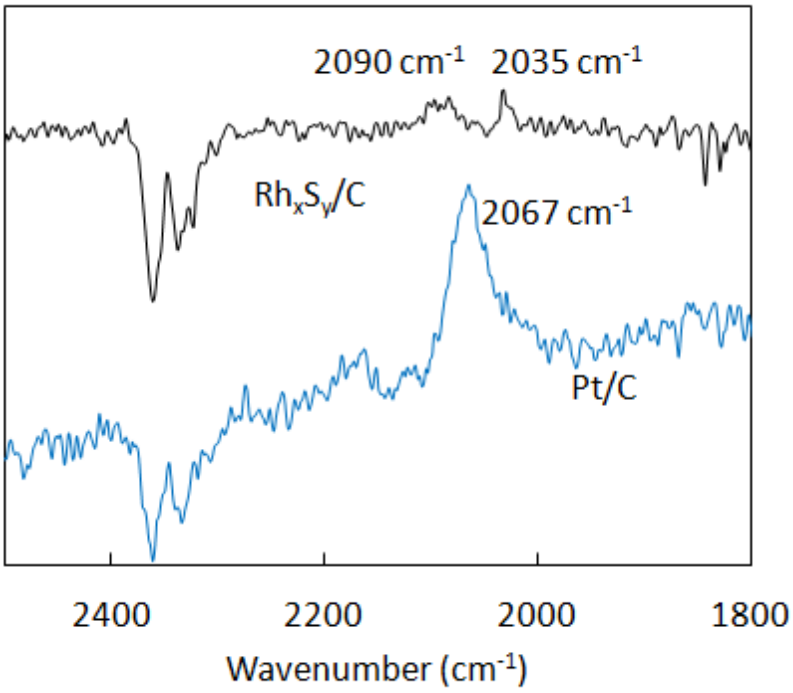

Figure 5. DRIFTS of CO adsorbed on the Rh_xS_y/C and Pt/C (samples were mixed with KBr to increase signal to noise). Background was subtracted. Spectra taken at 10 °C after 2 hour CO adsorption step at room temperature under 10% CO flow in argon.

The infrared vibration spectra of adsorbed CO has previously been shown to be different on sulfided compared to unsulfided rhodium [14–17]. On Rh/SiO_2, linear CO (2073 cm^{-1}), bridged CO (1898 cm^{-1}), symmetrical (2104 cm^{-1}) and asymmetrical (2037 cm^{-1}) C-O stretching of the gem dicarbonyl are seen, while linearly adsorbed CO (2090 cm^{-1}) and weakly adsorbed CO (2029 cm^{-1} and 2005 cm^{-1}) are seen on the sulfided rhodium catalyst [14]. Adsorbed sulfur on rhodium inhibits chemisorption of bridging CO (1912 cm^{-1}), but not symmetrical and antisymmetrical (2090 cm^{-1} and 2037 cm^{-1}) germinal carbonyl species, along with linear CO (2068 cm^{-1}) [15]. Sulfided rhodium has terminally bonded CO

on Rh^0 or Rh^{1+} (2071 cm^{-1}) and CO bridge bonded to two Rh^0 sites (1882 cm^{-1}) [16]. Rh/SiO_2 has linearly adsorbed CO (2070 cm^{-1}), bridged CO (1894 cm^{-1}), symmetrical (2102 cm^{-1}) and asymmetrical (2036 cm^{-1}) gem-dicarbonyl, while sulfided Rh/SiO_2 has linear CO bonds (2073 cm^{-1}) weak bridged CO (1873 cm^{-1}), asymmetric gem-dicarbonyl (2031 cm^{-1}) and symmetric gem-dicarbonyl and a linear CO adsorbed on Rh^+ (2095 cm^{-1}). The higher wavenumbers for CO are known to be seen for Rh^+ compared to Rh^0 [17].

5. Calculated CO Binding Energy and Vibrational Spectra of Carbon Monoxide on the Rh_2S_3 (001), Rh_3S_4 (100) and $Rh_{17}S_{15}$ (100) Surfaces

All calculations are subject to the periodic boundary condition with vacuum space larger than 13Å and the atomic positions in the bottom layer are fixed to their bulk positions. The 2x2x1 k-point grids are chosen to sample the Brillouin.

Rh_2S_3 is a small gap material. Our bulk calculations found a gap around 0.2eV [25,27]. The electronic structure of a 2x2x3 Rh_2S_3 (001) slab (See Figure 6a and Figure S4 in the Supporting Information) is that of a semiconductor. All surface Rh sites (denoted as M) are 5-coordinated (while six in bulk). There are two kinds of surface sulfur atoms (labeled as S1 and S2 in Figure 6a): S1 is three coordinated while S2 is four coordinated (as in the bulk). One expects that the more highly coordinated S2 sites would be less active chemically.

The surface structures of a 2x1x2 Rh_3S_4 (100) slab shown in Figure 6b can be partitioned by two regions (see the top view of Figure 6b): the region containing Rh_6 and the other region formed by octahedral RhS_6. Each Rh_6 unit provides surface metal sites forming as a triangular 3Rh (labeled as two M1 sites and one M2 site). The Rh-Rh bond lengths are 2.97Å and 3.32Å between M1-M2 sites and M1-M1' sites respectively. The surface has four non-equivalent surface sulfur sites indicated as S1, S2, S3 and S4 (see Figure 6b). The S1,

S2 and S3 atoms are under-coordinated by three (the full-coordination in the bulk is six), they bind to zero, one or two surface Rh atoms respectively. The S4 sulfurs have higher coordination than the others, and the calculations found that they adsorb CO or H_2 more weakly.

The 1x1x2 $Rh_{17}S_{15}$ (100) slab consists of two atomic layers where each layer the cage structure formed by Rh atoms (see Figure 6c) [25,28]. When the (100) facet is formed, the Rh_8 cubes in bulk [5] are truncated leaving a Rh_4 square on the surface. The atoms in the square are denoted by M1. The Rh-Rh distance between the M1 atoms is 2.76Å which is shorter than in the bulk where it is 2.85Å. The other nonequivalent surface metal site denoted as M2 in Figure 6c is cut from RhS_4 chains in bulk. The M2 site is 5-coordined missing one metal atom (as compare to the bulk), and the distance between M2 and the Rh underneath is 2.59Å which is also slightly shortened when comparing with 2.61Å in bulk. There are four M1 sites and one M2 site per supercell. The surface sulfurs labeled S1 are bound to 4Rh to form a square pyramid outward from the cage structure. The sulfur labeled S2 belongs to RhS_4 chain. There are four S1 and two S2 sites per supercell.

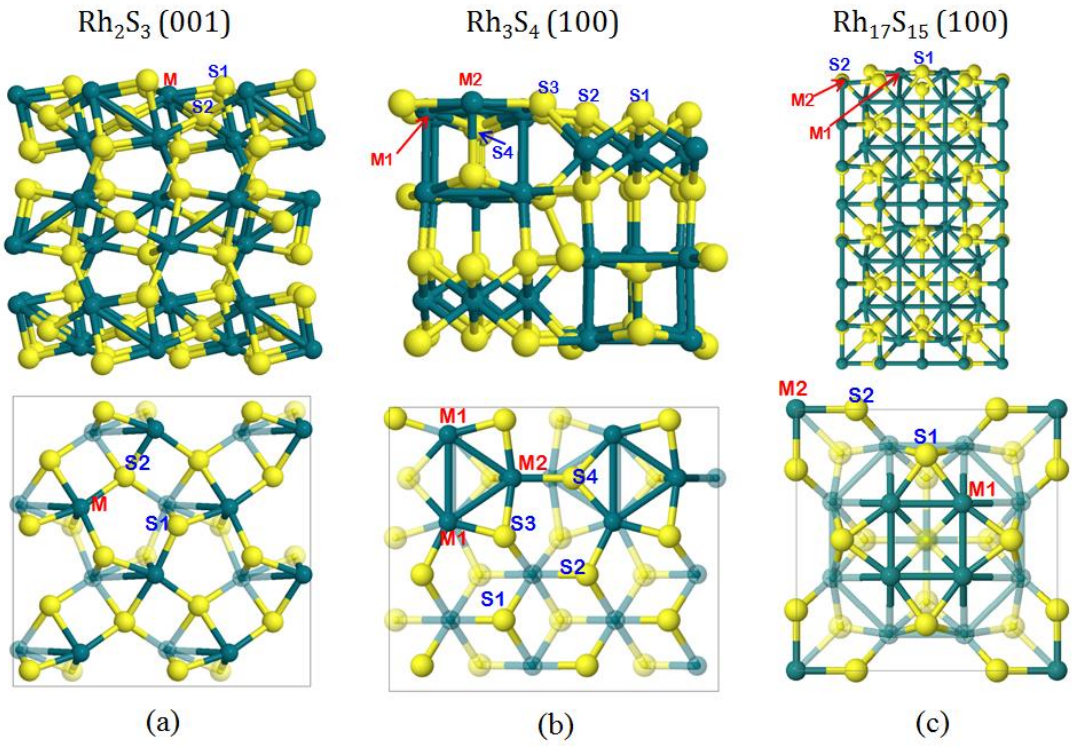

Figure 6. Side (upper) and top (lower) views of slab models: (a) Rh_2S_3 (001), (b) Rh_3S_4 (100) and (c) $Rh_{17}S_{15}$ (100) surfaces. Sulfur atoms are represented by yellow spheres and rhodium metal atoms by teal spheres.

We computed the CO binding strength to the surfaces according to the following equation:

$$E_{CO*} = E(CO/slab) - E(slab) - E(CO_{(g)}). \quad (1)$$

The CO binding geometries are summarized in Figure 7. The HER descriptor [29], is the hydrogen adsorption free energy ΔG_{H*} at standard conditions with the contribution from configuration entropy neglected. W calculated ΔG_{H*} using the methodology described in our previous work [3]. The computational results are given in Table 1.

The Rh_2S_3 (001) surface is likely inactive to hydrogen adsorption as the calculated ΔG_{H*} is uphill by ΔG_{H*}= +0.32 eV on the Rh sites and ΔG_{H*}= +0.43 eV on the sulfur sites (Table 1). Although both Rh_3S_4 (100) and $Rh_{17}S_{15}$ (100) surfaces have a metallic character (see Figure S4), their ability to bind hydrogen is significantly different. Hydrogen does not

bind to the $Rh_{17}S_{15}$ (100) surface, while the Rh_3S_4 (100) surface is reactive to hydrogen. In addition, on the Rh_3S_4 (100) surface, hydrogen tends to bind on sulfur more strongly than on rhodium. The interesting adsorption metal site is the hollow site (see the equivalent adsorption geometry in Figure 7m_b-h), which provides a thermodynamically allowed site to adsorb hydrogen with a rather weak adsorption free energy of ΔG_{H^*}= -0.08eV. Nevertheless, our DFT results could not exclude the S1 and S2 sulfur sites (see the equivalent adsorption geometries in Figure 7s_b1 and 7s_b2) from potential active HER sites.

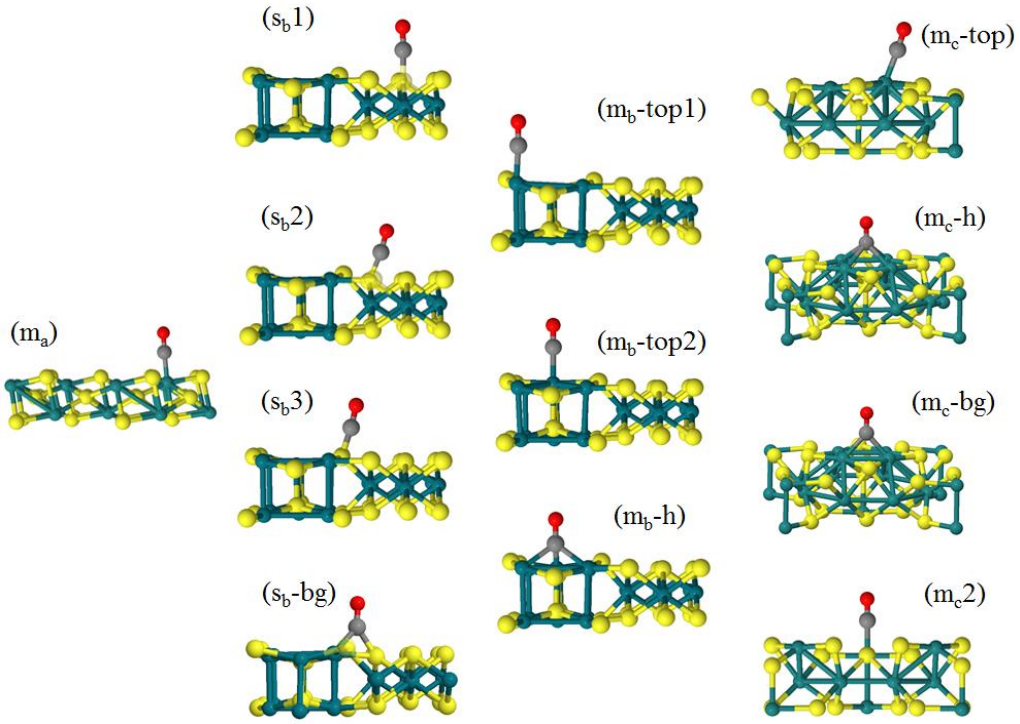

Figure 7. Summary of CO adsorption geometries. (s_x) and (m_x) denotes sulfur and rhodium metal sites respectively, with the subscript x denoting surface models. i.e. (a) for the Rh_2S_3 (001) surface, (b) for the Rh_3S_4 (100) surface and (c) for the $Rh_{17}S_{15}$ (100) surface. Sulfur atoms are represented by yellow spheres, rhodium metal atoms by teal spheres, carbon atoms by gray spheres and oxygen atoms by red spheres.

Comparing the CO binding strength onto the Rh and the sulfur sites of these three rhodium sulfide surfaces, our calculations suggest that CO binds much more strongly (magnitude >1eV) to the Rh sites than to the S sites (see Table 1). This could be understood

by stronger binding interaction of *d*-π* (Rh-CO) than that of π-π* (S-CO) electron. The adsorption sites such as the hollow sites are likely blocked by CO, and this likely explains the reduced HER current shown in Figure 1 or the reduced H_2-D_2 exchange seen in Figure 2.

Table 1. DFT calculations of CO binding energies (see equation (1)) and hydrogen adsorption free energies (in eV) on the Rh_2S_3 (001), Rh_3S_4 (100), and $Rh_{17}S_{15}$ (100) surfaces in Figure 6.

	Rh_2S_3 (001)		Rh_3S_4 (100)				$Rh_{17}S_{15}$ (100)			
	S site	Rh site	S site		Rh site		S site		Rh site	
CO binding energy (eV) of $CO_{(g)} + * \rightarrow CO*$	unstable	**–1.95**	(1) (2) (3) (bridge)	+0.22 –0.01 +0.23 –0.73	(top1) (top2) (h)	–1.01 –1.00 **–1.31**	(1) (2)	unstable unstable	(top) (h) (bridge) (2)	**–1.23** –0.67 –0.99 –0.62
Adsorption free energy (eV) of $½\ H_{2(g)} + * \rightarrow H*$	+0.32	+0.43	(1) (2) (3) (bridge)	**–0.11** **–0.09** –0.26 unstable	(top1) (top2) (h)	+0.76 +0.63 **–0.08**	(1) (2)	+0.6 +0.18	(top) (h) (bridge) (2)	unstable unstable +0.23 +0.7

To see how the presence of CO on the surface influences hydrogen adsorption on the Rh_3S_4 (100) surface, we further examined hydrogen adsorption onto the surface with pre-adsorbed CO. The slab model of (m_b-h) in Figure 7 with the strongest CO binding to the surface is chosen to illustrate this effect. The ΔG_{H^*}s calculated according to the reaction $½H_{2(g)}$ + $CO/Rh_3S_4 \rightarrow H/CO/Rh_3S_4$ are –0.10eV, –0.16eV and –0.14eV for hydrogen adsorbed at the (s_b1), (s_b2) and (s_b3) sites respectively. The adsorption of CO onto the Rh_3S_4 (100) surface weakens the hydrogen adsorption energy by 0.1eV at the (s_b3) site, while this change seems not to alter the nature of rather large ΔG_{H^*} at this site. Our results also show a relatively small effect on hydrogen adsorption at the other two sulfur sites (see (s_b1) and (s_b2) in Figure 7) with the presence of CO on the Rh_3S_4 (100) surface.

To compute the C-O stretching frequency, we used the method of central differences for determining the dynamic matrix under the harmonic approximation. The displacements

of ±0.02Å are applied for C and O atoms from their equilibrium positions in each direction. Table 2 presents the main C-O stretching modes associated with metal adsorption sites. The equilibrium bond lengths of Rh-C (l_{Rh-C}) and C-O (l_{C-O}) are listed in Table 2. Although the binding energy of CO on Rh_2S_3 is the strongest among the rhodium surface models considered, the C-O bond length (1.157Å and with 2039 cm^{-1} vibrational frequency) is very close to that of CO in gas phase (1.159Å and with 2090 cm^{-1} vibrational frequency from DFT calculations). On the other hand, the C-O bond lengths of adsorbed CO on the Rh_3S_4 and $Rh_{17}S_{15}$ surfaces are longer (>1.7 Å) indicating that the vibrational motions are influenced by adsorption to the surface. The calculated C-O stretching frequency is lower than that on the Rh_2S_3 surface.

At lower temperature, the surfaces adsorb more CO. We examined the C-O vibrations at high coverage (uniformly distributed COs on Rh_2S_3 (001) surfaces, and non-uniform CO configurations on Rh_3S_4 and $Rh_{17}S_{15}$ surfaces, see Figure S5 and Table S2). The C-O stretching of adsorbed CO on Rh_2S_3 surface changes little when increasing CO coverage (2039 cm^{-1} vs. 2041 cm^{-1}). On the Rh_3S_4 and $Rh_{17}S_{15}$ surfaces, the change in coverage affects the collective, low frequency C-O vibrational modes (involving non-vertical displacements of C and O, see Table S2).

While the accuracy of DFT-based computational method on molecular vibrational frequency had been studied carefully [30], in this study we rely on the computed frequency shifts. Since the observed absorptions in the vibrational spectra at low temperature (2035 cm^{-1} and 2090 cm^{-1}) are likely from the C-O vibration modes on top sites of the different sulfide phases, our DFT results suggest that the observed C-O frequencies shift of approximately 50 cm^{-1} is in good agreement with the computed frequencies from CO on the top site geometries, i.e. 2039 cm^{-1}, 2001 cm^{-1}, and 1982 cm^{-1} on the Rh_2S_3, Rh_3S_4, and

$Rh_{17}S_{15}$ surfaces respectively. Supported with computed binding energy of CO, the adsorption of CO on the Rh_2S_3 phase is highly feasible.

Table 2. Calculated C-O vibrational frequencies, Rh-C ($\boldsymbol{l_{Rh\text{-}C}}$) and C-O ($\boldsymbol{l_{C\text{-}O}}$) bond lengths on Rh_2S_3 (001), Rh_3S_4 (100) and $Rh_{17}S_{15}$ (100) surfaces.

Surfaces	Metal sites	$l_{Rh\text{-}C}$ and $l_{C\text{-}O}$
Rh_2S_3 (001)	2039	1.879, 1.157
Rh_3S_4 (100)	(top1) 2001	1.875, 1.173
	(top2) 1990	1.872, 1.174
	(h) 1862	(2.15,2.09,2.09), 1.21
$Rh_{17}S_{15}$ (100)	(top) 1982	1.898,1.175
	(h) 1713	2.285,1.21
	(bridge) 1872	2.01,1.197
	(2) 1994	1.888,1.172

D. Conclusions

Experiments performed with a mixture of the three sulfides show that CO poisons both the H_2-D_2 exchange reaction and the electrochemical hydrogen evolution reaction. The free energy for dissociative adsorption of H_2 is negative (reaction is exoergic) only on Rh_3S_4(100); it is positive on Rh_2S_3(001) and $Rh_{17}S_{15}$(100) (reaction is exoergic). The free energy diagram for $H_2 \rightarrow H^+$ has an uphill intermediate state (H adsorbed on the surface) in the case Rh_2S_3(001) and $Rh_{17}S_{15}$(100) at zero potential. In the case of Rh_3S_4 the free energy of the intermediate state is close to zero for the adsorption of H on the hollow site at the center of the cluster of six Rh atoms (three on the surface and three in the layer below). The CO adsorbs preferentially on a surface metal site for all three sulfides. The binding energy is strongest on Rh_2S_3. The most interesting case is that of Rh_3S_4 which is the most likely the most active for HER. On this surface CO binds more strongly than hydrogen to the Rh cluster on which the H_2 dissociates. Therefore we conclude that CO poisoning takes place primarily by CO adsorption on the Rh atoms of the Rh_3S_4 surface.

Acknowledgements

N.S. is supported by a Fellowship from the ConvEne IGERT Program (NSF-DGE 0801627). Financial support was by the National Science Foundation (EFRI-1038234) and the Department of Energy, Office of Science, Office of Basic Energy Sciences DE-FG03-89ER14048.

References

[1] G.H. Schuetz, P.J. Fiebelmann, Electrolysis of Hydrobromic Acid, Int. J. Hydrogen Energy. 5 (1980) 305–316.

[2] R.S. Yeo, D.-T. Chin, A Hydrogen-Bromine Cell for Energy Storage Applications, J. Electrochem. Soc. 127 (1980) 549–555.

[3] A. Ivanovskaya, N. Singh, R.-F. Liu, H. Kreutzer, J. Baltrusaitis, T. Van Nguyen, et al., Transition metal sulfide hydrogen evolution catalysts for hydrobromic acid electrolysis., Langmuir. 29 (2013) 480–492. doi:10.1021/la3032489.

[4] A.F. Gullá, L. Gancs, R.J. Allen, S. Mukerjee, Carbon-supported low-loading rhodium sulfide electrocatalysts for oxygen depolarized cathode applications, Appl. Catal. A Gen. 326 (2007) 227–235. doi:10.1016/j.apcata.2007.04.013.

[5] J.M. Ziegelbauer, D. Gatewood, A.F. Gullá, M.J. Guinel, F. Ernst, D.E. Ramaker, et al., Fundamental Investigation of Oxygen Reduction Reaction on Rhodium Sulfide-Based Chalcogenides, J. Phys. Chem. C. 113 (2009) 6955–6968.

[6] J. Ziegelbauer, V. Murthi, C. Olaoire, A. Gullá, S. Mukerjee, Electrochemical kinetics and X-ray absorption spectroscopy investigations of select chalcogenide electrocatalysts for oxygen reduction reaction applications, Electrochim. Acta. 53 (2008) 5587–5596. doi:10.1016/j.electacta.2008.02.091.

[7] J.M. Ziegelbauer, A.F. Gullá, C. O'Laoire, C. Urgeghe, R.J. Allen, S. Mukerjee, Chalcogenide electrocatalysts for oxygen-depolarized aqueous hydrochloric acid electrolysis, Electrochim. Acta. 52 (2007) 6282–6294. doi:10.1016/j.electacta.2007.04.048.

[8] J.M. Ziegelbauer, D. Gatewood, S. Mukerjee, D.E. Ramaker, In Situ X-ray Absorption Spectroscopy Studies Of Water Activation On Novel Electrocatalysts For Oxygen Reduction Reaction In Acid Electrolyte, ECS Trans. 1 (2006) 119–128.

[9] Q. Li, R. He, J.-A. Gao, J.O. Jensen, N.J. Bjerrum, The CO Poisoning Effect in PEMFCs Operational at Temperatures up to 200°C, J. Electrochem. Soc. 150 (2003) A1599. doi:10.1149/1.1619984.

[10] M. Johansson, O. Lytken, I. Chorkendorff, The sticking probability for H2 in presence of CO on some transition metals at a hydrogen pressure of 1 bar, Surf. Sci. 602 (2008) 1863–1870. doi:10.1016/j.susc.2008.03.025.

[11] E.M. Fiordaliso, S. Murphy, R.M. Nielsen, S. Dahl, I. Chorkendorff, H2 splitting on Pt, Ru and Rh nanoparticles supported on sputtered HOPG, Surf. Sci. 606 (2012) 263–272. doi:10.1016/j.susc.2011.10.004.

[12] M.A. Mattox, M.W. Henney, A. Johnson, S. Zou, Adsorption and Electrooxidation of Carbon Monoxide on Platinum Surfaces Modified with Sulfur, J. Electrochem. 18 (2012) 16–19.

[13] C.R. Zhang H, Verde-Gomez Y., Jacobson A., Ramirez A., Preparation and Characterization of Metal Sulfide Electro-catalysts for PEM Fuel Cells, Mater. Res. Soc. Symp. Proc. 756 (2003) FF5.7.1–FF5.7.6.

[14] S.S.C. Chuang, S.I. Pien, Infrared Study of the CO Insertion Reaction on Reduced, Oxidized, and Sulfided Rh/SiO2 Catalysts, J. Catal. 135 (1992) 618–634.

[15] Y. Konishi, M. Ichikawa, W.M.H. Sachtler, Hydrogenation and Hydroformylation with Supported Rhodium Catalysts. Effect of Adsorbed Sulfur, J. Phys. Chem. 91 (1987) 6286–6291.

[16] P. Mills, D.C. Phillips, B.P. Woodruff, R. Main, M.E. Bussell, Investigation of the Adsorption and Reactions of Thiophene on Sulfided Cu, Mo, and Rh Catalysts †, J. Phys. Chem. B. 104 (2000) 3237–3249. doi:10.1021/jp993299k.

[17] G. Srinivas, S.S.C. Chuang, An in-Situ Infrared Study of the Formation of n- and iso-Butyraldehyde from Propylene Hydroformylation on Rh/SiO2 and Sulfided Rh/SiO2, J. Catal. 144 (1993) 131–147.

[18] K. Foger, J.R. Anderson, Temperature programmed desorption of carbon monoxide adsorbed on supported platinum catalysts, Appl. Surf. Sci. 2 (1979) 335–351.

[19] P. Hohenberg, W. Kohn, Inhomogeneous Electron Gas, Phys. Rev. 136 (1964).

[20] W. Kohn, L.J. Sham, Self-Consistent Equations Including Exchange and Correlation Effects, Phys. Rev. 140 (1965) A1133–A1138.

[21] J. Perdew, K. Burke, M. Ernzerhof, Generalized Gradient Approximation Made Simple., Phys. Rev. Lett. 77 (1996) 3865–3868. http://www.ncbi.nlm.nih.gov/pubmed/10062328.

[22] P.E. Blöchl, Projector augmented-wave method, Phys. Rev. B. 50 (1994) 17953–17979.

[23] G. Kresse, D. Joubert, From ultrasoft pseudopotentials to the projector augmented-wave method, 59 (1999) 11–19.

[24] E. Parthé, E. Hohnke, F. Hulliger, A new structure type with octahedron pairs for Rh2S3 , Rh2Se3 and Ir2S3, Acta Crystallogr. 23 (1967) 832–840. doi:10.1107/S0365110X67003767.

[25] O. Diéguez, First-principles characterization of the structure and electronic structure of α-S and Rh-S chalcogenides, Phys. Rev. B. 80 (2009) 1–6. doi:10.1103/PhysRevB.80.214115.

[26] B. Hammer, L. Hansen, J. Nørskov, Improved adsorption energetics within density-functional theory using revised Perdew-Burke-Ernzerhof functionals, Phys. Rev. B. 59 (1999) 7413–7421. doi:10.1103/PhysRevB.59.7413.

[27] P. Raybaud, J. Hafner, G. Kresse, H. Toulhoat, Ab initio density functional studies of transition-metal sulphides : II . Electronic structure, J. Phys. Condens. Matter. 9 (1997) 11107.

[28] H.R. Naren, A. Tamizhavel, S. Ramakrishnan, A.K. Nigam, Strongly correlated superconductivity in Rh17S15, J. Phys. Conf. Ser. 150 (2009) 052184. doi:10.1088/1742-6596/150/5/052184.

[29] R. Parsons, The rate of electrolytic hydrogen evolution and the heat of adsorption of hydrogen, Trans. Faraday Soc. 54 (1957) 1053–1063.

[30] A.P. Scott, L. Radom, Harmonic Vibrational Frequencies: An Evaluation of Hartree - Fock, Møller - Plesset, Quadratic Configuration Interaction, Density Functional Theory, and Semiempirical Scale Factors, J. Phys. Chem. 100 (1996) 16502–16513.

VIII. Investigation of the Electrocatalytic Activity of Rhodium Sulfide for Hydrogen Evolution and Hydrogen Oxidation

Reprinted from Electrochimica Acta, 145, N. Singh, J. Hiller, H. Metiu, E. McFarland, Investigation of the Electrocatalytic Activity of Rhodium Sulfide for Hydrogen Evolution and Hydrogen Oxidation, 224-230, Copyright 2014, with permission from Elsevier.

Abstract

We report the synthesis of unsupported and carbon-supported, mixed phase, rhodium sulfide, using both a hydrogen sulfide source and a solid sulfur source. Samples with several different distributions of rhodium sulfide phases (Rh_2S_3, $Rh_{17}S_{15}$, RhS_2 and metallic Rh) were obtained by varying the temperature and exposure time to H_2S or sulfur to rhodium ratio when using solid sulfur. Samples were characterized by X-ray diffraction (XRD), and the unsupported rhodium sulfide compounds studied using Raman spectroscopy to link Raman spectra to catalyst phases. The electrocatalytic activity of the rhodium sulfide compounds for hydrogen evolution and oxidation was measured using rotating disk electrode measurements in acidic conditions to simulate use in a flow cell. The most active phases for hydrogen evolution were found to be Rh_3S_4 and $Rh_{17}S_{15}$ (-0.34V vs. Ag/AgCl required for 20 mA/cm^2), while Rh_2S_3 and RhS_2 phases were relatively inactive (-0.46 V vs. Ag/AgCl required for 20 mA/cm^2 using RhS_2/C). The hydrogen oxidation activity of all rhodium sulfide phases is significantly lower than the hydrogen evolution activity and is not associated with conductivity limitations.

A. Introduction

Cost-effective electrical energy storage is important for matching power production to power utilization and to optimize the use of time varying renewable resources. Flow batteries have the potential to be among the lowest cost alternatives [1,2]. The H_2-Br_2 flow battery has the advantages of lower overpotentials than many other flow cell systems, a high power density, a high energy density, and relatively high reliability [3–5].

The H_2-Br_2 cell consists of a hydrogen half reaction:

1) $2H^+ + 2\ e^- \leftrightarrow H_2$ 0.0 V vs. RHE

and a bromine half reaction:

2) $2Br^- \leftrightarrow Br_2 + 2e^-$ 1.09 V vs. RHE

A proton-conducting membrane separates the hydrogen electrode from the bromine electrode and allows transport of the protons involved in the hydrogen reaction. The bromine electrode reaction proceeds rapidly on carbon without a metal catalyst [5,6]. The hydrogen electrode reactions, however, require a catalyst for the hydrogen evolution reaction (HER) during charge and the hydrogen oxidation reaction (HOR) during discharge. For the H_2-Br_2 cell, the hydrogen electrocatalyst must be stable in the presence of bromide and bromine. Nanoparticulate metals such as platinum supported on carbon, though initially active [7,8], are subject to corrosion or deactivation due to bromine/bromide crossover through the membrane [6] .

Metal sulfides supported on carbon including rhodium sulfide (Rh_xS_y/C), are used commercially as oxygen depolarized cathodes in HCl [9–13]. These materials are also active as HER/HOR catalysts and are more stable than Pt/C, even in the corrosive HBr/Br_2 electrolyte [6,14,15]. However, the activity for HOR of rhodium sulfide is low compared to

the activity for HER, even in the absence of bromide ions [6,14], unlike platinum, which is equally active for both hydrogen evolution and oxidation, until bromide/bromine crossover occurs [6]. For the H_2-Br_2 flow cell to operate reliably at high efficiency, the HOR activity of the stable Rh_xS_y/C must be understood and improved.

One possible explanation for the low HOR activity of the multi-phase rhodium sulfide is its conductivity. Semiconductor electrodes in the absence of illumination can be poor bi-directional conductors due to the lack of mobile charge carriers. For example, an n-type semiconductor (such as RuS_2) may be capable of reduction reactions under forward bias, but hindered for oxidation reactions under reverse bias [16,17]. The rhodium sulfide catalyst consists of several phases ($Rh_{17}S_{15}$,Rh_2S_3 and Rh_3S_4) [10], with $Rh_{17}S_{15}$ and Rh_3S_4 being reported as conducting semi-metals [18,19], and Rh_2S_3 reported as a true semiconductor [10,20–23]. The low hydrogen oxidation activity of the Rh_xS_y/C catalyst may therefore be due to the semiconducting properties of the Rh_2S_3 phase.

It should be possible to determine which phases contribute to the HER activity and what limits the HOR activity by isolating the rhodium sulfide phases both with and without a carbon support. For the oxygen reduction reaction in HCl on the Rh_xS_y/C catalyst, the Rh_3S_4 phase is believed to be the active phase, based on local structure analysis using X-ray absorption spectroscopy [9,10]. For the Rh_xS_y/C catalyst, it is thought that the Rh_3S_4 and Rh_2S_3 are amorphous, but present in the catalyst, making them difficult to characterize by X-ray diffraction [24]. Determination of the most active distribution of phases within a catalyst is not straightforward, as an intermediate mixture of $Rh_{17}S_{15}$-Rh was found to be most active for ORR [25].

Alternative routes exist to synthesize unsupported, crystalline Rh_2S_3 [26]. Depending upon the annealing conditions, Rh_2S_3 can be converted to the other phases by loss of sulfur

[18]. Rh_3S_4 can also be synthesized and characterized by X-ray diffraction [27,28], but $Rh_{17}S_{15}$ is still present in the mixture [19]. The phases formed are dependent on the temperature and stoichiometry of the sulfur and rhodium [19,27,28]. At a temperature of 1100 °C Rh_3S_4 or Rh_2S_3, may result depending on the stoichiometry of the rhodium and sulfur [27].

We are interested in understanding the relationship of the electrocatalytic activity of rhodium sulfide to the phases present in the catalysts. By synthesizing rhodium sulfide electrodes with different phases, their contributions to the hydrogen evolution activity can be determined. Further, with unsupported electrocatalysts the conductivity and photoconductivity of the semiconducting phases can be assessed. The unsupported electrodes can also be used for spectroscopic measurements such as Raman, without the confounding effects of the carbon support. This understanding of which phase is active will enable us to specifically synthesize more active catalyst phases while minimizing rhodium use. Further we hope this, with the help of theory will lead to understanding why hydrogen oxidation is not as active as hydrogen evolution. In this communication we address the following specific questions: 1) How can synthesis conditions (precursor, temperature, time, and ramp rate) be used to control the final phases of Rh_xS_y unsupported and supported on carbon? 2) What is the relation of Rh_xS_y phases to the activity of HER and HOR? 3) How does charge transfer conductivity of the Rh_xS_y phases compare to metallic catalysts, and does it limit the HOR activity?

B. Experimental

1. Carbon supported catalysts synthesis.

Pt/C was purchased from ETEK. Commercial Rh_xS_y/C was obtained from BASF. The commercial catalyst is synthesized by the addition of thio-containing compounds to a solution of rhodium salt, followed by heat treating. For the rhodium sulfide compounds on carbon synthesized in this work the sulfur source was H_2S, similar to that used for other metal sulfides [14,24], with the advantage of lower temperatures and thus potentially lower particle sizes [24]. The rhodium sulfide on carbon samples were synthesized by adding a 1M solution of $RhCl_3$ or $Rh(NO_3)_3$ to XC72 carbon then drying at 110 °C in air for one hour. The loading was selected to make 30 wt% metal. The dried precursor on carbon was heated in Ar or in 1:1 N_2:H_2S, and held at a given temperature in 1:1 N_2:H_2S before cooling (again either in Ar or in H_2S depending on the synthesis recipe). Conditions such as the ramp rate during heating, temperature, and time at maximum temperature were varied in an attempt to modify the final product. Certain samples were post-treated by annealing in argon.

2. Unsupported catalysts synthesis by hydrogen sulfide.

Hydrogen sulfide was reacted with a $Rh(NO_3)_3$ precursor in crucibles in a similar manner as the carbon supported catalysts. $Rh(NO_3)_3$ was used instead of rhodium chloride because it was easier to work with as a precursor when weighing out appropriate amounts of the rhodium due to the hygroscopic nature of the salt. Unsupported catalysts were also prepared using elemental sulfur by combining Rh, $RhCl_3$ or Rh/$RhCl_3$ and S in a quartz ampoule that was evacuated to 10^{-4} Torr and then heated to temperatures ranging from 1035-

1100 °C for 2 days. This method has previously been used to form Rh_3S_4, as well as Rh_2S_3 and $Rh_{17}S_{15}$ [19].

3. X-Ray Diffraction and Electron Microscopy.

X-ray diffraction (XRD) data was collected on a PANalytical, Inc. X'Pert powder diffractometer using a Cu Kα source (1.54 Å photon wavelength). Rietveld refinements to find the weight fraction of the crystalline phase were done using PyGSAS [29]. CIF files for Rh_2S_3, $Rh_{17}S_{15}$, Rh, RhS_2 and Rh_3S_4 were used for the refinement. Transmission electron micrographs of the catalyst were obtained using a TEM FEI T20-EDX.

4. Preparation of electrocatalyst inks and electrodes.

Inks of the electrocatalysts were synthesized by mixing 6 mg of the catalyst with 1 mL of 1:1 isopropanol:water, with 32 µL of a 5 wt% Nafion solution. This solution was ultrasonicated for 24 hours before use. The catalyst on carbon were synthesized at a slightly lower concentration, using 3 mg of catalyst on carbon with 5 mL of 1:1 isopropanol:water with 16 µL of a 5 wt% Nafion solution. Electrodes were prepared by depositing the ultrasonicated ink on a glassy carbon disk in a rotating disk electrode in 8 µL aliquots (for a total of 16 µL) and drying at 100 °C.

5. Hydrogen evolution and oxidation activity.

The HER activity of the electrocatalyst was measured by conducting a cyclic voltammogram in 1 M H_2SO_4 using a Pt counter electrode, a Ag/AgCl reference electrode, and a VSP Bio-Logic potentiostat. A Pine Instruments rotating disk electrode was used with 1500 rpm rotation rate. IR compensation was done with EC-Lab software (PEIS). The HOR activity was measured after bubbling hydrogen into 1 M H_2SO_4 solution while rotating at

specified speed until the open circuit voltage reached a constant value, then conducting a linear sweep voltammogram. The photoresponse of the unsupported catalysts was measured by turning on and off illumination from a Cuda Products white-light solar simulator halogen lamp to the catalyst and measuring the current response.

6. Double layer capacitance for surface area normalization.

Double layer capacitance was assumed to be proportional to the surface area of the catalyst-electrolyte interface. This surface area was used to normalize the hydrogen evolution currents of the unsupported electrodes. The capacitance was measured by conducting cyclic voltammetry in 1.0 M H_2SO_4 in the region of 0.4 to 0.6 V vs. Ag/AgCl at different scan rates (1000 to 20 mV/s). The total difference from the anodic and cathodic current at 0.5 V vs. Ag/AgCl is plotted against the scan rate. The slope of the trendline is proportional to the double layer capacitance and was used to normalize the current to the surface area of the electrocatalyst contacting the electrolyte [30]. The capacitance was assumed to be proportional to the surface area of the catalyst, regardless of the catalyst phase, as the area-average capacitance was unknown for the samples. Thus the finalized current densities are normalized, but do not give quantitative values for current density.

7. Raman spectra.

The samples were prepared for Raman measurements by depositing the electrocatalyst ink on a glass slide. The Raman spectra were taken using LabRam system (Horiba Jobin Yvon). Continuous wave 633 nm He-Ne laser was used for the incident light and the Raman emission was collected in a back scattering geometry using a confocal microscope.

8. Electrochemical charge transfer.

The charge transfer of the electrocatalyst was tested by running a cyclic voltammogram in 0.05 M Fe^{2+}/Fe^{3+} sulfate solution in 0.5M H_2SO_4 or in a solution containing methyl viologen dichloride. The counter electrode used was Pt and the reference electrode was Ag/AgCl.

C. Results and discussion

1. Effect of Synthesis Conditions on Crystalline Phases of Rhodium Sulfide

The crystalline structures present in rhodium sulfide samples synthesized using H_2S sulfidization were found by analysis of their X-ray diffraction patterns (Figures S1-6). The samples synthesized by solid sulfur and rhodium chloride in quartz ampoules were also characterized by X-ray diffraction (Figure S7-8).

Figure 1 shows the variation in rhodium sulfide phases due to synthesis temperature and the time of exposure to H_2S. All the conditions used for synthesis are summarized in Figure 1.

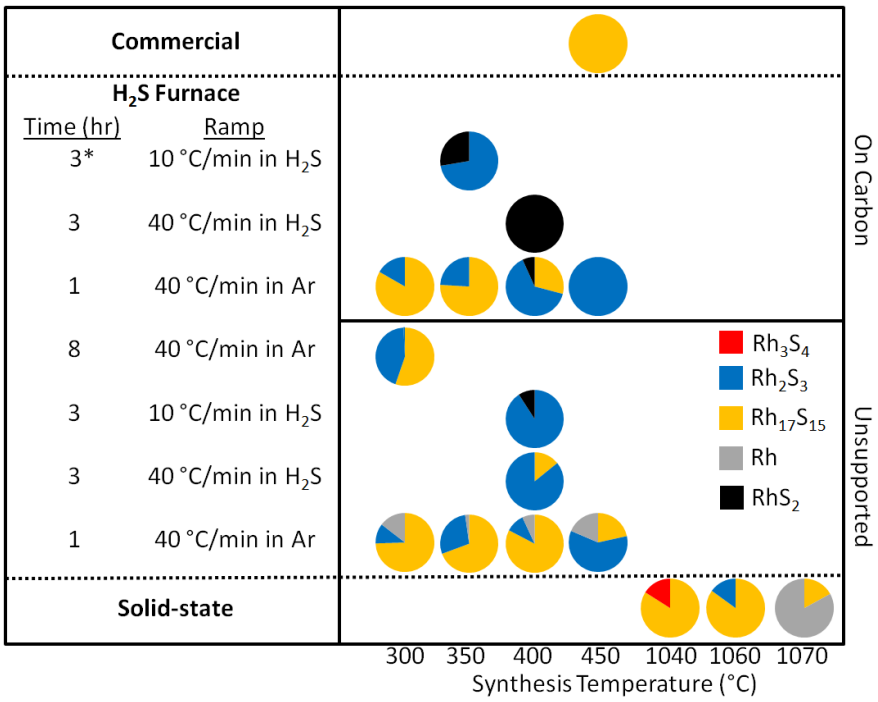

Figure 1. Synthesis conditions and resulting rhodium sulfide phase crystalline weight fractions determined by X-ray diffraction and quantified using Rietveld refinement. The y-axis is labeled with the method of synthesis. For the samples made in the H_2S furnace, they are labeled by the time the sample was held in flowing H_2S at given temperature, and the ramp rate to reach that temperature. During the ramp, it is specified whether a sample was ramped in H_2S or Argon (and then switched to H_2S). For the sample with an asterisk, the sample was annealed in Argon at 500 °C for 1 hour following cooling and removal from the H_2S furnace. The commercial Rh_xS_y/C catalyst (not synthesized using H_2S) is also shown for comparison, with weight fractions calculated from this work. For the solid-state samples, the reaction time was 2 days at temperature, with varying ratios of S to Rh/$RhCl_3$. All data represent crystalline phases only.

The stoichiometry of S to Rh precursors is known to affect the final phases formed [18,27], and the general trends are consistent with prior reports. The phase composition is based on the XRD and thus amorphous or small crystallites not detectable by XRD may exist in the samples and are not represented here. The commercial Rh_xS_y/C catalyst is reported to be $Rh_{17}S_{15}$ by XRD, with small grain sizes or amorphous clusters of Rh_2S_3 and Rh_3S_4 [9,10,24]. Here, by powder XRD and Rietveld refinement (Figure S1b) the composition of the commercial Rh_xS_y/C is solely $Rh_{17}S_{15}$ (Figure 1); however, the presence of Rh_2S_3 and Rh_3S_4 as small crystallites or amorphous clusters cannot be ruled out.

For the unsupported catalyst prepared using H_2S, by varying the synthesis temperature, ramp rate and time, the crystalline phase of the unsupported catalyst consists of different compositions of RhS_2, Rh_2S_3, $Rh_{17}S_{15}$ and metallic Rh. No Rh_3S_4 phase was seen from XRD for any of the H_2S-prepared unsupported samples. The samples that were heated in Ar to the synthesis temperature then exposed to H_2S, compared to the samples that were heated in the presence of H_2S had greater quantities of detectable metallic Rh. Metallic Rh was formed while heating, and was not given sufficient time at temperature to sulfidize to a rhodium sulfide phase (Figure 1). Also, exposing the precursor at 300 °C in H_2S for 8 hours formed an Rh_2S_3-heavier phase (rather than predominantly $Rh_{17}S_{15}$ phase when only exposed for 1 hour) indicating longer synthesis times, not unexpectedly, resulted in a more sulfidized product (Rh_2S_3). Under the same conditions, a carbon supported and unsupported catalyst showed different crystalline structure (Figure 1), likely due to the different kinetics of sulfidizing a nanoparticulate catalyst (carbon supported) compared to a larger catalyst particle (unsupported). An unreactive support (silica, not shown) formed similar crystalline phases to carbon supported under the same conditions.

Although the temperature of synthesis did not show a definitive trend towards a certain phase for the unsupported samples, lower temperatures for the carbon supported samples did appear to form less phases of rhodium sulfide with less sulfur ($Rh_{17}S_{15}$ compared to RhS_2 and Rh_2S_3). The trend observed was a higher S:Rh ratio with longer synthesis time, and/or at higher temperatures (allowing for more rapid reaction).

Phases not observable by XRD can also be present. It is possible that the Rh_3S_4 phase may be present but difficult to detect by XRD due to low crystallinity. Unlike the commercial catalyst which is heated-at higher temperatures, most of these catalysts are not exposed to temperatures above 450 °C, which may result in lower crystallinity undetectable

by XRD. Based on our formation mechanism hypothesis, in which the catalyst goes from least sulfidized ($Rh_{17}S_{15}$) to most sulfidized (Rh_2S_3 and RhS_2) as synthesis time in the presence of sulfur-containing reactants increases, it is possible that amorphous or small crystallite of Rh_3S_4 may be an intermediate sulfidized state in the transition between $Rh_{17}S_{15}$ to Rh_2S_3/RhS_2. The small window of synthesis of Rh_3S_4 between Rh_2S_3 and $Rh_{17}S_{15}$ has previously been reported [19]. However, without further characterization, we cannot definitely claim nor eliminate Rh_3S_4 as being synthesized by H_2S treatment of rhodium salts in this work.

At the higher temperatures investigated using the solid state synthesis of S and $RhCl_3$, some of the samples did result in formation of Rh_3S_4 (Figure S8). The presence of Rh_3S_4 based on XRD may be due to the higher temperature and time resulting in greater crystallinity of the Rh_3S_4 particles, allowing them to be detected.

2. Supported Rhodium Sulfide Electrocatalysts Activity for Hydrogen Evolution

The activity of the electrocatalysts supported on carbon may depend on the crystalline (detected by XRD) or amorphous (undetected by XRD) phases, and/or interactions between the two. Other characterization methods such as Raman spectroscopy were difficult to perform on the supported catalysts because of absorption by the carbon support. For the purpose of discussing the catalyst activity, the main phase detected by X-ray diffraction is discussed, unless otherwise denoted.

The Rh_xS_y/C catalyst is a commercially available catalyst that is a mixture of $Rh_{17}S_{15}$, Rh_2S_3 and Rh_3S_4 (Figure S1b). The other carbon supported catalysts tested shows predominantly the Rh_2S_3, RhS_2 or $Rh_{17}S_{15}$ (Figure S1a) phases by XRD, and their distribution is shown in Figure 1 (and in the caption of Figure 2). TEM of the Rh_xS_y/C

shows nanoparticulate Rh_xS_y clusters on carbon (Figure 2 inset). The commercial Rh_xS_y/C is the most active for hydrogen evolution (Figure 2), and the higher activity is due to either higher surface area or faster kinetics of the Rh_3S_4 and $Rh_{17}S_{15}$ phases compared to the Rh_2S_3 and RhS_2 phases. The voltage vs. Ag/AgCl required for a hydrogen evolution current density of -20 mA/cm^2 is -0.46 V for RhS_2/C, -0.40 V for Rh_2S_3/C, -0.40 V for $Rh_{17}S_{15}$/C and -0.34 V Rh_xS_y/C and for -50 mA/cm^2 the voltage required is -0.46 V for Rh_2S_3/C, -0.44V for $Rh_{17}S_{15}$/C and -0.4V for Rh_xS_y/C. It is not unexpected that catalysts with the same structure by XRD do not have the same activity; the active site may not be crystalline at all (such as Rh_3S_4 in the Rh_xS_y/C catalyst).

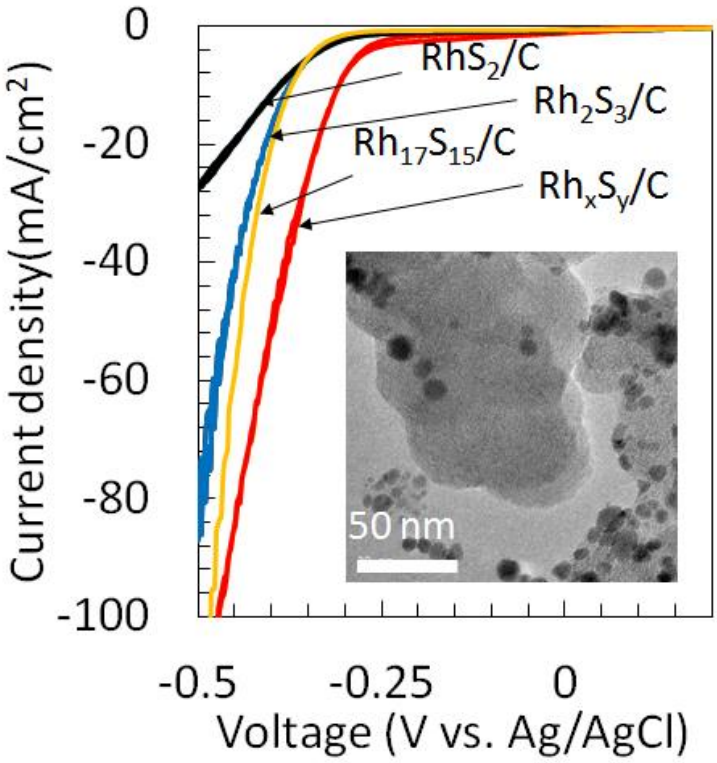

Figure 2. Hydrogen evolution activity of the RhS_2/C (pure RhS_2, in black), Rh_2S_3/C (72% Rh_2S_3 and 28% RhS_2, in blue), $Rh_{17}S_{15}$/C (83% $Rh_{17}S_{15}$ and 17% Rh_2S_3, in orange) and commercial Rh_xS_y/C ($Rh_{17}S_{15}$ in red) electrocatalysts on a rotating disk electrode in 0.5 M HBr at 2500 rpm with a Pt mesh counter electrode purged with Argon gas. The inset is a TEM image of the commercial Rh_xS_y/C catalyst.

The total charge transferred for hydrogen adsorption can be used as a way to normalize electrochemical active surface area [31] but the Rh_2S_3/C sample does not have appreciable hydrogen adsorption currents [26], and thus its active surface area cannot be determined to compare to the Rh_xS_y/C catalyst. To determine whether the difference in activity is due to a difference in the surface area, or to the presence of different phases (or mixture of phases), measurements on the unsupported catalyst were utilized because the surface area of the catalyst (without the carbon interference) can be measured by capacitance (Figure S11).

3. Unsupported Rhodium Sulfide Electrocatalysts for Hydrogen Evolution

For the unsupported catalysts prepared by H_2S, the crystalline phase of the unsupported catalyst consisted of varying fractions of RhS_2, Rh_2S_3, $Rh_{17}S_{15}$, and metallic rhodium (Figure S5-6). As mentioned previously, none of the unsupported samples prepared using H_2S as the sulfur source showed evidence of the Rh_3S_4 phase. However, several of the samples synthesized by solid state sulfur and rhodium precursors at high temperatures resulted in combinations of Rh_2S_3, Rh_3S_4, and $Rh_{17}S_{15}$ (by XRD, Figure S7-S8). The X-ray diffraction peaks of the samples synthesized by H_2S were much broader than the solid sulfur samples, indicating smaller crystallite sizes (20 nm or larger compared to 45 nm or larger, see discussion in SI). The cause of this is likely the higher temperatures used in the solid sulfur synthesis (>1000 °C, compared to ~400 °C for the H_2S). This appeared to affect the activity of the catalysts, as the samples prepared by solid sulfur had low activity for the same mass loading. The lower activity might be due to a lower surface area per mass, but even when normalizing to the electrochemical double layer, the activity of the solid sulfur synthesized samples was lower than the samples prepared at 400 °C in H_2S (Figure S13-14).

The effect of temperature on activity has been observed previously for the commercial catalyst, where a decrease in activity for oxygen reduction is measured when the catalyst is prepared at 725 °C compared to 650 °C [32], as the sample's crystallinity is increased (and possibly defects are reduced). In addition to the change in crystallinity with temperature, the distribution of phases may change (such as seen in the present work). It is difficult to determine whether crystallinity, phase distribution or defects are responsible for the change in activity (for ORR in previous work or HER in the present work). This indicates that synthesizing a particular phase of the catalyst (such as Rh_3S_4) may not necessarily give the highest activity. Factors such as dispersion, crystallinity, defects, and phases present may all contribute to the performance of the catalyst.

The Raman spectra indicated a change in the catalyst from the catalysts with $Rh_{17}S_{15}$ (synthesized at 450 °C, see Figure 1) to RhS_2/Rh_2S_3 heavy catalyst, which can be compared to the sparse Raman literature [33]. From the previously reported literature, $Rh_{17}S_{15}$ has Raman peaks at 160 cm^{-1}, a small peak at 185 cm^{-1}, and a set of peaks at ~230 and 260 cm^{-1} with shoulders at 300 cm^{-1} and 338 cm^{-1} [33]. Rh_2S_3 has Raman peaks at 170 cm^{-1}, 188 cm^{-1}, 270 cm^{-1}, 305 cm^{-1}, 338 cm^{-1}, and 378 cm^{-1} [33]. The peak at 113 cm^{-1} appears for the samples that show $Rh_{17}S_{15}$ by XRD and is absent in the Rh_2S_3 heavy sample. A peak at 164 cm^{-1} also appears for the samples with $Rh_{17}S_{15}$, matching that seen in the literature [33]. A peak at 200 cm^{-1} is present in the Rh_2S_3 phase as well as the $Rh_{17}S_{15}$ samples, but is not present in the literature, although the 185 cm^{-1} peaks seen in the literature may correspond to the same peaks. All samples include peaks at 275 cm^{-1} and 300 cm^{-1}, which are also present in the literature samples for both Rh_2S_3 and $Rh_{17}S_{15}$ [33]. The peak at 348 cm^{-1} in the Rh_2S_3 sample disappears for the samples that show less Rh_2S_3 by XRD. This 348 cm^{-1} peak is not

seen in the literature, and may correspond to other phases. Other unsupported $Rh_{17}S_{15}$ phases showed similar Raman to the 450 °C sample (Figure S9).

The higher HER activity of both the supported and unsupported Rh_xS_y catalyst (Figure 2 and Figure 3b) compared to the Rh_2S_3/RhS_2 catalyst indicates the activity is mainly from phases other than Rh_2S_3/RhS_2, although it does not appear to be that a pure $Rh_{17}S_{15}$ phase is the most active, as the phase that has mostly $Rh_{17}S_{15}$ with some Rh (400° C) is not the most active phase. In fact, the Rh metal present seems to contribute mostly to the activity, as the samples with a higher fraction of Rh (and higher ratio of Rh to S) seem to perform better. The voltage required to operate at a given hydrogen evolution current is -0.48V vs. Ag/AgCl for Rh_2S_3, -0.4 V for the sample synthesized at 350 °C, -0.38 V for the sample synthesized at 400 °C or 300 °C and -0.36 V for the sample synthesized at 450 °C. The presence of metallic Rh, although beneficial for hydrogen evolution activity, is not desirable due to the corrosion of Rh that occurs in HBr/Br_2. Thus an ideal catalyst would have high activity but without Rh present as a metal.

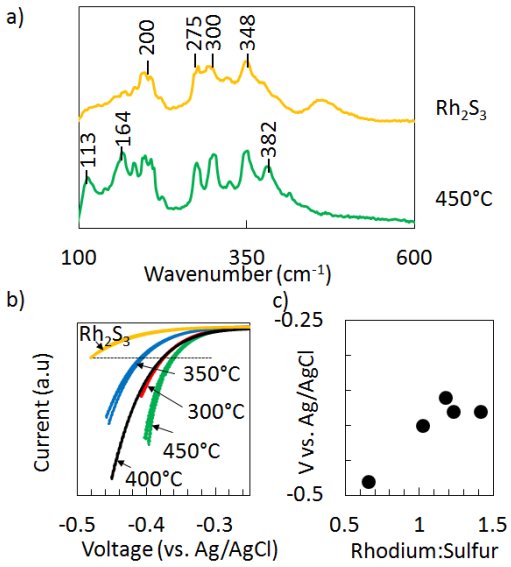

Figure 3. a) Raman spectra of the Rh_2S_3/RhS_2 catalyst and $Rh_{17}S_{15}/Rh_2S_3/Rh$ catalysts. b) Hydrogen evolution of electrocatalysts normalized to the capacitance of the electrode (to normalize to surface area), measured in 1 M H_2SO_4 at 1500 rpm against a Ag/AgCl reference electrode. Electrocatalyst phase fractions are shown in Figure 1. The samples labeled by a temperature indicate the synthesis temperature after a 40 °C/min ramp rate, and a synthesis time of 1 hour at the temperature indicated. The Rh_2S_3 catalyst was synthesized at 400 °C using a 10 °C/min ramp rate and contains majority Rh_2S_3 with some RhS_2. c) Voltage required to reach a set HER current for the 5 catalysts in b) marked by the dotted line, plotted against the weight ratio of Rh to S in the catalyst, determined from XRD and Rietveld analysis (shown in Figure 1).

For the unsupported samples, the current density was normalized to the capacitance of the sample (measured in a non-Faradaic region). Without this normalization (and IR compensation) sample to sample variation (of the same catalyst) was fairly great, but using the normalization technique the samples from the same synthesis gave identical activities (Figures S10-12). Based on investigation of both the unsupported and carbon-supported samples, it appears that the order of activity for the rhodium sulfide phases is $RhS_2 < Rh_2S_3 < Rh_{17}S_{15} < Rh_3S_4$, with Rh also having high activity but not useful in H_2-Br_2 flow cells due to stability issues. It is possible that the active site is also either a mixture of phases, or an amorphous cluster that is not identifiable by XRD, which is also supported by the fact that

samples synthesized at higher temperatures (using solid sulfur technique) are less active, even when correcting for surface area.

4. Influence of Charge Transfer on HER/HOR Activity

As mentioned, Rh_xS_y/C has been shown to be an excellent HER catalyst, but a less active HOR catalyst in a flow cell [6,14]. It is possible that the semiconducting properties of the catalyst (potentially of the Rh_2S_3,) is limiting electrode current and inhibiting oxidation reactions under reverse bias, but not reduction reactions under forward bias. It is also possible that the applied potential changes the surface of the electrocatalyst, similar to Pt being an excellent ORR catalyst but a poor OER catalyst, due to the formation of a platinum oxide species on the surface.[34] In addition to what has been observed in flow cells and fuel cells, Pt/C has higher HOR activity in an electrochemical cell than the Rh_xS_y/C catalyst (Figure 4), until mass transfer becomes limiting. At a hydrogen oxidation current density of 1.4 mA/cm^2 the voltage needed for Pt/C was 0.046 V vs. SHE and Rh_xS_y/C was 0.081 V vs. SHE indicating the low activity of HOR for Rh_xS_y/C is due to the catalyst itself, and not due to some effect of the construction of the membrane electrode assembly used in a flow cell.

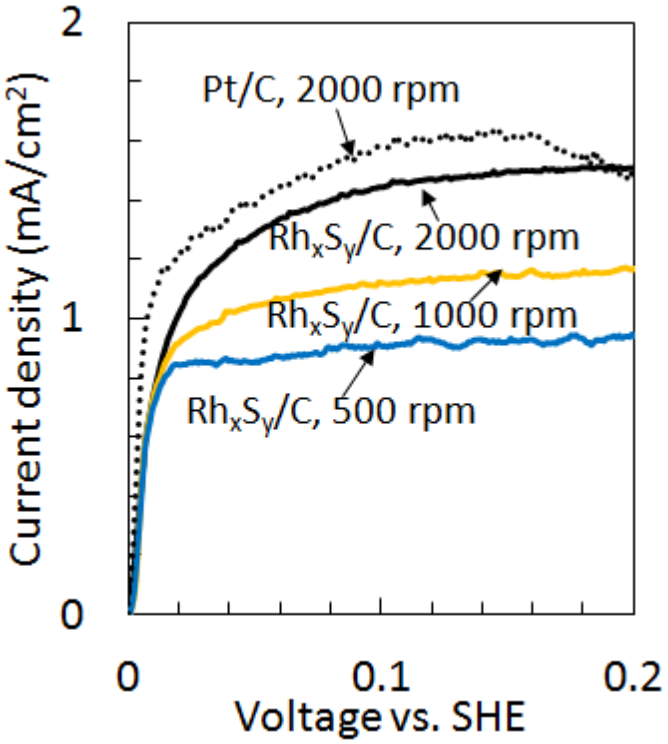

Figure 4. Hydrogen oxidation currents of Rh_xS_y/C and Pt/C, measured by varying the voltage from OCV (0 V vs. SHE) to more positive potentials at a scan rate of 20 mV/s. Displayed are Pt/C at 2000 rpm (black dotted line), Rh_xS_y/C at 2000 rpm (black solid line), Rh_xS_y/C at 1000 rpm (orange), and Rh_xS_y/C at 500 rpm (blue). Electrolyte was 1 M H_2SO_4, and the voltage was corrected from Ag/AgCl to SHE (open circuit voltage when bubbling 1 atmosphere H_2 onto catalyst). Counter electrode was a Pt mesh.

The increase in limiting hydrogen oxidation current with increasing rotation rate of the Rh_xS_y/C catalyst (Figure 4) indicates the hydrogen oxidation reaction is not charge transfer limited [16]. The current of a charge transfer limited reaction should be independent of rotation rate, as the current would be limited by the number of charge carriers, which is independent of mass transfer [16].

Similar to the carbon supported catalyst, the HER activity and HOR activity of an unsupported rhodium sulfide was tested (Figure S15a). This unsupported sample was chosen for investigation because its XRD (Figure S7) showed evidence of $Rh_{17}S_{15}$ and Rh_2S_3, but without the presence of Rh metal peaks. The presence of Rh metal would prevent the

separate evaluation of hydrogen oxidation and hydrogen evolution as the metals are bifunctional without any charge transfer limitations.

Based on the presence of the $Rh_{17}S_{15}$ and Rh_2S_3 peaks, it is possible that understanding the unsupported rhodium sulfide may give insight into the carbon supported rhodium sulfide. However, two major differences between unsupported and carbon supported catalysts are the size and number of defect states (not measured here) which could translate to differences in charge transfer.

One test for detecting if the semiconductor conductivity is limiting the oxidation reaction is to illuminate the sample. If the electrode is a semiconductor, electrons are excited to form charge carriers which can increase the current for an electrochemical reaction. For the carbon supported sample, this test is difficult because the carbon support acts to absorb much of the light, and it is difficult to determine if the catalyst is actually absorbing light. However, when the unsupported catalyst (from XRD shown to be mostly $Rh_{17}S_{15}$ and Rh_2S_3) was illuminated (using a distribution of photon energy simulating sunlight) no photogenerated carriers were observed as an increase in current during hydrogen oxidation (Figure S15a) supporting the proposition that the semiconductor conductivity did not limit the reaction, and corroborating the rotating disk measurements (Figure 4) [16].

An additional way to test the conductivity of an electrode is to use a non-catalytic redox couple (such as Fe^{2+}/Fe^{3+}). Metals such as Pt are capable of Fe^{2+} oxidation and Fe^{3+} reduction (Figure S15b). The unsupported Rh_2S_3 matched the Pt activity for Fe^{2+}/Fe^{3+} reactions (Figure S15b). Similar results were seen for methyl viologen reduction/oxidation. A semiconductor electrode that is oxidation limited would not show oxidation current in the absence of light [16]. Although theoretically a semiconductor, the Rh_2S_3 containing catalyst

was therefore observed to be an efficient bi-directional conductor possibly due to degenerate doping during synthesis.

An alternative reason for the low hydrogen oxidation current may be changes in the surface as a function of potential. Again, there is the possibility that nanoparticles in the carbon supported samples could behave differently than the unsupported catalyst, and it is possible that although the unsupported rhodium sulfide catalysts are not charge transfer limited, the carbon supported nanoparticles may still be. However, as mentioned the carbon support makes it impossible to directly test the conductivity of the catalyst by the methods described above.

D. Conclusions

The synthesis of rhodium sulfide by exposure of a rhodium precursor to hydrogen sulfide appears to follow a pathway of conversion from the precursor ($Rh(NO_3)_3$) to a distribution of Rh, RhS_2, Rh_2S_3, $Rh_{17}S_{15}$ and Rh. The synthesis products depend on the temperature and time exposed to H_2S; longer times give rise to catalysts with higher sulfur content phases (Rh_2S_3). The presence of the carbon support decreases the time or temperature required to form the same crystalline phase during synthesis as the unsupported catalyst.

The most active catalyst of supported or unsupported Rh_xS_y for HER was observed to contain both Rh_3S_4 and $Rh_{17}S_{15}$, in a mixture with Rh_2S_3 phase which does not, independently, add to the activity. Based on the lower activity of a mixture containing mostly $Rh_{17}S_{15}$, it is likely that Rh_3S_4 is contributing the majority of the HER activity, similar to what is observed for oxygen reduction. Although metallic Rh is highly active, it is not ideal for a H_2-Br_2 flow cell due to the instability of the metal in the electrolyte. The

conductivity of rhodium sulfide does not limit the hydrogen evolution or the hydrogen oxidation reactions, even thought the, theoretically semiconducting, Rh_2S_3 phase may be present. The difference in activity for hydrogen evolution and oxidation that has been observed in flow batteries and fuel cells and may be due to changes in the catalyst surface as a function of the electrode potential. The ideal catalyst therefore would be one with minimum amounts of Rh metal (due to its instability), minimal Rh_2S_3 and RhS_2 (due to their low activity) and a high concentration of Rh_3S_4 possibly requiring $Rh_{17}S_{15}$ for an as-yet-undefined synergistic role. The ideal catalyst surface would be stabilized for all potentials of interest (hydrogen evolution and hydrogen oxidation). The goal for improving the present catalysts is to modify synthesis conditions to maximize the proportion of Rh_3S_4 , while maintaining a high degree of dispersion in the catalyst to maximize the surface area of the active phase.

Acknowledgements

Financial support was by the National Science Foundation (EFRI-1038234). N. S is supported by the ConvEne IGERT Program (NSF-DGE 0801627). The authors made use of the MRL facilities at UCSB. The MRL facilities are supported by the MRSEC program of the NSF under award number DMR-1121053. The authors would like to thank Dr. Sylvia Lee for help with TEM measurements, Dr. Mubeen Syed Hussaini for help with Raman measurements and interpretation and Michael Gaultois for his help in using PyGSAS.

References

[1] A.Z. Weber, M.M. Mench, J.P. Meyers, P.N. Ross, J.T. Gostick, Q. Liu, Redox flow batteries: a review, J. Appl. Electrochem. 41 (2011) 1137–1164. doi:10.1007/s10800-011-0348-2.

[2] B. Dunn, H. Kamath, J.-M. Tarascon, Electrical energy storage for the grid: a battery of choices., Science (80-.). 334 (2011) 928–35. doi:10.1126/science.1212741.

[3] W. Glass, G.H. Boyle, Performance of Hydrogen-Bromine Fuel Cells, in: Fuel Cell Syst., 1969: pp. 203–220.

[4] G.G. Barno, S.N. Frank, T.H. Teherani, L.D. Weedon, Lifetime Studies in H2/Br2 Fuel Cells, J. Electrochem. Soc. 131 (1984) 1973–1980.

[5] K.T. Cho, P. Ridgway, A.Z. Weber, S. Haussener, V. Battaglia, V. Srinivasan, High Performance Hydrogen/Bromine Redox Flow Battery for Grid-Scale Energy Storage, J. Electrochem. Soc. 159 (2012) A1806–A1815. doi:10.1149/2.018211jes.

[6] T. Van Nguyen, H. Kreutzer, V. Yarlagadda, E. McFarland, N. Singh, HER/HOR Catalysts for the H2-Br2 Fuel Cell System, ECS Trans. 53 (2013) 75–81.

[7] V. Livshits, A. Ulus, E. Peled, High-power H2/Br2 fuel cell, Electrochem. Commun. 8 (2006) 1358–1362. doi:10.1016/j.elecom.2006.06.021.

[8] H. Kreutzer, V. Yarlagadda, T. Van Nguyen, Performance Evaluation of a Regenerative Hydrogen-Bromine Fuel Cell, J. Electrochem. Soc. 159 (2012) F331–F337. doi:10.1149/2.086207jes.

[9] J.M. Ziegelbauer, D. Gatewood, A.F. Gullá, M.J. Guinel, F. Ernst, D.E. Ramaker, et al., Fundamental Investigation of Oxygen Reduction Reaction on Rhodium Sulfide-Based Chalcogenides, J. Phys. Chem. C. 113 (2009) 6955–6968.

[10] J.M. Ziegelbauer, D. Gatewood, A.F. Gullá, D.E. Ramaker, S. Mukerjee, X-Ray Absorption Spectroscopy Studies of Water Activation on an Rh[sub x]S[sub y] Electrocatalyst for Oxygen Reduction Reaction Applications, Electrochem. Solid-State Lett. 9 (2006) A430. doi:10.1149/1.2218304.

[11] J.M. Ziegelbauer, D. Gatewood, S. Mukerjee, D.E. Ramaker, In Situ X-ray Absorption Spectroscopy Studies Of Water Activation On Novel Electrocatalysts For Oxygen Reduction Reaction In Acid Electrolyte, ECS Trans. 1 (2006) 119–128.

[12] J. Ziegelbauer, V. Murthi, C. Olaoire, A. Gullá, S. Mukerjee, Electrochemical kinetics and X-ray absorption spectroscopy investigations of select chalcogenide electrocatalysts for oxygen reduction reaction applications, Electrochim. Acta. 53 (2008) 5587–5596. doi:10.1016/j.electacta.2008.02.091.

[13] F.F. De Castro E., Tsou Y., Allen R., Martelli G., Oxygen-Depolarized Cathode for Aqueous Hydrochloric Acid Electrolysis: Part II, 2000.

[14] A. Ivanovskaya, N. Singh, R.-F. Liu, H. Kreutzer, J. Baltrusaitis, T. Van Nguyen, et al., Transition metal sulfide hydrogen evolution catalysts for hydrobromic acid electrolysis., Langmuir. 29 (2013) 480–492. doi:10.1021/la3032489.

[15] N. Singh, S. Mubeen, J. Lee, H. Metiu, M. Moskovits, E.W. McFarland, Stable electrocatalysts for autonomous photoelectrolysis of hydrobromic acid using single-junction solar cells, Energy Environ. Sci. (2014) 1–4. doi:10.1039/c3ee43709d.

[16] H. Colell, N. Alonso-Vante, H. Tributsch, Interfacial behaviour of semiconducting RuS2 electrodes : a kinetic approach, J. Electroanal. Chem. 324 (1992) 127–144.

[17] N. Singh, D.C. Upham, H. Metiu, E.W. McFarland, Gas-Phase Chemistry to Understand Electrochemical Hydrogen Evolution and Oxidation on Doped Transition Metal Sulfides, J. Electrochem. Soc. 160 (2013) A1902–A1906. doi:10.1149/2.002311jes.

[18] W. Zhang, K. Yanagisawa, S. Kamiya, T. Shou, Phase Controllable Synthesis of Well-Crystallized Rhodium Sulfides by the Hydrothermal Method, Cryst. Growth Des. 9 (2009) 3765–3770. doi:10.1021/cg900454g.

[19] J. Beck, T. Hilbert, An "old" Rhodiumsulfide with surprising Structure - Synthesis, Crystal Structure, and Electronic Properties of Rh3S4, Zeitschrift Für Anorg. Und Allg. Chemie. 626 (2000) 72–79.

[20] F. Hulliger, Crystal structure and electrical properties of some cobalt-group chalcogenides, Nature. 204 (1964) 644–646.

[21] A. Tan, S. Harris, Electronic Structure of Rh2S3 and RuS2, Two Very Active Hydrodesulfurization Catalysts, Inorg. Chem. 37 (1998) 2215–2222.

[22] O. Diéguez, First-principles characterization of the structure and electronic structure of α-S and Rh-S chalcogenides, Phys. Rev. B. 80 (2009) 1–6. doi:10.1103/PhysRevB.80.214115.

[23] B.S. Dey, V.K. Jain, Platinum Group Metal Chalcogenides, 2 (2004) 16–29.

[24] J.M. Ziegelbauer, A.F. Gullá, C. O'Laoire, C. Urgeghe, R.J. Allen, S. Mukerjee, Chalcogenide electrocatalysts for oxygen-depolarized aqueous hydrochloric acid electrolysis, Electrochim. Acta. 52 (2007) 6282–6294. doi:10.1016/j.electacta.2007.04.048.

[25] J. Ji, S. Lv, H. Liu, F. Wang, Z. Li, J. Liu, et al., Carbon-Supported Rh17S15-Rh Electrocatalysts Applied in the Oxygen Reduction Reaction, Electroanalysis. 26 (2014) 1099–1107. doi:10.1002/elan.201400069.

[26] A.F. Gullá, L. Gancs, R.J. Allen, S. Mukerjee, Carbon-supported low-loading rhodium sulfide electrocatalysts for oxygen depolarized cathode applications, Appl. Catal. A Gen. 326 (2007) 227–235. doi:10.1016/j.apcata.2007.04.013.

[27] K.T. Jacob, P. Gupta, Gibbs free energy of formation of rhodium sulfides, J. Chem. Thermodyn. 70 (2014) 39–45. doi:10.1016/j.jct.2013.10.011.

[28] J.R. Taylor, A knudsen cell study of molten sulfides: Thermodynamics of the Rh-S system, Metall. Trans. B. 12 (1981) 47–54. doi:10.1007/BF02674757.

[29] B.H. Toby, R.B. Von Dreele, GSAS-II : the genesis of a modern open-source all purpose crystallography software package, J. Appl. Crystallogr. 46 (2013) 544–549. doi:10.1107/S0021889813003531.

[30] D. Merki, H. Vrubel, L. Rovelli, S. Fierro, X. Hu, Fe, Co, and Ni ions promote the catalytic activity of amorphous molybdenum sulfide films for hydrogen evolution, Chem. Sci. 3 (2012) 2515. doi:10.1039/c2sc20539d.

[31] J.M. Doña Rodríguez, J.A. Herrera Melián, J. Pérez Peña, Determination of the Real Surface Area of Pt Electrodes by Hydrogen Adsorption Using Cyclic Voltammetry, J. Chem. Educ. 77 (2000) 1195. doi:10.1021/ed077p1195.

[32] K.S. Robert J. Allen, James R. Giallombardo, Daniel Czerwiec, Emory S. De Castro, Rhodium electrocatalyst and method of preparation, 2000.

[33] D.R. T., The RRUFF Project: an integrated study of the chemistry, crystallography, Raman and infrared spectroscopy of minerals, in: Programs Abstr. 19th Gen. Meet. Int. Mineral. Assoc. Kobe, Japan, 2006: pp. O03–13.

[34] B.E. Conway, T.-C. Liu, Characterization of Electrocatalysis in the Oxygen Evolution Reaction at Platinum by Evaluation of Behavior of Surface Intermediate States at the Oxide Film, Langmuir. 6 (1990) 268–276.

IX. Transition metal-rhodium thiospinels and platinum group metals incorporated into rhodium sulfide as acid stable electrocatalysts for hydrogen evolution and oxidation

Abstract

Rhodium thiospinels including $CuRh_2S_4$, $CoRh_2S_4$, $FeRh_2S_4$ and $NiRh_2S_4$ are synthesized on carbon by reacting metal chlorides with hydrogen sulfide at 350 °C. Low concentrations of palladium, ruthenium or iridium salts are mixed with rhodium chloride and reacted with hydrogen sulfide forming $Rh_{17}S_{15}$ on carbon ($Rh_{17}S_{15}$/C) with the minority metals Pd, Ru or Ir incorporated into the structure at low concentrations, and/or phase segregated. Rhodium sulfide samples with 1% Ir, Pd, and Ru have 12-16 nm crystallite size, measured by X-Ray Diffraction, compared to 11 nm for the pure rhodium sulfide. The hydrogen evolution and oxidation activities of the thiospinels in sulfuric acid are lower than pure $Rh_{17}S_{15}$/C, with $NiRh_2S_4$/C showing the highest activity of the thiospinels. $CuRh_2S_4$/C is unstable in the sulfuric acid electrolyte. The hydrogen evolution and oxidation activities for the 1% Pd, Ru and Ir in $Rh_{17}S_{15}$/C are slightly lower than pure $Rh_{17}S_{15}$/C based on i) geometric area for the same mass of deposited catalyst, ii) surface area of the carbon support measured by capacitance, and iii) electrocatalyst area calculated based on the crystallite sizes.

A. Introduction

A shift from fossil fuels to renewable energy sources such as solar and wind will require inexpensive energy storage. One potential clean method to store energy is through the electrochemical production of hydrogen. The electrochemical production of hydrogen

typically comes from protons in acidic environments such as proton-exchange-membrane electrolyzers or hydrohalic acids [1,2]. An electrocatalyst is required for the hydrogen evolution and oxidation reaction;

$$2H^+ + 2\,e^- \underset{\text{charge}}{\overset{\text{discharge}}{\rightleftharpoons}} H_2, \qquad E^0 = 0.00\ V$$

Although Pt/C is a stable electrocatalyst for the hydrogen evolution and oxidation reaction in acids, it suffers from stability issues in hydrohalic acids. Another class of promising acid-stable hydrogen evolution and oxidation electrocatalysts are metal sulfides. Metal sulfides are active for hydrogen evolution and hydrogen oxidation, while maintaining stability in hydrobromic acid and bromine, and doping can improve their electrocatalytic activity [4,5]. Of the metal sulfides, rhodium sulfide (Rh_xS_y/C), used also for oxygen depolarized cathodes in hydrochloric acid [6,7], is the best performing electrocatalyst for hydrogen evolution and oxidation [1], with the activity believed to be from the Rh sites in the $Rh_{17}S_{15}$ and Rh_3S_4 phases [8–10]. However, the effect of dopant metals on the stability and activity of Rh_xS_y/C has not been investigated.

Incorporating dopant metals into Rh_xS_y might improve the activity for hydrogen evolution or oxidation, or allow lower quantities of Rh to be used. Incorporation of non-Rh atoms into metallic Rh has been theorized to improve the hydrogen evolution activity [11], and a $NiRh_2S_4$ thiospinel prepared by co-precipitation had hydrodesulfurization activity above that of Rh_2S_3 or Ni_3S_2 compounds [12]. Thiospinels of Cu, Ni and Co also have improved hydrogen evolution activity and stability compared to nickel electrodes [13], and thiospinels consisting of Fe, Ni and Co have activity for oxygen reduction [14]. Dopants have also been shown to improve the electrochemical activity for hydrogen evolution on

metal sulfides [4]. We have hypothesized that the addition of platinum group or selected transition metals into Rh_xS_y will alter the electrocatalytic properties.

In this work we address the following questions:

1. What transition metal and platinum group metals can be incorporated into the Rh_xS_y structure, and at what concentrations does phase segregation between the rhodium and other metal compounds occur?
2. What is the influence of incorporated metal atoms into Rh_xS_y on electrochemical activity?
3. What is the activity of mixed metal-rhodium sulfide compounds, such as thiospinels, for hydrogen evolution and hydrogen oxidation?

B. Experimental methods

1. Electrocatalyst synthesis and physical characterization

Precursor solutions (precursor salts dissolved to 1 M in water) were deposited and mixed into XC-72 conductive carbon and dried at 110 °C for 1 hour to result in a final 30% metal weight fraction on carbon. The precursors and their concentrations relative to total metal atoms in the sample are indicated in Table 1. The precursors on carbon were then heated in argon to 350 °C, then reacted with hydrogen sulfide for 1 hour at 350 °C to form the metal sulfides then cooled in argon to room temperature. This process has been shown to form rhodium sulfide characterized by X-ray diffraction as predominantly $Rh_{17}S_{15}$ [10]. Using a similar approach with mixed salts reacted with H_2S has been shown to produce doped RuS_2 [4].

Table 1. Precursors' fractions (relative to total metal atoms) for mixed metal sulfides

Metal	Precursor	Precursor fractions used
Rh	$RhCl_3•x(H_2O)$	N/A

Fe	$FeCl_3 \cdot 6H_2O$	0.2, 0.3, 0.4
Co	$CoCl_2 \cdot 6H_2O$	0.2, 0.3, 0.4
Ni	$NiCl_2$	0.2, 0.3, 0.4
Cu	$CuCl_2 \cdot 2H_2O$	0.1, 0.15, 0.2, 0.3, 0.4
Ru	$RuCl_3 \cdot 3H_2O$	0.01, 0.1, 0.15, 0.2, 0.3, 0.4
Pd	$Pd(NO_3)_2 \cdot H_2O$	0.01, 0.1, 0.15, 0.2, 0.3, 0.4
Ir	$IrCl_3 \cdot 3H_2O$	0.01, 0.2, 0.4

The samples were characterized by X-Ray Diffraction using a PANalytical Empyrean Powder Diffractometer with a Cu Kα source.

2. Electrode preparation

Electrocatalyst inks were prepared by mixing 3 mg of electrocatalyst with 17.5 microliters of 5% Nafion solution, 2.5 mL water and 2.5 mL isopropanol. The inks were then ultrasonicated for 24 hours before use. Electrocatalysts were prepared on a rotating disk electrode by depositing 8 μL of ink on a glassy carbon disk, then drying at 120 °C for 20 minutes. This process was repeated to result in 16 total μL of ink deposited (although for some samples the amount of deposited material was varied to construct a calibration curve of deposited amount compared to capacitance).

3. Electrochemical characterization

Experiments were performed in 1M H_2SO_4 prepared using deionized water (18.2 MΩ cm, Millipore) and 18 M sulfuric acid (Sigma). Fresh electrolyte was used for each experiment to avoid contamination between samples. Cyclic voltammograms at 50 mV s^{-1} with no rotation were taken using a VSP Bio-Logic potentiostat to analyze the capacitance of the sample, as well as detect any hydrogen adsorption/desorption peaks, in 1 M H_2SO_4 purged for 20 minutes with argon, using an Ag/AgCl reference electrode and carbon counter

electrode. The Ag/AgCl reference electrode was calibrated by bubbling hydrogen through a 1 M H_2SO_4 solution and measuring against a cleaned Pt wire.

The electrocatalytic activity for hydrogen evolution and hydrogen oxidation was then measured at 1500 rpm in 1 M H_2SO_4 sparged with H_2 using an Ag/AgCl reference electrode and a carbon counter electrode (to avoid any dissolution and redeposition of Pt counter electrode on the working electrode). The resistance was compensated using Potentio Electrochemical Impedance Spectroscopy (PEIS).

C. Results and discussion

1. Crystalline structure of rhodium sulfide compounds

The Rh_xS_y samples with Fe, Co, Ni and Cu made using precursor concentrations of 10 to 40% show a combination of the thiospinel structure ($MeRh_2S4$, where Me = Fe, Co, Ni or Cu) and $Rh_{17}S_{15}$. At 30% of additive metal salt, X-ray diffraction of the electrocatalysts with Fe, Cu, Co and Ni showed the formation of predominantly a thiospinel structure, Figure 1. The pure Rh_xS_y shows a $Rh_{17}S_{15}$ crystal structure, evident by the peak fingerprint from approximately 38-42 °, which are absent in the mixed metal sulfides.

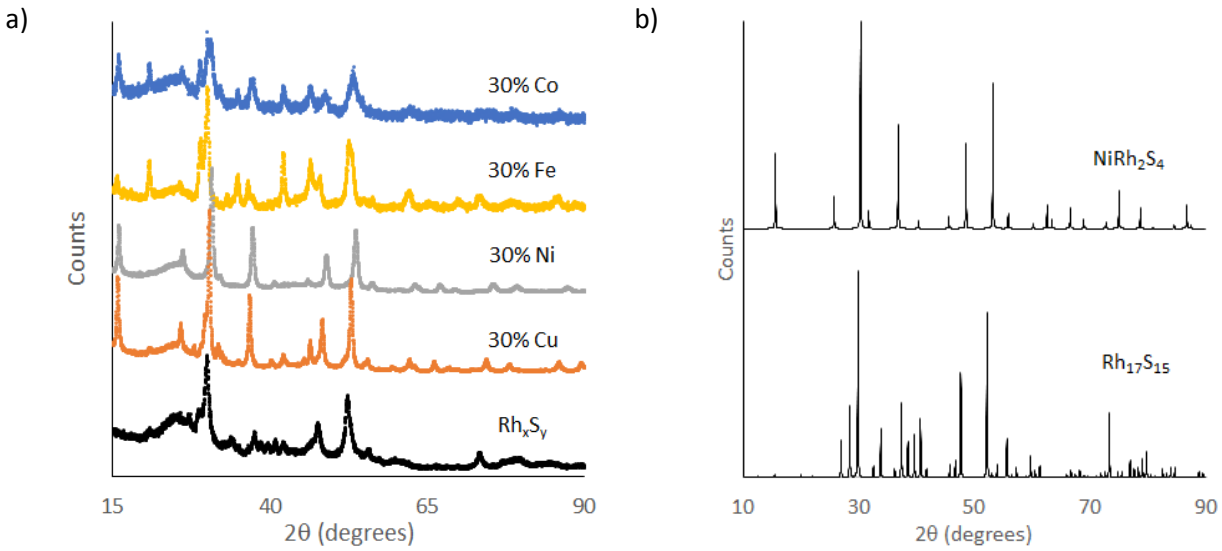

Figure 1. X-ray diffraction peaks of a) pure rhodium sulfide sample (Rh_xS_y) and with 30% Cu, Ni, Fe, and Co, all supported on carbon, and b) X-ray diffractograms from CIF files of $NiRh_2S_4$ and $Rh_{17}S_{15}$

At low concentrations of different transition metals (20%, Figure S1a) the $Rh_{17}S_{15}$ phase is prevalent, with some evidence of thiospinel. At higher concentrations (30%, Figure 1 and 40%, Figure S1b), the thiospinel is predominant, and less $Rh_{17}S_{15}$ is observed. Secondary phases begin to form when the non-Rh metal salt concentration exceeded 30%, e.g. Co_9S_8 for the Co/Rh mixture. This is expected since the ratio of Rh to the other metal in the thiospinel is 2:1. For non-Rh metal amounts below 33%, there is insufficient transition metal to completely form the thiospinel, leaving excess rhodium precursor to form the $Rh_{17}S_{15}$ phase. Above 33% there is excess transition metal precursor to form a separate, non-rhodium phase. It is unclear whether some of the transition metal is incorporating into the $Rh_{17}S_{15}$ structure in addition to the thiospinel formation, but the thiospinel appears to be more favorable for the added transition metal. The crystallite size determined from X-Ray Diffraction using the Scherrer Equation is slightly larger for the thiospinels than for the 1% Ir, Pd and Ru and pure phase rhodium samples (Table 2), indicating potentially lower dispersion of the thiospinel electrocatalysts.

Table 2. Electrocatalyst predominant structure by X-ray diffraction and crystallite size calculated by Scherrer Equation assuming shape factor of 1

Electrocatalyst precursors	Structure by XRD	Peak position (°2θ)	FWHM (°2θ)	Crystallite size (nm)
100% Rh	$Rh_{17}S_{15}$	52.26	0.877	11
30% Fe, 70% Rh	$FeRh_2S_4$	52.87	0.474	21
30% Co, 70% Rh	$CoRh_2S_4$	53.67	0.678	15
30% Ni, 70% Rh	$NiRh_2S_4$	52.42	0.642	15
30% Cu, 70% Rh	$CuRh_2S_4$	42.05	0.563	17
1% Ru, 99% Rh	$Rh_{17}S_{15}$	52.28	0.688	14
1% Pd, 99% Rh	$Rh_{17}S_{15}$	52.26	0.614	16
1% Ir, 99% Rh	$Rh_{17}S_{15}$	52.08	0.814	12

For the samples with platinum group metals (Ru, Ir, Pd) mixed with rhodium at higher concentrations, phases other than $Rh_{17}S_{15}$ form. Unlike Fe, Co, Ni and Cu, the platinum group metals do not appear to form a thiospinel. Instead, a separate secondary phase is observed, as observed for more than 10% Ru (Figure 2a) where the secondary phase observed is RuS_2, rather than a phase incorporated with rhodium sulfide.

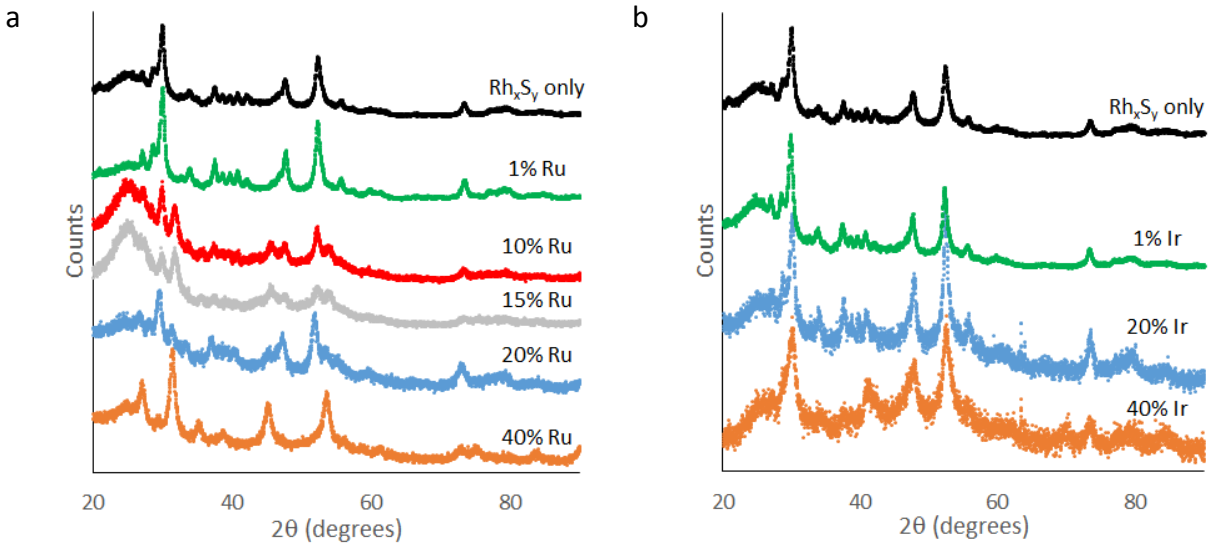

Figure 2. X-ray diffractograms of samples with a) ruthenium precursor and b) iridium precursor mixed with rhodium precursor on carbon and exposed to hydrogen sulfide.

For Ir (Figure 2b) and Pd (Figure 3a) mixed with rhodium sulfide, changes to the crystal structure also occur at higher concentrations. For 20% Ir the X-ray diffractogram is

similar to the pure rhodium sulfide, but at 40% a change in the $Rh_{17}S_{15}$ structure is evident. Although the absence of a secondary phase at 1% concentration (precursor) may be due to detection limitations of the instrument, lattice parameter changes are observed when the non-Rh PGM is added, by a shift in the peak locations seen in XRD (Figure 3b). The lattice parameter shift may be due to lattice strain caused by incorporation of a Pd atom into the $Rh_{17}S_{15}$ structure, rather than the Pd forming separate phases (as they do at higher concentrations). Although typically the lattice parameter shift can be predicted using Vegard's relations if the incorporated atom has a similar structure (for example, Fe being incorporated into a RuS_2 structure where both the RuS_2 and FeS_2 lattice parameters are known), information for $Pd_{17}S_{15}$ is not available to determine whether the parameter shift seen in Figure 3 is proportional to what would be expected from a Vegard's relation. The lattice parameter shift could also be due to changes in crystallite sizes, such as seen between the pure rhodium sulfide and 1% Pd in rhodium sulfide (Table 2).

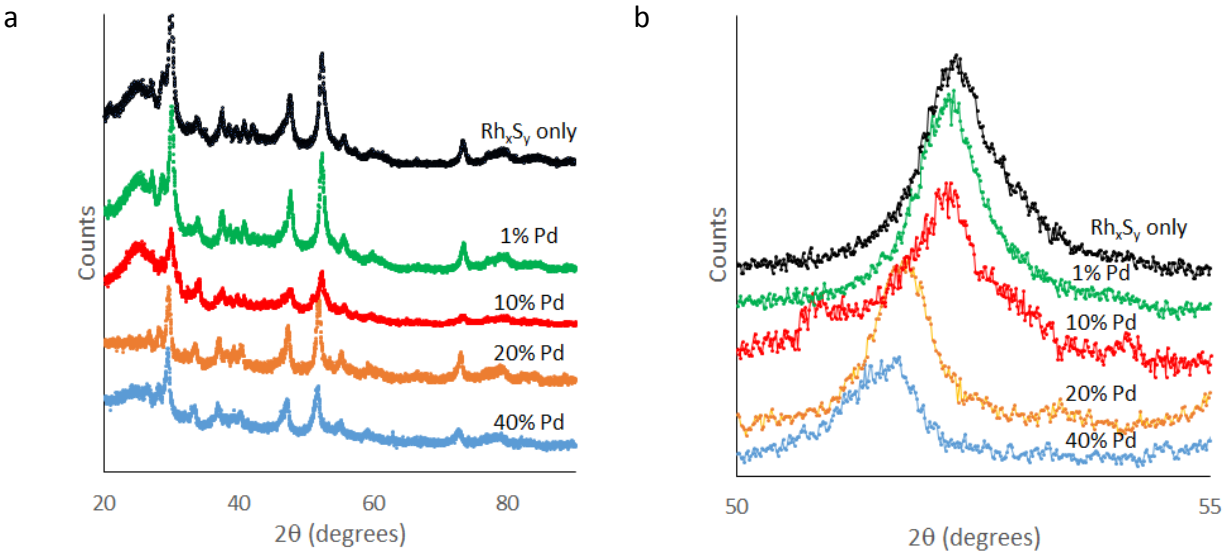

Figure 3. X-ray diffractograms of samples with palladium precursor mixed with rhodium precursor on carbon and exposed to hydrogen sulfide from a) 20 to 90 degrees 2θ and b) 50 to 55 degrees 2θ to show the shift in peak location.

For the purpose of electrochemical investigation, the low concentrations of the platinum group metals (1%) in rhodium sulfide are considered, along with the stoichiometric thiospinel structures formed (30% non-Rh transition metal).

2. Hydrogen evolution and oxidation stability and activity of rhodium sulfide compounds

Before testing the HER and HOR activity, the stability of the rhodium sulfide-based materials was evaluated by cyclic voltammetry. The 30% Cu in rhodium sulfide (predominantly $CuRh_2S_4$ as characterized by XRD) appeared to be unstable, evident by an anodic and cathodic (around -0.25 V vs. Ag/AgCl) current peak possibly attributed to Cu oxidation and reduction (Figure S2). The hydrogen evolution activity of the $CuRh_2S_4$/C catalyst also decreased following these oxidation and reduction reactions. Whether this is due to dissolution or conversion of the active phase, or oxidation of copper ions followed by re-deposition on and poisoning of the active phase is unclear. The $FeRh_2S_4$/C, $CoRh_2S_4$/C and $NiRh_2S_4$/C and $Rh_{17}S_{15}$/C electrocatalysts did not have similar redox peaks. Thus, the $CuRh_2S_4$/C electrocatalyst was not further evaluated in this study.

The capacitances were measured for deposited $NiRh_2S_4$/C, $CoRh_2S_4$/C, and $FeRh_2S_4$/C (Figure S3) and the 1% Ru, Pd, Ir samples (Figure S4) by cyclic voltammetry to determine an approximation for the carbon support surface area. The capacitance, assumed to be mostly due to the carbon support, is thought to be proportional to the catalyst support surface area, and can be approximated using a capacitance per unit area of 10-30 $\mu F\ cm^{-2}$ (20 $\mu F\ cm^{-2}$ was used in this work) [15]. The amount of deposited electrocatalyst was adjusted to ensure that the electrocatalyst capacitance of all samples was the same order of magnitude, and sufficiently larger than the background capacitance of the glassy carbon disk.

By modelling the crystallites as cubes with sizes determined using X-ray diffraction data, where one cube face was in contact with the carbon support [16], an approximate surface area of metal sulfides is determined (Table 3). This assumes a uniform distribution of sizes, and the absence of amorphous metal sulfide (or that the amorphous particles are the same size as the crystallites). Therefore, the surface area should be seen as an approximation, whose main purpose is to differentiate between changes in current density due to inherent activity of the electrocatalyst and changes in the current density due to crystallite sizes and electrocatalyst dispersion.

The lower density of the metal sulfides compared to platinum means for the same carbon area the metal sulfides have a higher surface area than a metal-only electrocatalyst such as Pt, even if the crystallite sizes are the same. Note the mass is 30% metal on carbon, and slightly higher on a metal sulfide basis

Table 3. Capacitance from Figure S3-4 (measured from current at 0.1 V vs. Ag/AgCl), estimated carbon area, crystallite size measured by XRD (from Table 2) and estimated metal sulfide area based on modelling as cubes of crystallite size length. Geometric surface area of RDE was 0.28 cm^2.

	Capacitance (μF)	Estimated carbon area (cm^2)	Density (g cm^{-3})	Crystallite size (nm)	Estimated metal sulfide area (cm^2)
$Rh_{17}S_{15}$/C	64	3.2	7.61	11	0.29
$FeRh_2S_4$/C	114	5.7	5.35	21	0.45
$CoRh_2S_4$/C	75	3.7	5.62	15	0.40
$NiRh_2S_4$/C	93	4.7	5.71	15	0.48
1% Ru	72	3.6	7.61	14	0.26
1% Pd	72	3.6	7.61	16	0.23
1% Ir	67	3.4	7.61	12	0.28

Although this is an imperfect approximation, using it for a Pt/C sample shows it can give a reasonable approximation (factor of 2) for the active area. This is discussed in the Supporting Information (including Figure S5-6 and Table S1). The actual electrochemical surface area of Pt can be determined based on hydrogen underpotential deposition [17].

On a geometric current density basis, the HER and HOR activity of the thiospinels, is lower than the pure rhodium sulfide electrocatalyst, Figure S7. When normalizing, instead, to the estimated metal sulfide area based on XRD data, the pure rhodium sulfide electrocatalyst is still more active (Figure 4). The smaller crystallite size and thus higher dispersion of the rhodium sulfide electrocatalyst makes it appear more active on a geometric surface area rather than estimated electrocatalyst area, but even with normalization, the thiospinels are less active, even when accounting for the lower amount of rhodium compared to other metal. Of the thiospinels, the $NiRh_2S_4$ was the most active, but was still less active than the $Rh_{17}S_{15}$ catalyst. To be an active electrocatalyst for both oxidation and reduction reactions, it is preferable that the material has metallic-conductivity. $Rh_{17}S_{15}$ has metallic behavior [8], $CuRh_2S_4$ has simple metallic behavior [18,19], $NiRh_2S_4$ has metallic conductivity [19,20], but $FeRh_2S_4$ [21] and $CoRh_2S_4$ [21,22] have semiconducting behavior. Thus it is possible that $FeRh_2S_4$ and $CoRh_2S_4$ are not as good electrocatalysts for oxidation and reduction reactions because of their semiconducting behavior.

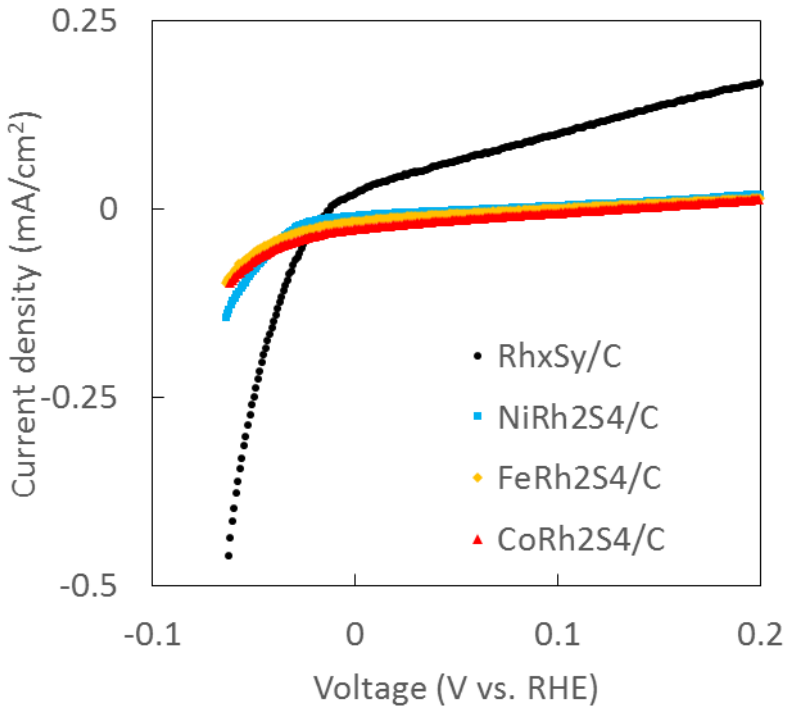

Figure 4. Hydrogen evolution and oxidation activity for $NiRh_2S_4$, $FeRh_2S_4$ and pure rhodium sulfide in 1 M H_2SO_4 with 1500 rpm rotation. IR compensated and current density based on approximated surface area of the metal sulfide from crystallite size and carbon surface area due to capacitance.

Although the metal-to-sulfur ratio of the thiospinels is the same as that of Rh_3S_4, believed to be active for HER/HOR [8–10], the thiospinels do not contain the six-Rh cluster believed to be the active site of Rh_3S_4 [8].

The HER and HOR activity of the 1% Ru, Ir and Pd samples appears to be lower than the pure rhodium sulfide electrocatalysts on both geometric current density (Figure S8), and when normalizing to the estimated metal sulfide surface area (Figure 5). However, when accounting for these possible differences in electrocatalyst area, Ru and Pd (which had slightly lower crystallite sizes than the pure rhodium sulfide) have more comparable activity to the pure rhodium sulfide.

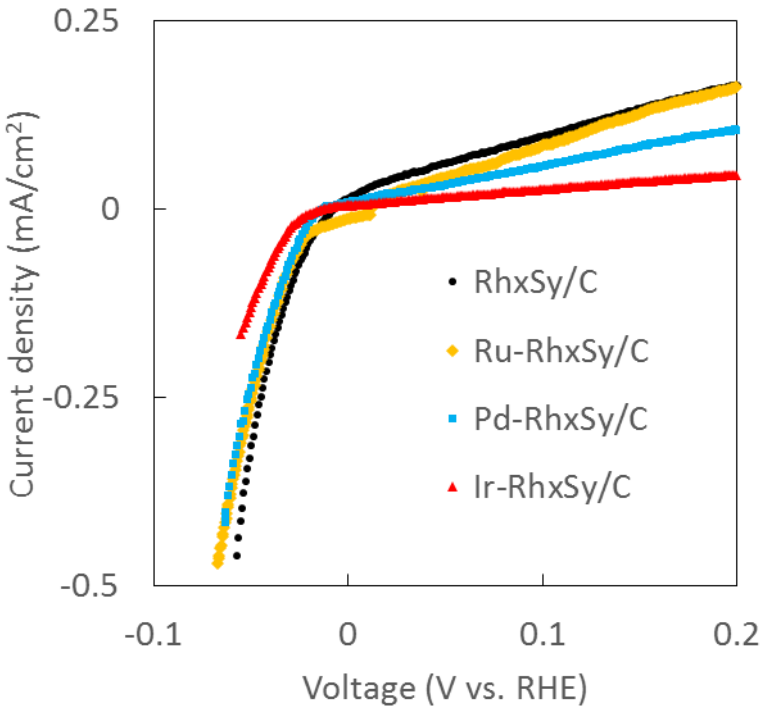

Figure 5. Hydrogen evolution and oxidation activity for 1% Ru, Pd, Ir and pure rhodium sulfide in 1 M H_2SO_4 with 1500 rpm rotation. IR compensated and current density based on approximated surface area of the metal sulfide from crystallite size and carbon surface area due to capacitance.

Unlike the thiospinels, any differences in the activity between the pure rhodium sulfide and non-Rh PGM electrocatalysts are believed to be due to the effect of incorporated Ru, Ir or Pd atoms, as additional, new phases of metal sulfides are not identified by X-ray diffraction. Thus, Ir, Ru and Pd incorporation into the structure do not appear to improve the $Rh_{17}S_{15}$ activity. However, if the incorporation of atoms is not near the surface, it is possible that the electrocatalytic activity (which is dependent on the surface) may not be affected.

D. Conclusions

A rhodium thiospinel structure forms for mixtures of rhodium with transition metals Cu, Fe, Co, and Ni, but as the precursor concentration deviates from the stoichiometric 2:1 ratio of Rh to transition metal in the $MeRh_2S_4$ structure, $Rh_{17}S_{15}$ dominates (for transition

metal concentrations below 30%) or segregated phases, such as Co_9S_8 for Co, appear (for 40%). Although it is possible that the transition metals are incorporating into the $Rh_{17}S_{15}$ structure, the thiospinel structure is favored. The thiospinel structure is not formed when using platinum group metal precursors (Ru, Ir, Pd) along with rhodium. Instead, it appears that the non-Rh platinum group metals incorporate into the $Rh_{17}S_{15}$ structure at low concentrations, and at 10% and higher concentrations, secondary phases are formed, such as RuS_2 or metallic crystals, or the $Rh_{17}S_{15}$ structure is lost.

The thiospinels showed low activity for hydrogen evolution and oxidation compared to $Rh_{17}S_{15}$/C, with $NiRh_2S_4$/C showing the highest activity of the thiospinels, and $CuRh_2S_4$/C showing instability in sulfuric acid. The $Rh_{17}S_{15}$/C incorporated with 1% Ir showed lower activity than the $Rh_{17}S_{15}$/C on a mass of catalyst basis, geometric surface area, carbon support surface area basis and based on approximated metal sulfide surface area, and the Ru and Pd showed lower activity, however this appeared to be partially due to the lower particle sizes of these samples, resulting in lower dispersion.

Acknowledgements

Financial support was by the National Science Foundation (EFRI-1038234). The MRL Shared Experimental Facilities are supported by the MRSEC Program of the NSF under Award No. DMR 1121053; a member of the NSF-funded Materials Research Facilities Network.

References

[1] T. Van Nguyen, H. Kreutzer, V. Yarlagadda, E. McFarland, N. Singh, HER/HOR Catalysts for the H2-Br2 Fuel Cell System, ECS Trans. 53 (2013) 75–81.

[2] K.T. Cho, P. Ridgway, A.Z. Weber, S. Haussener, V. Battaglia, V. Srinivasan, High Performance Hydrogen/Bromine Redox Flow Battery for Grid-Scale Energy Storage, J. Electrochem. Soc. 159 (2012) A1806–A1815. doi:10.1149/2.018211jes.

[3] N. Singh, E.W. McFarland, Levelized cost of energy and sensitivity analysis for the hydrogen–bromine flow battery, J. Power Sources. 288 (2015) 187–198. doi:10.1016/j.jpowsour.2015.04.114.

[4] A. Ivanovskaya, N. Singh, R.-F. Liu, H. Kreutzer, J. Baltrusaitis, T. Van Nguyen, et al., Transition metal sulfide hydrogen evolution catalysts for hydrobromic acid electrolysis., Langmuir. 29 (2013) 480–492. doi:10.1021/la3032489.

[5] N. Singh, D.C. Upham, H. Metiu, E.W. McFarland, Gas-Phase Chemistry to Understand Electrochemical Hydrogen Evolution and Oxidation on Doped Transition Metal Sulfides, J. Electrochem. Soc. 160 (2013) A1902–A1906. doi:10.1149/2.002311jes.

[6] A.F. Gullá, L. Gancs, R.J. Allen, S. Mukerjee, Carbon-supported low-loading rhodium sulfide electrocatalysts for oxygen depolarized cathode applications, Appl. Catal. A Gen. 326 (2007) 227–235. doi:10.1016/j.apcata.2007.04.013.

[7] J.M. Ziegelbauer, A.F. Gullá, C. O'Laoire, C. Urgeghe, R.J. Allen, S. Mukerjee, Chalcogenide electrocatalysts for oxygen-depolarized aqueous hydrochloric acid electrolysis, Electrochim. Acta. 52 (2007) 6282–6294. doi:10.1016/j.electacta.2007.04.048.

[8] N. Singh, D.C. Upham, R.-F. Liu, J. Burk, N. Economou, S. Buratto, et al., Investigation of the active sites of rhodium sulfide for hydrogen evolution/oxidation using carbon monoxide as a probe., Langmuir. 30 (2014) 5662–8. doi:10.1021/la500723y.

[9] J. Masud, T. Van Nguyen, N. Singh, E. McFarland, M. Ikenberry, K. Hohn, et al., A RhxSy/C Catalyst for the Hydrogen Oxidation and Hydrogen Evolution Reactions in HBr, J. Electrochem. Soc. 162 (2015) F455–F462. doi:10.1149/2.0901504jes.

[10] N. Singh, J. Hiller, H. Metiu, E. McFarland, Investigation of the Electrocatalytic Activity of Rhodium Sulfide for Hydrogen Evolution and Hydrogen Oxidation, Electrochim. Acta. 145 (2014) 224–230. doi:10.1016/j.electacta.2014.09.012.

[11] J. Greeley, T.F. Jaramillo, J. Bonde, I.B. Chorkendorff, J.K. Nørskov, Computational high-throughput screening of electrocatalytic materials for hydrogen evolution., Nat. Mater. 5 (2006) 909–13. doi:10.1038/nmat1752.

[12] H. Yasuda, C. Geantet, P. Afanasiev, M. Aouine, T. Epicier, M. Vrinat, Preparation, structural and hydrotreating catalytic properties of unsupported NiRh2S4, New J. Chem. 26 (2002) 1196–1200. doi:10.1039/b200914p.

[13] N.M. Yurchuk, A.N. Sofronkov, L.I. Korolenko, V.P. Petrosyan, Hydrogen Evolution Overvoltage on Thiospinels of Metals with Variable Oxidation State and Their Corrosion Resistance, Russ. J. Appl. Chem. 71 (1998) 1267–1268.

[14] H. Behret, H. Binder, G. Sandstede, Electrocatalytic oxygen reduction with thiospinels and other sulphides of transition metals, Electrochim. Acta. 20 (1975) 111–117. doi:10.1016/0013-4686(75)90047-X.

[15] H. Kim, B.N. Popov, Characterization of hydrous ruthenium oxide/carbon nanocomposite supercapacitors prepared by a colloidal method, J. Power Sources. 104 (2002) 52–61. doi:10.1016/S0378-7753(01)00903-X.

[16] J.F. Connolly, R.J. Flannery, G. Aronowitz, Electrochemical Measurement of the Available Surface Area of Carbon-Supported Platinum, J. Electrochem. Soc. 113 (1966) 577. doi:10.1149/1.2424030.

[17] W. Sheng, H.A. Gasteiger, Y. Shao-Horn, Hydrogen Oxidation and Evolution Reaction Kinetics on Platinum: Acid vs Alkaline Electrolytes, J. Electrochem. Soc. 157 (2010) B1529. doi:10.1149/1.3483106.

[18] G. Blasse, D.J. Schipper, Sulphospinels containing rhodium, J. Inorg. Nucl. Chem. 26 (1964) 1467–1468.

[19] N. Matsumoto, R. Endoh, S. Nagata, T. Furubayashi, T. Matsumoto, Metal-insulator transition and superconductivity in the spinel-type Cu(Ir1-xRhx)2S4 system, Phys. Rev. B. 60 (1999) 5258–5265.

[20] H. Itoh, A New Ferromagnetic Spinel System Ni(Rh1-xCrx)2S4 (0.15<x<0.40) with Metallic Conduction, J. Phys. Soc. Japan. 46 (1979) 1127–1130.

[21] H. Kondo, Mossbauer Study of FexCo1-xRh2S4 with Spinel Structure, J. Phys. Soc. Japan. 41 (1976) 1247–1254.

[22] G. Blasse, Antiferromagnetism of CoRh2S4, Phys. Lett. 19 (1965) 1965.